

aimed at accurately reflecting environmental processes. In this paper we examine the potential effects of microbial activity on repository performance and present a perspective for future directions to better understand and predict these effects. Specifically, we provide an assessment of standard and non-standard microbiological techniques with respect to their potential for providing information of use to the Yucca Mountain Project.

6.2.2.1 Biodegradation of Polymers. While natural polymers are readily broken down by microbes, synthetic polymers are more resistant. One reason for this is that a main source of energy for micro-organisms is the breaking of the carbon-hydrogen bonds which release energy. Another reason is that the enzymes required to break down these synthetic polymers are not found in nature. The biodegradation of polymers is also dependent upon the intrinsic viscosity and the product structure. For example, a flexible foam will degrade faster than a rigid foam which will degrade faster than a solid product. A last reason is that the most important type of enzymatic polymer cleavage reaction is hydrolysis which occurs exclusively inside microbial cells. Thus high molecular mass polymers would need to enter the cytoplasm before depolymerization (Schink et al., 1992). It would seem that by copolymerizing a synthetic polymer with a natural polymer, degradation could be achieved. This, however, is not the case. Studies in which starch is incorporated into the polymer structure have shown that while the starch components do degrade, the synthetic polymer structure only collapses into smaller pieces which still resist degradation. However, many degradation products of polymers are biodegradable.

Because *polyamides* are hydrophilic it seems that they might be susceptible to microbial attacks. This, however, has been refuted in many tests and "it is well known that these compounds are generally resistant to microbial degradation as their chemical structures are not found in natural polymers (Andreoni et al., 1993). Although, polyamides have been created which can be degraded, this is a far cry from the degradation of a commercial nylon product. Even nylon 6, which tends to have less desirable properties than the widely used nylon 6,6 are not biodegradable when the number average molecular weight is greater than 1000 (Andreoni et al., 1993) (a polymer of this small size would not be useful for any commercial products).

Polyesters used in the manufacture of a polyurethane have been shown to be degraded by fungi. The polyester segment of a the polymer is the main site for attack which could be degraded within two weeks (Kay et al., 1993). However, these experiments were supplemented with yeast and the assumption was made that the polymer was consumed as a result of cometabolism. In another study of bacterial

degradation of polyester polyurethane (Kay et al., 1991), it was found that bacteria could not degrade the polymer within a 12 week test period. Clearly as in most cases of biodegradation the type of microorganism and the environmental conditions are important variables.

There has been some study of the possible degradation of *polyethylene* as it would be something desirable from the standpoint of diminishing the growth of land fill. It has been found that polyethylene does not readily biodegrade. One study tested several types of bacteria on their ability to degrade polyethylene. It was found that only one type could degrade the polyethylene and then only when the sample was put in a medium which was desirable for the bacteria; no degradation of the control samples occurred. The study further hypothesized that polyethylene is degraded into its simple components (Awasthi, 1993). In addition, it was found that degradation increased when oxygen levels were increased. Polyester *polyurethanes* have been found to degrade via microbial attack. Polyether *polyurethanes* have been found to be more resistant polyester polyurethanes (Kay, 1993). Thus, it is assumed that the weak "link" is the polyester rather than the polyurethane. In another study, it was found that polyester polyurethane could not be degraded by bacteria (Kay, 1991).

6.2.2.2 Microbes at Yucca Mountain. Given the wide variety of microbially mediated effects and the complexity of microbial processes, studies to assess potential impacts of microbial activity on the Yucca Mountain repository should include a variety of techniques. These investigations should include laboratory studies of Yucca Mountain-derived microbial isolates (representative of both native and introduced populations) chosen to determine bounding conditions for various microbially-mediated reactions. Carefully chosen analog studies can also supplement characterization of in situ reaction rates to best predict long-term microbial effects. Assessment of microbially-mediated transport of radionuclides can best be examined using perfusion analyses and determination of the binding and transformative capabilities of Yucca Mountain microbial community members. Traditionally, microorganisms are grouped and identified using physiological and metabolic typing criteria. Identification of organisms therefore provides a means of estimating their potential involvement in significant chemical impacts. These studies will generate a roster of the organisms present to the level of genus (and species, where possible and necessary), under selected temperature, humidity, and radiation conditions. The identification of entire microbial communities will allow the establishment of boundary conditions for microbial survival and activity. Traditional culturing techniques that rely on the growth of collected organisms as a means of identification are not entirely

representational. Therefore, these techniques should be supplemented with molecular means of characterizing and quantifying extant Yucca Mountain microorganisms under varying conditions.

The next step is to determine whether these activities are ongoing in both perturbed and unperturbed microbial communities, and assess the magnitude and rates of those reactions that are expected to alter the repository environment. Traditional biochemical assay techniques are available to determine biogenic acid production, hydrogen sulfide generation, metal transformations, and the soluble gas evolution. However, these techniques are not wholly amenable for the determination of in situ reaction rates. Therefore, they too can be supplemented with more advanced molecular techniques to better predict the impact of microbial affects on geochemistry and repository components.

Growth of Whole YM Communities. Samples of Topopah Spring tuff were initially aseptically collected from a mined Fran Ridge outcrop (the Large Block Test Site, LB), and rock excavated during construction of the Exploratory Studies Facility (ESF, Yucca Mountain, NV). The aim was to collect rock samples which had been exposed to construction activities and were representative of the post-construction repository environment. Bacteria which had been introduced by construction machinery, introduced materials, and human intervention could thus be included in subsequent isolations and testing.

Growth rates of YM-derived microbial communities were determined by adding 10 g of crushed rock samples (1.7-2.4 mm grain size) to 50 mL of R2 broth, a low nutrient formulation (Reasoner and Geldreich, 1985). Samples were incubated aerobically by shaking in covered flasks at ambient temperature, 30 °C, and 50 °C. Sterile controls were prepared by repeated cycles of autoclaving (120 °C) and incubation. Growth was monitored by periodic live plating of appropriate dilutions on R2 agar (Difco).

Growth rates of whole communities of YM-derived microorganisms in low nutrient R2 broth varied somewhat, depending on the temperature of incubation. While communities grown at room temperature or 30 °C showed altered doubling times with respect to those grown at 50 °C, all cultures, demonstrated significant increases in cell numbers, ranging to over 20,000 cells/mL of media, at the conclusion of the 30 h growth period (Fig. 6-21). Additionally, it was found that some bacterial isolates, most likely spore-forming species, survived repeated exposure to 120 °C.

These results reveal that even a modest nutrient source supports significant logarithmic growth of native and introduced YM bacteria, and total microbial cell

densities reach similar levels regardless of the temperature of incubation (Fig. 6-21). Probable spore-forming microbial species were able to survive repeated autoclaving (120 °C), demonstrating that even at the highly elevated temperatures expected to occur after waste emplacement in the repository, some of the endogenous microbiota may be able to survive through these extended periods of intense heat.

Isolation of Individual YM Bacterial Strains. Microorganisms were isolated both aerobically and anaerobically from whole and aseptically-crushed (1.7-2.4mm) rock samples at room temperature by plating directly, or washing rock samples with Artificial Pore Water (APW, equivalent in composition to J13 well water in the YM area; Amy et al., 1992), and plating onto low nutrient R2 agar. Organisms that survive in nutrient-depleted environments and at elevated temperature were isolated from crushed samples (1.0 g) after extended growth (aerobic incubation, 72 h.; anaerobic incubation, 17 days) in R2 broth at room temperatures and 50 °C. After extended cultivation, samples were incubated on R2 agar at the temperature of previous growth.

Plating of whole and crushed rock/washes at room temperature on R2 agar showed higher species diversity contained in LB samples than those obtained from ESF samples. Also, crushed rock/washes displayed generally lower species diversity and cell numbers than those arising from whole rock (e.g., Fig. 6-22). Finally, greater diversity and cells numbers were obtained after growth under aerobic conditions than under anaerobic culture conditions.

Extended growth at room temperature and 50 °C showed generally a low diversity of microbial forms (one to three cell types). However, high cell numbers were reached after extended growth under aerobic conditions (2×10^8 - 10^9 cells/mL), while anaerobic conditions produced low cell densities (e.g., 140 cells/mL), and no growth was evident after extended anaerobic incubation at 50 °C.

Since manipulation of rock samples has been reported to alter the kinds and numbers of organisms recovered (Haldeman et al., 1994), our results regarding the number and types of organisms from whole versus crushed rock are thus consistent with past findings.

YM tuff was collected and crushed exposed to the ambient air, also initial transfers of organisms cultivated on oxygen-depleted agar plates and broth were briefly exposed to air. Therefore, it must be assumed that those organisms cultivated under reduced conditions are either somewhat aero-tolerant (i.e., oxygen is not completely toxic to them, for at least brief periods), or they are capable of both oxic and anoxic growth (so-called "facultative anaerobes"). This became more evident in the results of subsequent experiments (below).

It may also be expected that both higher temperatures and anoxic conditions could result in lower cell numbers and diversity of those microbes obtained under these culture conditions. Topopah Spring tuff and its associated pore water has been characterized as generally containing a significant amount of oxygen (Buscheck and Nitao, 1994), such that strictly anaerobic, or even facultatively anaerobic organisms, might be expected in lower abundance relative to strict aerobes. Since elevated temperatures are not the norm in the subsurface, those organisms adapted to growth at 50 °C may not likewise be immediately expected to be present in high abundance. However again, the demonstration that at least some organisms at the YM site are capable of growth at higher temperatures and under lower oxygen tensions shows that a subset of the extant YM microbial community harbor the potential to grow and survive at elevated temperatures and under reducing conditions.

LB samples, originating from a Fran Ridge outcrop that more closely resembles the geological characteristics of the repository unit, display greater microbial diversity (on R2 agar) than those from the ESF-excavated rock, which had not yet reached the repository horizon. Thus, greater microbial diversity may be extant in the repository horizon than in overlying geological units.

The paucity of microbial forms after extended growth is expected. It is accepted that under stressed conditions, such as those created by the depletion of nutrients, that only a few members of the community are equally well-adapted to exploit the minimal resources available; these will outgrow those species less able to compete.

While any given growth media (e.g., R2) permits only the growth of a small fraction of a microbial community (Atlas, 1982; Roznak and Colwell, 1987), a multiplicity of microbial types were still detected from whole and crushed YM rock on R2 media; henceforth these were treated as a sample of the total microbial community present at this site. A representative group of distinct individual isolates were purified by repeated streaking of single colonies, many of these were identified by fatty acid analysis (Welch, 1991; Analytical Services, Inc., VT), but some remain unidentified. All purified isolates (ca. 60) were preserved for use in further experiments.

Identified and preserved YM bacterial isolates included representatives of the following genera: *Bacillus*, *Arthrobacter*, *Cellulomonas*, *Corynebacterium*, *Pseudomonas*, *Staphylococcus*, *Xanthomonas*, and *Flavobacterium*. These bacterial classes collectively contain members that are capable of forming spores, producing acids, degrading a wide variety of organic compounds, and remaining active under both oxic and anoxic conditions.

Enrichment of Corrosion-Specific Bacteria from YM Tuff. The oxidation of Fe(II) to Fe(III) and the reduction of sulfate to sulfide are elements of different microbial metabolic pathways that have been linked to metal corrosion processes (Lee et al., 1994; Borenstein, 1994). Therefore, efforts were made to culture organisms that carry out these transformations from YM geologic samples.

Iron oxidizers, such as species of bacteria of the genus *Thiobacillus*, utilize Fe(II) as an energy (electron) source with the concomitant production of Fe(III), and they obtain carbon for cellular growth by fixing carbon dioxide from the surrounding atmosphere. The ferric iron produced by these bacteria can react with iron sulfide (pyrite) spontaneously to form more ferrous ions and sulfuric acid. As a result, iron oxidizing bacteria have evolved to function under very acidic conditions.

Iron oxidizing microorganisms were cultured from YM tuff by inoculating 5 g samples of crushed tuff into media previously reported to support the growth of these organisms (i.e., ATCC Media #64, containing Fe(III), no exogenous carbon source, and at pH 2.8; Gherna et al., 1989). As a control for suitable growth conditions, three known and characterized iron-oxidizing microbial strains were grown in parallel with those enriched from YM tuff (*Thiobacillus ferrooxidans* ATCC#21834, #14119, #33020; Gherna et al., 1989).

Sulfate reducing bacteria use sulfate as a terminal electron sink, thereby transforming it to sulfide. These organisms typically are grown with lactate as a carbon and electron source. Thus, to encourage the growth of these organisms from YM geologic media, 5 g samples of aseptically ground tuff were similarly inoculated into two types of media containing sulfate and lactate (Baar's media and sulfate-reducing media; Gherna et al., 1989; Atlas of Microbiological Media-ref). The suitability of growth conditions was judged by the growth of a known sulfate-reducer, *Desulfovibrio vulgaris* ATCC#29579 (Gherna et al., 1989), grown in parallel with test samples.

All cultures were incubated at room temperature and periodically, 5-10% of the culture was transferred to fresh media; a total of four transfers were made over several months of incubation. In this fashion, if iron-oxidizing or sulfate-reducing organisms were extant within the samples, their growth would be encouraged due to hospitable culture conditions, over other members of the microbial community.

All control strains grew well under the conditions provided, showing that the media and conditions used did allow growth of these types of organisms. The iron-oxidizing enrichments from both LB and ESF geologic samples, likewise produced iron-oxidizing cultures (as judged by later plating on solid ISP media; Manning, 1975; e.g., Fig. 6-23). However, sulfate reducing bacteria were not recovered from all ESF geologic samples,

despite repeated attempts using two types of sulfate reducing media and the growth of the control strain under the same conditions. Sulfate reducing bacteria were recovered using the same enrichment techniques from some select sites within the ESF however, demonstrating that the presence of sulfate reducing bacteria, key players in the corrosion process, are not ubiquitous.

Enrichment cultures may or may not be a single bacterial species or strain. Thus, it must be assumed in the absence of further characterization, to be a consortium of bacteria having either predominantly sulfate-reducing or iron-oxidizing metabolic modes. Iron-oxidizing enrichment cultures were frozen for preservation and use in further experiments, as were the sulfate reducers that were obtained outside the immediate YM site.

Iron reducing strains, which use Fe(III) as a terminal electron acceptor producing Fe(II), may effect corrosion directly by anodic depolarization (Westlake et al., 1986), and affect the availability and source of Fe(II) for subsequent microbial iron oxidation. As an initial attempt to enrich these organisms from YM rock, 5 g of crushed ESF and LB material was inoculated into a media formulation that provided lactate as a carbon and energy source and nitrate as an electron acceptor (Meyers and Neilson, 1990). This type of media has been shown to support the growth of iron reducing strains under aerobic growth conditions, however it should be noted that it will also support the growth of other types of organisms as well. A characterized iron reducer, *Shewanella putrifaciens* ATCC#8071 (Gherna et al., 1989), was grown in parallel as a control. Growth was observed of both the control strain and arising from crushed YM rock samples, and periodic transfer of the cultures were carried out (as above). Finally, after four transfers, the enrichment culture was frozen for future analysis.

Calorimetric assays for determining the concentrations of Fe(II) and Fe(III) using ferrozine reagent (Lovley and Phillips, 1987; Greenberg et al., 1985) were tested using water as a solvent. Linear standard curves were obtained [with a dynamic range extending 5-100 ppm Fe(II)] under these conditions. Iron oxidizing and possible iron-reducing consortia will be analyzed to quantify their rates of iron reduction/oxidation using these assay techniques.

Screening for Acid-Producing Bacteria. The production of organic acids as products of microbial central metabolism is well-documented (Horn and Meike, 1995). The generation of acids has been both directly and indirectly linked to metal corrosion. Microbially-generated acids have been shown to directly dissolve the protective calcareous film on stainless steel (Little, 1987). Coupling of protons with electrons results in electron removal from the cathode (Borenstein, 1994), and forms hydrogen

which is a substrate for microbial sulfate reduction (Fig. 6-24; Pope et al., 1994). Therefore, the library of YM isolates that were recovered from LB and ESF geologic samples (above) were screened for those that demonstrated a decrease in pH during active growth.

As an initial screen to identify acid-producing strains among the preserved YM microbial isolates, all isolated strains were grown separately in R2B media (with or without amendment of 0.5% glucose), using the pH indicators bromocresol purple ($pK_{\text{indicator}}=5.3$) or methyl red ($pK_{\text{indicator}}=4.1$). Under these conditions, a change in the color of the culture indicates the production of acid, thereby providing a rapid means of assessing acid production by the 46 strains tested. Anaerobically-grown strains were incubated under anaerobic conditions, while aerobically-isolated strains were cultivated with aeration, and all strains were incubated at either room temperature or 50 °C, depending on their temperature of isolation. Sterile, uninoculated controls were included in all experiments. The pH endpoint was determined using a standard pH meter for at least one trial.

Results revealed that both growth and acid production were generally more rapid when the media was amended with glucose. This is not surprising given that acid production is largely a result of carbon utilization; addition of glucose provides at once more carbon and energy for growth, together with a greater potential rate of acid generation. When 46 bacterial isolates were tested with glucose amendment, 10 (21.7%) of these displayed a decrease in pH (from about pH 7.0) to pH 5.3 or less after a period of growth lasting from 3 to 16 days. When glucose was not added to the media, only 5 strains tested showed similar extents of acid production. Sterile control cultures maintained the initial pH of the media. While there was some interference of the pH indicator with measurement of the pH endpoint (probably due to titration of protons by the indicator) and even growth in some instances, the lowest pH attained was 4.46 after a 76 hour incubation by a *Pseudomonas stutzeri* LB isolate in media with added glucose and the methyl red indicator.

These results indicated that microbially-induced metal corrosion will be accelerated with inclusion of a readily metabolizable carbon source which promotes both growth and acid production. Thus, materials testing should include added glucose in the media, as glucose will contribute towards accelerated testing conditions. Compilation of the screening results revealed eleven strains that produce acid under the described conditions of growth, which included members of the genera *Cellulomonas*, *Pseudomonas*, *Flavobacterium*, *Bacillus*, and *Arachnia*. (Table 6-12). Five of these strains were further analyzed to determine their rates and extents of acid generation, and to further

determine conditions under which acid is produced; these strains would be considered for specific inclusion in accelerated materials testing (below).

Screening for Sulfide Producing Bacteria. Microbially-produced sulfide may be corrosive to metals, as are the ferrous sulfides that form when produced sulfide reacts with solubilized ferrous ions. Most often these activities are associated with sulfate reducing bacteria, which directly promote corrosion by depolarizing the cathode through consumption of available hydrogen from the metal surface (Borenstein, 1994). Attempts to isolate sulfate reducers from the immediate YM environs demonstrated that these organisms are not uniformly distributed. However, microbes can also produce sulfide by the decomposition of proteins, a process known as "putrefaction" or "desulfurylation," in which the sulfur-containing amino acids methionine and cysteine are broken down, releasing sulfide in the process.

While the evidence that sulfide and ferrous sulfide *directly* contribute to metal corrosion is not entirely conclusive (Licina, 1988), a screening technique was devised to detect desulfurylating microbes among the preserved isolates contained in the YM library. These efforts were aimed at determining whether YM microorganisms harbor desulfurylation capabilities, assessing the potential contribution of desulfurylation to metal corrosion (i.e., the direct effects of sulfide and ferrous sulfide), and to ascertaining those alloys that may be more resistant to these microbial products.

All preserved isolates were screened in test tubes containing R2 agar supplemented with 0.75% proteose peptone #3 (Difco), to provide an excess supply of amino acids for desulfurylation reactions (R2 normally contains only 0.05% of peptone; Reasoner and Geldreich, 1985). Additionally, the media contained 0.05% lead acetate, which precipitates as lead sulfide when sulfide is produced as result of microbially-driven peptone decomposition; the resulting lead sulfide is detected by its blackening of the agar medium.

The library of YM bacteria were each individually inoculated into R2+peptone+lead acetate agar media contained in screw-top test tubes, by streaking on top of the agar surface (exposed to the air in the headspace of the tube) and stabbing into the agar within the tube (under which conditions growth is anoxic or micro-aerobic). Sterile, uninoculated control tubes were monitored in parallel with inoculated ones. All samples were incubated at room temperature or 50 °C, depending on the temperature of strain isolation. Growth and (lead) sulfide generation was monitored over a 34 day period.

Twenty-one of the forty-five aerobic strains tested (46.7%) demonstrated sulfide production in the oxic area of the culture (none of these were strains that were isolated

and incubated at 50 °C), whereas only three of the aerobically-isolated strains (all 50 °C isolates) showed sulfide production in the anoxic area of the culture. Three of the 17 (17.6%) anaerobically-isolated bacteria tested showed sulfide production in the anoxic butt of the tube, one of these had significant sulfide production under aerobic conditions as well. A total of 7 of the 17 (41.2%) anaerobic isolates displayed some detectable sulfide production under aerobic conditions. No sulfide production was detected in any of the sterile controls.

These results demonstrate that a significant proportion of YM bacterial isolates are capable of producing sulfide *via* putrefaction under both oxic and anoxic conditions, at least when provided with excess protein substrate. Isolates of *Pseudomonas*, *Flavobacterium*, *Bacillus*, *Arachnia*, and *Cellulomonas* were all found to produce sulfide; four of these isolates were found to produce both acid and sulfide using these screening techniques. The use of these putrefying bacteria in accelerated corrosion tests should allow a more precise determination of whether hydrogen sulfide and associated metal sulfides are directly capable of causing corrosion to waste package alloys. Since these microbes generate sulfides in the absence of sulfate reduction (and hydrogen utilization), the effects of *only* sulfides on corrosion can be assessed absent cathodic depolarization effects.

All strains were incubated under aerobic conditions, by streaking on top of the agar, as well as under [somewhat] reducing conditions by stabbing into the semi-solid agar surface. Many of the aerobic strains were capable of growth within the agar (all of the 50 °C-incubated cultures grew well under these anoxic conditions), and some of the anaerobes were also capable of growth under aerobic conditions. This may have been expected since the selection and transfer protocols used (above) precluded the isolation of "strict" anaerobes (i.e., those to which oxygen is toxic). Employed methods resulted in isolation of organisms that were at least tolerant to limited exposure to oxygen or so-called "facultative anaerobes," which are capable of both oxic and anoxic metabolism. Likewise, some of the "aerobes" can be facultatively capable of anoxic growth. Several of the identified sulfide producers were further quantitatively analyzed for their rates and extents of sulfide production (below).

Screening for Slime under Varying Culture Conditions. The production and export of polysaccharides (long chain sugar polymers) to the exterior of cells is characteristic of many bacterial species. Exopolysaccharide production results in the build-up of a slime layer which protects, embeds, and allows anchorage of cells to solid surfaces. The microenvironments contained within slime layers (or "biofilms") can be drastically altered from the general conditions in the exterior milieu, and from other

areas within the biofilm. Generally, it can be expected that differential nutrient concentrations, relative humidity, and oxygen tensions exist throughout the film (Costerton and Geesey, 1985). Consortia composed of different microbial species can become embedded by polysaccharide produced by one or more consortial members. These slime capsules provide a three dimensional spatial matrix that permits concentration gradients and facilitates intermicrobial interactions. Slime producing organisms probably indirectly contribute to corrosion by permitting adherence and facilitating interactions among the different types of organisms that cause corrosion. Direct effects of slime on corrosion include the creation of differential aeration cells and localized elevations of ions, which in turn form crevices under which corrosion is accelerated (Borenstein, 1994; Costerton and Boivin, 1991).

Since slime production is an integral element of microbially-induced corrosion, the library of YM bacterial isolates was screened for slime production first on R2 agar and then R2 + 0.5% glucose agar, R2 + 0.75% peptone agar, and R2 + 0.5% glucose + 0.75% peptone agar. All isolates were incubated anaerobically or aerobically at room temperature or 50 °C, depending on their mode of isolation. Slime production was assessed by observation of gross colony morphology: the appearance and quantity of a viscous slime layer was noted and scored (e.g., Fig. 6-25).

Prodigious amounts of polysaccharide were produced by two *Bacillus* isolates and two as yet unidentified isolates with very similar colony morphologies. All of these strains were identified as sulfide producers in former screening analyses, however none of these were identified acid-producers. Moderate quantities of slime were generated by five other YM strains that included representatives of the genera *Arthrobacter* and *Pseudomonas*. Retesting of six of these slime generators on R2 agar supplemented with peptone and glucose revealed that slime production varied with media type. The greatest degree slime production occurred on media containing glucose for two of the strains tested. This observation is in agreement with the fact that the synthesis of polysaccharides requires sugar precursors; amended glucose provides a source of building blocks to support slime synthesis. The other isolates showed little difference in the quantity of polysaccharide produced between media types, and one strain showed no growth at all on R2 + peptone. A single anaerobic isolate demonstrated copious slime generation on R2 agar.

These results demonstrate that YM isolates are capable of slime production under low nutrient conditions, and could therefore play a role in corrosion of waste package materials. Generally it appears that the availability of carbohydrates could increase slime production, and possibly accelerate corrosive microbial activities.

Rates of Acid Production Under Varying Growth Conditions. Five strains identified in preliminary screening for the production of acids (above) were further analyzed for their rates and extents of acid generation in R2 media containing additional peptone and glucose. Each strain was separately inoculated into R2, R2+0.5% glucose, R2+0.75% peptone, and R2+peptone+glucose. Cultures were incubated either anaerobically in serum bottles with pre-reduced media, or aerobically in shake flasks at either 30 °C or 50 °C, depending upon the mode of isolation. The pH was monitored in withdrawn samples periodically over a three to five day period (Fig. 6-26).

The two anaerobic strains (one a possible *Arachnia propionica*, the other unidentified) showed a negligible effect of added glucose and peptone, and the pH did not fall below pH5.2 in either of these cultures. The aerobically-incubated strains, however, showed greater dependence of the composition of the growth media on the production of acids. The *Pseudomonas stutzeri* isolate, LB-71h-RT-13, only generated acid when glucose was added to the R2 media, displaying a decrease to pH4.2. The pH probably did not decrease coordinately after growth of the *P. stutzeri* in R2+glucose+peptone media due to deamination of amino acids contained in the added peptone, which releases alkaline amines, counteracting the effects of acid production. This counter-effect of added peptone was not as evident in the *Flavobacterium esteroaromaticum* isolate, ESF-71h-RT-4, which showed decreases in pH after growth in both R2+glucose and R2+glucose+peptone, as did a 50 °C-isolated strain, LB-71h-50-3 (most probably a *Bacillus*) (Fig. 6-26).

In summary, the effect of available nutrients on the production acids by YM isolates varies by strain. Some isolates are only capable of acid production when supplied with an added carbon source, others are less affected by this requirement and are capable of acid generation even when available carbohydrate concentrations are minimal. Also, the presence of other metabolizable nutrient sources can affect overall pH; if end products include alkaline compounds (such as amines produced by deamination of amino acids), then acid production can be mitigated. The rates of acid production, in view of the long time spans that must be considered to evaluate the integrity of the YM repository, are significant. Rates of acid production over a three to seven day period are measurable and result in orders of magnitude differences in proton concentrations.

Rates of Sulfide Production by YM Isolates. Seven YM isolates identified as sulfide producers (*via* desulfurylation) were analyzed for their rates of sulfide production under aerobic and anaerobic conditions, because it had already been shown that many isolates are capable of growth at high or low oxygen tensions (above). All strains were inoculated into R2 media amended with 0.75% peptone. Both anaerobic (contained in

serum bottles with pre-reduced media, cysteine as a reducing agent and rezasurin as a redox indicator) and aerobic (contained in flasks) were incubated at 30 °C or 50 °C unshaken to minimize air stripping of the produced hydrogen sulfide. Uninoculated media was also incubated to detect spontaneous abiotic sulfide production.

Periodically, samples were withdrawn, cells removed by filtration, and the supernatants analyzed using a modification of the methylene blue assay, which relies on the reaction of sulfide, ferric chloride and dimethyl-*p*-phenylenediamine to produce methylene blue (measured spectrophotometrically, 664 nm; Greenberg et al., 1985). Standard curves were prepared using sodium sulfide diluted in the appropriate media, and sample sulfide concentrations were calculated by interpolation of the standard curve.

Preliminary results (depicted in Fig. 6-27) showed that sulfide production *via* desulfurylation increased for all tested strains within a two day incubation period, even in anaerobic cultures which metabolize and grow more slowly than do aerobic cultures. Sulfide concentrations increased to about 500 ppb for all strains grown under anaerobic conditions and to approximately 150 ppb for the same isolates incubated aerobically. Sulfide concentrations continued to increase in aerobically grown cultures, reaching a maximum of approximately 330 ppb over a 7 day period, although extents of maximal sulfide concentrations varied between the strains tested. Thereafter, aerobic sulfide production, in general, decreased until 22 days after initiation of growth, when there was again a trend towards increasing sulfide found in the media.

These aerobic incubation results could be explained by volatilization of hydrogen sulfide from the culture (or precipitation from the soluble phase), combined with an initial growth phase, followed by cell death. In "batch" cultures such as those tested (which are not continually fed), growth of aerated cultures continues for a relatively short time, probably at the most for a week, after which nutrients are exhausted. While efforts were made to minimize the loss of sulfide through volatilization, sulfide losses could have resulted from inadvertent air-stripping or precipitation by media components in the death phase of the cultures where little or no new sulfide production could replace that which had been lost. The final increase at day 22 may be due to the growth of surviving cells on those that had died, with concomitant sulfide production resulting from metabolism of the amino acid content of dead cells.

Anaerobically-grown cultures also displayed a decrease in sulfide concentrations, starting after two days of incubation. In most cases, these decreased to zero over a 17 day period of incubation. These cultures were contained in sealed vials, and maintained under reducing conditions. Thus, loss of hydrogen sulfide from the media through volatilization is unlikely. Rather, since the employed assay only detects the presence of

soluble sulfides, it is likely that sulfide may have precipitated by interacting with other media components.

While these preliminary analyses are not entirely conclusive, it is important to note that microbially induced sulfide production increased significantly above background levels, was detected among a wide variety of YM isolates under both aerobic and anaerobic conditions, at least when strains were provided with an excess amino acid source (in the form of added peptone). These preliminary results additionally aid in determining conditions under which to conduct accelerated testing of alloy candidates, and which strains to include in accelerated corrosion tests.

Significance to YMP. Native microorganisms reside within the potential repository environment. Microbial communities have been characterized from a variety of deep subsurface environments, and ongoing work has already identified some of the native microbiota in the Yucca Mountain region (e.g., Russell et al., 1994).

Microbes vary widely in their types of metabolic activities, and the consequent alterations to the surrounding environment that they can facilitate (Horn and Meike, 1995). Historically, bacteria (and the closely related *Archea*) have been classified according to their individual metabolic types. The potential reactions actually performed by bacteria are dictated by both innate metabolic ability, and the conditions to which they are exposed. The type of metabolic activities that are possible are governed by the availability of substrates. For example, sulfate reduction with the concomitant generation of hydrogen sulfide is only possible if sulfate reducing bacteria are present and sulfate is available to this class of organisms. Presumably, native microbes that are currently present have or have had adequate resources. The establishment of bacteria introduced through drift construction will likewise be dependent on adequate nutrient supplies and their rates of adaptation to the repository environment.

Conditions anticipated upon waste emplacement in the proposed Yucca Mountain repository will include extreme heat, desiccation, and possibly high levels of ionizing radiation. The initial presence of extreme conditions within the repository may not completely preclude microbial activity; even if general conditions extend beyond those able to support microbial activity there may be microenvironments in which environmental extremes are mitigated. In any case, eventual repopulation of the near-field environment through reentry of water carrying both nutrients and microbes, is anticipated as overall repository conditions become less extreme. We may expect that organisms that thrive at high temperatures and those that form spores under adverse conditions will be extant within the native or introduced microbial communities at

Yucca Mountain, and maintain or regain activity as conditions become favorable. Microbial populations may acidify and otherwise alter the pore water chemistry of the near field repository environment, as well as directly affect the corrosion of repository waste packages. The degradation of materials and the consequent alteration of the aqueous chemical environment, with accompanying effects on repository performance, will depend on the presence of adequate nutrients and water to maintain at least a minimum level of activity.

The demands of establishing boundary conditions for microbial activity in the context of a radioactive waste repository extend beyond the information that is presently available in the literature. As a first step organisms collected from the ESF have been cultured and assembled into a YMP library. These microbes were grown in low nutrient media with various amendments and screened for various activities of significance to the long term chemical and hydrological properties of the NFE. Both the production of acid and slime was assessed under these conditions. The generation of both acid and slime for at least some isolates was increased when an easily metabolized carbohydrate (glucose) was incorporated into the media. Other culled YM acid and slime producers did not demonstrate a dependence of corrosion activities on sugar availability. It might be noted however, that the availability of carbohydrates should increase growth rates of those organisms depending on reduced carbon sources for food, such that even if sugars are not required directly for these processes, increased growth rates might be expected to indirectly contribute to increasing acid and slime production rates. These microbes have been used in estimating the required conditions for corrosion-related microbial activities, and to further optimize conditions for accelerated testing of candidate barrier alloys.

The analysis of acid production in different media types revealed that other metabolites (i.e., bacterial products), might ameliorate the results of acid production. If alkaline products are secreted to the media then acid generation is mitigated.

Taken together, while media composition plays a part in the rates and extents of acid and slime production for some isolates, it appears to have little direct effect on other isolated organisms. This demonstrates that even with a minimal supply of nutrients both of these processes are possible. Further analyses should include assessment of these activities under a broader set of conditions, including those which more closely mimic anticipated repository conditions.

Sulfide and metal sulfides have been identified as probable corrosive bacterially-generated products, most often associated with the activity of sulfate reducing microorganisms. The distribution of sulfate reducers at the proposed YM repository site

was not found to be ubiquitous, thus an alternative pathway for microbial sulfide production was explored. Many of the YM microbes contained within the assembled library were found to have the capacity to make sulfides through desulfurization of sulfur-containing amino acids; this process occurred under both anaerobic and aerobic conditions when a supplementary source of amino acids was added to the media. YM microorganisms were not tested for sulfide production in the absence of amended amino acids, however it was found in preliminary experiments that the rates of desulfurylation and concomitant sulfide accumulation increased quickly up to 0.5 ppm. Thereafter, most probably due to the culture conditions employed, sulfide concentrations were found to decrease.

Use of these desulfurylating YM organisms alone in accelerated corrosion tests should indicate the degree to which they can promote corrosion. If the contribution of sulfides and their metal derivatives is significant in increasing corrosion rates, then these processes should be analyzed further to determine their bounding conditions, rates, and contribution to other corrosive processes. The rates of these processes were very rapid when compared to the long term periods that must be considered for repository performance. Given adequate nutrients, slime, acid and sulfide generation rose to their highest levels within a matter of days or weeks. Thus, the period required for these organisms to reach their greatest corrosive potential, given the right conditions, is almost instantaneous in comparison to the functional lifetime of the repository.

6.2.3 Discussion

It is clear that the addition of man-made materials to the near-field environment (NFE) may modify the chemical environment and influence the geochemical reactions that may occur. An example of the interaction between introduced materials, rock and water is as follows. The repository horizon and the adjacent horizons contain zeolites, or they may develop zeolites during interaction of water with rock at elevated temperatures. Zeolites are common molecular sieves and sorbates. Clinoptilolite, for example, is used as a molecular sieve for the ammonium ion (Barrer, 1978b; Breck, 1974), which has the potential to degrade the repository environment. This potential beneficial effect may be counteracted by other man-made materials that could destroy the zeolite structure or provide preferentially adsorbed ions. The balance of these effects at the repository is unknown at present. Application of geochemical models to this area, where the appropriate databases exist will provide guidance and some bounding

constraints for repository design and performance assessment. Modeling and databases are described in the next section.

6.3 Understanding the Processes

6.3.1 Experimental Studies

In order to predict chemical properties over a long period of time we need to know fundamental properties of the appropriate materials. These fundamental properties are often better known for geological materials because the interest in very long term chemical prediction has existed for decades. A similar interest in fabricated materials has appeared only relatively recently, and most commonly in relationship to radioactive waste disposal efforts. Previous efforts in the area of fabricated materials has focused on optimizing fabrication conditions. This is hardly the data that is needed for predicting processes in which the environment will not be controlled. It is for this reason that an application driven program finds itself in need of generating fundamental data.

6.3.1.1 Data Availability and Modeling Requirements Regarding Cementitious Materials. Of the major reactant phases of cement powder—alite, belite, possible residual glass, gypsum, and ferrite [$C_2(A,F)$] (See Appendix B for standard cement formula nomenclature)—only the thermochemical data for gypsum are complete. Data are available for the pure calcium end-member equivalents of alite and belite (Haas et al., 1981), but not for their solid solutions. The significance of solid-solution characteristics of alite and belite to performance assessment may be great because not only do alkalis and other minor impurities stabilize phases, but substitution of Al_2O_3 and Fe_2O_3 may affect reaction kinetics. It is suspected that aluminum and iron substitution do not affect early hydration but slow hydration over a period of 24 hr (Ghosh, 1983). The stabilization of phases by alkali substitution has been investigated (Xiuji and Shizong, 1986) but remains poorly understood. Most of the detailed kinetic studies of hydration have employed the pure calcium end-members C_3S and $\beta-C_2S$. The thermochemical data for the calcium aluminates have been rigorously evaluated by Ellezer et al. (1981). However, no calorimetric measurements were found for the $C_2(A,F)$ solid solution, which has been characterized structurally by Jeffrey (1964).

Most of the hydrous phases of cement and the anhydrous and hydrous solid solutions lack calorimetric data. The kinetics of transformation of C-S-H into other phases at its upper temperature limit is significant to predictions of cement behavior in the repository, which will stay at 80 to 120°C for an extended time. Of prime importance

for 25°C performance modeling are calorimetric data for ettringite and tobermorite and well characterized solid solutions of these phases. The prediction of chemical reactions at greater temperatures requires more data than is presently available. Geochemical codes are also useful in the absence of these data for conducting a sensitivity analysis to determine the solid solutions or end-member phases that are critical for calorimetry. The original ΔH of formation (20°C) from CaO and silica gel thermodynamic data for all Ca_2SiO_4 phases are evaluated by Haas et al. (1981). Qualitative rate information has been obtained for ettringite components (Majling et al., 1985). Other than an enthalpy of dehydration (Maycock et al., 1974) and C_p data (Ederova and Satava, 1979) obtained over the range of 273 to 333°K, thermochemical data for ettringite are calculated (Sarker et al., 1982; Babushkin et al., 1985). The only experimental data for "monosulfate" ($\text{C}_4\text{ASH}_{12}$) located to date is C_p data from 273 to 353°K (Ederova and Satava, 1979). As discussed previously, the kinetics of the relevant reactions are even less well understood.

Comparisons of cement leachates with calculations performed using available data and standard thermochemical tables (Barnes and Roy, 1983) suggest the best agreement with the solutions buffered by tobermorite and possibly gyrolite. Calculated activity products have been compared with (1) experimentally obtained solution compositions (Ca^{++} , Na^+ , K^+ , pH, and $\text{SO}_4^{=}$, but not Al or $\text{CO}_3^{=}$) from cement hydrated for up to 3 hr (Gartner et al., 1985), and (2) pure C_3S . The comparisons suggest that although no difference in supersaturation was observed with respect to portlandite, gypsum, and syngenite [$\text{CaK}_2(\text{SO}_4)_2 \cdot \text{H}_2\text{O}$], thermodynamic equilibrium is not achieved during early hydration (Moragues et al., 1987, 1988), and high ionic concentrations of the solutions cause departure from Debye-Huckel theory. The most successful chemical models to date have been achieved by working with a limited number of equations that include C-S-H solid solutions, monosulfate solid solution, and ferrite solid solution. Glasser et al. (1985) analyze a simplified cement system as the ternary $\text{CaO-SiO}_2\text{-H}_2\text{O}$. Barret and Bertrandie (1986) make a similar analysis of the system $\text{CaO-Al}_2\text{O}_3\text{-CO}_2\text{-H}_2\text{O}$. Incorporation of aggregate into repository concrete will increase the complexity of geochemical modeling. Calculations that include portland cement, special cements, and concretes that incorporate bfs, fly ash, and silica fume (Berner, 1987) have achieved some success for equilibrium-solid-phase and pore-solution-composition data obtained from experiment, but they do not readily take reaction progress into account.

The use of numerical simulations to integrate the effects of the variables described in Sec. 6.2 complements experimental and historical investigations. Eventually, coupled chemical effects that are difficult or inaccessible through experiment can be examined.

However, even the present chemical data base (Sarker et al., 1982; Babushkin et al., 1985), although limited, can be manipulated to obtain insight into some effects that may be expected due to man-made materials. Conversely, the data base will be enhanced over time by incorporation of new thermodynamic data from the experimental and historical investigations.

6.3.1.2 Generation of short term thermodynamic data. The work that has been conducted in the area of generating more thermodynamic data has focused on phases that are expected to be part of the drift scale chemical system at elevated temperatures if OPC cement is a significant element of drift construction. As described by Meike (1995), much of the data required for long term modeling of the same caliber that presently allows us to predict the chemical interactions of the natural system is unavailable. A program was begun to obtain that data. Synthesis of Ca-Si-H₂O phases had been completed and measurement of thermodynamic data had just begun when the program was halted in November 1995. Heat capacity and entropy measurements were obtained for 11Å tobermorite using heat pulse calorimetry, but the data has not yet been analyzed. The work on other phases was halted.

In order to provide a means of verifying experimental data, and ultimately developing a means to calculate necessary thermodynamic parameters and better understand the relationship between relative humidity and the stability of Ca-Si-H₂O phases a program was initiated to conduct electronic structure calculations of Ca-Si-Hydrates (Sterne and Meike, 1995). Given the difficulties inherent in direct measurement of the thermodynamic parameters of these phases we have undertaken a set of first principles electronic structure calculations.

Electronic structure calculations, and the Linear Muffin Tin Orbital (LMTO) theory in particular are standard methods for approaching the physical properties of metals and metal alloys, semi-conductors and simple insulators (see, for example, Anderson, 1975; Skriver, 1984). In the past these methods have been confined to small systems of less than 20 atoms in a unit cell. Thus calculations for wollastonite and xonotlite, which contain a 30 atom unit cell and 62 atom unit cell respectively would have been out of reach normally. However, recent developments in algorithms and computer power have brought larger systems within the range of these calculational techniques.

The goal of this modeling effort is to determine the energetics of hydration for crystalline Ca-Si-hydrate phases. The work performed to date represents an initial step in this direction. The initial results for the first phases undertaken for phases representing the water poor end members, wollastonite (CaSiO₃) and xonotlite

(Ca₆Si₆O₆17(OH)₂). The results, reported in Sterne and Meike (1995), are summarized below.

The calculated ground state properties of wollastonite and xonotlite are in very good agreement with experiment, and provide equilibrium lattice parameters within 1-1.4% of the experimentally reported values. The roles of the different types of oxygen atoms, which are fundamental to understanding the energetics of crystalline Ca-Si-hydrates, examined in terms of their electronic state densities, appear to be in good agreement with experiment for the lattice parameters and internally consistent when comparisons are drawn between the two structures. The exercise, completed with wollastonite and xonotlite, demonstrates the applicability of these electronic structure methods in calculating the fundamental properties of these phases. The electronic structure calculation methods are demonstrated to give reliable results, even for the relatively large wollastonite and xonotlite unit cells. Thus, the application of this new approach to the study of calcium silicate hydrates appears to be fruitful not only in terms of the ability to calculate heats of formation, but also by virtue of the insight that it can provide into the nature of hydration and dehydration.

6.3.1.3 Generation of short term kinetic data. The need for kinetic data is similar to that described above for thermodynamic data, but was also halted in November 1995. However, in the process of conducting the diesel fuel experiments described above, we have obtained some data regarding the degradation of cementitious material, specifically Fibercrete™. In all experiments containing Fibercrete™ (DF3, DF4, and DF6), 11Å-tobermorite formed. Thus, 11Å-tobermorite appears to be a stable, or at least metastable, phase at 200°C. As is observed in experiment DF6, the precipitation of 11Å-tobermorite, calcite and cristobalite may control geochemistry and effect porosity and permeability for waters contacting both cements and Topopah Spring tuff. The importance in the dissolution and precipitation kinetics can be seen in the slow changes in solution pH and dissolved silica concentrations and the small fraction of the initial starting material dissolved to form secondary precipitates at the Fibercrete™ and Topopah Spring tuff surfaces. In the absence of Fibercrete™, cristobalite appears to be the dominant secondary mineral formed in Topopah Spring Tuff experiments, in agreement with previous studies (Knauss et al., 1985; Knauss and Peifer, 1986; Knauss et al., 1987).

Calculations using the current data base appear to be contradictory. Aqueous chemical modeling results suggest that mesolite should precipitate from the solution. They predict that the chemical system is saturated with respect to quartz and calcite after 20 days of reaction and undersaturated with respect to 11Å-tobermorite. Zeolites

were not detected in any of the experiments, suggesting either that the thermodynamic data is not correct, that zeolite nucleation from solution has a very large activation energy, or that zeolite precipitate rates are very slow even in very supersaturated solutions. Given the painful lack of thermodynamic and kinetic data pertinent aqueous degradation of Ca-Si-H₂O phases the first option is very likely. Thermodynamic data for Ca-Si-H₂O phases are sparse and contradictory (Vieillard and Rassineux, 1992; Bruton et al., 1994; Meike et al., 1994). The constant 11Å-tobermorite saturation index after 40 days of reaction and the identification of 11Å-tobermorite in the final solid material indicates that the solubility of 11Å-tobermorite is over estimated in the current data base. Previous experiments which have investigated the stability of various phases are typically only a couple of days (Lea, 1971). Atkins et al. (1991) determined the solubility of cement hydrate phases after four weeks of reaction at 25°C. Clearly longer reaction periods are required for the crystalline phases to reach equilibrium.

From the present work, it is possible to calculate a 11Å-tobermorite solubility constant (K) at 200°C to be $10^{39.7(\pm 0.6)}$, using the experimental ion activity product for the following solubility expression for each aqueous sample after 20 days of reaction:



$$\text{IAP}(200^\circ\text{C}) = \frac{[\text{Ca}^{2+}]^5[\text{SiO}_2]^6}{(\text{H}^+)^{10}} \quad (9)$$

assuming $a_{\text{H}_2\text{O}} = 1$ and unit activity of the solid phase. This simplifying assumption is also taken that only crystalline tobermorite of pure composition is involved in the chemical reaction. In the absence of other data, this IAP may prove to be a useful guide: However, the derivation does not allow for the interaction of complexes or other amorphous or crystalline Ca-Si-H₂O phases that are known to precipitate under these conditions. This calculation thus requires verification using independent checks for internal consistency.

6.3.1.4 Material behavior as a function of pH. A major unknown in the prediction of the chemistry of the potential Yucca Mountain repository is pH. A large part of that has to do with cementitious materials, if they are present as invert or stabilizing material. The pH of water in contact with relatively young cement can be relatively high (10-12). However, there are a number of considerations that lend a good deal of uncertainty to a general assumption that the pH of water in contact with cement will be high throughout the lifetime of the repository.

The first consideration is the temperature. The reason that the pH of water in contact with cements equilibrates at such a high value is that the water is in equilibrium with the amorphous Ca-Si-H₂O gel and other metastable phases. These phases will transform into less hydrous and more stable crystalline phases with time and with elevated temperature. It has not been established that the newly formed Ca-Si-H₂O phases also are in equilibrium with water at such elevated pH. In fact, there is evidence to the contrary. Hillebrandite and wollastonite, water poor end-members of the Ca-Si-H₂O system do not produce such elevated pH.

The second consideration is microbial. In general the microbial activity of pumping protons through a chemical system serves to reduce pH. This is beneficial for the microorganism because it tends to solubilize solids and thus provide nutrients.

6.3.1.5 Material behavior as a function of RH. Water adsorption studies of okenite (Ca₁₀Si₁₈O₄₆·18H₂O) conducted at ambient temperature, (Martin et al., 1995) demonstrate the extreme sensitivity of some of the crystalline Ca-Si-H₂O phases to relative humidity.

As part of an experimental and modeling program to characterize the effect that cement will have on the water budget at the potential Yucca Mountain repository, water sorption studies of crystalline calcium silicate hydrate phases are being performed. An adsorption study was conducted on okenite (Ca₁₀Si₁₈O₄₆·18H₂O) at ambient temperature over a range (3.5-97%) of relative humidity (RH) conditions. A sample of okenite from Poona, India, equilibrated at ambient RH, was divided and dried over phosphorus pentoxide (P₂O₅) and placed in chambers containing saturated salt solutions to control the RH. X-ray diffraction analysis (XRD) indicated that interlamellar swelling occurred along the (001) axis. An increase in the d(001) spacing with hydration was on the order of 2.5Å at a RH of 11% and remained unchanged at higher RH. This swelling is consistent with a monomolecular water layer in the interlamellar space. Comparison of the XRD peak positions from the 97% RH sample with an undried, natural sample (33% RH) indicates that the interlamellar water adsorption is reversible. A broadening of the XRD peaks after drying the sample over P₂O₅ was noted and the peaks remained broad with subsequent wetting suggesting that the dehydration process caused some disordering. A comparison of the adsorption isotherm with the XRD data allows us to conclude that water adsorbed at 97% RH (11% by weight) included water located within the crystal structure as well as that externally adsorbed and capillary condensate. Future experiments will be performed at elevated temperatures with a sorption system fitted with an evaporator to control the RH and the results will be compared with those at ambient temperature.

6.3.1.6 Material behavior as a function of growth of microbial biomass. The impacts of the native and introduced bacteria on the performance of geologic nuclear waste disposal facilities were evaluated because these bacteria could promote corrosion of repository components and alteration of chemical and hydrological properties of the surrounding engineered and rock barriers. As a first step towards investigating these potentialities, native and introduced bacteria obtained from post-construction Yucca Mountain (YM) rock were isolated under varying conditions, including elevated temperature, low nutrient availability, and the absence of available oxygen. Individual isolates are being screened for activities associated with microbially induced corrosion of metals (MIC). Preliminary determination of growth rates of whole YM microbial communities under varying conditions was also undertaken. This work is reported in Horn et al. (1996).

Methods. Samples of Topopah Springs tuff collected from a mined Fran Ridge outcrop, and rock excavated during construction of the Exploratory Studies Facility tunnel (Yucca Mountain, NV) were collected aseptically. Microorganisms were isolated both aerobically and anaerobically from whole and aseptically crushed (1.7-2.4 mm) rock samples at room temperature by plating onto low nutrient R2 agar (Difco). Organisms that survive in nutrient-depleted environments and at elevated temperature (50°C) were isolated from crushed samples (1.0 g) using low nutrient R2¹ broth. The resulting whole microbial communities were grown for extended periods (aerobic incubation, 72 h; anaerobic incubation, 17 days) at room temperatures and 50°C. After extended cultivation, samples were incubated on R2 agar at the temperature of previous growth. A representative group of morphologically distinct individual isolates were purified by repeated streaking of single colonies, which were identified primarily using fatty acid analysis. The growth of microbes that possess sulfate-reducing and iron-oxidizing capabilities was encouraged from crushed rock samples using other specialized growth media.

Growth rates were determined by adding 10g of crushed rock samples to 50 mL of R2 broth. Samples were incubated aerobically by shaking in covered flasks at ambient temperature, 30°C, and 50°C. Sterile controls were prepared by repeated cycles of autoclaving (120°C) and incubation. Growth was monitored by periodic live plating of appropriate dilutions on R2 agar.

Crude calorimetric screens were used to identify individual strains that produced the greatest quantity of a range of MIC-related capabilities. Acid producers were identified after growth of individual isolates in R2 broth containing pH indicators, the color change of which gave a qualitative indication of acid production. Production of

hydrogen sulfide by individual isolates was detected by the ability to precipitate ferrous iron after growth in various media. Generation of exopolysaccharide capsular material was assessed after gross examination of colony morphology. Ferrous iron was assayed calorimetrically using ferrozine reagent.²

Results. While any given growth media permits only the growth of a small fraction of a microbial community, a multiplicity of microbial types were still detected from whole and crushed YM rock on R2 media; henceforth these were treated as a sample of the total microbial community present at this site. In general, the greatest diversity of those microorganisms culturable on R2 arose from plated rock samples grown under aerobic conditions at room temperature, although 17 anaerobic strains were purified from rock samples incubated at ambient temperature under anoxic conditions. Extended growth at room temperature and 50°C showed a low diversity of microbial forms (one or two cell types). However, high cell numbers were reached after extended growth under aerobic conditions (2×10^8 – 10^9 cells/mL), while anaerobic conditions produced low cell densities (e.g., 140 cells/mL), and no growth was evident after extended anaerobic incubation at 50°C. In total, a group of over 60 isolates were preserved for further study. After one month, growth of iron oxidizers and sulfate reducers is not evident in specialized media, although efforts continue to isolate these types of organisms.

Growth rates of whole communities of YM-derived microorganisms in low nutrient R2 broth varied depending on the temperature of incubation. While communities grown at room temperature or 30°C showed an average mean doubling time of 1.8 h, those growing at 50°C demonstrated doubling times of 3.2 h over a 9 or 10 hour growth period. All cultures, however, demonstrated significant increases in cell numbers, ranging to over 20,000 cells/mL of media, at the conclusion of the 10 h growth period.

Preliminary screening of over 60 YM-isolates shows that 27% produced enough acid to decrease the pH of the growth media ($\text{pH} \leq 5.3$) under aerobic conditions; 5 of these strains produced acid when incubated at 50°C. 44% of those examined after growth in anoxic conditions generated acid. Several isolates demonstrated marked production of capsular exopolysaccharide material. Studies aimed at screening isolates for sulfide production and iron oxidation are ongoing.

Discussion. We expect that both native microorganisms and those introduced as a result of construction activities are represented in our samples. While identification of *all* microbial community members requires application of alternative techniques (i.e., ribosomal DNA analyses), these studies examined that portion of the YM community capable of growth on R2 media under the conditions specified. These primary findings

demonstrate that microbes present at the YM site are capable of survival and growth under conditions approaching those anticipated after waste deposition. Some examined members of the total microbial community can grow in the absence of oxygen and at temperatures of at least 50°C. Growth rates are measurable at ambient and elevated temperatures, and probable spore-forming organisms are even capable of surviving repeated exposure to 120°C. Further *in vitro* determinations will aid in determining *in situ* rates of growth, which can then be correlated with hydrologic flow rates. Depleted nutrient conditions favor the growth of only a select group of community members, but these are capable of reaching high cell densities under aerobic conditions, even at 50°C. Of those anaerobic isolates capable of growth on R2 media, it appears the combination of elevated temperatures and depleted nutrients are deleterious to growth.

Initial studies of MIC-associated activities demonstrate that YM microbial inhabitants possess the abilities to both produce acidic conditions and biofilm-generating materials. Production of biofilm "slimes" could facilitate the growth of organisms even at a very low relative humidity. Other microbial activities identified with MIC are currently being assessed and crude screening methods are being followed by more refined analysis to better characterize those isolates identified in primary screening protocols. Finally, microbial isolates that demonstrate the highest MIC-associated activity rates will be used to assess the MIC resistance of various alloys intended for use in waste deposition.

Clearly, further correlation of environmental conditions and their effects on relevant microbial activities is required to accurately predict the effects of microorganisms on waste containment. However, these studies provide evidence that microbial impacts are pertinent to risk assessment of nuclear waste storage facilities.

6.3.1.7 Material behavior as a function of gradients of chemical potential, concentration, temperature. As was discussed previously, at the drift scale a radioactive waste repository is extremely heterogeneous. This heterogeneity is the basis for the existence of gradients in chemical composition, temperature, relative humidity and even porosity. These gradients are the basis of thermodynamic driving forces: chemical potential, fugacity, concentration, temperature. As such they can drive reactions and cause substances to dissolve and precipitate in a manner that is not predicted based on average values for those parameters.

6.3.2 Historical Analogs as Long Term Experiments

In order to verify predictive capability we need to compare predictions to test cases where similar processes are occurring. These analogs need not mimic the potential

repository in all aspects, but rather must be able to provide information regarding a significant process in detail.

6.3.2.1 New Zealand. Microbially influenced degradation (MID) of concrete is thought to occur when microorganisms present in the environment produce mineral or organic acids that dissolve or disintegrate the concrete matrix. Three groups of bacteria are known to create conditions which are conducive to destroying concrete integrity. These microorganism are ubiquitous in the environment. They will, therefore, eventually be found in any repository facility, regardless of depth, because of the free movement of environmental contaminates into the confined space. The concrete facility of interest is an operational, passive cooling tower shell located at the Ohaaki Power Station near Wairakei, New Zealand.

Concrete samples from the tower walls were obtained by coring, chiseling, and scraping. Biofilm was retrieved by peeling it from the wall surface. Holes left from the removal of cored samples were used for the emplacement of five concrete specimens (including two proposed for the YMP) made from different cement formulations.

Altogether a total of 29 specimens were recovered. The presence of microbes known to be involved in MID have been verified. Further work in this area was canceled due to lack of funds.

Reference concrete and concrete-waste package composite specimens were emplaced in hydrothermal springs along with the specimens described in the geochemistry section. The samples were retrieved, but have not been analyzed because the program was canceled.

6.3.3 Modeling Activities

The license application (LA) for a potential nuclear waste repository at Yucca Mountain in Nevada must be submitted in the near future. As part of this application process, we must better understand the long-term chemical implications of introducing natural and fabricated materials as well as microbes into a radioactive waste repository. Some of these materials are introduced as a necessity of construction and others are introduced passively and even unintentionally. Of the former explicitly chosen materials, there may be an option to substitute alternates for some materials. Other materials may not be interchangeable.

There are three reasons for using modeling to understand the chemical modifications of the natural environment in a repository setting. The first is that the chemical consequences of some of the materials under consideration are not common to our experience for the long periods of time and/or the conditions of an underground

radioactive waste repository. Computer modeling using fundamental chemical principles allows us to project chemical conditions far into the future and to examine the system from selected points in time. The second reason is that modeling can significantly reduce the number of experimental trials required to demonstrate a similar understanding of chemical processes. Modeling chemical processes is economical and efficient for both simulating long periods of time and for investigating the consequences of multiple combinations of materials. The third reason is to maintain the flexibility required to support repository design and performance assessment efforts at this stage in the design decision process where the advantages and disadvantages of multiple options are being considered.

Modeling is effective, not as an end in itself, or as a tool to be used independently of other efforts, but rather as a facet of a program that is coordinated with experimental and historical analog activities. Such a coordinated program on a small scale is demonstrated in progress report on the long-term chemical impact of diesel exhaust (Meike et al., 1994). The strategy to model drift scale chemistry has been to focus on two areas. First, we are developing materials specific modules that can be either operated independently or can be inter-connected to simulate design and construction options under consideration. Secondly and concurrently to the first, we are developing the capability to simulate and visualize chemical processes in three-dimensions within the geological context of the Yucca Mountain. Conceptually, the modeling program was most advanced in the area of cementitious materials (ordinary Portland cement (OPC) grouts and concretes.

The most important role of the material specific chemical module is to reflect the material's chemical significance in the most streamlined manner possible. Thus, if it can be demonstrated that a material has no effect on the chemical environment, then it can be eliminated from the modeling of that scenario. Similarly, and probably more realistically, if it can be demonstrated that a material is involved to a significant extent only in certain chemical processes, then there is only need for computer simulation of those processes. Of course, the modules are only as robust as their foundations, and thus the chemical role that any materials play must be examined carefully across the range of changing parameters to assure that overly simplistic assumptions have not been made. If done correctly the modular approach can streamline the computer modeling significantly without affecting the capability to comment on questions significant to repository design.

At present our chemical modeling strengths lie in the ability to model the abiotic geological system over long periods and a range of temperature and chemical

conditions using aqueous geochemical modeling packages such as EQ3/6. This code is based on fundamental chemical principles and thus should be adaptable to any materials. However, the adaptation of this code to simulate the long term chemical degradation of non-traditionally geologic materials involves two considerations: first, the adequate representation of significant chemical processes, and second the representation of data for the appropriate phases in materials specific databases that support the modeling packages. The database needs will be described in detail below with respect to cement. In the process, it is hoped that some general considerations involving the databases will become clear. There are two aspects of chemical processes to consider. First are those processes that have not yet been included in the code, abiotic processes such as redox processes that are fundamentally important to modeling the degradation of metals (and this is presently being developed within the Geochemical Modeling Task). Second are those processes which were not intended to be part of the code. These include all biotic processes, specifically the chemical consequences of microbial activity.

With respect to biotic processes, the needs of chemical modeling in the repository diverge significantly from the abilities of the traditional geological models. Abiotic chemistry has seemed to adequately describe the rates and results of chemical processes in systems of traditional geological interest. This may not be the case for a radioactive waste repository. The abiotic chemistry is only one part of the chemical needs because, in a natural system even in the deep subsurface, as is discussed by Horn and Meike (1995) microbes are bound to be present (native and introduced), and many of the materials that may be introduced into a radioactive waste repository may provide nutrient sources to initiate microbial blooms.

At present no work is being conducted in the modeling area.

6.3.3.1 Drift scale thermochemical models. Our intent is to work from drift scale to repository and ultimately mountain scale progressively establishing those spatial and temporal characteristics that need to be transferred to the next larger scale. Thus, we have not chosen a software program that has provided ease in initial rendering of the engineered features. Rather, we have worked closely with a software company (Dynamic Graphics, Inc.) to push the limits of a geological modeling program (EarthVision™) in its ability to render engineering details.

The purpose of this work was to determine whether it would be possible to represent repository design features at an appropriate level of detail within the EarthVision™ software modeling framework. This is not a simple computer generated architectural design (CAD) program. In fact, developing the visual display was much

less straight forward than might be immediately apparent. The various features that are shown in these models were produced by routines that were originally formulated to produce geological features. Therefore, all of the physical features were produced by combinations of faulting, deposition, erosion and drilling "wells".

Certainly the work that went into producing these three-dimensional representations of potential repository designs would not be worthwhile if they were only intended as graphical representations. However, once built, the potential ultimate benefits are great. Our goal is to use these representations for drift, repository and mountain scale hydrological and chemical modeling that include modifications due to construction. The advantage of this software is that physical attributes can be assigned to the various forms and thus they can be used to visualize the evolution of complex chemical, hydrological and coupled chemical-hydrological models. An additional intention is to locate materials, calculate volumes with ease, and locate the interfaces between materials of interest.

EarthVision™ software has a number of significant potential advantages: 1) the ability to use existing Nevada State Survey coordinate data to interface with existing geochemical and hydrogeologic models. 2) the ability to develop an interactive approach between drift, repository and mountain scales to address hydrological and chemical questions. We expect that the first use of this software will be in support of drift scale hydrological and chemical modeling, using the chemical formulations for grout and steel that have been used in the ESF.

This exercise has pushed the limits of the EarthVision™ software in a number of ways. The capabilities of the software are demonstrated in the figures. The representation of a repository layout presently under consideration (Fig. 6-28) is plotted using Nevada State coordinate grid references, so that it can easily be placed into any other EarthVision representation of Yucca Mountain processes. The actual relative sizes of main and emplacement drifts are shown. We have demonstrated a level of detail sufficient to initiate modeling in support of major hydrological and chemical questions concerning repository construction.

Figures 6-29 and 6-30 illustrate various aspects of the emplacement tunnel. The cut-away view of the emplacement tunnel demonstrates the capability of the EarthVision™ software to represent discontinuous shapes (Fig. 6-29). It was found that waste packages were more easily modeled with rounded ends. Although the depiction in this case is for computational simplicity, the shape may have some merits for structural integrity. Figure 6-30 is illustrated to scale: a 25 m section of 4.3 m diam. emplacement tunnel, with concrete invert, gantry tracks and concrete waste package supports.

Various aspects of the service tunnel are depicted in Figs. 6-31 through 6-33. The simplified cross-section rendering of a 20-m section of 7.6 m diam. service tunnel (Fig. 6-31) shows concrete invert, shotcrete layer, and rockbolts for the metal grate platform anchored into the surrounding rock. The metal platform supports are placed at roughly 2 m intervals. A similar length of exposed service tunnel (Fig. 6-32) demonstrates the level of detail that can be obtained for chemical and hydrological modeling at the scale of tens of meters. The cementitious materials, concrete invert and shotcrete are illustrated. The metal materials illustrated are the gantry car rails, platform supports, platform and platform anchor rockbolts. Rock support rockbolts are illustrated in Figs. 6-33 through 6-37. The oblique view of the service tunnel (Fig. 6-33) illustrates rockbolt holes. Given standard spacing (1.5 m) as depicted on engineering drawings, 104 rockbolts would be found in this length of tunnel. A cross-sectional rendering (Fig. 6-34) and cut-away view (Fig. 6-35) of service tunnel showing rockbolt holes. The cross-sectional rendering (Fig. 6-36) and cut-away view (Fig. 6-37) show 36 rockbolts in a 20-m section of emplacement tunnel, given the standard spacing (1.5 m) as depicted on engineering drawings. Using these visual/calculational tools we can examine the chemical and hydrological effects of a plume of fluids equilibrated with cement (e.g. elevated pH) moving into the mountain. It is also clear that the orientation and spacing of rockbolts can heavily influence hydrology. Using EarthVision™ software it will be possible to examine the influence of rockbolts on hydrology on a number of scales from single drifts to the repository and the entire mountain.

Because of its level of detail, EarthVision™ allows the display and manipulation of individual rockbolts with grout (Figures 6-38, 6-39). We have also pushed the ability to model finite objects. Calculation of material volumes is straightforward, as is illustrated in the calculation of the volume of cementitious materials (approximately 54.1 m³) (Fig. 6-40), and the calculation of volume of metal materials (approximately 14.4 m³) (including the waste packages of wall thickness ~0.2 m) in a 20-m section of 4.3 diam. emplacement drift (Fig. 6-41).

6.3.3.2 Abiotic Models . The EQ3NR/EQ6 software package (Wolery, 1992; Wolery and Daveler, 1992) is composed of three executable programs (EQPT, EQ3NR and EQ6) and a number of databases that are used at the modeler's discretion (Fig. 6-42). EQPT simply formats databases to be readable by EQ3NR and EQ6, and is not shown in the figure. The input file for EQ3NR contains the analytical composition of the solution (including total concentrations of dissolved components, pH, Eh and oxygen fugacity). The code calculates the distribution of chemical species, using thermodynamic data located in the selected database. The output consists of an output and a pickup file,

which is used to initialize the EQ6 input file. EQ6 models the reaction of the aqueous solution with a set of minerals and gases, as well as fluid mixing and temperature changes. A set of five data files is now available. Three of these (COM, SUP and NEA) may be used with either the Davies equation, or the B-dot equation to calculate the activity coefficients. Their use is restricted to rather dilute solutions (ionic strength less than the sea water reference value). The two other data files (HMW, PIT) use Pitzer's equations (Pitzer, 1979), and are suitable for the modeling of high concentrations solutions. These databases are outlined below.

1. *SUP database*. Based entirely on the SUPCRT92 program (Johnson et al., 1992), this database has a high level of internal consistency. The database covers a wide range of chemical species. However for the purpose of drift scale chemical modeling it doesn't contain necessary data related to calcium-silicate-hydrate species that might be formed in cements at temperatures between 60 and 300°C.
2. *NEA database*. This database was produced by the Data Bank of the Nuclear Energy Agency of the European Community (Grenthe, 1992), and is specifically tailored to conduct uranium studies.
3. *HMW database*. This dataset is based on Harvie, Moller and Weare (1984). It can be applied to both dilute solutions and concentrated brines, at 25°C. It has also a very high degree of internal consistency but it only treats the components present in the "sea-salt-water" system. Important elements to the modeling of cement in a geologic repository, like Al and Si are not included in this database.
4. *PIT database*. This database is based primarily on data summarized by Pitzer (1979). This data file can also be applied to concentrated brines between 25°C and 100°C. It covers a larger set of species than the HMW database, but it does not address the silica and inorganic carbon species that are necessary to model cement in a geologic repository. In addition, it contains some internal inconsistencies.
5. *COM database*. This dataset represents a melange of data found in the SUP and NEA datasets, as well as data from the HMW dataset. Other data in this database have been obtained by correlation or interpolation. This set therefore offers the least assurance of internal consistency. However, it is the only means available to model problems with a high degree of compositional complexity.

The development of a cement specific database that would allow the modeling of cement-water, and ultimately cement-water-rock interactions has been interrupted.

EXPLORER™ software is most often utilized to visualize complex data sets from existing FORTRAN and C programs, especially those for which properties are linked to

a three dimensional spatial coordinate system. However, because it has the capacity to accept user-built modules it can also be used to encapsulate an existing program (in FORTRAN or in C) into a "module" (Fig. 6-43). Our intention is to utilize the complex chemical modeling capabilities and the modular format to develop materials specific modules and preserve entire complex

It is our intention is to use EXPLORER™ as a tool to encapsulate the EQ3/6 software package into three modules: EQPT, EQ3NR and EQ6. The ability to produce module maps and to imbed whole maps inside modules creates a functional hierarchy of computational maps that facilitates the series of complex and repetitive calculations that must be conducted over a number of levels as the scenarios are developed and compared. Each three module set will be encapsulated into a material specific module using the appropriate default settings, databases and integrating the appropriate biotic modules.

The material specific modules are powerful tools for repository design. They allow the flexibility to deal with variable levels of uncertainty and the ability to model and compare materials specific drift scale implications of repository design.

The material specific modules are the building blocks of design specific drift scale modeling that can be saved as "maps" in Explorer. The maps, which store complex chemical modeling paths at a level above what can be done with current modeling routines, can thus be used to retrace complex calculational steps and minimize operator error. As such it also represents a step forward in the documentation of computer modeling. The maps will interface with the EarthVision model described above to provide access to time stepped three-dimensional understanding of repository chemistry and hydrology.

6.3.3.3 Biotic Models (modeling microbiological activities). Although it is not possible to produce rigorous models of microbially related chemistry at this time, much progress can be made toward determining the relative significance of microbial effects with a simple box model. A box model treats microbial processes as a simplified chemical reactor. We can view microbial reactions as enzymatically-controlled chemical processes which are governed by the size, identity and metabolic state of the microbial community as well as the traditional abiotic chemical parameters such as pH and temperature. Each microbe must have an energy supply, a source of carbon, and a set of nutrients essential for life. The energy supply generally involves an electron acceptor-donor process, the carbon supply is usually some form of organic matter or carbon dioxide, and most microbes need sufficient amounts of nitrogen, phosphorous, and sulfur to live. Other elements are needed in trace amounts but are generally not limiting

in terms of microbial growth, especially in a heterogeneous repository environment. Water is also essential, and temperature is an important limiting factor. For a review of these considerations with regard to a potential repository at Yucca Mountain, see Horn and Meike (1995). Although specific microbes exist over subsets of this range, it is possible to establish, for this first step, a range of temperature over which microbes are active, as opposed to inactive (e.g. spore, dormant or dead state).

The first step in using a box model to understand microbial effects in a repository is to establish limits to the total amount of microbial activity possible in the repository based on the microbial needs listed above (e.g. energy, carbon, nutrients, water, appropriate temperature). This type of approach is described well by McKinley & Hagenlocher (1993) for the Swiss High Level Waste (HLW) and Low/Intermediate Level Waste (ILLW) repositories. They examine the energies available from all redox reactions possible for the materials present in the repository which can be utilized by microbes. This information is combined with an estimate of how much energy is needed to synthesize the compounds which make up biomass (this number is 0.1 mole of ATP to produce one gram of dry cell mass, which is equivalent to 450 kJ/mol if the efficiency of energy utilization is 10%). With this approach, the total biomass that can be sustained can be related to the masses of redox species that are present. Finally, if one can assume an average biomass metabolic rate, then the chemical effects of the biomass in terms of corrosion enhancement, ligand production, gas production or any other rate of chemical change can be estimated and related to overall repository behavior.

A similar simplified approach can be used to determine the maximum possible biomass based on the amounts of essential nutrients (phosphorous, nitrogen, and sulfur) present in the repository. An average biomass is defined in McKinley & Hagenlocher (1993), to have the composition $C_{160}(H_{250}O_{80})N_{30}P_2S$. The total amount of possible biomass is simply the total amount of accessible nutrient divided by its weight fraction in biomass.

This is complicated somewhat by the fact that nutrient availability may be a function of corrosion rates of repository materials, whose rates themselves depend on active biomass. Some nutrients are available only if they are released during corrosion of repository materials. The overall process is therefore coupled and amenable to modeling provided that some quantitative information on the type of coupling is available.

Applying this approach to the Swiss HLW repository, McKinley & Hagenlocher (1993) found that for a bounding calculation not limited by microbe mobility, the overall biomass was limited by energy availability, and not nutrient availability. The amounts

of nitrogen, phosphorous, and sulfur available in the backfill in particular are much higher than the total mass of electron donors needed to fuel microbial growth. The only exception is during the first ten years of repository existence where the availability of oxygen is expected to be high and, as a consequence, energy availability should also be high. The availability of O₂ over time in a potential Yucca Mountain repository drift is still under discussion. This is because the availability of air through the mountain's fracture system, the amount of time that the repository drifts will be ventilated artificially, and the amount of chemically conditioned backfill that may affect the f O₂ have not yet been bounded. The proposed Yucca Mountain repository differs from the Swiss in many ways, for example, the former is an unsaturated environment. However although the Swiss conditions are not necessarily analogous to the Yucca Mountain repository in many important aspects including, for example fO₂, it is illustrative to follow through the calculation as an exercise.

The biomass production rates calculated for the Swiss HLW repository range decrease from an initial rate of about 300 grams dry biomass/year/waste package to long-term rates of about 0.3 g/y/wp. These values can be used to constrain likely production rates of by-products such as organic ligands and gas generation, which in turn affect radionuclide transport rates and repository performance. For this case, even at maximum biological activity, the total production of organic complexing agents is only approximately equal to the estimated release rates of radionuclides. The net effect of microbial activity in terms of solubilization of radionuclides is therefore small for this repository.

Given that the conditions of the Swiss repository (e.g. granitic rock, repository design, saturated rock) are quite different, the findings of McKinley & Hagenlocher (1993) cannot be directly applied to the proposed Yucca Mountain repository. Information gained from this simple box model approach should be used to prioritize and guide more detailed work on microbial effects. More sophisticated models of microbial effects should then be generated using this more detailed information. However, because of the complex nature of microbial processes, and in particular their abilities to evolve with time, express new genes when environmental conditions change, and the diverse nature of microbial communities, it is unlikely that we could produce a reliable mechanistic chemical model for microbial behavior in the short term. Our best approach is to use our information on microbial behavior to define worst-case scenarios, identify parameters that limit microbial productivity, and incorporate these results into our task of designing the engineered barrier system.

Thermal and other perturbations of a microbially mediated chemical system occur as a complex function of microbial identity, microbial activity and colony growth (biomass). In addition, individual species function over a relatively narrow temperature range. Thus, even with respect to the traditional chemical parameters, biological reactions operate according to different laws than the abiotic reactions. However, although not identical to the abiotic case, it should be productive to take an approach similar to existing abiotic chemical modeling to use the chemical laws of microbial chemistry to predict long-term chemistry. This approach is also consistent with the ultimate goal which is to develop models which can be operated in tandem with the abiotic models.

The net chemical effect of a community of microbes can be thought of as a set of mass inputs and outputs. For example, an autotrophic bacteria may take in bicarbonate as a carbon source, and oxidize iron to ferrous iron as an energy source. As by-products, the bacteria may make acetate and as a consequence of oxidizing iron, lower the pH. Based on experimental observations of this type of bacteria in an environment similar to an anticipated repository environment, it should be possible to write a reaction that describes the overall chemical effects of this bacterial population. For each gram of active biomass, there can be related a positive flux of acetate and acid generation, and a negative flux of iron and bicarbonate.

At the most simple level, models of microbial activity can be used as input into EQ3/6 (Wolery, 1992). This approach offers the potential for modeling at a fairly high level of complexity in a short period of time. Although microbial activity is not explicitly provided for, the overall effect of microbial activity on repository corrosion processes can be. Such an approach allows the net effects, in terms of how microbes alter the local chemistry of their environments, to be accounted for. Thus the chemical effects of microbial activity can be rigorously coupled to materials interactions in the repository without specific identification of all microbial species in the repository or explicitly providing for the details of microbial activity.

This type of model obviously lacks feedback from system parameters to the microbial processes. Feedback between environmental conditions and microbial activity is the most difficult part of implementing microbial activity into the simulation. But if empirical relationships between microbial activity and environmental parameters such as temperature and pH are available, they can readily be incorporated into the simulation. For example, microbial productivity is almost certainly pH dependent. Most bacteria live only over a restricted pH range.

The next step in making this type of model more realistic would be to incorporate feedback between environmental parameters and microbial productivity. If the pH changed significantly, it is likely that a new type of microbial population would exist, with a different set of chemical effects. Likewise, if microbial activity were to change the pH, the equilibrium condition between the aqueous fluid and the material with which it is in contact, is changed. EQ3/6 currently has the capability to incorporate these types of complexities into the simulation. Experimental data on the biomass production rates of any variety of microbial populations which are dependent on pH, or on any other parameter related to the chemical response or influence of microbial activity, can be entered as reactants in the simulation. Kinetic control of these rates is also possible if appropriate rate data are known. Given the complexity and interdependency of some of these factors, it may be necessary to enter the numerical relationships as reactants into EQ3/6 and in a step-wise or iterative fashion to take into account the chemical effects of the microbial population.

The presence of other repository materials can also be included in the simulation so that coupling between all chemical processes is properly accounted for. For example, the simulation may include the host rock, a metal canister, and cement. As the reaction proceeds, the effect of acid generation on pH stability, the effect of acetate generation on metal corrosion, the affects of bicarbonate utilization are all accounted for. The system will evolve and have a pH which is controlled by the coupled interactions of all these pH-dependent reactions. Likewise, the complete solution composition can be calculated for any step along this reaction progress. The ability to do this stage of modeling will be enhanced by the use of Explorer™ software.

Our ultimate aim is to find an approach that can be integrated into a sophisticated feedback linkage with the existing EQ3/6 code. We aim to frame descriptions of microbial activity in forms that mimic the abiotic thermodynamic and kinetic descriptions. To do this we must distinguish between the two types of processes: those that can be seen as perturbations from an equilibrium state, or as part of a new, microbially mediated equilibrium state and thus comprise a module that will interact with EQ3, and those considerations that affect rates of change and thus the kinetics and thus comprise a module that will interact with EQ6 (Fig. 6-44). In developing the descriptions we seek to define microbial activities in terms of three types of processes: processes or conditions that can represent standard states, processes that can be described in terms of rates of change, and processes in which transfer of mass, energy or other quantifiable units sum to zero. The advantage of these definitions is that they translate well into the pre-existing abiotic thermodynamic/kinetic framework. We will

define standard states as points of reference that will allow us to quantify deviations from those points. Describing processes in terms of equations that sum to zero has many advantages. For example it ensures internal consistency and provides a foundation for expanding from simple to multi-component systems.

6.4 Summary and Conclusions

Progress has been made in the identification and quantification of materials that may be used as part of the construction of a radioactive waste repository at Yucca Mountain. The major significant processes affecting the chemical impact of those materials on the Near Field Environment and the waste packages have also been identified, as well as the data that is required to be able to predict the outcome of many of these processes over long periods of time. In the past we have emphasized those processes and materials that would take the water chemistry or certain processes outside of the bounds that are assumed based on the natural geochemistry, or the limited knowledge of long term behavior. Our work in the near future is to use this information to provide some bounds for chemical and mechanical modeling, but also to narrow those bounds where they make a significant difference to performance assessment modeling. Many of the fundamental tools are in place to better bound chemistries and behaviors, but others are still missing.

To date the most significant unknowns that have been identified in the area of introduced materials are the effects of microbial activity on water chemistry and degradation rate of important materials (and our ability to model those effects), the effects of cement-water-rock chemistry over time, and the effect of metals corrosion over time.

6.5 Acknowledgments

W. Bourcier, M. Caffee, L. Clodic, S. A. Carrol, A. Miller, M. Sprague, and P. A. Sterne contributed to this chapter.

6.6 References

- Aminabhavi, T. M., and U. S. Aithal (1990), *J. Appl. Polym. Sci.* **41**, 2113–2131.
- Andersson, K., B. Allard, M. Bengtsson and B. Magnusson (1989) Chemical composition of cement pore solutions. *Cem. Concr. Res.* **19**, 327-332.
- Andreoni, V., G. Baggi, C. Guaita, and P. Manfrin (1993). *Int. Biodeterioration Biodegradation* **31**, 41–53.

Atkins, M., F. P. Glasser, A. Kindness, and D. E. Macphee (1991), *Solubility Data for Cement Hydrate Phases (25°C)*, U.S. Department of Energy, Washington, DC, DOE/HMIP/RR/91/032.

Atlas, R. M. (1982), *Enumeration and Estimation of Biomass of Microbial Components in the Biosphere*, in *Experimental Microbial Ecology*, R. G. Burns and J. H. Slater, Eds., (Blackwell Scientific Publishers, Oxford, England), pp. 84–102.

Awasthi, S. (1993), *Natl. Acad. Sci. Lett.* **16**, 143–144.

Babushkin, V. I., G. M. Matveyev and O. P. Mchedlov-Petrosyan (1985) *Thermodynamics of Silicates*. Springer-Verlag. 459 pp.

Barnes, I., T. S. Presser, M. Saines, P. Dickson, and A. F. K. van Groow (1982), "Geochemistry of Highly Basic Calcium Hydroxide Groundwater" in *Jordan, Chem. Geol.* **35**, 147–154.

Barnes, M. W., and D. M. Roy (1983), The Buffering Mechanisms in Leaching of Composites of Cement with Radioactive Waste, *Mater. Res. Soc. Symp. Proc.* **15**, 159–166. NNA.19920131.0250

Barns, S. M., R. E. Fundyga, M. W. Jeffries, and N. R. Pace (1994), Remarkable Archaeal Diversity Detected in a Yellowstone National Park Hot Spring Environment, *Proc. Natl. Acad. Sci USA* **91**, 1609–1613.

Barr-Kumarakulasinghe, S. A. (1994), *Polymer* **35**, 995–1003.

Barrer, R.M., (1978), *Zeolites and Clay Minerals as Sorbents and Molecular Sieves*, Academic Press, New York, 497 p.

Barret, P. and D. Bertrandie (1986) Fundamental hydration kinetic features of the major cement constituents: Ca_3SiO_5 and $\text{b-Ca}_2\text{SiO}_4$. *J. Chemie Phys.* **83**, 765-775.

Bell J. L. S., D. A. Palmer, and H. L. Barnes (1992), *Acetate in Hydrothermal Solutions: Decomposition Kinetics and Metal Complexation, in Water-Rock Interaction*, Y. Kharaka and A. Maest, Eds., (Balkema, Rotterdam), pp. 307–310.

Bennett, P. C., M. E. Melcer, D. I. Siegel, and J. P. Hassett (1988), The Dissolution of Quartz in Dilute Aqueous Solution of Organic Acids at 25°C, *Geochim. Cosmochim. Acta* **52**, 1521–1530. NNA.19921106.0027

Bensted, J. (1983a) *Hydration of portland cement*. p. 307-347 in Ghosh, S. N. (ed.) (1983a).

Bensted, J. (1983b) Early hydration of portland cement - effects of water/cement ratio. *Cem. Concr. Res.* **13**, 493-498.

Bensted, J. (1989) Oil well cements - a general review. *Chem. Ind.*, 20 Feb. 1989, p. 100-105.

Berner, U. R. (1987). Modelling porewater chemistry in hydrated portland cement. *Mat. Res. Soc. Symp. Proc.* **84**, 319-330.

Berry, W. E. (1983), *Durability of Marker Materials for Nuclear Waste Isolation Sites*, Office of Nuclear Waste Isolation, Battelle Memorial Institute. NNA.19920131.0430

Bethke, C. M. *The Geochemist's Workbench™ A Users Guide to RXN, ACT2, TACT, REACT, and GTPLOT*. Urbana, Illinois: C. Bethke, c1992.

Bish, D. L., F. A. Caporuscio, J. F. Copp, B. M. Crowe, J. D. Purson, J. R. Smyth, and R. G. Warren (1981), *Preliminary Stratigraphic and Petrologic Characterization of Core Samples from USW G-1, Yucca Mountain, Nevada*, Los Alamos National Laboratory, Los Alamos, NM, LA-8840-MS. NNA.19870406.0099

Bisi, M., C. Nicoletta, E. Palazzi, M. Rovatti, and G. Ferraiolo (1994), *Chem. Eng. Technol.* **17**, 67-72.

Borenstein, S.W. (1994). *Microbially Influenced Corrosion Handbook*. New York, NY, Industrial Press Inc.

Braithwaite, W. R., and K. A. Lichti (1981), *Surface Corrosion of Metals in Geothermal Fluids at Broadlands, New Zealand*, American Society for Testing and Materials.

Brandrup, J., and E. H. Immergut, Eds. (1975), *Polymer Handbook* (John Wiley, New York, NY).

Breck, D.W. (1974). *Zeolite Molecular Sieves*, J. Wiley and Sons, New York, 771 p.

Brock, T. D., and M. T. Madigan (1991), *Biology of Microorganisms* (Prentice-Hall, Englewood Cliffs, NJ).

Brown, P. W., E. Franz, G. Frohnsdorff, and H. F. W. Taylor (1984). Analyses of the aqueous phase during early C₃S hydration. *Cem. Concr. Res.* **14**, 257-262.

Brown, P. W., J. Pommersheim and G. Frohnsdorff (1985). A kinetic model for the hydration of tricalcium silicate. *Cem. Concr. Res.* **15**, 35-41.

Bruton, C. J., B. L. Phillips, A. Meike, S. Martin, and B. E. Viani (1994), *Cement Minerals at Elevated Temperature: Thermodynamic and Structural Characteristics*, *Mater. Res. Soc. Symp. Proc.* **333**, 327-334, UCRL-JC-115796. NNA.19940318.0011

Bruton, C. J., W. E. Glassley, et al. (1995), *Geothermal Areas as Analogues to Chemical Processes in the Near-Field and Altered Zone of the Potential Yucca Mountain, Nevada Repository*, LLNL, Lawrence Livermore National Laboratory, Livermore, CA, UCRL-ID-119842. MOL.19960408.0210

Burnay, S. G., Ed. (1990), *A Practical Model for Prediction of the Lifetime of Elastomeric Seals in Nuclear Environments* (American Chemical Society, Washington, DC), pp. 524-533.

Burnett, N. C., R. D. Hooton, R. B. Heimann and M. Onofrei (1985). The development of durable cementitious materials for use in a nuclear fuel waste disposal facility. *Mat. Res. Soc. Symp. Proc.* 50, 461-468.

Burton, B. L. (1993). *J. Appl. Polym. Sci.* 47, 1821-1837.

Buscheck, T.A. and J.J. Nitao (1994). *The impact of buoyant gas-phase flow and heterogeneity on thermo-hydrological behavior at Yucca Mountain*. Proceedings of the International High Level Radioactive Waste Management Conference, 22-26 May, 1994, Las Vegas, NV and Dept. of Energy, Lawrence Livermore Natl. Laboratory Report #UCRL-JC-115351.

Carlson, V. E.O. Bennett, and J.A. Rowe. (1961). Microbial flora in anumber of oilfield water injection systems. *J. Soc. Pet. Eng.* 1, 72.

Carroll, S. A., M. Alai, and S. A. Copenhaver (in press), *Experimental Investigation of Hydrous Pyrolysis of Diesel Fuel: Potential Impact on the Proposed High-Level Radioactive Waste Repository, Yucca Mountain, Nevada*, Lawrence Livermore National Laboratory, Livermore, CA, UCRL-ID (in press).

Chapman, N. and I. McKinley (1990), Radioactive Waste: Back to the Future? *New Scientist* (May 5, 1990), 36-40.

Chapman, N., P. Cloke, et al. (1995), *Applications of Natural Analogue Studies to Yucca Mountain as a Potential High Level Radioactive Waste Repository*, The Natural Analogue Review Group. MOL.19960508.0064

Chessa, G., G. Marangoni, B. Pitteri, N. Stevanato, and A. Vavasori (1991), *Reactive Polym.* 14, 143-150.

Chiantore, O., M. P. L. d. Cortemiglia, and M. Guaita (1989), *Makromolekulare Chemie* 190, 3143-3152.

Costerton, J.W. and G.G. Geesey. (1985) The microbial ecology of surface colonization and of consequent corrosion. *Proceedings of the International Conference on Biologically Induced Corrosion, June 10-12, 1985*, Gaithersburg, MD.

Costerton, J.W. and J. Boivin. (1991) *The role of biofilms in microbial corrosion in Microbially Influenced Corrosion and Biodeterioration*, N.J.E. Dowling, M.W. Mittleman, and J.S. Danko, eds. National Association of Corrosion Engineers, Houston, TX.

Coughlin, J. P. and C. J. O'Brien (1957). High temperature heat contents of calcium orthosilicate. *Am. Chem. Soc. J.* 61, 767-769.

Crammond, N. (1996) *The thaumasite form of sulphate attack-Discussion of possible reaction mechanisms* Gordon Research Conference, Plymouth, New Hampshire, July, 1996.

- Culivicchi, G., C. G. Palmerini, and V. Scholari (1985). Behaviour of Materials in Geothermal Environments, *Geothermics* 14(1), 73-90.
- Dickie, R. A., J. W. Holubka, and J. E. Devries (1990), *J. Adhesion Sci. Technol.* 4, 57-67.
- Dodd, F. J., A. E. Johnson, and W. C. Ham (1960), Material and Corrosion Testing at the Geysers Geothermal Power Plant, Department of Eng. Research, Pacific Gas and Electric Company.
- Dole, M., Ed. (1973), *The Radiation Chemistry of Macromolecules* (Academic Press, New York, NY).
- Ederova, J. and V. Satava (1979). Heat capacities of C₃AH₆, C₄ASH₁₂ and C₆AS₃H₃₂. *Thermochim. Acta* 31, 126-128.
- El-Agramy, A. A. Shabaka (1990), *Isotopenpraxis* 26, 229-231.
- El-Sonbati, A. Z., A. A. El-Bindary, M. A. Diab, M. A. El-Ela, and S. A. Mazrouh (1994), *Polymer* 35, 647-652.
- Ellezer, I., N. Ellezer, R. A. Howald and P. Viswanadham (1981). Thermodynamic properties of calcium aluminates. *J. Phys. Chem.* 85, 2835-2838.
- Ellison, M. S., S. H. Zeronian, and Q. Xie (1989), *Textile Res. J.* 59, 657-660.
- EPA (Environmental Protection Agency), 1985, *Environmental Standards for the Management and Disposal of Spent Nuclear Fuel, High-Level and Transuranic Wastes: Final Rule*, U.S. Code of Federal Regulations, 40 CFR Part 191, Washington, DC. HQO.19871113.0033
- Fein, J. B. (1991), Experimental Study of Aluminum-, Calcium-, and Magnesium-Acetate Complexing at 80°C, *Geochim. Cosmochim. Acta* 55, 955-964.
- Fontana, M. G., and N. D. Breen (1978), *Corrosion Engineering* (McGraw-Hill Publishing, New York, NY), pp. 263-265. NNA.19891018.0176
- Foster, P. K., and A. Tombs (1962), Corrosion by Hydrothermal Fluids, *New Zealand J. Science* 5 (1), 28-41.
- Freemantle, M. (1994), Chemical Techniques Help Conserve Artifacts Raised from Titanic Wreck, *Chem. Eng. News*, 49-52.
- Fujii, X. and W. Kondo (1983). Estimation of thermochemical data for calcium silicate hydrate (C-S-H). *Am. Ceram. Soc. J.* 66, C220-C221.
- Garrett, R. W., et al. (1990), *Temperature Dependence of the Radiation Chemistry of Polymers* (American Chemical Society, Washington, DC).
- Gartner, E. M., F. J. Tang and S. J. Weiss (1985). Saturation factors for calcium hydroxide and calcium sulfates in fresh portland cement pastes. *Am. Ceram. Soc. J.* 68, 667-673.

Gestsdottir, K., and D. A. C. Manning (1992), *An Experimental Study of the Dissolution of Albite in the Presence of Organic Acids, in Water-Rock Interaction*, Y. Kharaka and A. Maest, Eds., (Balkema, Rotterdam), pp. 315–318.

Gettens, R. J. and C. Frondel (1956). *Studies in Conservation*, 2, 64.

Gherna, R., P. Pienta, and R. Cote., eds. (1989). *Catalogue of Bacteria and Bacteriophages*. 17th edition. Rockville, MD, American Type Culture Collection.

Ghosh, S. N. (1983) Portland cement phases: polymorphism, solid solution, defect structure and hydraulicity. in Ghosh (ed) *Advances in Cement Technology*. Pergamon Press. pp. 289-305.

Gilfric, H. P., and H. Wilski (1992), *Int. J. Rad. Applic. Instrumen. C* 39, 401–405.

Gillen, K. T., and R. L. Clough (1989), *Polymer Degradation and Stability* 24, 137–168.

Glasser, F. P., A. A. Rahman, D. Macphee, M. Atkins, N. Beckley and E. E. Lachowski (1986) *Immobilization of radioactive waste in cement-based matrices*. United Kingdom Dept. of the Environment Report DOE RW 86.084. 110 pp.

Glasser, F. P., S. Diamond and D. M. Roy (1987b) Hydration reactions in cement pastes incorporating fly ash and other pozzolanic materials. *Mat. Res. Soc. Proc.* 85, 167-186. [This paper also appears in *Mat. Res. Soc. Proc.* 86]

Glasser, F. P., M. J. Angus, C. E. McCulloch, D. Macphee and A. A. Rahman (1985) The chemical environment in cements. *Mat. Res. Soc. Proc.* 44, 849-858.

Grassi, N., and G. Scott, Eds. (1985), *Polymer Degradation and Stabilisation* (Cambridge University Press, Cambridge).

Greenberg, A.E., R.R. Trussell, L.S. Clesceri, and M.A.H. Franson, eds. (1985). *Standard Methods for the Examination of Water and Wastewater*. 16th edition. Washington, D.C., American Public Health Association.

Greenfield, B. F., C. M. Linklater, A. D. Moreton, M. W. Spindler, and S. J. Williams (1993), *The Effects of Organic Degradation Products on Actinide Disposal, AEA Technol.*

Grutzeck, M. W. and A. R. Ramachandran (1987) An integration of tricalcium silicate hydration models in light of recent data. *Cem. Concr. Res.* 17, 164-170.

Haas, J. L. Jr., G. R. Robinson, Jr. and B. S. Hemingway (1981) Thermodynamic tabulations for selected phases in the system $\text{CaO-Al}_2\text{O}_3\text{-H}_2\text{O}$ at 101.325 KPa (1 atm) between 273.15 and 1800 K. *J. Phys. Chem. Ref. Data* 10, 575-669.

Hajash, A., S. P. Franklin and C. L. Reed (1992), Experimental Feldspar Dissolution in Acetic and Oxalic Acids at 100°C, in *Water-Rock Interaction*, Y. Kharaka and A. Maest, Eds., (Balkema, Rotterdam), pp. 325–328.

Haldeman, D. L., and P. S. Amy (1993), Bacterial Heterogeneity in Deep Subsurface Tunnels at Rainier Mesa, Nevada Test Site, *Microb. Ecol.* 25, 183–194.

Haldeman, D. L., P. S. Amy, D. Ringelberg, and D. C. White (1993), Characterization of the Microbiology within a 21-m³ Section of Rock from the Deep Subsurface, *Microb. Ecol.* 26, 145-159.

Haldeman, D.L., P.S. Amy, D.C. White, and D. Ringelberg. (1994). Changes in bacteria recoverable from subsurface volcanic rock samples during storage at 4°C. *Appl. Environ. Microbiol.* 60, 2697-2703.

Hanck, J. A., and G. Nekoxa (1980), *Corrosion Rate Monitoring at The Geysers Geothermal Power Plant*, Department of Eng. Research, Pacific Gas and Electric Company.

Hedges, R. E. M. (1976), On the Occurrence of Bromine in Corroded Silver, Studies in *Conservatism* 21, 44-46. NNA.19931005.0006

Hedrick, D. B., and D. C. White (1986), Microbial Respiratory Quinones in the Environment. I. A Sensitive Liquid Chromatographic Method, *J. Microbiol. Meth.* 5, 243-254.

Heimann, R. B. (1988a) Interaction of cement and radioactive waste forms in multicomponent systems tests at 200°C. Part 1: Leaching and sorption of cesium, strontium and actinides. *Cem. Concr. Res.* 18, 389-400.

Heimann, R. B. (1988b) Interaction of cement and radioactive waste forms in multicomponent systems tests at 200°C. Part 2: Mineralogical changes of cement. *Cem. Concr. Res.* 18, 554-560.

Heimann, R. B. and R. D. Hooton (1986) Mineralogical changes of various cement formulations during reaction with groundwater in the presence of Ca and Na-bentonite at 150°C. *Can. Min.* 24, 289-302. Also issued as AECL-8895.

Hermannsson, S. (1970), Corrosion of Metals and the Forming of a Protective Coating on the Inside of Pipes Carrying Thermal Waters Used by the Reykjavik Municipal District Heating Service, *Geothermics 2* (Special Issue: U.N. Symposium on the Development and Utilization of Geothermal Resources, Pisa), pp. 1602-1611.

Horn, J. M., and A. Meike (1995), *Microbial Activity at Yucca Mountain*, Lawrence Livermore National Laboratory, Livermore, CA, UCRL-ID-122256.

Horn, J. M., and A. Meike (1996), A Program to Assess Microbial Impacts on Nuclear Waste Containment, in *Proceedings of the 1996 High Level Radioactive Waste Meeting*, Las Vegas Nevada, Lawrence Livermore National Laboratory, Livermore, CA, UCRL-JC-122732. MOL.19960409.0194

Horn, J. M., B. Economides, A. Meike, and R. D. McCright (1996), Initial Studies to Assess Microbial Impacts on Nuclear Waste Disposal, in *Proceedings of the 1996 High*

- Level Radioactive Waste Meeting*, Las Vegas Nevada, Lawrence Livermore National Laboratory, Livermore, CA, UCRL-JC-122587. MOL.19960409.0710
- Imasaka, T., M. Hozumi, and N. Ishibashi (1992) *Anal. Chem.* 64, 2206–2209.
- Ishigaki, I., and F. Yoshii (1992), Radiation Physics and Chemistry, *Int. J. Rad. Applic. Instrum. C* 39, 527–533.
- Ivan, B., B. Turcsanyi, T. Kelen, and F. Tudos (1991), *Die Angewandte Makromolekulare Chemie* 189, 35–49.
- Jackson, K. J., A. K. Burnham, R. L. Braun, and K. G. Knauss (1992), *Measurement of Pressure Effects on N-Hexadecane Cracking Rates*, 37, 1614–1620.
- Jackson, K. J., and S. A. Carroll (1994), Experimental Investigation of Hydrous Pyrolysis of Diesel Fuel and the Effect of Pyrolysis Products on Performance of the Candidate Nuclear Waste Repository at Yucca Mountain, *Mater. Res. Soc. Symp. Proc.* 333, 841–847, UCRL-JC-116352. MOL.19950728.0064
- Jeffrey, J. W. (1964) The crystal structures of the anhydrous compounds. pp. 131-164 in Taylor, H.F.W. (ed.) *The Chemistry of Cements*. Academic Press.
- Johnson, A. B. J., and B. Francis (1980), *Durability of Metals from Archaeological Objects, Metal Meteorites, and Native Metals*, Pacific Northwest Laboratory, U.S. Department of Energy. NNA.19910604.0005
- Johnson, J. W., and S. R. Lundeen (in press), *GEMBOCHS Thermodynamic Data Files for Use with the EQ3/6 Software Package*, Lawrence Livermore National Laboratory, Livermore, CA, UCRL-ID.
- Jones, P. A. (1992), *Principles and Prevention of Corrosion* (MacMillan Publishing, New York, NY), 392–393.
- Kaplan, M. L. (1991), *Polym. Eng. Sci.* 31, 689–698.
- Kay, M. J., L. H. G. Morton, and E. L. Prince (1991), *Int. Biodeterioration* 21, 204–222.
- Kay, M. J., R. W. McCabe, and L. H. G. Morton (1993). *Int. Biodeterioration Biodegradation* 31, 209–225.
- Kenny, J. M., L. Torre, and L. Nicolais (1993), *Thermochim. Acta* 227, 97–106.
- Kharaka, Y., P. D. Lundegard, G. Ambats, W. C. Evans, and J. L. Bischoff (1993), Generation of Aliphatic Acid Anions and Carbon Dioxide by Hydrous Pyrolysis of Crude Oils, *Appl. Geochem.* 8, 317–324.
- Khare, A. R., N. A. Peppas, G. Massimo, and P. Colombo (1992), *J. Controlled Release* 22, 239–244.
- Khinnavar, R. S., and T. M. Aminabhavi (1992), *J. Appl. Polym. Sci.* 46, 909–920.

Khoury, H. N., E. Salameh, and Q. Abdul-Jaber (1985), Characteristics of an Unusual Highly Alkaline Water from the Maqarin Area, Northern Jordan, *J. Hydrol.* 81, 79–91. NNA.19920131.0287

Khoylou, F., and A. A. Katbab (1993), *Radiation Phys. Chem.* 42, 219–222.

Kim, N. D., and S. J. Hill (1993), *Environ. Technol.* 14, 1015–1026.

Knauss, K. G., and W. J. Beiriger (1984), *Report on Static Hydrothermal Alteration Studies of Topopah Spring Tuff Wafers in J-13 Water at 150 °C*, Lawrence Livermore National Laboratory, Livermore, CA, UCRL-53576. HQS.19880517.2007

Knauss, K. G., W. J. Beiriger, and D. W. Peifer (1985a), *Hydrothermal Interaction of Solid Wafers of Topopah Spring Tuff and J-13 Water at 90, 150, and 250 °C Using Dickson-Type, Gold-Bag Rocking Autoclaves: 1. Short-Term Experiments*, Lawrence Livermore National Laboratory, Livermore, CA, UCRL-53645. NNA.19900207.0282

Knauss, K. G., W. J. Beiriger, and D. W. Peifer (1985b), *Hydrothermal Interaction of Crushed Topopah Spring Tuff and J-13 Water at 90, 150, and 250 °C Using Dickson-Type, Gold-Bag Rocking Autoclaves*, Lawrence Livermore National Laboratory, Livermore, CA, UCRL-53630. NNA.19931005.0010

Knauss, K. G. and D. W. Peifer (1986), *Reaction of Vitric Topopah Spring Tuff and J-13 Groundwater under Hydrothermal Conditions Using Dickson-Type, Gold-Bag Rocking Autoclaves*, Lawrence Livermore National Laboratory, Livermore, CA, UCRL-53795. NNA.19891102.0017

Knauss, K. G., W. J. Beiriger, and D. W. Peifer (1987), *Hydrothermal Interaction of Solid Wafers of Topopah Spring Tuff with J-13 Water and Distilled Water at 90 and 150 °C Using Dickson-Type, Gold-Bag Rocking Autoclaves: Long-Term Experiments*, Lawrence Livermore National Laboratory, Livermore, CA, UCRL-53722. NNA.19870713.0081

Komarneni, S. and D. M. Roy (1983) Hydrothermal interactions of cement or mortar with zeolites or montmorillonites. *Mat. Res. Soc. Symp. Proc.* 15, 55–62.

Kurnoskin, A. V. (1992), *J. Appl. Polym. Sci.* 46, 1509–1530.

Kutty, S. K. N., T. K. Chaki, and G. B. Nando (1992), *Polym. Degradation Stability* 38, 187–192.

Larrabee, C. P., and W. L. Mathay (1963), in F. L. LaQue and H.R. Copsum, Eds., *Corrosion Resistance of Metals and Alloys* (Reinhold Publishing Co.), 319–323. NNA.19870406.0431

Lea, F. M. (1971), *The Chemistry of Cement and Concrete* (Chemical Publishing Co.), 727 pp. NNA.19890713.0195

Leed, W. T., and R. J. Watters (1994), Assessment of Rock Bolt Systems for Underground Waste Storage. *High Level Radioactive Waste Management, Las Vegas, Nevada*, American Nuclear Society, Inc. American Society of Civil Engineers.

Licina, G.J. (1988). *Sourcebook for Microbiologically Influenced Corrosion in Nuclear Power Plants*. EPRI NP-5580, Electric Power Research Institute, Palo Alto, CA.

Little, B.J., P.A. Wagner, and D. Duquette. (1987) Microbially induced cathodic depolarization. *Corrosion/87*, National Association of Corrosion Engineers, Houston, TX.

Livingston, R. A., P. E. Stutzman, R. Mark and M. Erdik (1992) Preliminary analysis of the masonry of the Hagia Sophia Basilica, Istanbul. *Mat'l. Res. Soc. Symp. Proc.* Vol. 267, 721-735.

LLYMP9603087 (1996), Memo from A. Meike to J. Montgomery of M&O/Morrison-Knudsen Corp. *Subject: Assessment of Dust Suppression Additives*.

Lovley, D.R. and E.J.P. Phillips. (1987). Rapid assay for microbially reducible ferric iron in aquatic sediments. *Appl. Environ. Microbiol.* 53, 1536-1540.

Lucey, V. F. (1972), Developments Leading to the Present Understanding of the Mechanism of Pitting Corrosion of Copper, *Br. Corrosion J.* 7, 36-41.
NNA.19891004.0341

Lundegard, P. D., Y. K. Kharaka, and R. J. Rosenbauer (1992), Petroleum as a Potential Diagenetic Agent: Experimental Evidence, in *Water-Rock Interaction* Y. Kharaka and A. Maest, Eds., (Balkema, Rotterdam), pp. 329-335.

Lynch, W. (1978), *Handbook of Silicone Rubber Fabrication*. (Van Nostrand Reinhold Company, New York, NY).

Macphee, D. E., K. Luke, F. P. Glasser and E. E. Lachowski (1989) Solubility and aging of calcium silicate hydrates in alkaline solutions at 25°C. *Am. Ceram. Soc. J.* 72, 646-654.

Majling, J., V. Tomkova and E. Istenikova (1985) Calorimetric study of reactions in the system $C_4A_3S - CH - CS - H$. *Thermochim. Acta* 85, 219-222.

Manning, H.L. (1975). New medium for isolating iron-oxidizing and heterotrophic acidophilic bacteria from acid mine drainage. *Appl. Microbiol.* 30, 1010-1016.

Mark, H. S., N. M. Bikales, C. G. Overberge, G. Menge, and J. I. Kroschwitz, Eds. (1985), *Encyclopedia of Polymer Science and Engineering* (John Wiley, New York, NY).

Marshall, E. (1990), Clovis Counterrevolution, 249(August 17, 1990), pp. 738-741.

Martin, S. I, B. Viani, and A. Meike (1995), Synthesis of 1.1 nm Tobermorite: A Cement Phase Expected under Repository Conditions, in *Proceedings of the 1995 High*

Level Radioactive Waste Management Meeting, Las Vegas, Nevada, Lawrence Livermore National Laboratory, Livermore, CA, UCRL-JC-119131, MOL.19950913.0005

Martin, S. I, B. Viani, and A. Meike (1996), *Water Adsorption by Okenite (Ca₁₀Si₁₈O₄₆·18H₂O) at Ambient Temperature*, Lawrence Livermore National Laboratory, Livermore, CA, UCRL-ID (in preparation).

Maycock, J. N., J. Skalny and R. S. Kalyoncu (1974) Thermal decomposition of cementitious hydrates. pp. 697-711 in R. S. Porter and J. F. Johnson, eds. *Analytical Calorimetry*. Plenum.

McNeil, M.B., D.W. Mohr and B.J. Little (1990). *Correlation of laboratory results with observations on long-term corrosion of iron and copper alloys. Proceedings of the Materials Research Society 1990 Spring Meeting, Symposium on Materials Science in Archeology* (in press).

McNeill, I. C., M. Zulfiqar, and T. Kousar (1990), *Polym. Degradation Stability* 28, 131-151.

Meike, A. (1993), *Chemical and Mineralogical Concerns for the Use of Man-Made Materials in the Post-Emplacement Environment*, Lawrence Livermore National Laboratory, Livermore, CA, UCRL-ID-113383. MOL.19930809.0021

Meike, A. (1994), Chemical Implications for the Presence of Introduced Materials in the Post-Emplacement Environment, *Mater. Res. Soc. Symp. Proc.* 333, 835-840. NNA.19940408.0028

Meike, A., and C. Wittwer (1994), Introduced Materials and Colloid Formation: A Report on the Current State of Knowledge, in *Proceedings of the Materials Research Society* (Fall 1993), pp. 783-789, UCRL-JC-114122. NNA.19940316.0115

Meike, A., M. Onofrei, C. J. Bruton, and B. E. Viani (1994), Progress in Understanding the Structure and Thermodynamics of Calcium Silicate Hydrates, in *High Level Radioactive Waste Management, Proceedings of the Fifth Annual International Conference* (Las Vegas, NV, May 1994), pp. 2590-2596, UCRL-JC-116358. NNA.19940517.0127

Meike, A., W. L. Bourcier, M. Alai, D. L. Haldeman, P. S. Amy, T. Lagadinos, and L. Hersman (1994), *Long-Term Chemical Effects of Diesel Fuel Emissions on a Mining Environment: A Preliminary Assessment Based on Data from a Deep Subsurface Tunnel at Rainier Mesa, Nevada Test Site*, YMP-MOL-73. MOL.19950406.0141

Meike, A., and M. Spragge (1995) *Progress Report #1 on the Materials Identification, Characterization and Evaluation Activity: Acquisition of Materials Data from the Exploratory Studies Facility*, Yucca Mountain Site Characterization Project Milestone Report #MOL132. MOL.19960415.0416

Meike, A., Ed. (1995), *Potential Long-Term Chemical Effects of Diesel Fuel Emissions on a Mining Environment: A Preliminary Assessment Based on Data from a Deep, Subsurface Tunnel at Rainier Mesa, Nevada Test Site*, Lawrence Livermore National Laboratory, Livermore, CA, UCRL-ID-121046. MOL19950406.0141

Meike, A. (1996) Man-Made Materials, Chapter 6 in *Preliminary Near-Field Environment Report Update Volume II: Scientific Overview of Near-Field Environment and Phenomena*, D. G. Wilder, Ed., Lawrence Livermore National Laboratory, Livermore, CA, UCRL-ID (in preparation).

Meike, A., Ed. (in press), *The State of Chemical Modeling Modules for the Degradation of Concrete and Cements*, Lawrence Livermore National Laboratory, Livermore, CA, UCRL-ID 123275.

Milestone, N. B., T. Sugama, L. E. Kukacka and N. Carciello (1987) Carbonation of geothermal grouts - part 3: CO₂ attack on grouts containing bentonite. *Cem. Concr. Res.* 17, 295-306.

Mor, E. D., and A. M. Beccaria (1975), Behaviour of Copper in Artificial Sea Water Containing Sulphides, *Br. Corrosion J.* 10(1), 33-38. NNA.19920506.0040

Moragues, A., A. Macias and C. Andrade (1987) Equilibria of the chemical composition of the concrete pore solution. Part I: Comparative study of synthetic and extracted solutions. *Cem. Concr. Res.* 17, 173-182.

Moragues, A., A. Macias and J. Losada (1988) Equilibria of the chemical composition of the pore concrete solution, part II: Calculation of the equilibria constants of the synthetic solutions. *Cem. Concr. Res.* 18, 342-350.

Mordi, R. C., R. Fields, and J. Dwyer (1992), *J. Chem. Soc. Chem. Commun.* (February 15, 1992), 374-375.

Murakata, T., Y. Saito, T. Yosikawa, T. Suzuki, and S. Sato (1993), *Polymer* 34, 1436-1439.

Naqvi, M. K. (1991), *Polym. Degradation Stability* 33, 367-375.

Nas, L. I., and C. A. Heiberger, Eds. (1986), *Resin Manufacture and Properties* (Marcel Dekker, New York, NY).

Neal, C. and G. Stanger (1984) Calcium and magnesium hydroxide precipitation from alkaline groundwaters in Oman, and their significance to the process of serpentinization. *Min. Mag.* 48, 237-241.

Neal, C., and G. Stanger (1984), Calcium and Magnesium Hydroxide Precipitation from Alkaline Groundwaters in Oman, and Their Significance to the Process of Serpentinization, *Min. Mag.* 48, 237-241. NNA.19920131.0315

NRC (Nuclear Regulatory Commission), 1988, *Disposal of High-Level Radioactive Wastes in Geologic Repositories: Licensing Procedures*, Code of Federal Regulations, Energy, Title 10, Part 60, Washington, DC. NNA.19890715.0655

O'Donnell, J. H., and S. W. Shalabys, Eds. (1990), *Chemistry of Radiation Degradation of Polymers. Radiation Effects on Polymers* (American Chemical Society, Washington DC).

Okieimen, F. E., and J. E. Ebhoaye (1992), *Europ. Polym. J.* **28**, 1423-1425.

Olofsson, U., Allard, B., Andersson, K., and B. Torstenfelt (1981), Formation and Properties of Radiocolloids in Aqueous Solution-A Literature Survey. *Programradet for Radioaktivt Abfall*, National Council for Radioactive Waste, Report Proav 4.25.

Olofsson, U., Allard, B., Andersson, K., and B. Torstenfelt (1982a), Formation and Properties of Americium Colloids in Geologic Systems. *Scientific Basis For Nuclear Waste Management*, **4**, S. Topp, Ed.

Olofsson, U., Allard, B., Torstenfelt, B. and K. Andersson (1982b), Properties and Mobilities of Actinide Colloids in Geologic Systems. *Scientific Basis For Nuclear Waste Management*, **5**, W. Lutze, Ed., 755-764

Onofrei, M. (1987) Leaching studies of concrete materials for nuclear fuel waste immobilization containers. pp. 351-396 in Brookins, D. G. ed. *The Geological Disposal of High Level Radioactive Wastes*. Athens, Greece: Theophrastus Publications.

Pace, N. R., D. A. Stahl, D. J. Lane and G. J. Olsen (1986), The Analysis of Natural Microbial Populations by Ribosomal RNA Sequences, *Adv. Microb. Ecol.* **9**, 1-55.

Palmer, D. A., and S. E. Drummond (1986), Thermal Decarboxylation of Acetate. Part I. The Kinetics and Mechanism of Reaction in Aqueous Solution, *Geochim. Cosmochim. Acta* **50**, 813-823.

Parimala, H. V., and K. Vijayan (1993), *J. Mater. Sci. Lett.* **12**, 99-101.

Pollard, A.M., R.G. Thomas and P.A. Williams (1989), Synthesis and stabilities of the basic copper (II) chlorides atacamite, paratacamite and botallackite, *Mineral. Mag.*, **53**, 557-563.

Pope, D. H., S. Lockwood, A. Lee, R. Skultety, and K. Keas. (1994). Mitigation of microbiologically influenced corrosion in natural gas storage facilities. *Corrosion/94* National Association of Corrosion Engineers, Houston, TX.

Raber, E., and J. Garrison (1983), *Radioactive Waste Management and the Nuclear Fuel Cycle* **4**, 41-52.

Raloff, J. (1990), The colloid threat, *Science News*, March 17, 1990, p. 169.

Ravanetti, G. P., and M. Zini (1992), *Thermochim. Acta* **207**, 53-64.

Reasoner, D. J., and E. E. Geldreich (1985), A New Medium for the Enumeration and Subculture of Bacteria from Potable Water, *Appl. Environ. Microbiol.* **49**, 1-7.

- Rek, V., D. Hace, M. Bravar, and A. Jagodar (1990), *Die Angewandte Makromolekulare Chemie* 176, 135–146.
- Rhoderick, J. E. (1981) *Examination of samples of grout after 63 years exposure underground*. ONWI-248. 6 pp.
- Rhoderick, J. E., and A. D. Buck (1981a), *Petrographic Examination of Several Four-Year-Old Laboratory Developed Grout Mixtures*, U.S. Army Engineer Waterways Experiment Station, Structures Laboratory. SRX.19830722.0111
- Rhoderick, J. E., G. S. Wong, et al. (1981b), *Examination of Samples of Bell Canyon Test 1-FF Grout*, U.S. Army Engineer Waterways Experiment Station, Structures Laboratory. SRX.19811020.0177
- Rhoderick, J. E., and A. D. Buck (1981c), *Examinations of Simulated Borehole Specimens*, U.S. Army Engineer Waterways Experiment Station. SRX.19830107.0010
- Rogers, R.D. (1995), *Assessment of the Effects of Microbially Influenced Degradation on a Massive Concrete Structure. Final Report to Introduced Materials Task*. July 8, 1995, Lawrence Livermore National Laboratory, Livermore, CA, UCRL-CR-122068.
- Rose, N., M. L. Bras, R. Delobel, B. Costes, and Y. Henry (1993), *Polym. Degradation Stability* 42, 307–316.
- Roy, D. M., and C. A. Langton (1983), *Characterization of Cement Based Ancient Building Materials in Support of Repository Seal Materials Study*, BMI/ONWI-523. 139 pp. SRX.19870127.0146
- Roy, D. M., and C. A. Langton (1989), *Studies of Ancient Concrete as Analogs of Cementitious Sealing Materials for a Repository in Tuff*, Los Alamos National Laboratory, Los Alamos, NM, LA-11527-MS. 101 pp. HQS.19880517.3281
- Roy, D. M. and C. A. Langton (1989) *Studies of ancient concrete as analogs of cementitious sealing materials for a repository in tuff*. LA-11527-MS. 101 pp.
- Roznak, D.B. and R.R. Colwell. (1987). Survival strategies of bacteria in the natural environment. *Microbiol. Rev.* 51, 365-379.
- Russell, C. E., R. Jacobsen, D. L. Haldeman and P. S. Amy. (1994). Heterogeneity of deep subsurface microorganisms and correlations to hydrogeological and geochemical parameters. *Geomicrobiol. J.* 12, 37-51.
- Sarker, A. K., M. W. Barnes and D. M. Roy (1982) *Longevity of borehole and shaft sealing materials: Thermodynamic properties of cements and related phases applied to repository sealing*. ONWI-201. 47 pp.
- Sato, S., T. Murakata, S. Baba, Y. Saito, and S. Watanabe (1990), *J. Appl. Polym. Sci.* 40, 2065–2071.
- Schneider, B., D. Doskocilova, J. Stokr, and M. Svoboda (1993), *Polymer* 34, 432–436.

- Scott, D.A. (1985), Periodic corrosion phenomena in bronze antiquities, *Studies in Conservation*, 30, 49-57.
- Seyfried, W. E., D. R. Janecky, and M. E. Berndt (1987), *Rocking Autoclaves for Hydrothermal Experiments. II. The Flexible Reaction-Cell System*, in *Hydrothermal Experimental Techniques*, G. C. Ulmer and H. L. Barnes, Eds. Wiley and Sons, New York. pp. 216-239.
- Shewmon, P. G. (1963), *Diffusion in Solids* (McGraw-Hill, New York, NY).
- Shrivastava, O. P. and F. P. Glasser (1986) Ion-exchange properties of II-A tobermorite. *React. Solids* 2, 261-268 .
- Smirnov, V. V., and E. B. Dubova (1992), *High Energy Chem.* 26, 173-177.
- Soo, P. and L. W. Milian (1989) *Sulfate-attack resistance and gamma-irradiation resistance of some portland cement based mortars*. NUREG/CR-5279. 35 pp.
- Soylemezoglu, S., and R. Harper (1982), Oxygen Ingress into Geothermal Steam and Its Effect on Corrosion of Low Carbon Steel at Broadlands, New Zealand, *Geothermics* 11(1), 31-42.
- Spadaro, G. (1993), *Europ. Polym. J.* 29, 851-854.
- Sterne, P. A., and A. Meike (1995), Electronic Structure Calculations of Calcium Silicate Hydrates, in *Proceedings of the Materials Research Society* (Boston, MA, December 1995), Lawrence Livermore National Laboratory, Livermore, CA, UCRL-JC-121437.
- Suzuki, S., and E. Sinn. (1993), 1.4 nm Tobermorite-Like Calcium Silicate Hydrate Prepared at Room Temperature from Si(OH)₄ and CaCl₂ Solutions, *J. Mater. Sci. Lett.* 12, 542.
- Svoboda, M., J. Stokr, and B. Schneider (1990), *Collection of Czechoslovak Chemical Communications* 55, 2233-2243.
- Tannenbaum, E., and I. R. Kaplan (1985), Low-M_r Hydrocarbons Generated during Hydrous and Dry Pyrolysis of Kerogen, *Nature* 317, 708-709.
- Taylor, H. F. W. (1986) Proposed structure for calcium silicate hydrate gel. *Am. Ceram. Soc. J.* 69, 464-467.
- Taylor, H. F. W. (1990), *Cement Chemistry* (Academic Press, London, San Diego), 123 pp.
- Taylor, H. F. W. and D. M. Roy (1980) *Structure and composition of hydrates*. 7th Int. Congr. Chem. Cement II-2/1-13.
- Taylor, H. F. W. (1987) Bound water in cement pastes and its significance for pore solution compositions. *Mat. Res. Soc. Symp. Proc.* 85, 47-53.
- Torikai, A., R. Geetha, and S. Nagaya (1990), *J. Polym. Sci. A, Polym. Chem.* 28, 3639-3646.

- Torikai, A. (1994), *Die Angewandte Makromolekulare Chemie* 216, 225–241.
- Tylecote, R. F. (1979), *The Effect of Soil Conditions on the Long-Term Corrosion of Buried Tin-Bronzes and Copper*, British Nuclear Fuels Limited.
- Van Konynenburg, R.A. (1986), *Radiation Doses in Granite Around Emplacement Holes in the Spent Fuel Test - Climax* (Final Report). UCRL-53580. Lawrence Livermore National Laboratory, Livermore, CA.
- Vieillard, P., and F. Rassineux (1992), Thermodynamic and Geochemical Modelling of the Alteration of Two Cement Matrices, *Appl. Geochem. Suppl.* 1, 125–136.
- Wallius, S. (1993), *Die Angewandte Makromolekulare Chemie* 212, 103–119.
- Ward, D. M., R. Weller, and M. M. Bateson (1990), ¹⁶S rRNA Sequences Reveal Numerous Uncultured Microorganisms in a Natural Community, *Nature* 345, 63–65.
- Warren, R. S., F. M. Byers, and F. A. Caporuscio (1984), *Petrography and Mineral Chemistry of Units of the Topopah Spring, Calico Hills, and Crater Flat Tuffs, and Older Volcanic Units, with Emphasis on the Samples from Drill Hole USW G-1, Yucca Mountain, Nevada Test Site*, Los Alamos National Laboratory, Los Alamos, NM, LA-10003-MS. HQS.19880517.2569
- Welch, D.F. (1991). Applications of cellular fatty acid analysis. *Clin. Microbiol. Rev.* 4, 422–438.
- Weres, O., A. S. Newton, and L. Tsao (1988), Hydrous Pyrolysis of Alkanes, Alkenes, Alcohols and Ethers, *Org. Geochem.* 12, 433–444.
- West, K. A. (1988), *Nevada Nuclear Waste Storage Investigations Exploratory Shaft Facility Fluids and Materials Evaluation*, Los Alamos National Laboratory, Los Alamos, NM, LA-11398-MS. NN1.19981213.0021
- Westlake, D.W.S., K.M. Semple, and C.O. Obuekwe (1985). Corrosion by ferric iron-reducing bacteria isolated from oil production systems. *Proceedings of the International Conference on Biologically Induced Corrosion*, June 10–12, 1985, Gaithersburg, MD.
- Wheeler, D. R., and S. V. Pepper (1990), *J. Vac. Sci. Technol.* 8, 4046–4056.
- Williams, J. L., Ed. (1990), *Stability of Polypropylene to Gamma Irradiation* (American Chemical Society, Washington, DC), pp. 554–568.
- Wilski, H. (1990), *Influence of Ionizing Radiation on Thermoset Plastics* (American Chemical Society, Washington, DC).
- Winograd, I. J. (1986), *Archaeology and Public Perception of a Trans-Scientific Problem: Disposal of Toxic Wastes in the Unsaturated Zone*, U.S. Geological Survey. NNA.19910627.0007
- Woese, C. R. (1987), Bacterial Evolution, *Microbiol. Rev.* 51, 221–271.

Wolery, T., K. J. Jackson, et al. (1990), *Current Status of the EQ3/6 Software Package for Geochemical Modeling, in Chemical Modeling in Aqueous Systems II*. Lawrence Livermore National Laboratory Report. NNA.19900716.0363

Wu, Z-Q. and J. F. Young (1984) Formation of calcium hydroxide from aqueous suspensions of tricalcium silicate. *Am. Ceram. Soc. J.* **67**, 48–51.

Xiuji, F. and L. Shizong (1986) Investigation of the effect of minor ions on the stability of b-C₂S and the mechanism of stabilization. *Cem. Concr. Res.* **16**, 587–601.

Xu, P., D. Zhou, and D. Zhao (1989a), *Europ. Polym. J.* **25**, 581–583.

Young, J. F., H. S. Tong and R. L. Berger (1977) Compositions of solutions in contact with hydrating tricalcium silicate pastes. *Am. Ceram. Soc. J.* **60**, 193–198.

Appendix A: Polymer Chemistry

Polymerization. Polymerization occurs via addition or condensation polymerization. These basic chemical reactions are achieved through one of four primary techniques by which polymers are formed from monomers (bulk, solution, suspension, and emulsion). There are three properties which differentiate addition polymerization from condensation polymerization. First, the repeat unit in the polymer and the monomer have the same composition, although the bonding is different in each for addition polymerization. Second, the mechanism of these reactions places addition polymerization in the kinetic category of chain reactions, with either free radicals or ionic groups responsible for propagating the chain reaction. Lastly, the product molecules usually have a carbon chain backbone, with pendant substituent groups. Chain growth polymers include polyethylene, polystyrene, polyvinylchloride (PVC), polyisobutylene, and Teflon.

Chemical characterization. Chemical characterization of polymers is a complex issue because even within a given polymer class, it is not possible to make correlations between polymers and simpler but chemically similar molecules, because each polymer has its own unique set of properties that depend on chemical structures, chain lengths, conformations, and degrees of branching and crystallinity. This diversity is further complicated by the addition of filler, plasticizers, stabilizers as well as other additives. Two products of the same polymeric substance but with different additives can react differently to the same conditions. Thus, in order to completely understand the affects of a given product, the range of chemical composition must be known. Beginning in the 1920s cellulose nitrate and cellulose acetate became widely used as well as phenol-formaldehyde (Bakelite) which was the first synthetic thermoset (crosslinked) polymer. Given this relatively recent arrival, limited insight can be gained on long-term behavior through historical analogs. Thus, extension back in time will require a sound understanding of fundamental chemical principles, which are outlined below. It must be emphasized that the degradation behavior is based on relatively short term experiments and should only act as a first estimate for the prediction of long-term stability in the context of a radioactive waste repository.

Molecular Weight Distribution. A polymeric material is made up of many polymer molecules which are held together by entanglements and intermolecular forces and crosslinks. It is the exception when polymerization is carried out so that all polymers have the same degree of polymerization. Thus it is difficult to define useful

thermodynamic parameters for these materials. Molecular weight distribution reflects the number of bonds or degree of polymerization and is a fundamental diagnostic polymer property. Properties that are dependent on the number of molecules in a system, called colligative properties, are osmotic pressure, boiling point, and freezing point. Measurement of these properties can thus be used to determine the average molecular weight and the degree of polymerization. Colligative properties have also been used to assess the thermodynamic behavior of polymers in solution. The molecular weight distribution represents the variation from the average of the polymers within the material. A broad distribution in the degree of polymerization of a polymer population is represented as a large "degree of freedom".

Theta Condition. When a polymer is in the theta condition, the tendency to spread out is exactly balanced with the excluded volume effect (real polymer conformations should be more spread out than those predicted because only one polymer segment can take up a certain space at a given time). Solvents which yield this "equilibrium" are referred to as theta solvents and the temperature at which the theta condition is reached for a given polymer/solvent pair is known as the theta temperature.

Many parameters are known for a theta polymer thus, interpretation can be less complex if the polymer is in the theta condition. Given that much information about polymers is in the realm of synthesis, where a theta condition may be sought, it is to be expected that information for conditions outside of the theta condition (which will be the rule rather than the exception under repository conditions) are far less complete.

Thermoplastics vs Thermosets. All solid polymers can be categorized as either thermoplastics and thermosets. The polymer molecules of thermoplastics are held together by intermolecular forces. Thermoplastics soften when heated but do not degrade until a certain temperature. They can be molded and remolded with the use of heat. Examples of thermoplastics are nylon and polystyrene. Thermosets on the other hand contain polymer molecules which are joined by chemical crosslinks. They are achieved by a chemical reaction which creates a crosslinked polymer which can not be remolded once it is set. The crosslinks prevent bond motion (in some cases, the crosslinked polymer can be stretched but the crosslinks prevent the remolding possible with thermoplastics). Examples of thermosets are epoxy and vulcanized rubber. The polymer is still a polymer before crosslinking but it is primarily used in its crosslinked form. Polyester is an example of a polymer that is used as a thermoplastic and which can be crosslinked to become a thermoset.

Polymer Elasticity. Depending on the length of the polymer chains and on the temperature, a particular type of polymer may occur as a viscous liquid, a rubbery

solid, a glass or a partially crystalline solid. The longer the average length of the polymer chains, the less viscous the polymer at a given temperature. The polymer chains are coiled and intertwined with each other. If the polymer is stretched, then the chains slowly untangle and the polymer appears to flow. The relative movement of polymer chains can be decreased by connecting the polymer chains with chemical bonds called crosslinks. When the crosslinked network is stretched, the coils become elongated, but when the stress is released or more energy is put into the system, the polymer network returns to its original coiled state.

Transition Temperature. The physical state of polymers is temperature dependent. Like most materials, polymers have a melting point (T_m). In addition, within the solid state ($T < T_m$), polymers can be in a "glassy" state or in a "rubber" state (different from a crosslinked rubber). The glass transition temperature (T_g) determines the turning point between "glass," where there is not rotation around bonds and "rubber," where segmental bond motion begins. A polymer in the glass state, is stiff and often brittle, but upon passing through its glass transition temperature becomes flexible and malleable. Thus T_g and factors that affect T_g determine the mechanical characteristics of the polymer.

The T_g increases with molecular weight or degree of polymerization, as well as crystallinity. Side branching usually decreases T_g by leading to a less ordered structure as does heterogeneity of the polymer chain (i.e. copolymers). Chemical composition and configuration (syndiotactic, atactic, isotactic) both affect T_g . In addition, T_g can be lowered by the addition of plasticizers (a plasticizer is defined as any substance which when added to the polymer, lowers its glass transition temperature). For example, water acts as a plasticizer in nylon. Most thermoplastic polymers for consumer applications (e.g. plastic bags, nylon running shorts and 2-L soda bottles) have a glass transition temperature below room temperature for flexibility.

Crystalline and Amorphous States. The orientation of a polymer chain can be ordered by physical force. This is how fibers, as well as most plastic consumer products are formed. A force is applied to the material above the T_g and then the material is cooled. Because it is now a glass, the polymer will not return to its original disordered state. However, as soon as the thermoplastic polymer is heated, it will return to its original form. Crystalline regions are created by the packing of molecular chains together. The crystallinity is dependent on the material itself as well as the production method. For example, an isotactic polymer can be more easily packed than an atactic polymer. Crystals can only be formed above the T_g and below the melting temperature (T_m). Crystallinity can also be achieved by adding particles to the polymer melt which

create an area of reduced energy so that a crystal can propagate (more order means more energy). Crystallinity affects most polymer properties including T_g (increased crystallinity increases T_g), and wettability (crystallinity reduces wettability).

The noncrystalline or amorphous regions are important determinants of polymer properties. Amorphous regions allow for wettability and elasticity in the polymer. Many structures of polymers in terms of crystalline and amorphous regions have been suggested but the exact structure of polymers are not known.

Additives. Additives to polymer resins improve strength, flexibility, flame retardance, or appearance. The term antioxidant is broadly used to refer to inhibitors for autoxidation: heat stabilizers, melt stabilizers, light stabilizers, antifatigue agents and antiozonants. All of these agents interfere with the free radical reactions that lead to the incorporation of oxygen into macromolecules. For example, N-phenyl B-naphthylamine and butylated hydroxytoluene respectively are added to elastomers and plastics to reduce deterioration related to autoxidation (Mark et al., 1985). Plasticizers lower the glass transition temperature of a material making processing easier and the polymers more flexible. Phthalic esters are common plasticizers (Mark et al., 1985; Khinnavar and Aminabhavi, 1992).

Appendix B: Curing of Cementitious Material

Cement is predominantly composed of calcium-bearing phases that crystallize when water is added to a mixture of carbonate, silicate, and other phases. Table B-1 briefly describes the nomenclature and standards of cement chemistry. The reactions and structural changes take place over time scales of a few seconds to a year or longer and are sensitive to temperature within the range of interest to the repository. Table B-2 summarizes the chemistry of the major cement hydration reactions. Hydration reactions that predominate below 100°C as well as those that predominate above 100°C are summarized (Bensted, 1989). Table B-3 lists formulas of cement phases.

The most important reaction in curing cement at ambient conditions is probably the hydration of calcium silicates. Alite, C_3S , is known to hydrate considerably faster than belite, an impurity-stabilized form of C_2S at 25°C, and the former is thus the primary contributor to the early strength of concretes. Alite has often been chosen for detailed study because of this kinetic advantage. Other important phases in the hydration and crystallization process include a calcium silicate hydrate gel, C-S-H (no stoichiometry, crystallinity, structure, or degree of polymerization is implied), which is common to most cements. The literature distinguishes at least two forms of this "gel": an early phase that consumes most of the anhydrous starting material within about 28 days (Glasser et al., 1987), and a more polymerized phase that increases in length as the material ages. Although the details are poorly documented, some structural characteristics of the C-S-H phase are well known. The quasi-crystalline C-S-H phases that develop with aging are considerably more crystalline, with either an imperfect tobermorite-like structure or a jennite-like structure. Tobermorite-like phases appear to be favored as aging progresses in cements that contain siliceous blending agents (Shrivastava and Glasser, 1986). The microstructural changes that accompany these solid-state phase transformations may affect virtually all measurable thermal, mechanical, and physical properties. These effects have not been described, and they remain unpredictable. The polymers appear to incorporate a range of ions, and the C:S ratio can also vary. As a consequence, the kinetics and degree of polymerization may differ as a function of the composition of the starting materials.

Kinetic data are limited primarily to the formation of C-S-H from pure beta- C_2S and C_3S . A review of the literature on the kinetics of belite and alite hydration (Barret and Bertrandie, 1986) suggests that the mechanisms may be debated, but that the markedly slower hydration of belite is thought to be similar to alite. In both cases, rapid

dissolution within a few minutes of hydration is followed by a somewhat linear increase to a maximum ion concentration that represents supersaturation with respect to portlandite. Subsequently, the concentration decreases, first rapidly, then slowly and linearly (Wu and Young, 1984; Brown et al., 1984). Competition between chemical reactions that start at different times and differ in progress of reaction will determine the overall rate. Brown et al. (1985) proposed that an initial hydrate forms that eventually nucleates a more stable hydrate. The consequent increase in the rate of Ca^{++} and OH^- liberation eventually supersaturates the solution with respect to $\text{Ca}(\text{OH})_2$, which precipitates. The subsequent hydration of C_3S is diffusion-controlled. Grutzeck and Ramachandran (1987) propose that a precipitate of a very-fine-grained C-S-H initially forms on the surface of C_3S as a result of supersaturation and controls subsequent hydration via diffusion. New material forms at the solid/hydrate interface while the fine-grained outer layer dissolves. A sufficiently supersaturated solution at a pH of 11.5 will form relatively-coarse-grained C-S-H(II) at the expense of the fine-grained initial C-S-H. Bensted (1983a) finds that most of the initial ettringite is formed from C_3A at the greatest rate during the first 5 min, followed by a steady increase for up to 2 hr. After 8 to 26 hr, when the gypsum is gone, ettringite reacts with C_4AH_{13} to form monosulfate (Bensted, 1983b). The iron from ferrite is thus freed to participate in hydrous phases. Alkalis, whether present in the original grout or contributed by additives or aggregate, are released in temperature-sensitive reactions from clinker phases to the pore fluids within days (Glasser and Marr, 1984; Glasser et al., 1985), and reach concentrations of 0.05 to 1.0M. The presence of alkalis depresses calcium solubility and thus (1) determines the pH of the pore fluid (Macphee et al., 1989), and (2) affects the hydration of alite and belite (Wu and Young, 1984).

Ettringite is the most prevalent sulfate-bearing hydration product below 80°C and is an important trivalent-ion-bearing phase. Within broad limits, ettringite appears to form independently of the degree of hydration (Bensted, 1983a,b), but it is not stable above 75 to 80°C under 100% relative humidity. Prediction of the fate of much of the Al^{+++} and SO_4^- in the hydrated cement, and possibly Fe^{+++} , is dependent on the knowledge of ettringite thermochemistry. Ettringite formed from aluminate and ferrite phases composes a continuous hydrated solid-solution. Analogous solid-solutions of other phases may be formed from ferrite and aluminate. Above about 100°C , iron-rich monosulfate often forms as a consequence of reactions that consume ettringite, which loses much of its structural water on heating to 60°C and transforms to $\text{C}_6\text{AS}_3\text{H}_8$ at 110°C (Taylor, 1987) at pH 11. Ettringite ultimately decomposes to gypsum, aragonite, and $\text{Al}(\text{OH})_3$ (Grounds et al., 1985), and to crystalline calcium silicates that include

tobermorite, xonotolite, gyrolite, hydrogarnet, stratlingite, α -C₂SH, and C₆S₂H₃ (Bensted, 1989). Tobermorite-11Å is a disordered structure (Taylor, 1964) that precipitates in water at temperatures greater than 100°C, but which has been observed from cements leached at 25°C and those cured at 60°C (Barnes and Roy, 1983). "Normal" tobermorite-11Å decreases to 9.3-Å spacing by 300°C. These products are also expected of cement formed at ambient conditions, cured, and subsequently heated to $\geq 100^\circ\text{C}$ (Scheetz and Roy, 1989a,b), a scenario that is anticipated for the waste repository.

The consequences of incorporating aggregate materials, blending agents, and other additives such as fly ash, blast furnace slag (bfs), silica fume, rice husk ash, and natural pozzolan into cement have been investigated to a limited extent (Glasser et al., 1986; Macphree et al., 1989; Andersson et al., 1989). Glasser et al. (1987) provide a summary of the chemical and mineralogical effects of these cement additives. Pozzolanic aggregate materials react chemically to give the cement advantageous properties. A pertinent example of natural aggregates that behave as pozzolanas are some siliceous welded tuffaceous rocks. Other materials that may be added to cements to influence the rate at which they cure include an anhydrous material, "clinker" which is produced by cement kilns, and gypsum. Gypsum, which is added to prevent flash setting, can lose water during grinding with clinker to form hemihydrate. Rehydration of gypsum when water is added to the cement can compete with cement minerals such as ettringite and influence their aging kinetics. An aggregate of bfs creates a reducing environment and thus may influence the mobility of ions and complexes that are sensitive to oxidation conditions. The bfs additive contains materials foreign to the usual cement chemistry: large amounts of ferrous iron, considerably more Mg⁺⁺ than is present in usual cement formulations, and, possibly, dispersed iron metal and iron sulfide. Mg⁺⁺ is known to react with C-S-H to form Mg(OH)₂ and thus destroy the main cohesive phase of concretes. The oxidation of S and Fe could cause significant volumetric changes.

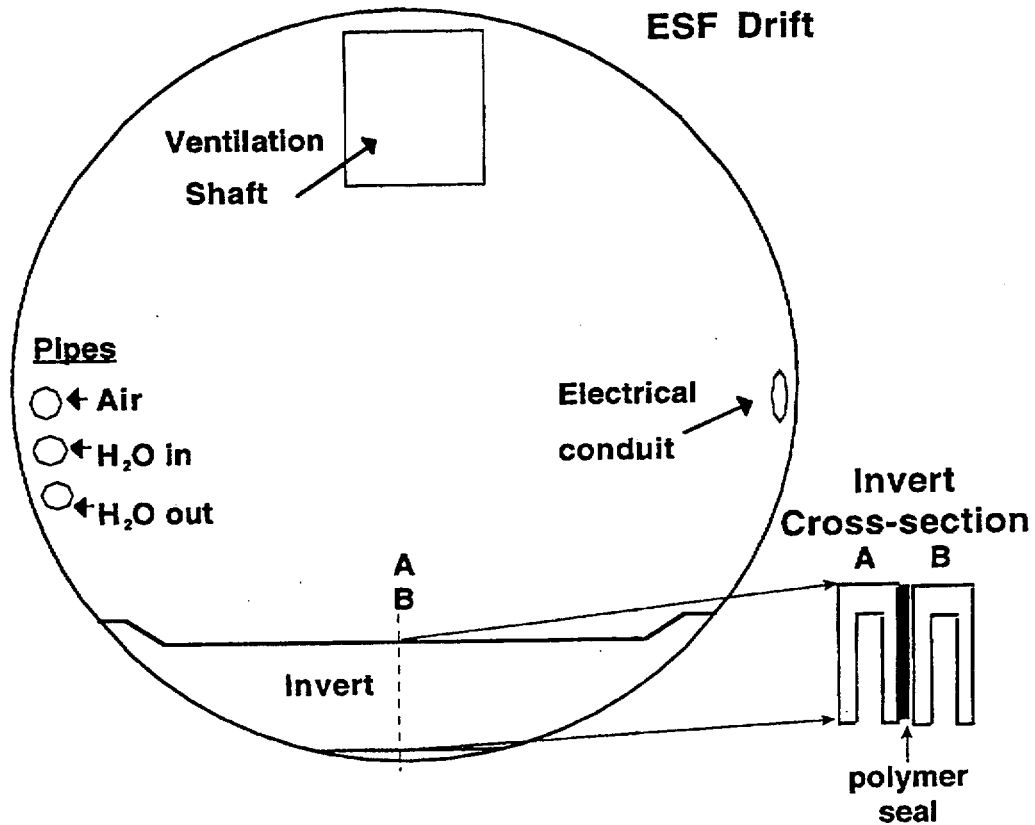


Figure 6-1. Schematic view (not to scale) of ESF drift cross-section illustrates the placement of some materials. The shape of the invert is illustrated in tunnel cross-section, and the invert cross-section parallel to the tunnel axis.

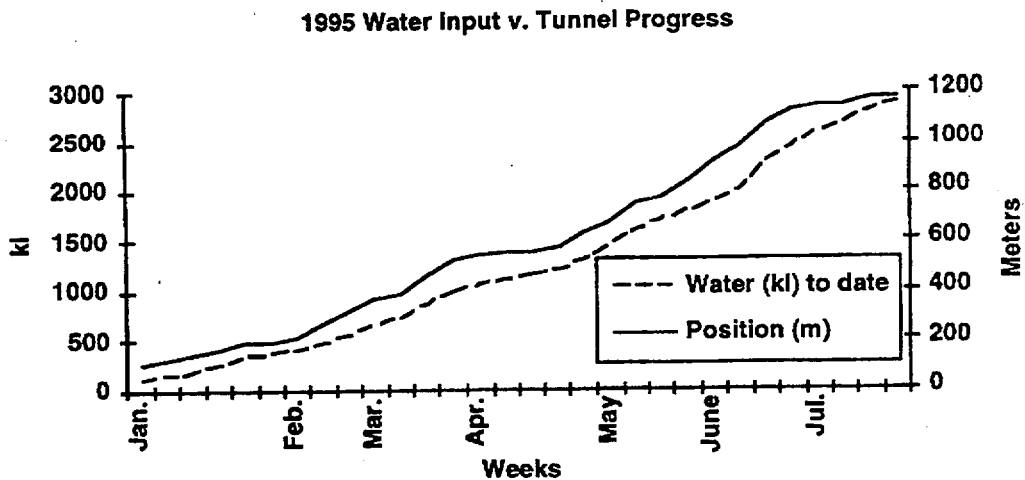
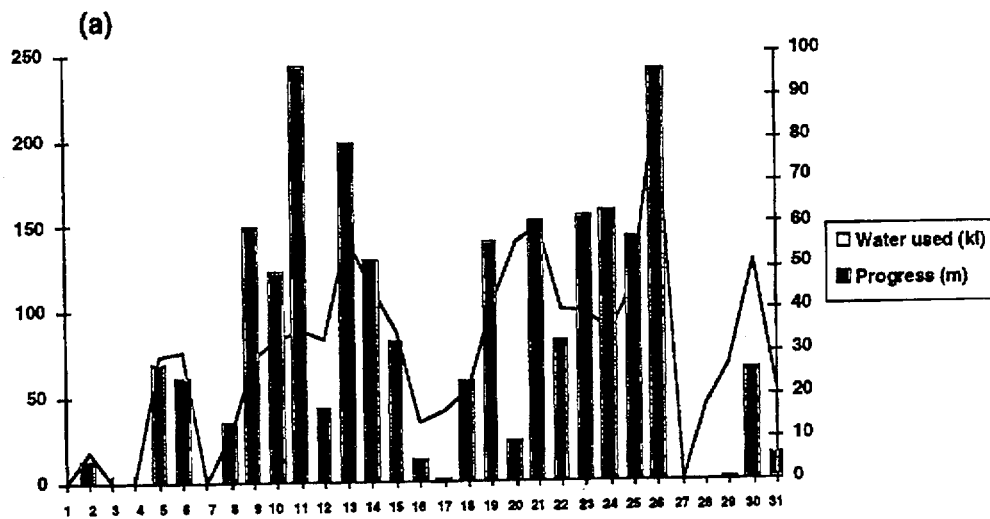


Figure 6-2. Total water usage and total meters excavated are plotted as a function of time. It is clear that the limit specified in the DIE, no more than 7.4 cubic meters of water per linear meter of tunnel excavated, has not been exceeded. Total water usage to date averages roughly 2.47 kL/m.



Weekly Water Usage 1995 (kL/m)

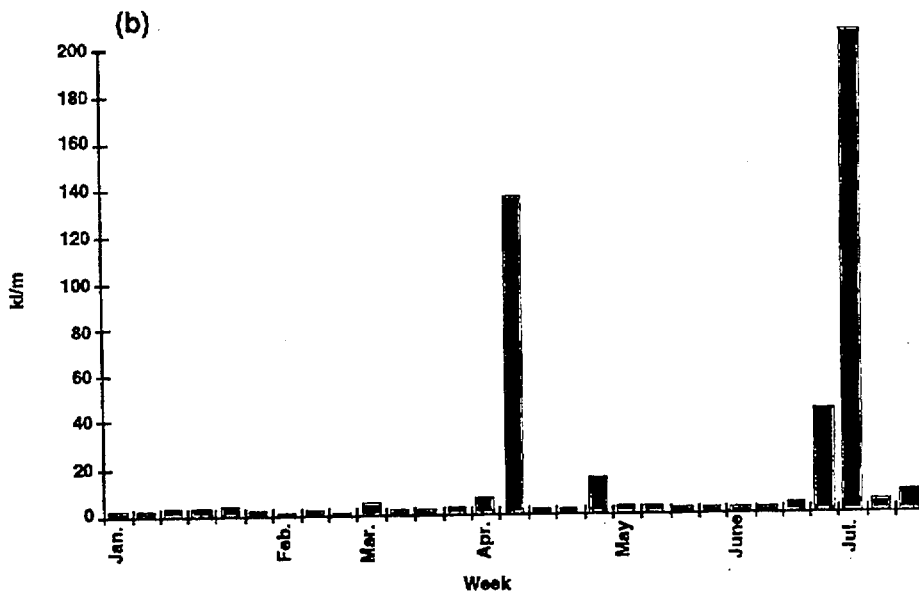


Figure 6-3. (a) A plot of weekly water usage and weekly excavation progress as a function of time suggests a strong correlation between water usage and excavation progress. (b) A plot of water usage as a function of time demonstrates that an average amount of water usage of between 2 and 4 kL/m is punctuated by episodes of large water usage.

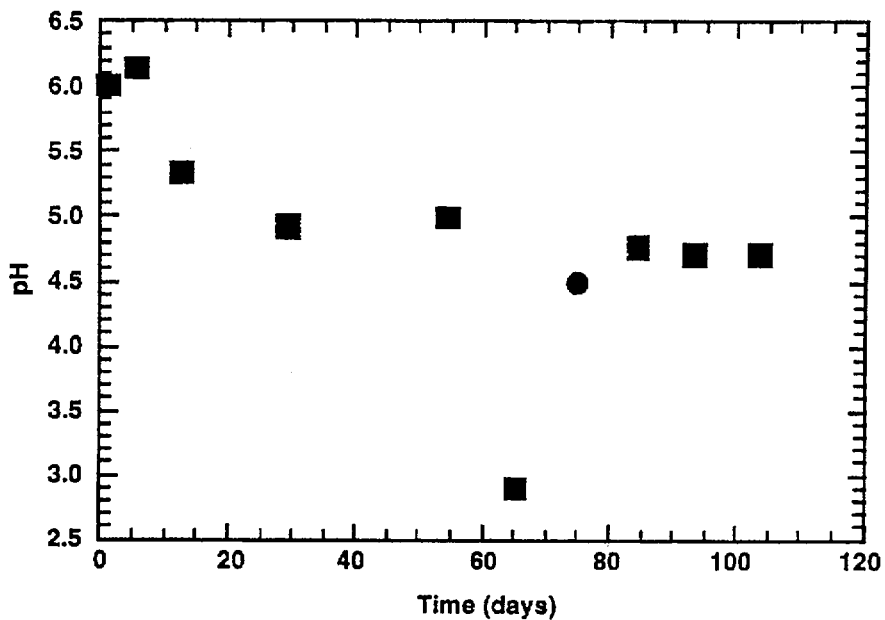


Figure 6-4. Experimental pH (25 °C) as a function of time from diesel fuel hydrous pyrolysis experiments DF1 at 200 °C (circle) and DF2 at 315 °C (squares).

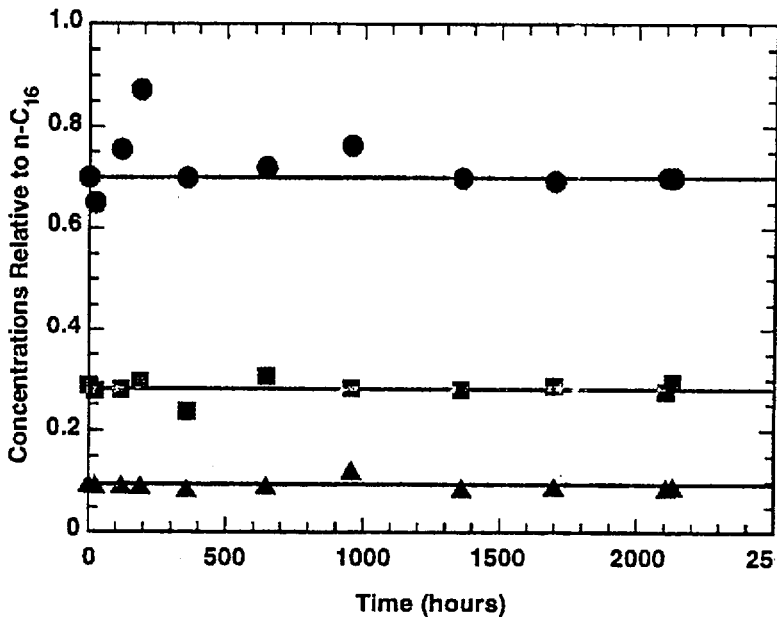


Figure 6-5. Diesel fuel relative concentrations of C₁₀₋₁₄ normalized with respect to C₁₆ as a function of time for experiment DF1. The circles, squares, and triangles are alkanes, C₁₄, C₁₂, and C₁₀ respectively.

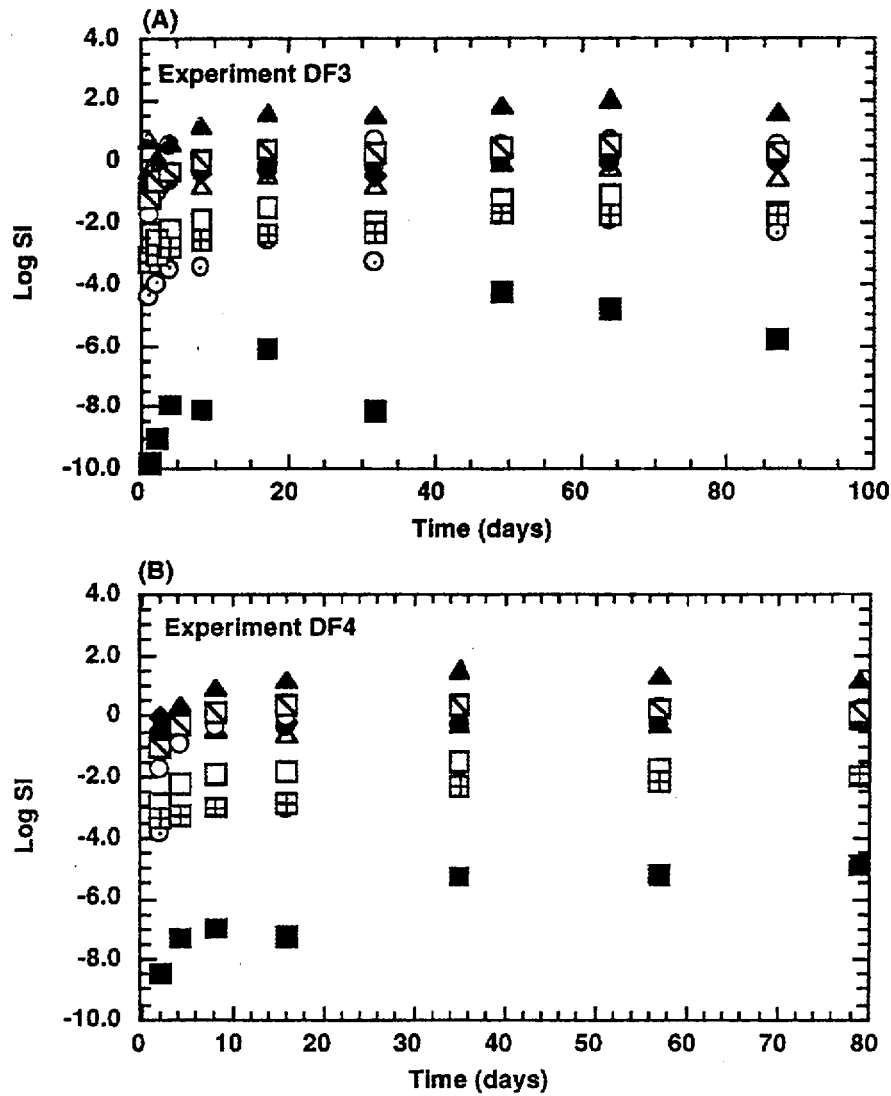


Figure 6-6. Experiment DF3 (A) and DF4 (B) Fibercrete™-water interactions plotted as the log SI with respect to quartz (solid circle), wollastonite (solid diamond), K-feldspar (square with a slash), albite (open circle), anorthite (open square), calcite (open triangle), mesolite (solid triangle), gyrolite (open circle with center dot), 11Å-tobermorite (solid square), and bassanite (open square with cross). The saturation index (SI) is equal to the IAP / K_{eq} for a given mineral. A log SI greater than, equal to, or less than zero, indicates that the solution is supersaturated, saturated, or undersaturated respectively in regard to a given mineral, where IAP is the ion activity product and K_{eq} is the equilibrium constant.

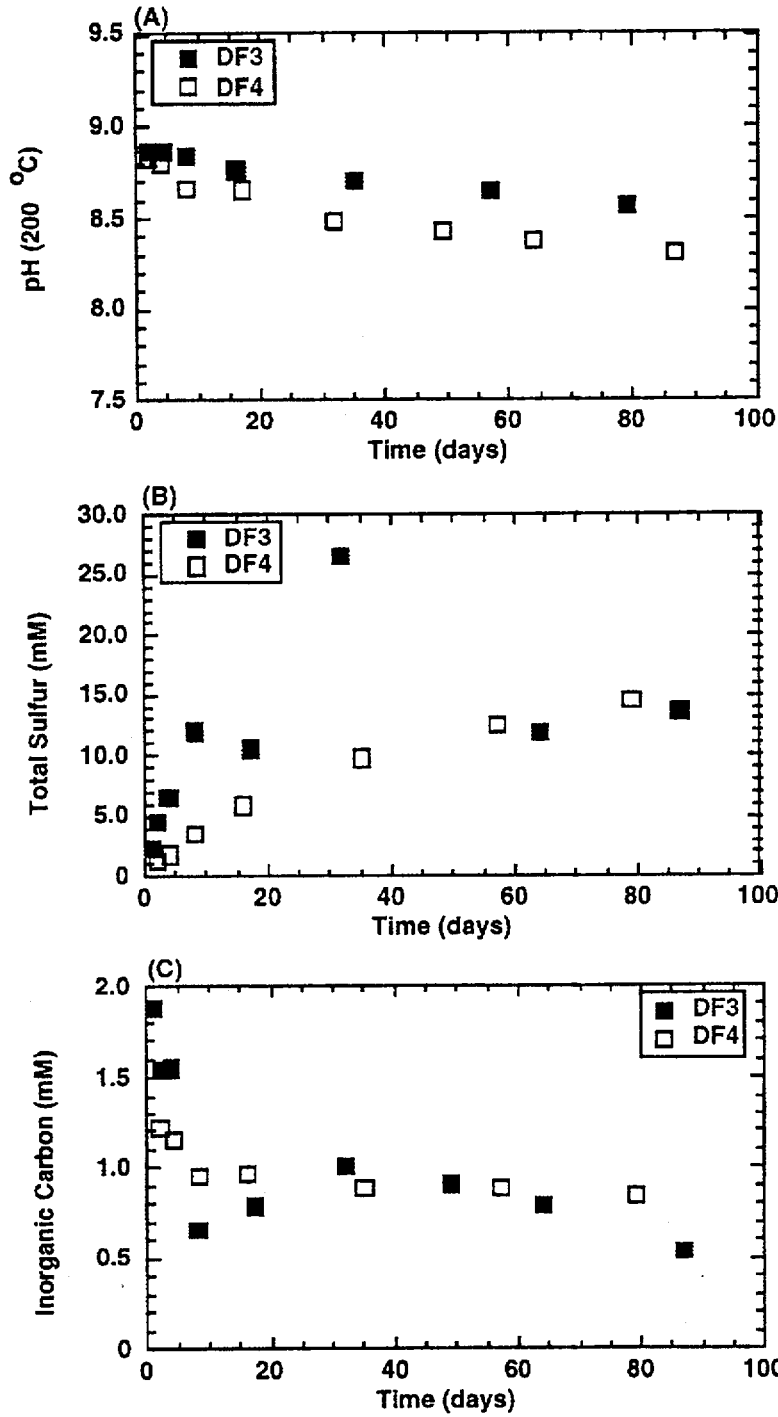


Figure 6-7. Aqueous composition of experiments DF3 and DF4. (A) pH (200 °C), (B) total sulfur, and (C) inorganic carbon are plotted as a function of time.

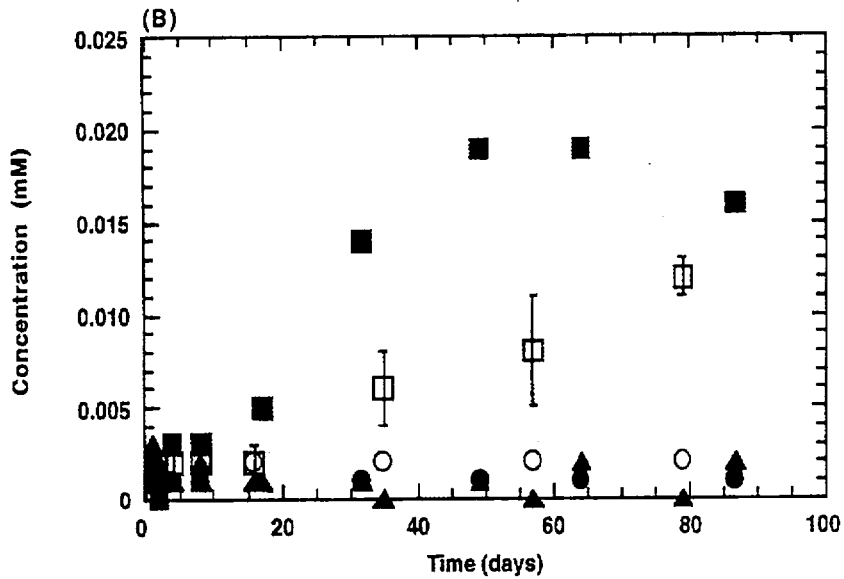
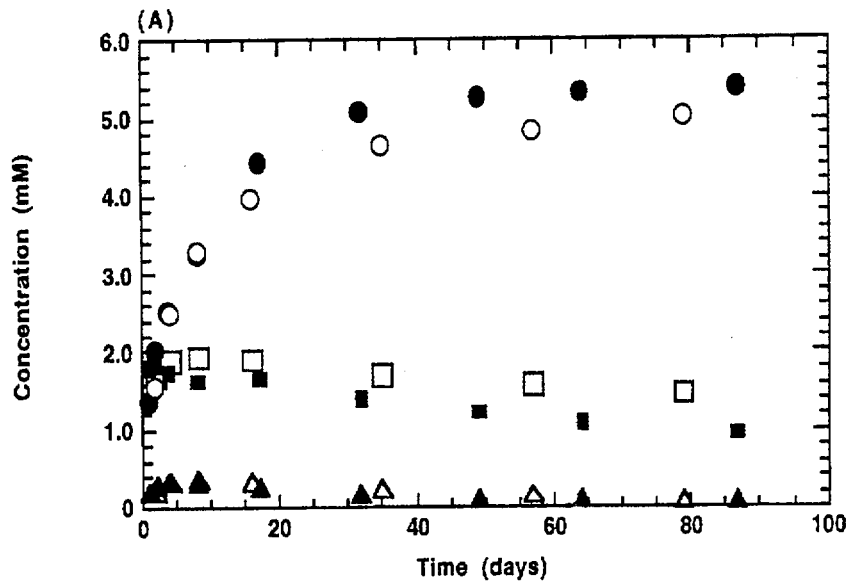


Figure 6-8. Aqueous composition of experiment DF3 (solid symbols) and DF4 (open symbols) plotted as function of time. (A) Si (circles), Al (triangles) and K (squares) and (B) Ca (squares), Mg (circles) and Fe (triangles).

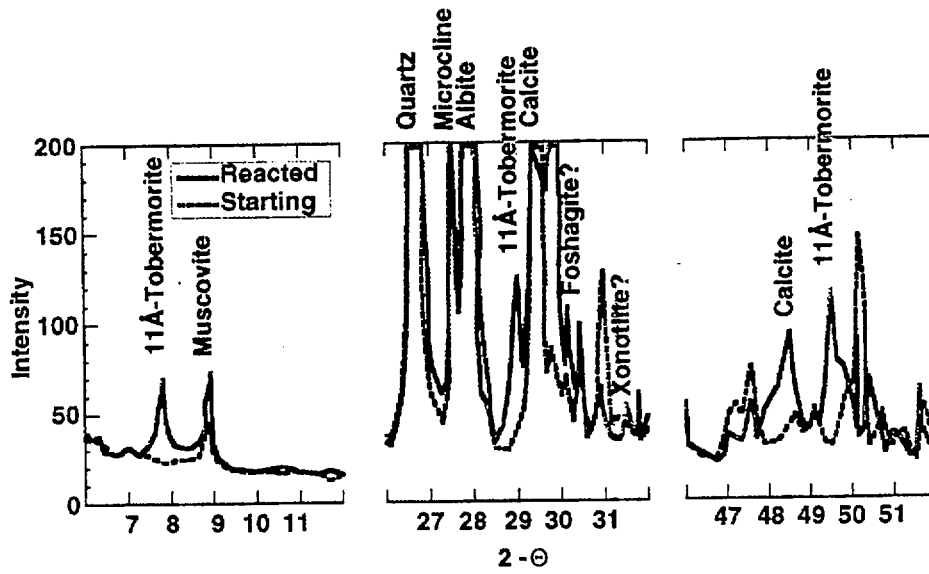


Figure 6-9. XRD pattern showing the three most intense peaks for 11Å-tobermorite in the reacted Fibercrete™.

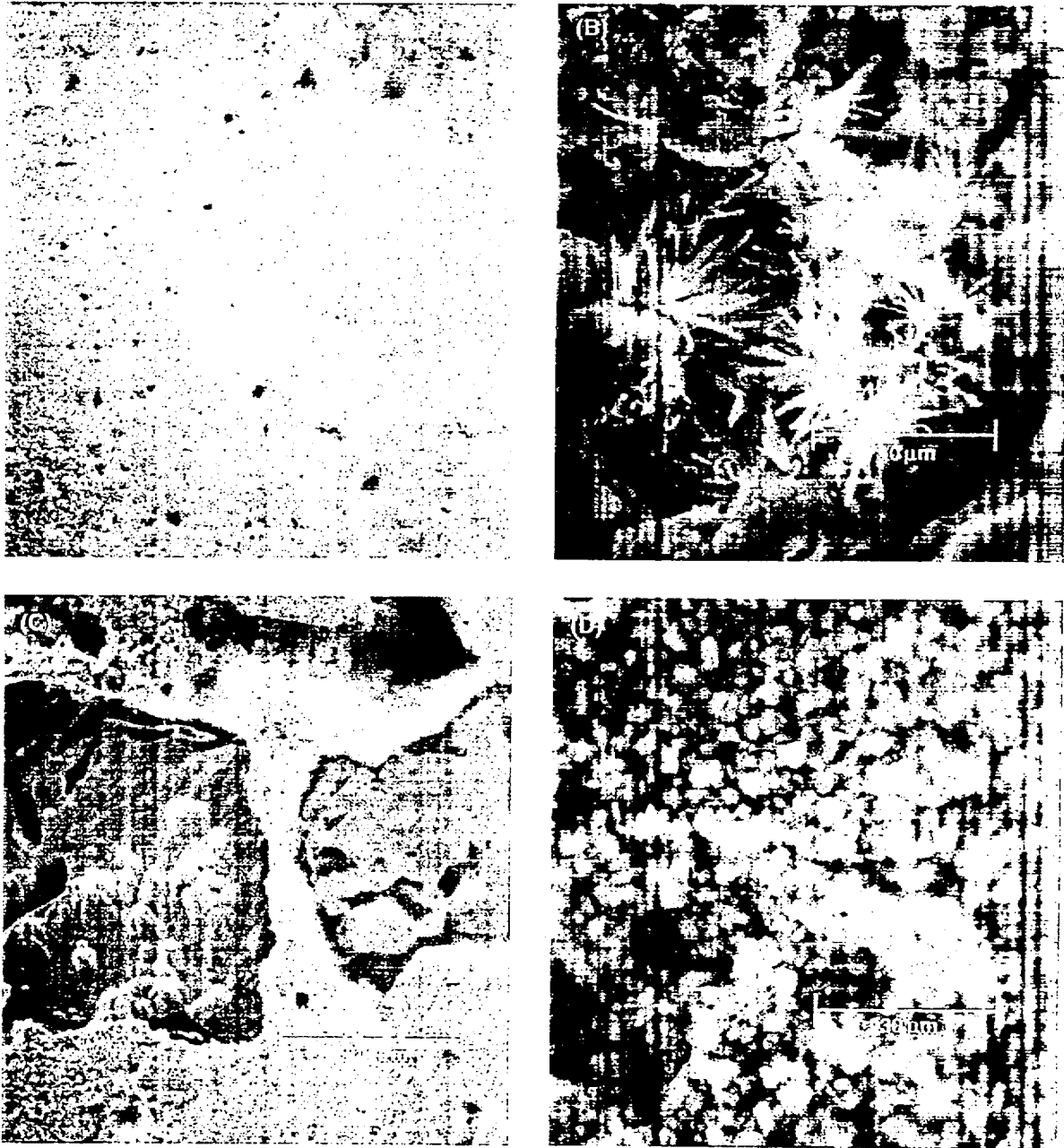


Figure 6-10. SEM photomicrographs of unreacted (A, B) and reacted Fibercrete™ (C, D). (A) Fibercrete™ consists of large quartz and feldspar aggregate minerals and steel fibers (light area near center) in a grout matrix. (B) Magnification of the grout matrix showing crystallites. (C) Reacted Fibercrete™ showing both dissolution precipitation features on the quartz aggregate minerals and the precipitation of Ca-rich phase at the Fibercrete™ surface. (D) Enlargement of the Ca-rich phase showing blocky morphology.

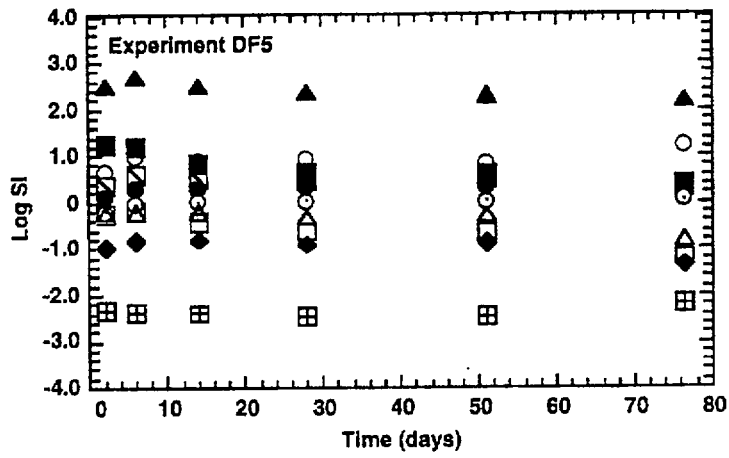


Figure 6-11. Experiment DF5. Topopah Spring tuff - water - diesel fuel interactions plotted as the log SI with respect to quartz (solid circle), cristobalite (open circle with center dot), wollastonite (solid diamond), K-feldspar (square with a slash), albite (open circle), anorthite (open square), muscovite (solid square), calcite (open triangle), mesolite (solid triangle), and bassanite (open square with cross).

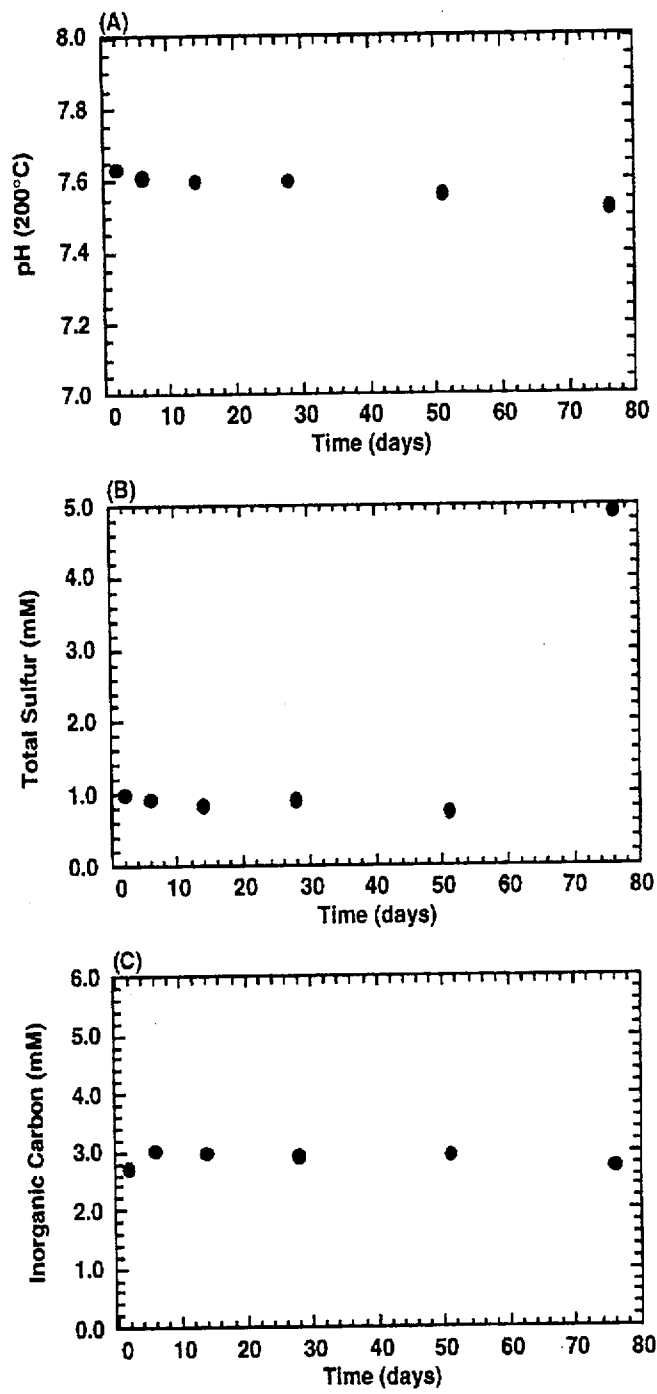


Figure 6-12. Aqueous (A) pH (200 °C), (B) total sulfur, and (C) inorganic carbon of experiment DF5 plotted as a function of time.

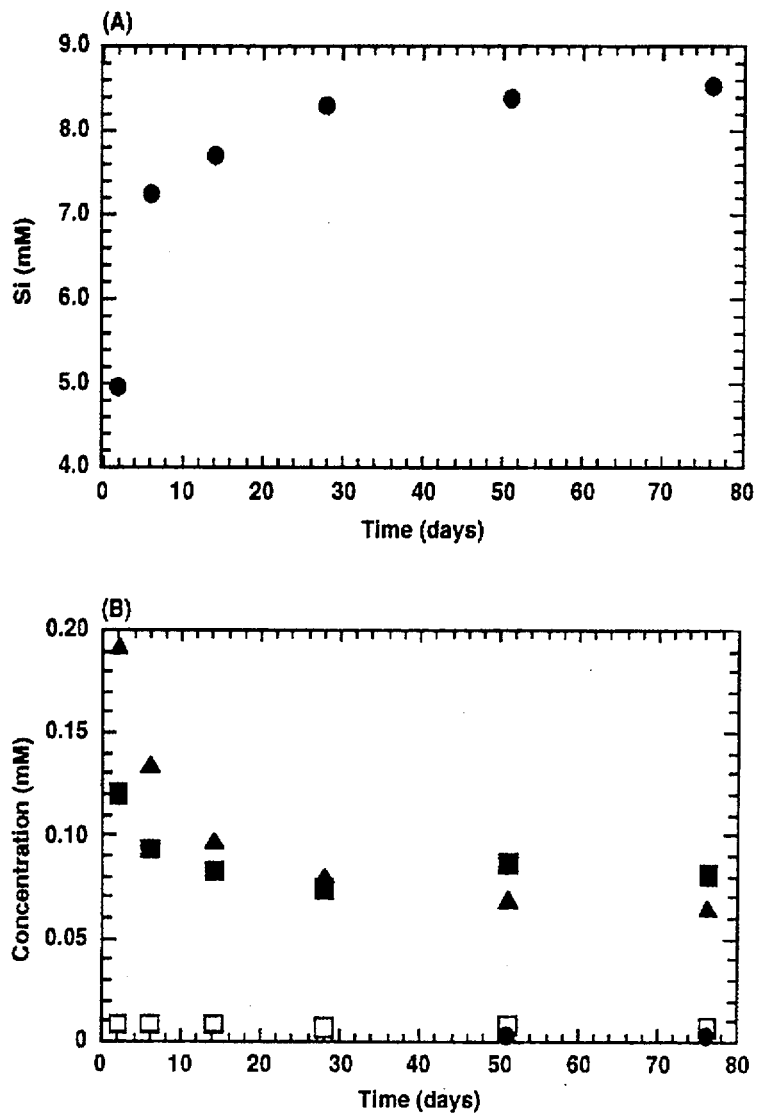


Figure 6-13. Aqueous (A) Si (circles) (B) Al (triangles), K (squares), Ca (open squares), and Mg (circles) of experiment DF5 plotted as function of time.

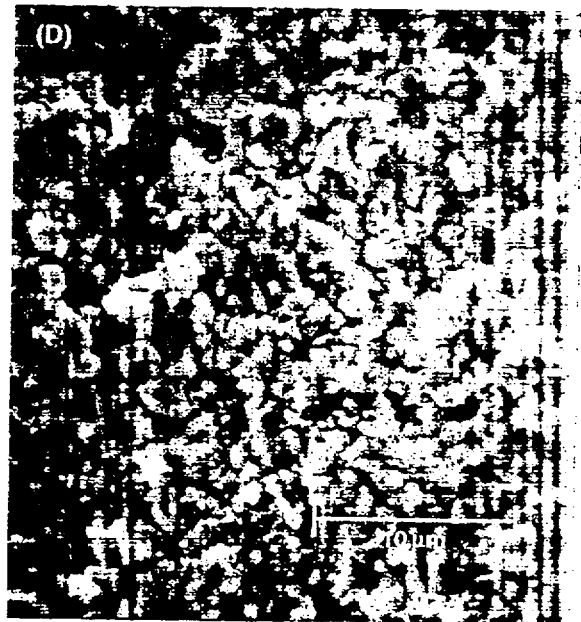
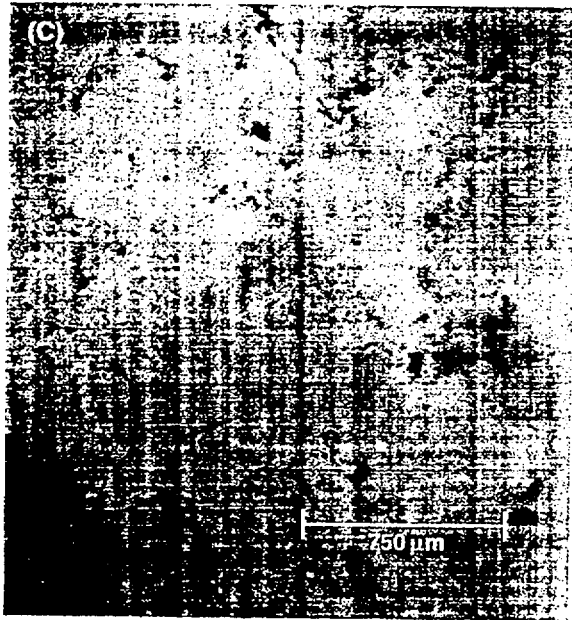


Figure 6-14. SEM photomicrographs of unreacted (A, B) and reacted Topopah Spring tuff (C, D). (B) Magnification of the glassy matrix in the tuff. (C) Reacted Topopah Spring tuff showing a precipitated Si-rich phase (D) Enlargement of the Si-rich precipitate.

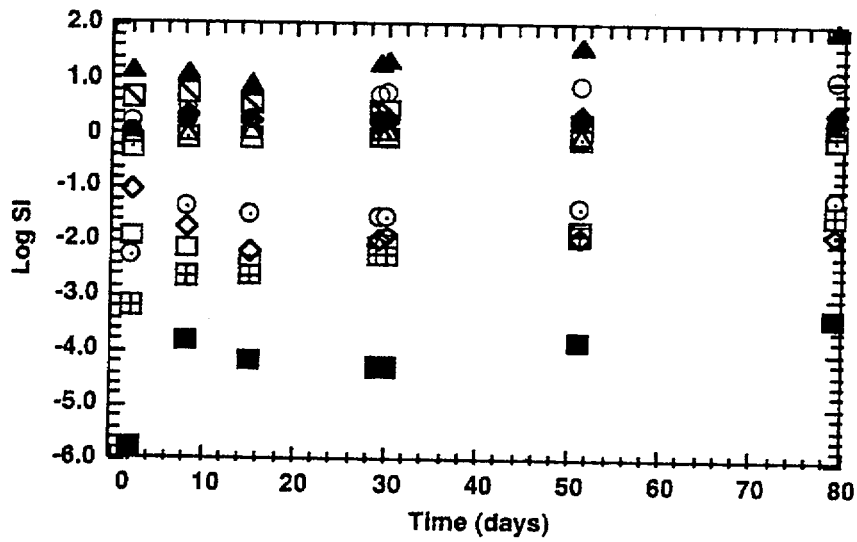


Figure 6-15. Experiment DF6. Topopah Spring tuff - Fibercrete™-water - diesel fuel interactions plotted as the log SI with respect to quartz (solid circle), cristobalite (open square with center dot), wollastonite (solid diamond), K-feldspar (square with a slash), albite (open circle), anorthite (open square), muscovite (open diamond), calcite (open triangle), mesolite (solid triangle), bassanite (open square with cross), gyrolite (open circle with center dot), and 11Å-tobermorite (solid square).

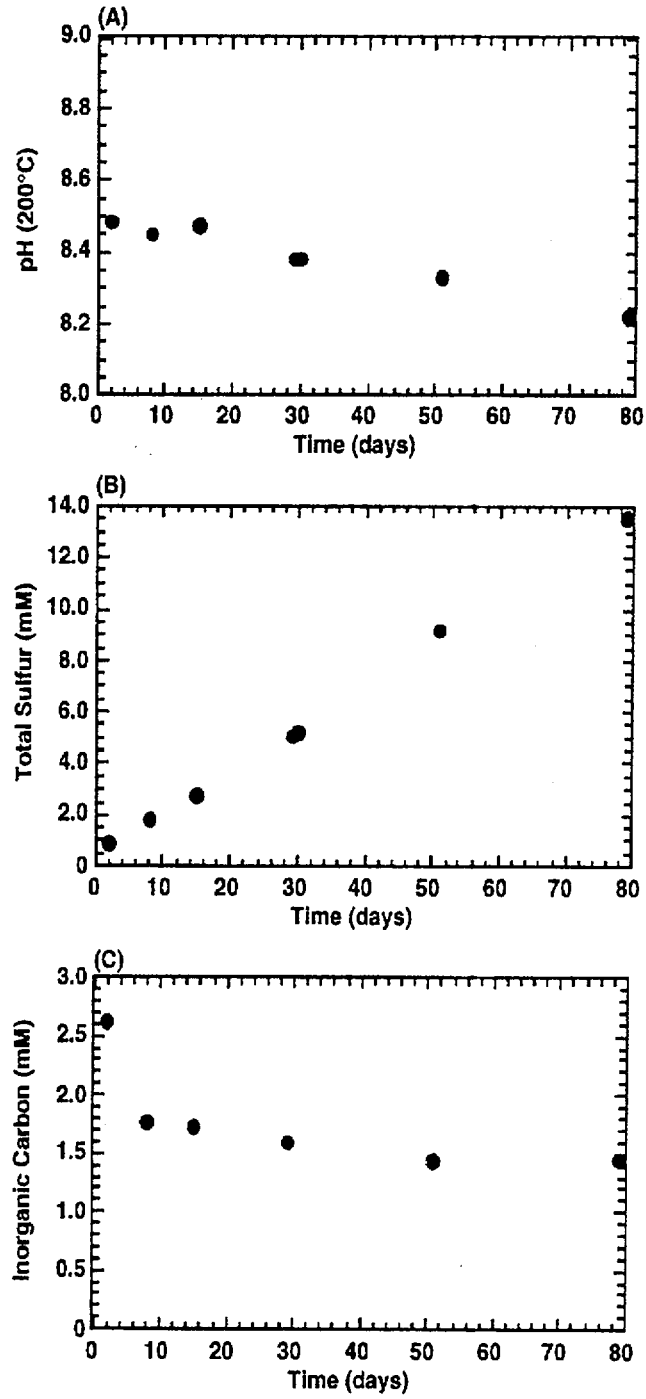


Figure 6-16. Aqueous (A) pH (200 °C), (B) total sulfur, and (C) inorganic carbon of experiment DF6 plotted as a function of time.

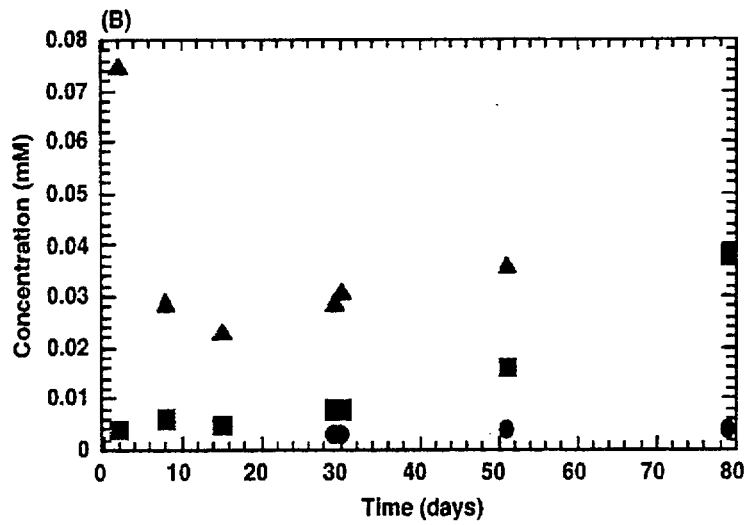
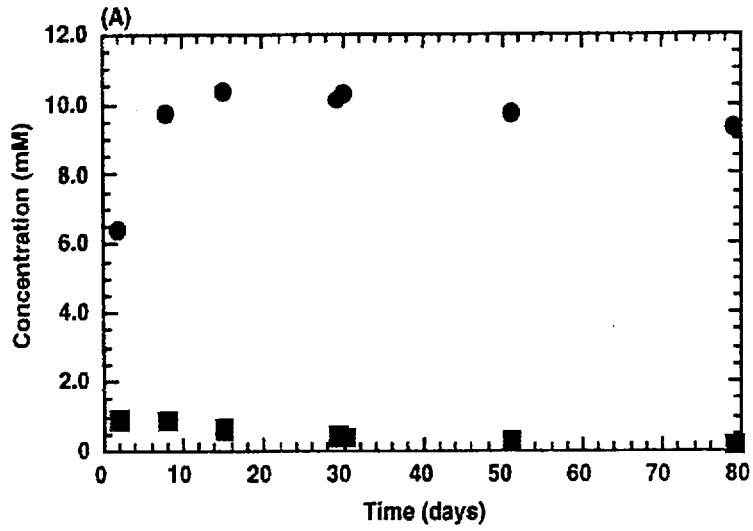


Figure 6-17. Composition of aqueous phase plotted as function of time, experiment DF6. (A) Si (circles) and K (squares) (B) Al (triangles), Ca (squares), and Mg (circles).



Figure 6-18. SEM photomicrographs from experiment DF6 of reacted Topopah Spring tuff (A, B) and reacted Fibercrete™ (C, D). (B) Enlargement of the precipitates that form on the tuff surface, showing books of layered Ca-silicate, calcite rhombs, and smaller pure silicate precipitate which may be cristobalite. (D) Enlargement of the Ca-silicate phase found on the reacted Fibercrete™ surface.

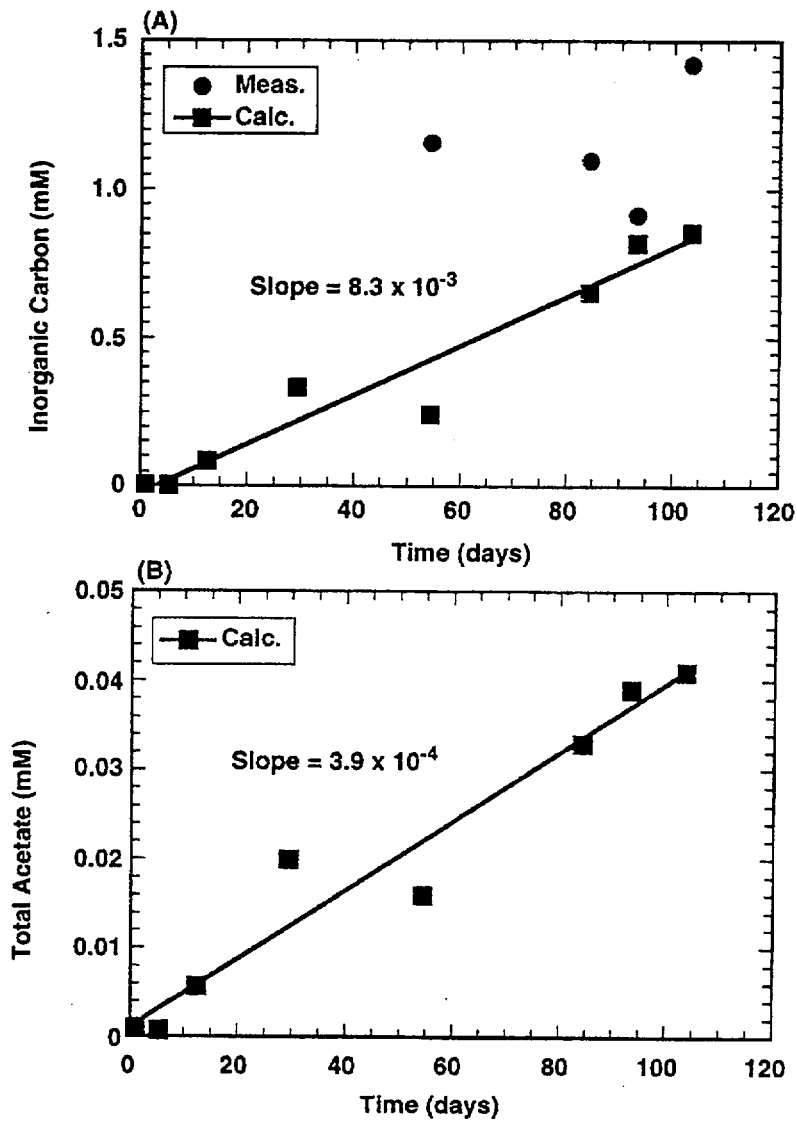


Figure 6-19. The calculated (A) inorganic carbon concentration, and (B) total acetate concentration in a solution of changing pH as a function of time. See text for detailed description of the assumptions and calculations.

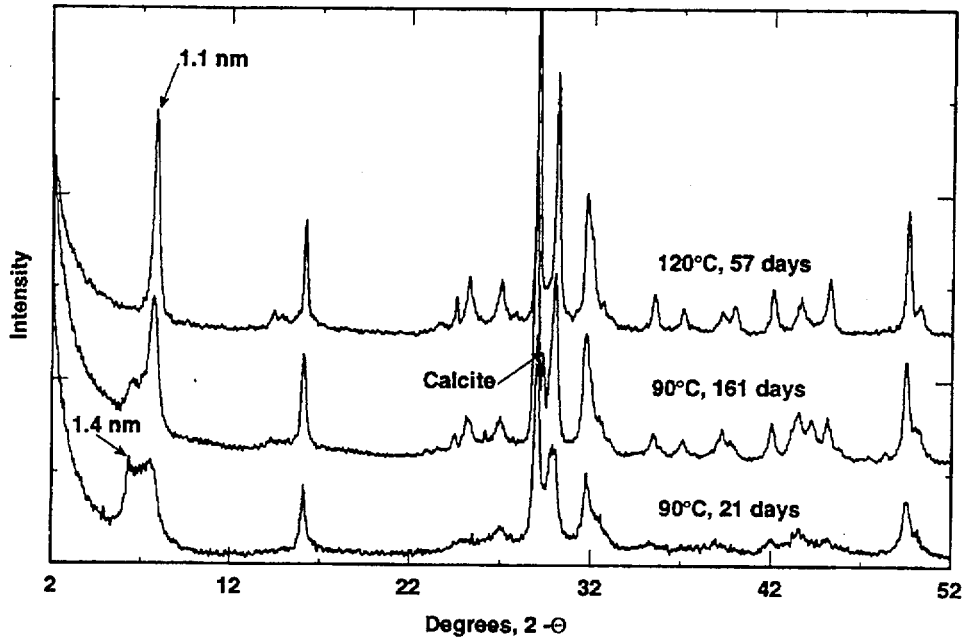


Figure 6-20. XRD patterns of tobermorite run products; the 90 °C XRD patterns show a peak shift from 1.4 to 1.1 nm tobermorite with time; the 120 °C XRD pattern shows only a single phase tobermorite; crystallinity increased with longer run times and higher temperature.

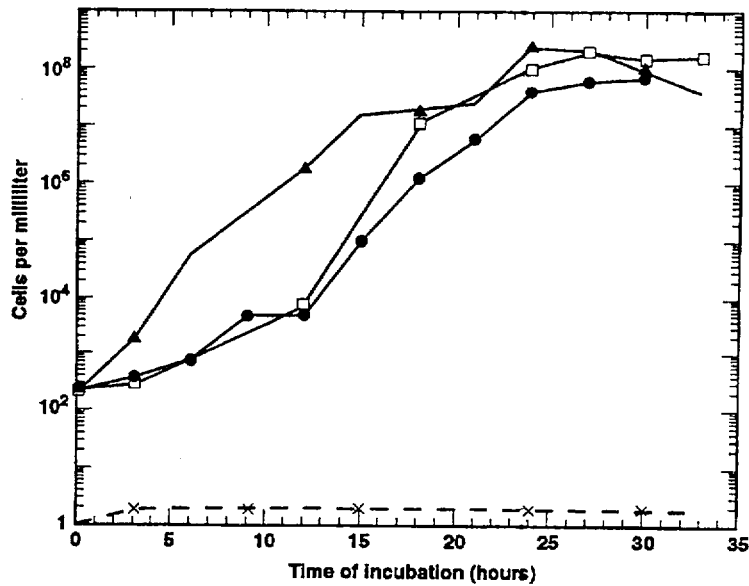


Figure 6-21. Effect of temperature on the growth rates of whole YM microbial communities in R2 media. Rates varied depending on temperature of incubation. Crushed YM tuff was inoculated in media and incubated aerobically at 20°C(●), 30°C(□), or 50°C(▲). Periodically samples were withdrawn and cell count was determined by live planting (x), sterile uninoculated media incubated at 20°C.

Bacteria derived from excavated ESF and Large Block Test rock

(A) ESF

(B) LB

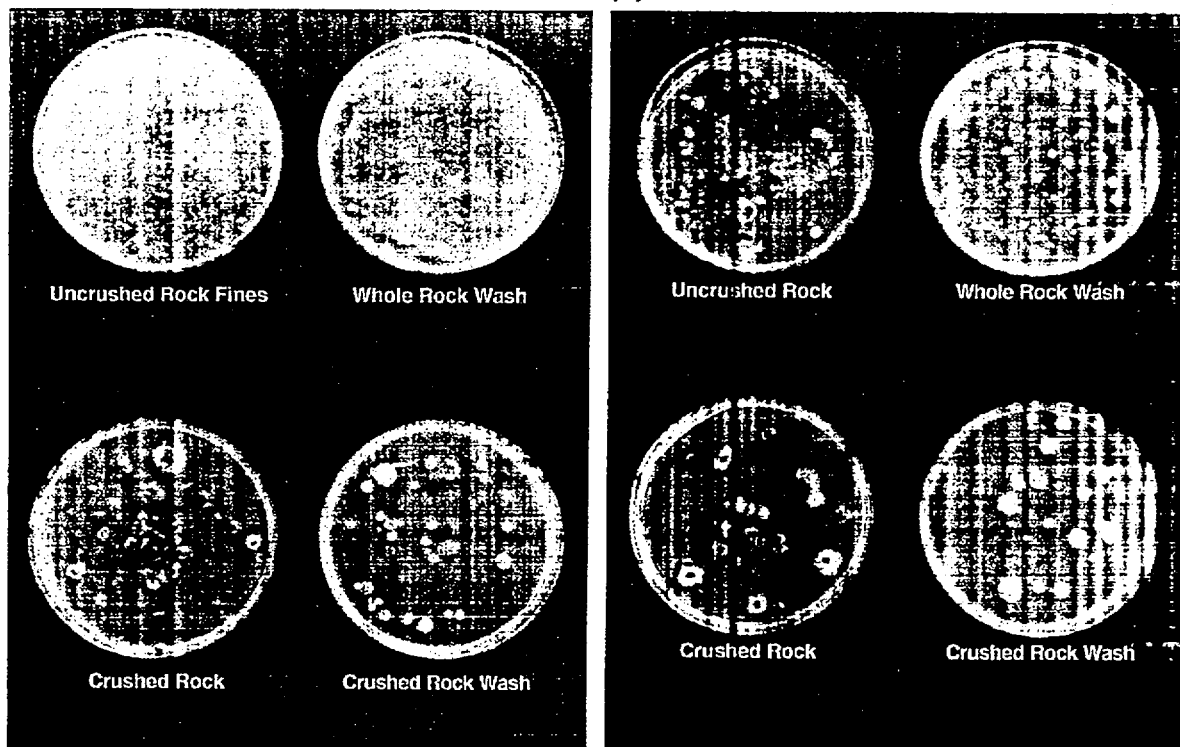


Figure 6-22. Plated samples of whole and crushed rock and rock washes (using sterilized artificial pore water) obtained from (A) the ESF muck pile and (B) the Large Block (LB) Test area suggest that the LB samples show greater culturable species diversity. Future DNA analyses will better indicate total diversity of culturable and unculturable species.

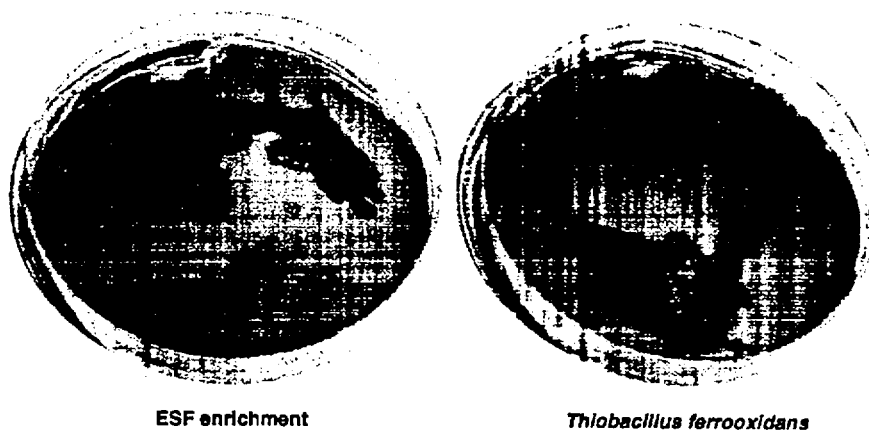


Figure 6-23. Screening tests for iron oxidizers indicate that ESF samples produced iron-oxidizing cultures.

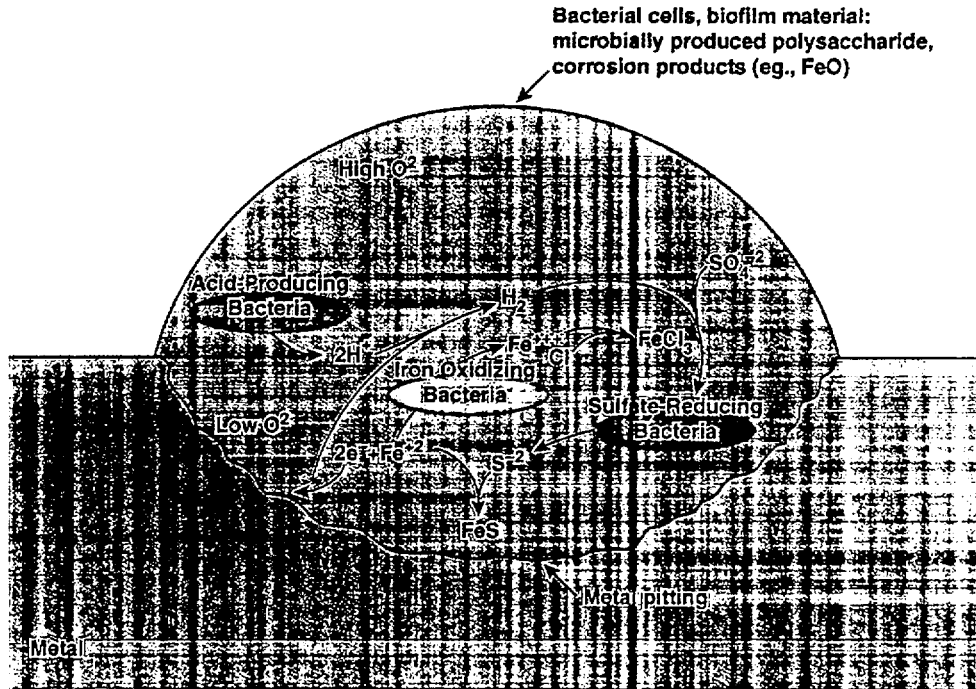


Figure 6-24. Microbially induced corrosion (MIC). Microbially-generated acids directly dissolve the protective calcareous film on stainless steel. Coupling of protons with electrons results in electron removal from the cathode, and forms hydrogen which is a substrate for microbial sulfate reduction.

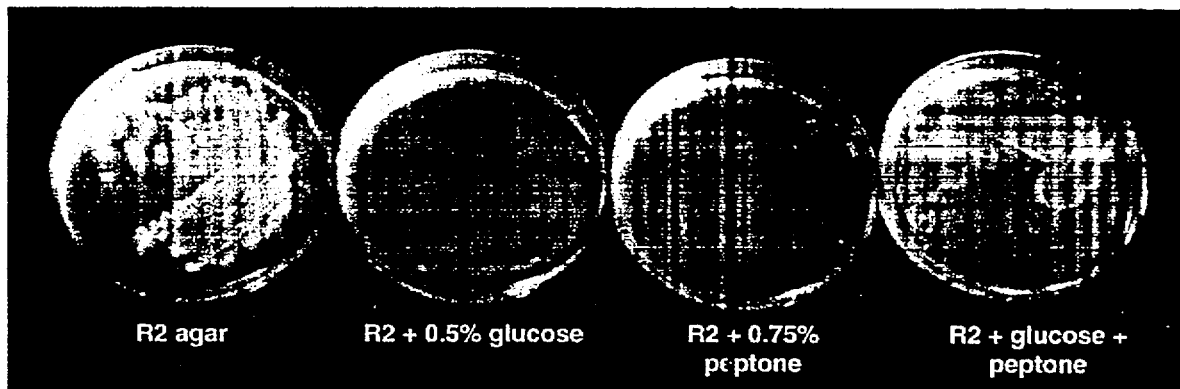


Figure 6-25. Screening tests for slime producers indicate that large quantities of slime can be produced by some bacteria that are extant in the ESF and LB.

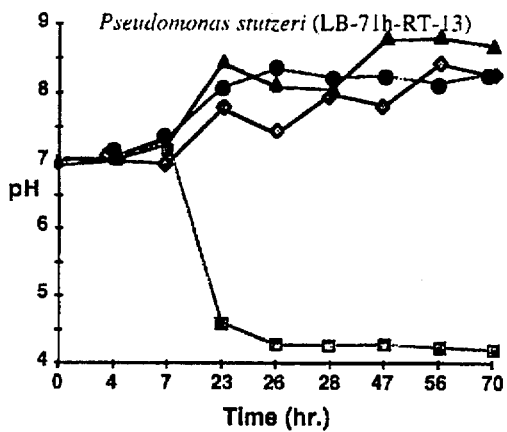
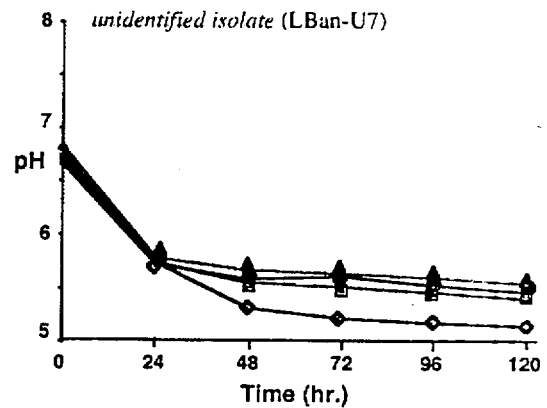
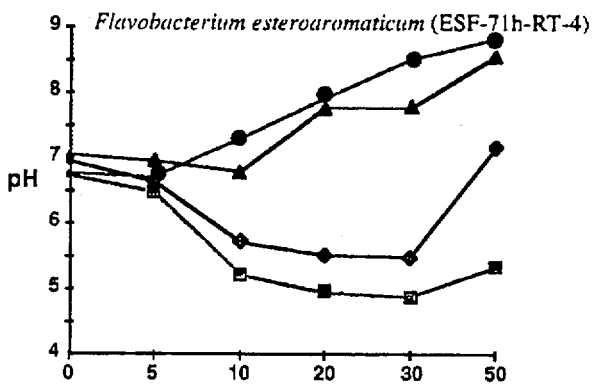
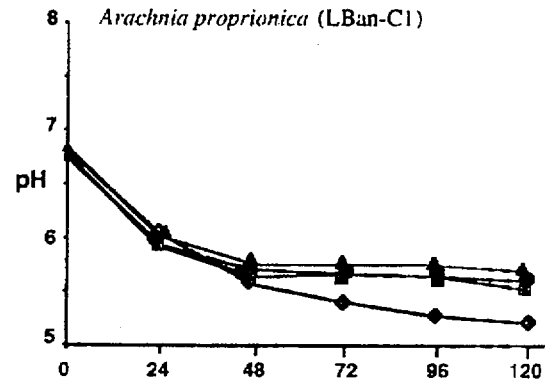
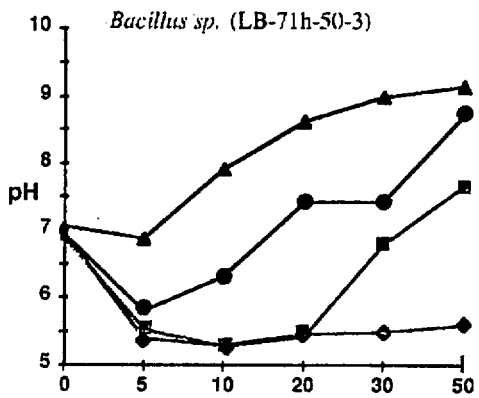


Figure 26. Effect of nutrients and growth on acid production in individual YM isolates. Each indicated isolate was inoculated into R2 media (●), R2 + 0.5% glucose (■), R2 + 0.75% proteose peptone #3 (▲), and R2 + glucose and peptone (◆). Periodically, through subsequent growth the pH of the media was determined.

ESF and LB Isolates: Hydrogen Sulfide Production

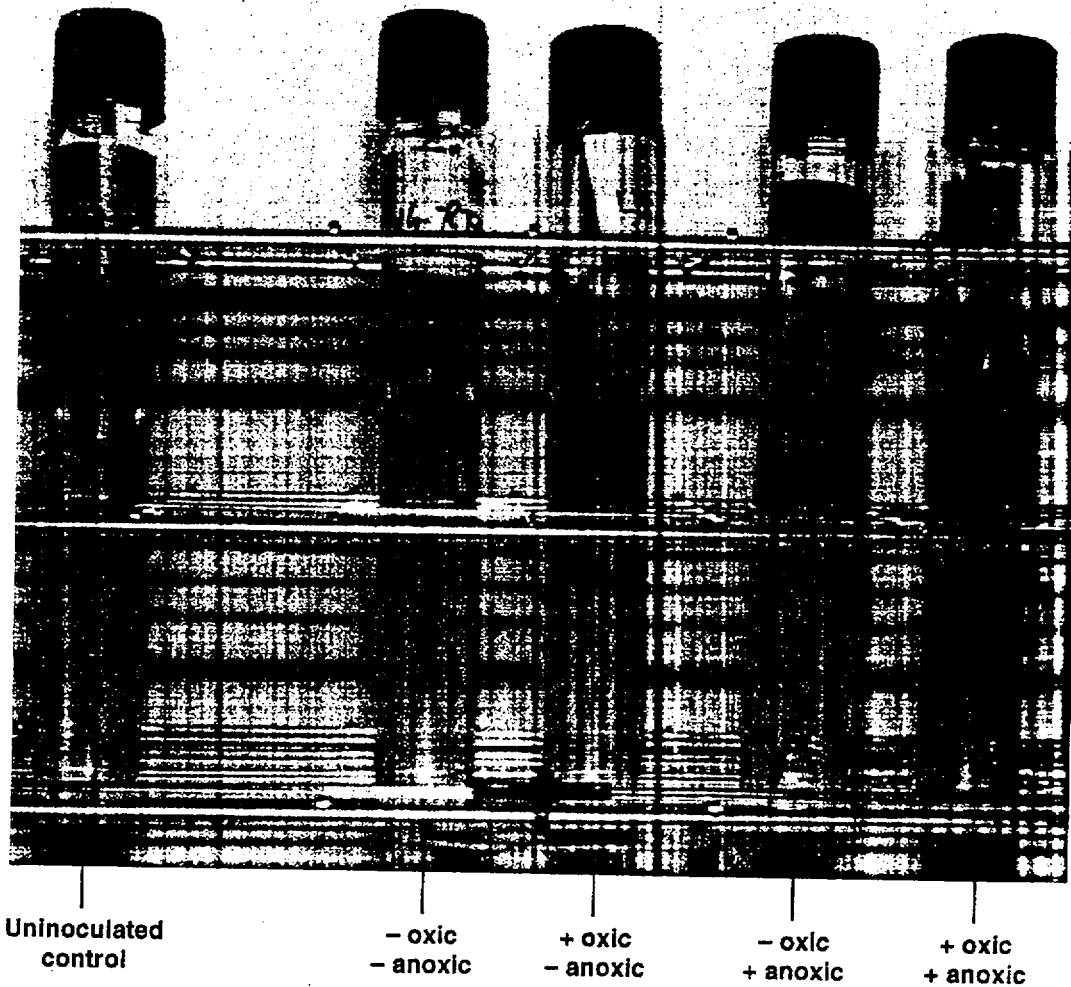


Figure 6-27. Preliminary results showed that sulfide production *via* desulfurylation increased for all tested strains within a two day incubation period, even in anaerobic cultures which metabolize and grow more slowly than do aerobic cultures. R2B media + 0.75% Proteose peptone #3, lead acetate 12 days incubation at room temperature and at 50°C.

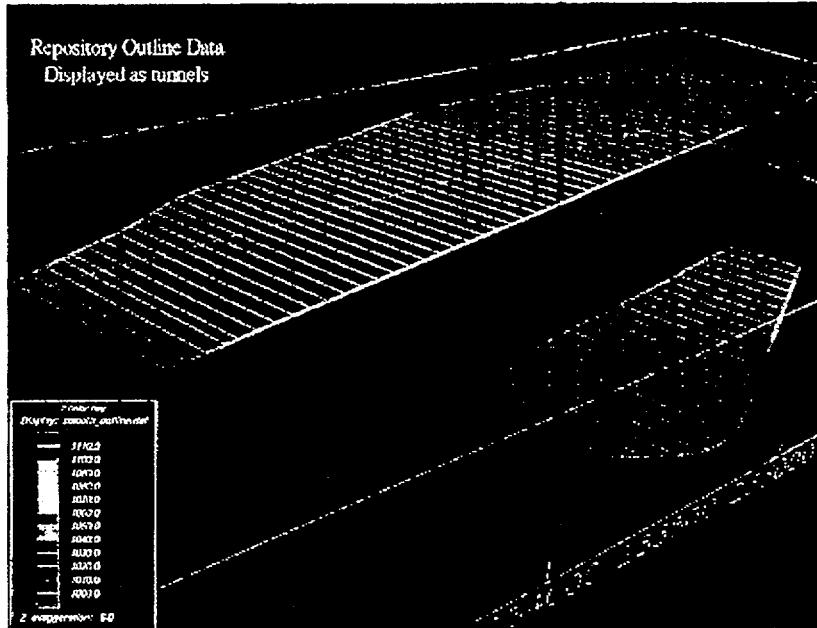


Figure 6-28. Emplacement tunnel footprint is illustrated in the Nevada State coordinate grid, which will allow for easy integration of existing Yucca Mountain geological data. Relative sizes of main and emplacement drifts are shown. Colors indicate elevation (see legend).

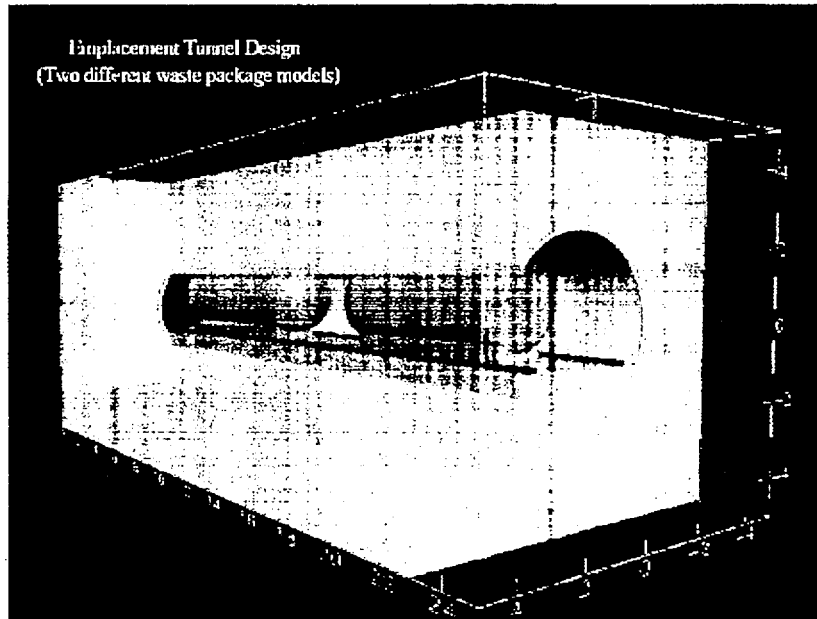


Figure 6-29. Cut away view of the emplacement tunnel demonstrates the capability of the EarthVision™ software to represent discontinuous shapes (scale bar in meters). In this simplified model waste packages (blue; 6 m x 0.2 m diam), cementitious materials (pink and lavender) gantry tracks (red) are installed in the surrounding rock (green).

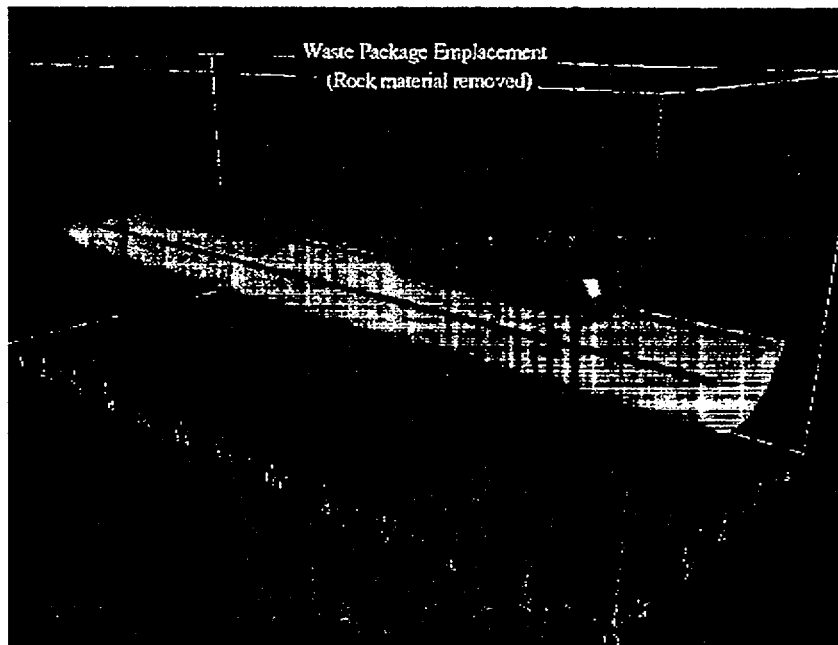


Figure 6-30. Illustration of a 25 m section of 4.3 m diam. emplacement tunnel (scale bar in meters). Waste packages (blue; 6.5 x 1.75 diam.), concrete invert (green; roughly 1.5 m x 4 m), gantry tracks (red; roughly 3.5 m between tracks), and concrete waste package supports (gold; 5.3 m length) are shown to scale.

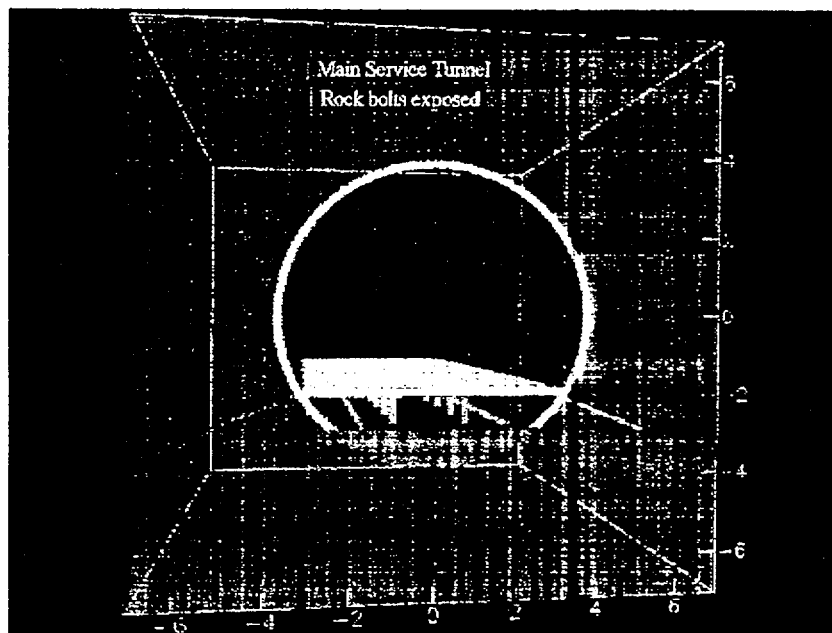


Figure 6-31. Simplified cross-section rendering of a 20-m section of 7.6-m diam. service tunnel (scale bar in meters) shows rockbolts (pink; approximately 3 m long and 0.10 diam.) for the metal grate platform (yellow; approximately 0.2 m thick) anchored into the surrounding rock (brown). The metal platform supports (light blue; approximately 0.2 x 0.3 x 1.0 m) are placed at roughly 2 m intervals. A concrete invert (purple; roughly 1.5 m) and shotcrete layer (gold; 0.2m thick) are shown.

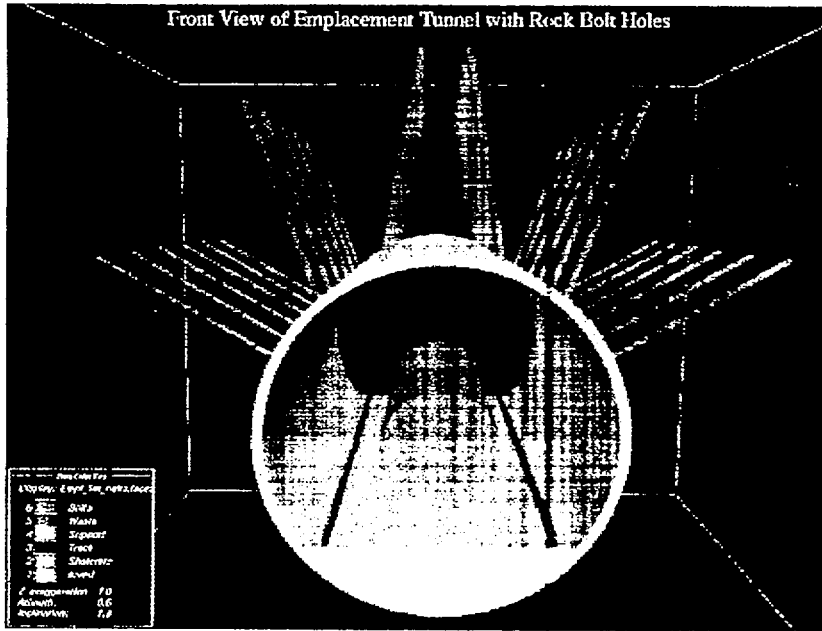


Figure 6-36. Cross-sectional rendering of 20-m section of 5.0-m diam. emplacement tunnel showing rockbolt holes. Given standard spacing (1.5m) as depicted on engineering drawings, 36 rockbolts would be found in this length of tunnel.

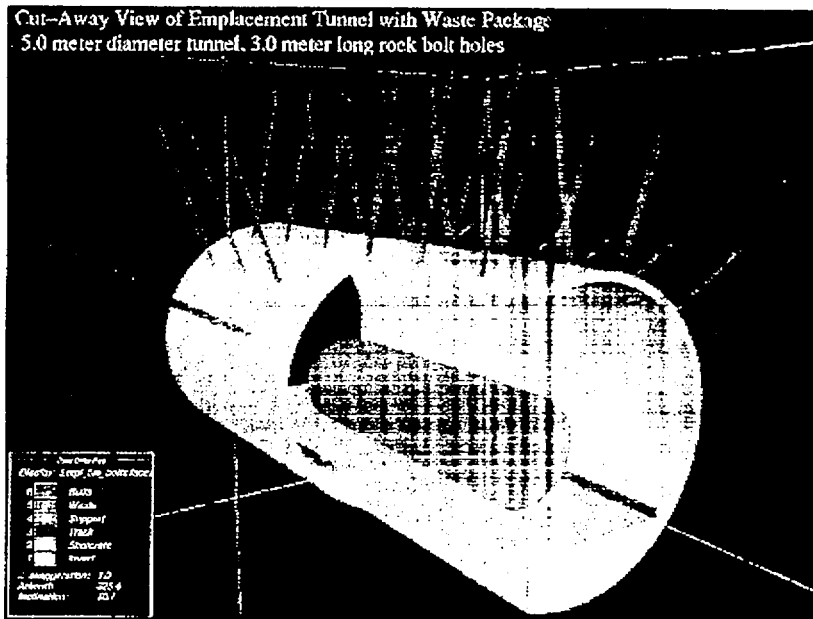


Figure 6-37. Cut-away view of 20-m section of 5.0-m diam. service tunnel showing rockbolt holes.

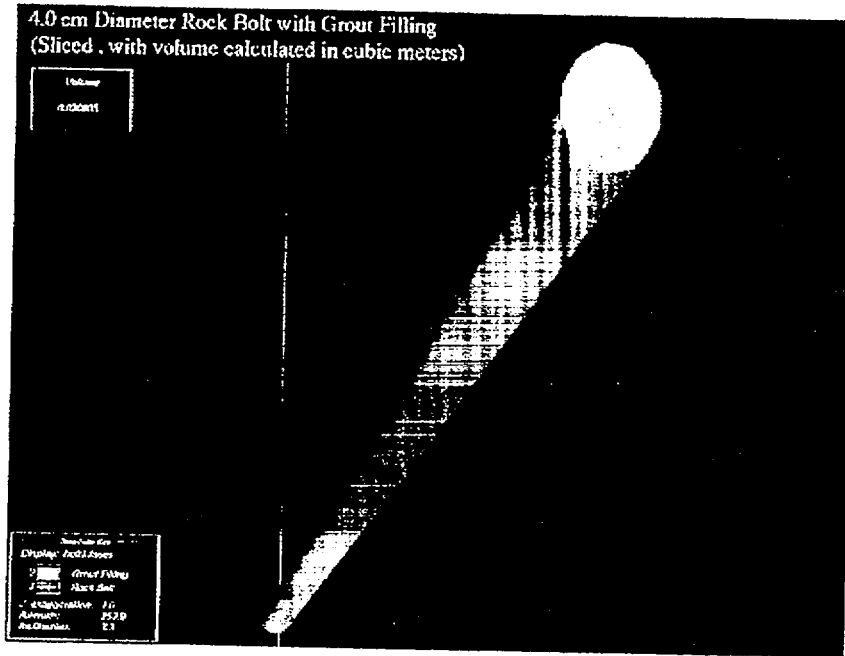


Figure 6-38. Rockbolt detail showing steel rockbolt (gray) and exterior grout filling.

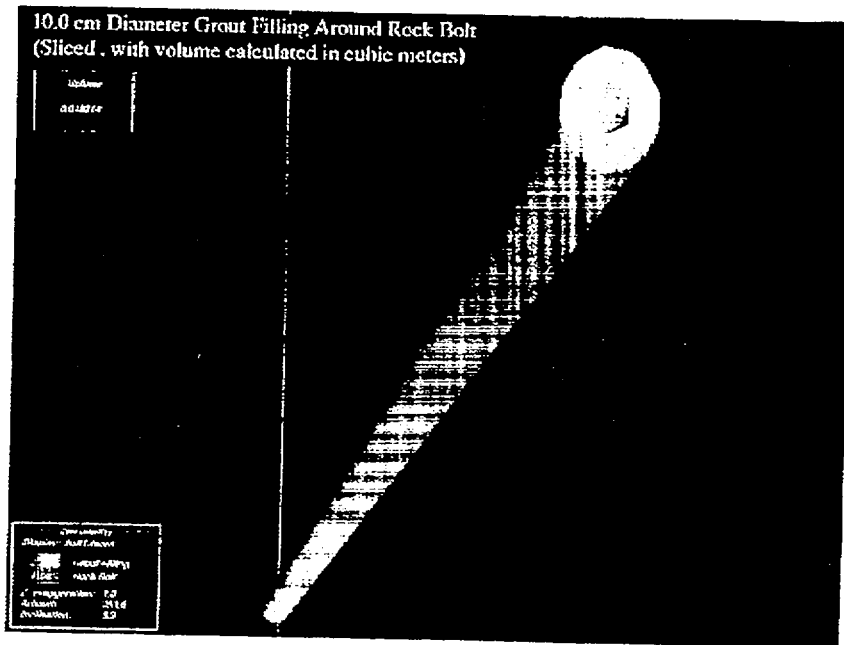


Figure 6-39. Calculational detail of volume of grout (0.018214 m) used for one rockbolt.

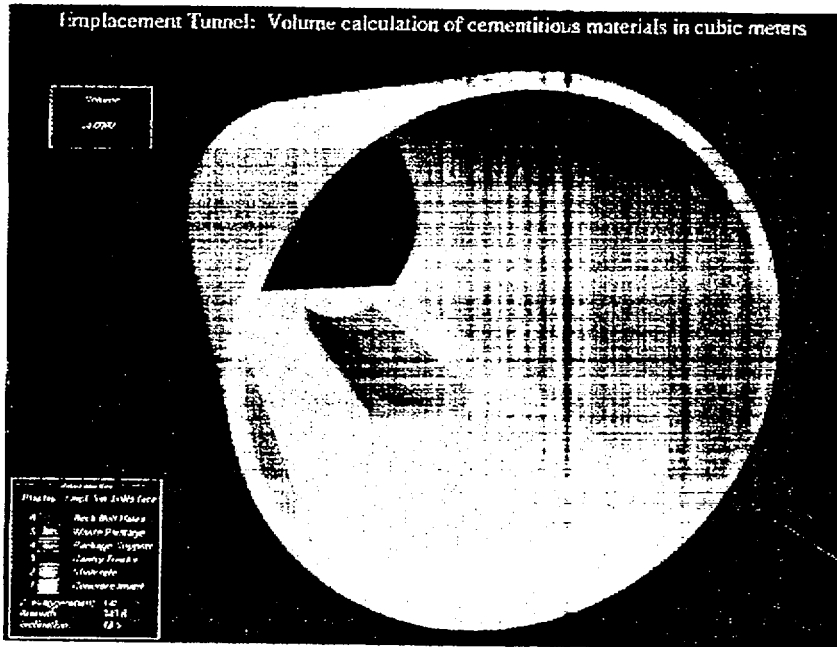


Figure 6-40. Calculation of material volumes is straightforward, as is illustrated in this calculation of the volume of cementitious materials (approximately 54.1 m³) in a 20-m section of 4.3 diam. emplacement drift.

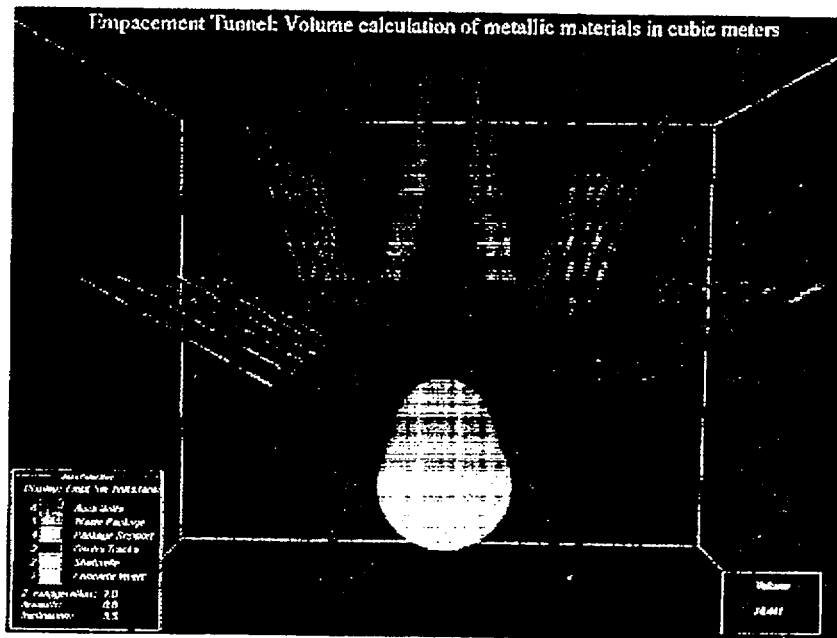


Figure 6-41. Calculation of volume of metal materials (approximately 14.4 m³) (including the waste packages of wall thickness of roughly 0.2 m) in a 20-m section of 4.3 diam. emplacement drift.

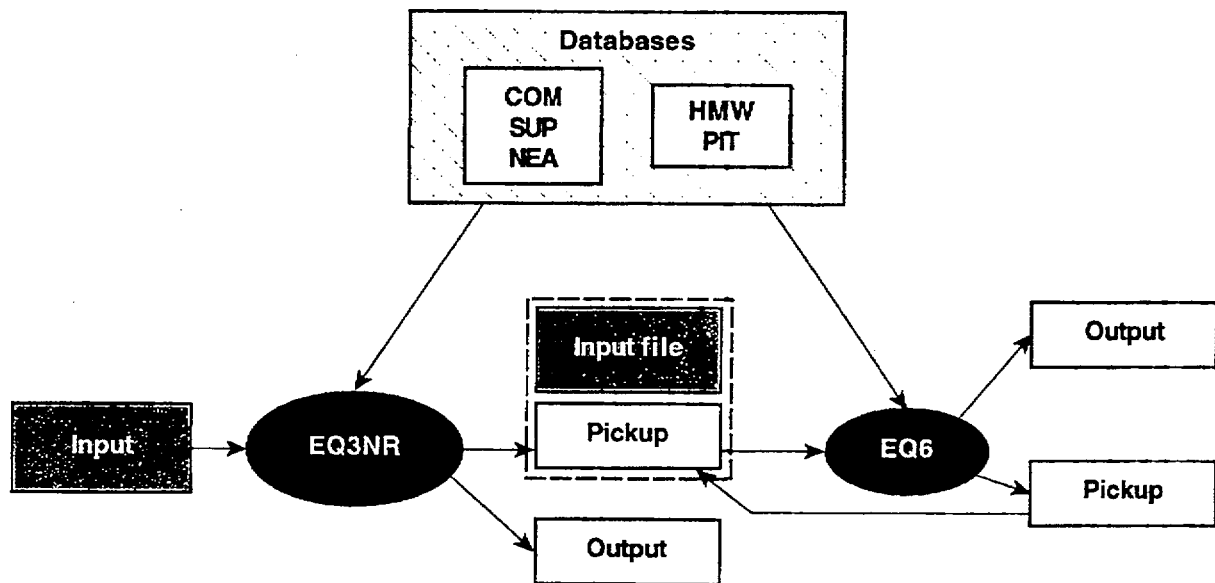


Figure 6-42. Diagram of interaction between various parts of EQ3/6. At present these interactions are conducted manually by the modeler. In order to simulate systems at a higher level of complexity, it will be necessary to automate some of these steps.

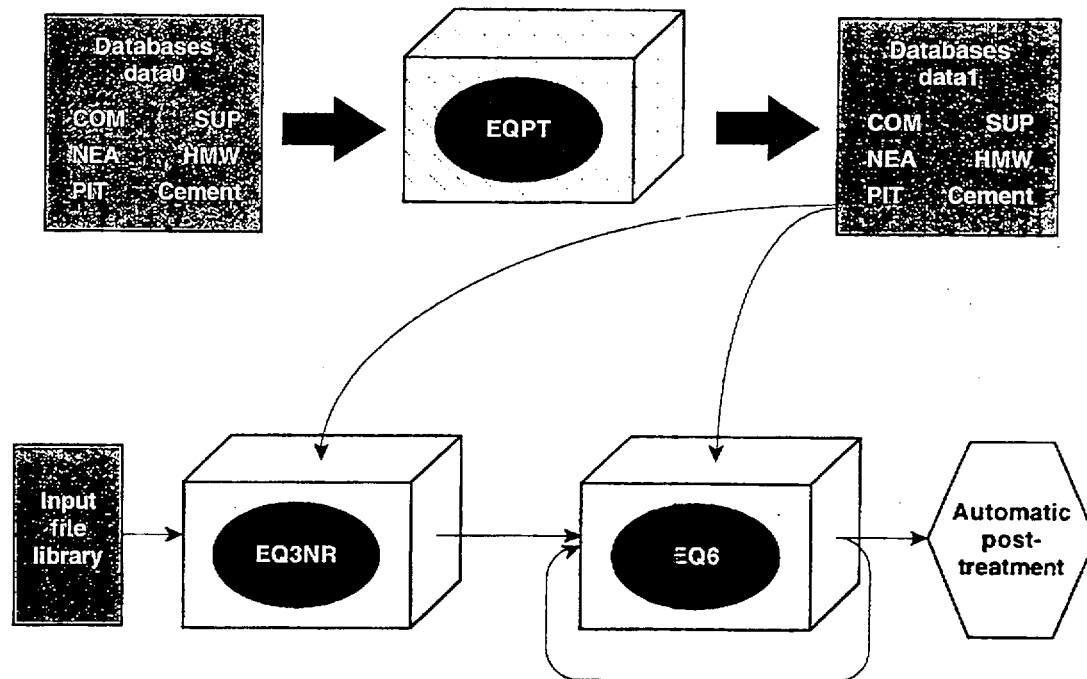


Figure 6-43. Schematic diagram of the flow of information between EQ3NR, EQ6, the databases and the input and output files.

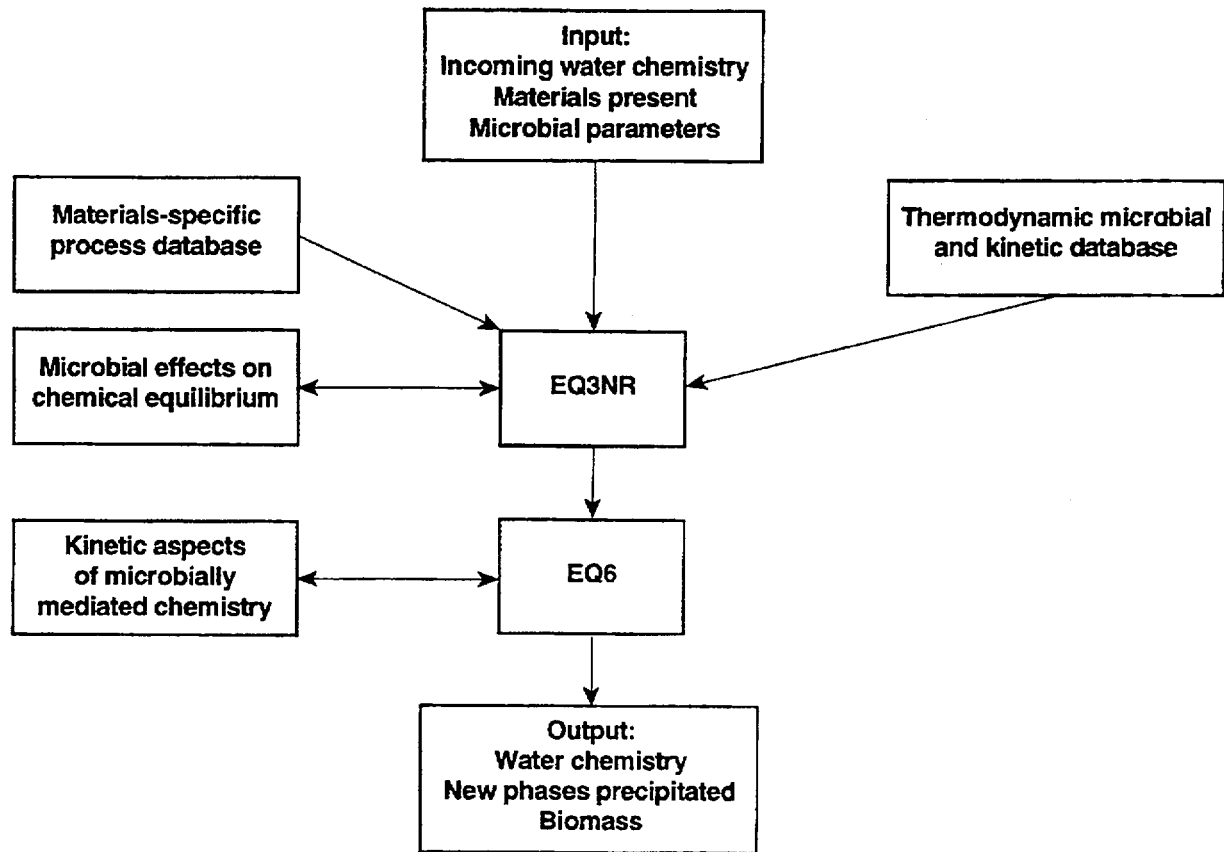


Figure 6-44. Conceptual view of interaction between EQ3/6 modules and modules that simulate biotic effects.

Table 6-1. Steel set materials and ESF locations.

Component *	Quantity between 00 + 58 and 02 + 00 ft	Quantity between 02 + 00 and 04 + 00 ft	Quantity between 04 + 00 and 06 + 00 ft
Item #1	116	83	132
Item #2	232	166	264
Item #3	232	166	264
Item #4	232	166	264
Item #5	468	835	1879
Item #6	3521	3567	6017
Item #7	1276	891	1430

*(1) Top component, MK#1A

(2) Bottom components, MK#1B (2 parts per set)

(3) Side components, MK#1C (2 parts per set)

(4) Steel set, shims and Dutchmen (2 parts per set)

(5) Steel Set Shims (reference drawing BABEAB000-01717-210041102-03)

(6) Steel Lagging, C8 x 11.5# Channel for Steel Sets ~4 ft in length

(7) Tie rods for steel sets (reference drawing BABEAB000-01717-2100-41102-03)

Table 6-2. Rockbolt types and associated materials

Rockbolt type	Explicitly referred to on engineering diagrams	Associated materials
Super Swellex™ ¹ (long and short)	long only (3000 mm. nom.)	water is applied at a regulated pressure to inflate the bolt
Solid #8 Threaded ¹ (long and short)	long only (3000 mm. nom.)	grouted into place
Williams™ Hollow Core ¹	(3000 mm. nom.)	grouted
Split Set ²	no	unknown

¹ BABEAB000-01717-2100-40157-01.

² Personal communication, Eugene Pokorny.

Table 6-3a. Grout mineralogy of Fibercrete™.

Grout mineralogy	Formula	Composition (wt%)
Tricalcium silicate	3(CaO)SiO ₂	61
Dicalcium silicate	2(CaO)SiO ₂	15
Tricalcium aluminate	3(CaO)Al ₂ O ₃	6
Tetracalcium aluminoferrite	4(CaO)Al ₂ O ₃ Fe ₂ O ₃	9

Table 6-3b. Grout composition of Fibercrete™.

Oxide	Composition (wt%)
SiO ₂	21.4
Al ₂ O ₃	4.3
Fe ₂ O ₃	2.9
CaO	64.9
MgO	1.7
SO ₃	2.7
Na ₂ O	0.53
Loss on ignition	0.87
Insoluble residue	0.2

Table 6-3c. Steel fiber composition of Fibercrete™.

Element	Composition (wt%)
Fe	99.8
C	0.018
Mn	0.075
P	0.040
S	0.050

Table 6-4. Details of spills 001 through 010.

Spill No.	Date	Tunnel station	Affected surface	Fluid
SRP-001	12/10/94	0+87	invert	oil
SRP-002	01/07/95	1+09	invert	oil
SRP-003	02/23/95	02+84	TBM	oil
SRP-004	03/03/95	04+05	invert segment	oil
SRP-005	03/21/95	04+60	unknown	oil
SRP-006	03/24/95	05+03	TBM	hydraulic fluid
SRP-006a	03/24/95	05+01	TBM	oil
SRP-007	03/25/95	05+13 ⁷⁶	TBM	oil
SRP-008	03/25/95	05+16 ⁶⁷	TBM	oil
SRP-009	03/28/95	05+10	TBM	hydraulic fluid
SRP-010	04/14/95	05+45	TBM	hydraulic fluid

Table 6-5. Spills reported through 09-August-95.

Spill No.	Date
SRP-011	05/06/95
SRP-012	05/31/95
SRP-013	06/01/95
SRP-014	06/06/95
SRP-014a	06/21/95
SRP-015	06/24/95
SRP-016	06/20/95
SRP-017	06/30/95
SRP-018	07/05/95
SRP-019	07/22/95
SRP-020	07/24/95
SRP-021	08/03/95
SRP-022	08/09/95

Table 6-6. Dust control agents that have been considered for use in the ESF.

Product name	Constituents	Company
Bio Cat 300-1	unknown	Applied Natural Systems, Inc.
Soil Master	PVAC/acrylic latex/tripolycate	ESSI/ EBCO
Petrotac	asphalt, vacuum gas, oil, metal tallate	SynTech Products Corp.
Coherex	petroleum hydrocarbons	Witco
Lignosite	calcium lignin sulfonate and sugars	Georgia Pacific
R-8376 Surfactant	sodium dodecylbenzene sulfonate	Nevada Dust Control
Agriloc	assumed hydrocarbon based on decomposition products	Swift Adhesives
Chem Loc 411	Vinyl acetate and acetaldehyde	Golden West Industries, Inc.
EMC Squared	assumed hydrocarbon based on physical properties	Soil Stabilization Products
Dustcon	citrus oil	Polo Citrus

Table 6-7. ^{14}C analyses of 50 mL diesel fuel samples collected at the ESF. Five samples were taken from the storage tank and three were collected from the locomotive motor. Prior to measurement using accelerator based mass spectrometry (AMS) an aliquot from each sample was combusted to graphite.

CAMS No.	Sample name	Fraction modern	\pm	D^{14}C	\pm	^{14}C age
26826	IM-DF-95-1	0.0003	0.0007	-999.7	0.7	>51200
26827	IM-DF-95-2	0.0005	0.0007	-999.5	0.7	>50300
26828	IM-DF-95-3	-0.0007	0.0007	-1000.7	0.7	>52800
26829	IM-DF-95-5	0.0001	0.0008	-999.9	0.8	>52200
26830	IM-DF-95-4	0.0006	0.0009	-999.4	0.9	>49900
26831	IM-DF-95-6	0.0009	0.0008	-999.1	0.8	>48800
26832	IM-DF-95-8	0.0001	0.0007	-999.9	0.7	>52200
26833	IM-DF-95-9	0.0000	0.0009	-1000.0	0.9	>52800
26834	IM-DF-95-7	0.0007	0.0007	-999.3	0.7	>49500

Table 6-8. Experimental matrix. Diesel Fuel Hydrous Pyrolysis.

Exp. No.	Temp. (°C)	Nominal pressure (bars)	Duration (days)	Rocking	Water comp.	Sample composition	Solid analysis	Organic liquid analysis	Aqueous phase analysis	Gas analysis
DF1	200	70	75	not continuous	MilliQ	1 water: 1 diesel fuel	n/a	GC (CS ₂ dilution)	HPLC	GMS
DF2	315	150	105	no	MilliQ	10 water: 1 diesel fuel	n/a	n.a.	HPLC GC CO ₂ gas anal.	GMS
DF3	200	70	87	continuous after 66 days	3 mM NaHCO ₃	water + Fibercrete wafer	XRD SEM /EDS	n.a.	ICP-AES IC CO ₂ gas anal.	GMS
DF4	200	70	80	yes	3 mM NaHCO ₃	10 water: 1 diesel fuel + Fibercrete wafer	XRD SEM /EDS	n.a.	HPLC GC CO ₂ gas anal. ICP-AES IC	GMS
DF5	200	70	76	yes	3 mM NaHCO ₃	10 water: 1 diesel fuel + Tpt wafer	XRD SEM /EDS	n.a.	HPLC GC CO ₂ gas anal. ICP-AES IC	GMS
D F6	200	70	79	yes	3 mM NaHCO ₃	10 water: 1 diesel fuel + Tpt and Fibercrete wafers	XRD SEM /EDS	n.a.	HPLC GC CO ₂ gas anal. ICP-AES IC	GMS

n/a: not applicable, n.a.: not analyzed

Table 6-9. Starting diesel fuel (LLNL motor pool) compositions measured by GC of CS₂ extractions.

Carbon No.	Average % peak area
C ₆ -C ₉	4.7 ± 0.6
C ₁₀ -C ₁₄	29.5 ± 1.6
C ₁₅ -C ₁₉	52.6 ± 2.6
C ₂₀ -C ₂₆	13.3 ± 1.9
Total	100.1

Table 6-10. Organic compounds identified by GMS analyses of gas extraction from aqueous samples from experiments DF1, DF2, DF4, DF5 and DF6.

Organic compound	Formula	DF1	DF2	DF4	DF5	DF6
methane	CH ₄	Y	Y	Y		
ethane	C ₂ H ₆		Y	Y		Y
propylene	C ₃ H ₆	Y	Y			
n-butane	C ₄ H ₁₀	Y	Y	Y		
i-butane	C ₄ H ₁₀	Y	Y	Y		
trans-2-butene	C ₄ H ₈		Y			
propane	C ₃ H ₈	Y	Y	Y		
i-pentane	C ₅ H ₁₂		Y	Y	Y	
n-pentane	C ₅ H ₁₂	Y	Y			
2-pentene	C ₅ H ₁₀	Y	Y			
2-methylpentane	C ₆ H ₁₄		Y		Y	
2-methyl-1-pentene	C ₆ H ₁₂		Y			
cyclohexene	C ₆ H ₁₀		Y			
2,2-dimethylbutane	C ₆ H ₁₄		Y			
benzene	C ₆ H ₆		Y	Y	Y	
2,hexene (cis,trans)	C ₆ H ₁₂		Y			
n-heptane	C ₇ H ₁₆		Y			
1-heptene	C ₇ H ₁₄		Y			
ethylcyclopentane	C ₇ H ₁₄		Y			
toluene	C ₇ H ₈		Y	Y	Y	Y
1-methylcyclohexene	C ₇ H ₁₂		Y			
1,1-dimethylcyclopentane	C ₇ H ₁₄		Y			
1,2-dimethylcyclopentane	C ₇ H ₁₄		Y			
1-ethylcyclohexene	C ₈ H ₁₄		Y			
xylene	C ₈ H ₁₀		Y	Y	Y	
n-octane	C ₈ H ₁₈		Y			
n-nonane	C ₉ H ₂₀		Y			

Table 6-11. Major hydrocarbons and their abundances relative to maximum peak area as determined by GCMS of final aqueous samples from experiments DF4, DF5, and DF6.

Retention time (min)	Compound	Boiling point (°C)	Percent of maximum peak area		
			DF4	DF5	DF6
13.06	benzene	80.1	23.66	18.32	25.87
18.86	toluene	110.6	100	100	100
24.56	ethyl benzene	136.2	31.37	28.21	21.65
25.19	p-xylene & m-xylene	138.3	82.19	80.45	66.77
26.51	o-xylene	144.4	49.38	40.82	35.79
30.22	1-ethyl 3-methyl benzene	161.3	26.90	24.43	17.27
30.56	1, 3, 5- trimethyl benzene	165	16.03	14.53	10.73
30.96	1-ethyl 2-methyl benzene	165.2	16.00	13.97	11.09
31.63	1,2,4-trimethyl benzene	169	52.67	49.77	37.08
32.64	1,2,3-trimethyl benzene)	176	30.60	26.84	21.05
33.03	indane	177.8	14.78	13.39	10.55
36.62	1-methyl-2-(2-propenyl) benzene	198	24.05		
36.91	tetrahydro naphthalene	207.6	20.48	14.74	12.53
37.44	naphthalene	218	39.45	33.9	30.35

Table 6-12. Yucca Mountain bacterial isolates displaying corrosion-related activities.

Strain# ^a	Species Identification ^b	Acid Production ^c	Sulfide Production ^d	Slime Production ^e
ESF-C1	<i>Cellulomonas flavigena</i>	X	X (oxic)	
LB-71h-RT-13	<i>Pseudomonas stutzeri</i>	X		
ESF-71h-RT-4	<i>Flavobacterium esteroaromaticum</i>	X	X (oxic)	
LBan-U7	uncharacterized	X		
LBan-UW2	<i>Cellulomonas turbata</i>	X		
LB-71h-50-3	probably <i>Bacillus sp.</i>	X		
ESFan-U4	<i>Bacillus circulans</i>	X		
LBan-C1	<i>Arachnia propionica</i> (poor match)	X	X (oxic/anoxic)	
LBan-UW2	<i>Cellulomonas turbata</i>	X		
LBan-U1	<i>Cellulomonas galida</i>	X		
LBan-U2	<i>Bacillus pabuli</i>	X	X (anoxic)	
LBan-U3	<i>Bacillus pantothenicus</i>		X (anoxic)	X
LB-71h-50-2	<i>Bacillus pumilus</i> subgroup B		X (anoxic)	
LB-71h-50-4	<i>Bacillus subtilis</i>		X (anoxic)	X
LB-71h-50-6	probably <i>Bacillus sp.</i>		X (anoxic)	X
ESF-71h-RT-1	<i>Flavobacterium esteroaromaticum</i>		X (oxic)	
LB-C1	uncharacterized		X (oxic)	X
LB-C2	uncharacterized		X (oxic)	
LB-C7	<i>Pseudomonas stutzeri</i>		X (oxic)	
LB-71h-RT-15	<i>Pseudomonas pseudoftava</i>			X
LB-71h-RT-4	<i>Pseudomonas pseudoftava</i>			X
LB-CW-6	<i>Arthrobacter oxydans</i>			X

^aESF=Exploratory Study Facility; LB=Large Block; an=isolated under anaerobic conditions; C=crushed rock isolate; U=uncrushed rock isolate; W=isolated from after washing rock; 71h=isolated after 71 hours of growth; RT=room temperature isolate; 50=50°C. isolate.

^bDetermined by fatty acid analysis using the MIDI/Hewlett Packard microbial identification system (MIS; Analytical Services, Inc., VT); identification of given isolates may be tentative due to a lesser degree of similarity with type organisms contained in the MIS database.

^cDetermined after growth in R2 media (Reasoner and Geldreich, 1985) with or without 0.5% glucose and pH indicators bromocresol purple and methyl red.

^dDetermined after growth in R2 agar media (Difco) containing 0.75% proteose peptone #3 (Difco) and lead acetate.

^eDetermined after growth on R2 agar (Difco).

Table B-1. Cement nomenclature and standards. Designations for cements are standardized by organizations such as the American Society for Testing and Materials (ASTM) and the American Petroleum Institute. Cement chemists have developed a nomenclature for phase composition that is based on ratios of oxides; the notation carries no structural implications. The following shorthand is standard.

Letter designation	Phase composition
C	CaO
S	SiO ₂
M	MgO
H	H ₂ O
\bar{C}	CO ₂
\bar{S}	SO ₃
N	Na ₂ O
P	P ₂ O ₅
A	Al ₂ O ₃
F	Fe ₂ O ₃
K	K ₂ O
AFt	Calcium aluminum trisulfate (e.g., ettringite)
AFm	Calcium aluminum monosulfate (e.g., "monosulfate")
OPC	Ordinary portland cement
SRPC	Sulphate-resisting portland cement

Table B-2. Summary of major hydration reactions (Bensted, 1989).

Below 100°C	
(1)	<i>Tricalcium silicate (alite):</i> $2C_3S + 6H \Rightarrow (C_3S_2H_3) + 3CH$ (C-S-H)
(2)	<i>Dicalcium silicate (belite):</i> $2C_2S + 4H \Rightarrow (C_3S_2H_3) + CH$
(3)	<i>Tricalcium aluminate (aluminate):</i>
	(a) $C_3A + 3\bar{C}\bar{S}H_2 + 26H \Rightarrow C_3A.3\bar{C}\bar{S}.H$ (ettringite)
	(b) When the gypsum is used up: $C_3A + CH + 12H \Rightarrow C_4AH_{13}$
	(c) This then reacts with the ettringite formed: $C_3A.3\bar{C}\bar{S}.H_{32} + 2C_4AH_{13} \Rightarrow 3(C_3A.\bar{C}\bar{S}.H_{12}) + 2CH + 2OH$ ("monosulphate")
(4)	<i>Calcium aluminoferrite (ferrite):</i>
	(a) $C_2A_{0.5}F_{0.5} + CH + 3CSH_2 + 25H \Rightarrow C_3A_{0.5}F_{0.5}.3\bar{C}\bar{S}.H_{32}$ (ettringite)
	(b) When the gypsum is used up: $C_2A_{0.5}F_{0.5} + 2CH + 11H \Rightarrow C_4A_{0.5}F_{0.5}H_{13}$
	(c) This then reacts with the ettringite formed: $2C_4A_{0.5}F_{0.5}H_{13} + C_3A_{0.5}F_{0.5}.3\bar{C}\bar{S}.H_{32} \Rightarrow 3(C_3A_{0.5}F_{0.5}.\bar{C}\bar{S}.H_{12}) + 2CH + 2OH$
Above 100°C	
(1)	Main product is α -dicalcium silicate hydrate, C_2SH , which has high permeability and low compressive strength; above 200°C it forms tricalcium silicate hydrate, $C_3S_2H_3$.
(2)	Additions of ~35 to 40% silica yield tobermorite, $C_5S_6H_5$, which has low permeability and good compressive strength; above 150°C it forms xonotlite, C_6S_6H and gyrolite, $C_7S_3H_2$, which has higher permeability and lower compressive strength.
(3)	Hydrogarnet, $Ca_3(Al, Fe)_2[SiO_4/(OH)_4]_3$ and stratlingite $Ca_2(Al, Fe)_2SiO_7 \cdot 8H_2O$ are also formed from the ferrite and aluminate phases.

Table B-3. Names, formulas, and standard terms of cement phases. CA is the chemical abstracts number.

Name	Formula	Cement Std	CA#
Hydrous (Product) Phases			
Calcium hydroxide Portlandite	Ca(OH)_2	CH	1305-62-0
Calcium silicate hydrates Afwillite	$\text{Ca}_3\text{Si}_2\text{O}_6(\text{OH})_2 \cdot 2\text{H}_2\text{O}$ $\text{Ca}_3\text{Si}_2\text{O}_7 \cdot 3\text{H}_2\text{O}$	$\text{C}_3\text{S}_2\text{H}_3$	16291-79-5 24189-31-9 14404-64-9
C-S-H gel C-S-H(I) C-S-H(II) Foshagite	$\text{Ca}_4(\text{SiO}_3)_3(\text{OH})_2$ $4\text{CaO} \cdot 3\text{SiO}_2 \cdot \text{H}_2\text{O}$ $\text{Ca}_8[\text{Si}_6\text{O}_{17}](\text{OH})_6$	$\text{C}_1\text{S}_1\text{H}_1$ $\text{C}_5\text{S}_{4-6}\text{H}_x$ $\text{C}_9\text{S}_{4-6}\text{H}_x$ $\text{C}_4\text{S}_3\text{H}$	12214-32-3
Gyrolite	$\text{Ca}_{16}\text{Si}_{24}\text{O}_{60}(\text{OH})_8 \cdot 14\text{H}_2\text{O}$ $\text{Ca}_4[\text{Si}_6\text{O}_{15}](\text{OH})_2 \cdot 4\text{H}_2\text{O}$	$\text{C}_2\text{S}_3\text{H}_2$	66899-82-9 16225-87-9
Hillebrandite	$2\text{CaO} \cdot \text{SiO}_2 \cdot \text{H}_2\text{O}$ $2\text{CaO} \cdot \text{SiO}_2 \cdot x\text{H}_2\text{O}$ anhydrous	C_2SH	15669-77-9 67412-69-5 13572-91-3
Jennite Metajennite Nekoite	$\text{Ca}_9(\text{Si}_6\text{O}_{18}\text{H}_2)(\text{OH})_8 \cdot x\text{H}_2\text{O}$ $\text{Ca}_9(\text{Si}_6\text{O}_{18}\text{H}_2)(\text{OH})_8 \cdot 2\text{H}_2\text{O}$ $\text{Ca}_3\text{Si}_6\text{O}_{15} \cdot 7\text{H}_2\text{O}$ $3\text{CaO} \cdot 6\text{SiO}_2 \cdot 8\text{H}_2\text{O}$ $\text{CaSi}_2\text{O}_5 \cdot x\text{H}_2\text{O}$ $\text{CaO} \cdot 2\text{SiO}_2 \cdot 2\text{H}_2\text{O}$	$\text{C}_9\text{S}_6\text{H}_{11}$ $\text{C}_9\text{S}_6\text{H}_7$ $\text{C}_3\text{S}_6\text{H}_7$ $\text{C}_3\text{S}_6\text{H}_8$	63701-45-1 12427-05-3 32237-29-9
Okenite	$\text{Ca}_{10}\text{Si}_{18}\text{O}_{46} \cdot 18\text{H}_2\text{O}$ $\text{CaSi}_2\text{O}_4(\text{OH})_2 \cdot \text{H}_2\text{O}$	$\text{C}_3\text{S}_6\text{H}_6$ CS_2H_2	14654-13-8
Plombierite Reyerite ¹ Riversideite-9Å Tobermorite-14Å	$\text{Ca}_{10}[\text{Si}_{12}\text{O}_{31}](\text{OH})_6 \cdot 18\text{H}_2\text{O}$ $(\text{Na},\text{K})_2\text{Ca}_{14}(\text{Si},\text{Al})_{24}\text{O}_{58}(\text{OH})_8 \cdot 6\text{H}_2\text{O}$ $\text{Ca}_5\text{H}_2(\text{SiO}_3)_6 \cdot 2\text{H}_2\text{O}$ $\text{Ca}_5\text{Si}_6\text{O}_{16}(\text{OH})_2 \cdot 8\text{H}_2\text{O}$ $\text{Ca}_5\text{Si}_6\text{O}_{16}(\text{OH})_2 \cdot 5\text{H}_2\text{O}$ $\text{Ca}_5\text{Si}_6\text{O}_{16}(\text{OH})_2 \cdot x\text{H}_2\text{O}$ $\text{Ca}_6\text{Si}_5\text{O}_{12}(\text{OH})_8 \cdot 2\text{H}_2\text{O}$	$\text{C}_5\text{S}_6\text{H}_{10.5}$ $\text{C}_5\text{S}_6\text{H}_{10.5}$ $\text{C}_5\text{S}_6\text{H}_9$	12420-83-6 12424-04-3 14706-42-4 1319-31-9 11074-26-3 58471-00-0 68810-15-1 67412-68-4 67070-27-3 66732-74-9 12423-17-5 12323-54-5 12141-65-0
Tobermorite-11Å	$5\text{CaO} \cdot 6\text{SiO}_2 \cdot 5\text{H}_2\text{O}$ $\text{Ca}_{4.5}(\text{Si}_6\text{O}_{15}(\text{OH})_3) \cdot 2\text{H}_2\text{O}$ $\text{Ca}_4(\text{Si}_6\text{O}_{14}(\text{OH})_4) \cdot 2\text{H}_2\text{O}$ $\text{Ca}_5(\text{Si}_6\text{O}_{16}(\text{OH})_2) \cdot 2\text{H}_2\text{O}$ $\text{Ca}_6(\text{Si}_6\text{O}_{18}) \cdot 2\text{H}_2\text{O}$	$\text{CSH}_{1.66}$ $\text{C}_5\text{S}_6\text{H}_{1.5}$ CSH_x $\text{C}_5\text{S}_6\text{H}_{2.5}$ $\text{C}_5\text{S}_6\text{H}_6$ $\text{C}_3\text{S}_2\text{H}_3$ $\text{C}_4\text{S}_5\text{H}_5$ $\text{C}_5\text{S}_6\text{H}_5$	
Tobermorite-10Å Tobermorite-9Å	$5\text{CaO} \cdot 6\text{SiO}_2 \cdot 3\text{H}_2\text{O}$	$\text{C}_5\text{S}_6\text{H}$	

Table 6-3. (Continued.)

Name	Formula	Cement Std	CA#
Anhydrous (Reactant) Phases			
Calcium oxide Lime	CaO	C	1305-78-8
Calcium silicates Belite	beta-Ca ₂ SiO ₄	β-C ₂ S	14981-10-3 10034-77-2
Alite	Ca ₃ SiO ₅	C ₃ S	12168-85-3
Calcium aluminates	CaAl ₄ O ₇ CaO·Al ₂ O ₃ Ca ₃ Al ₂ O ₆	CA ₂ CA C ₃ A	12042-78-3
Calcium iron aluminates "Ferrite"	Ca ₄ Fe ₄ O ₁₀ - Ca ₄ FeAl ₃ O ₁₀ solid solution	C ₂ (A,F)	

¹ Formula for end-member (Ca-Si-H₂O system) is not yet determined.

Contents

Chapter 7.0 Integrated Testing.....	7-2
7.1 Introduction.....	7-2
7.1.1 Scope of Integrated Testing Activities.....	7-2
7.1.2 Relationship of Integrated Testing Activities to Other YMP Activities	7-2
7.2 Data Inputs Required for Bounding Transport and Source Terms	7-3
7.3 Chemical, Mineralogical, and Physical Characteristics of EBS/NFE Components Expected to Significantly Affect Radionuclide Transport Through the EBS/NFE.....	7-4
7.3.1 Waste Form.....	7-4
7.3.2 Container Corrosion Products.....	7-5
7.3.3 Backfill.....	7-6
7.3.4 Characterization of Natural Colloids at Yucca Mountain	7-6
7.3.5 Cementitious Materials.....	7-9
7.3.6 Altered Host Rock Adjacent to the Engineered Barrier.....	7-10
7.4 Transport Studies in Host Rock and Minerals.....	7-10
7.4.1 Characterization of Repository Rock Pore Size Distribution and Diffusion of Actinides....	7-10
7.4.2 Diffusion of Radionuclides in Clinoptilolite.....	7-12
7.4.3 Flow and Transport Through Topopah Spring Tuff.....	7-14
7.5 Field Testing Sorption Models Under Conditions of Fracture Dominated Flow.....	7-19
7.5.1 Cation Exchange.....	7-20
7.5.2 Surface Complexation.....	7-24
7.6 Summary.....	7-29
7.7 Summary of Gaps in Information Required to Bound Radionuclide Transport in the EBS/NFE	7-30
7.8 References.....	7-31

Chapter 7.0 Integrated Testing

Brian E. Viani

7.1 Introduction

The role of the Integrated Radionuclide Release: Tests and Model Development activity (Integrated Testing) is to bound the flux of radionuclides that pass the Engineered Barrier System/Near Field Environment (EBS/NFE) (Viani, 1995a). The purpose of this activity is to measure and model the transport of radionuclide elements from the waste form through the introduced materials, their alteration products, and altered host rock that will comprise the post-containment near field environment of the potential repository at Yucca Mountain. Experimental measurements will be combined with conceptual and mechanistic models to bound the concentrations of radionuclide elements that will be released from the EBS/NFE for any given release from the waste form. The estimated releases will be used by the EBS/NFE Subsystem Performance Assessment task (EBS/NFE PA) to calculate the source term to be used in Total System Performance Assessment (TSPA).

7.1.1 Scope of Integrated Testing Activities

Integrated Testing activities are directly concerned with measuring and modeling the effects that hydrothermally altered EBS/NFE materials have on the transport of radionuclides released from the waste form as it interacts with groundwater re-entering the repository after the dry-out period. These interactions, which may include sorption, precipitation, and matrix imbibition, are an important element of the strategy for evaluating the Yucca Mountain site (CRWMS M&O, 1996). The most important materials to be addressed include: waste package corrosion products, backfill/packing, cementitious materials, and altered repository rock (Viani, 1995b).

7.1.2 Relationship of Integrated Testing Activities to Other YMP Activities

To address the issues of radionuclide dispersion, retardation, and depletion in the EBS/NFE, Integrated Testing activities will require material, data, and models from the following activities: ambient and altered zone geochemistry and thermohydrology, waste package materials and waste form testing, and man-made materials (Viani, 1995a).

7.1.2.1 Current Status of Integrated Testing Activities. As a result of the change in reference repository design from a borehole emplaced waste package to a drift emplaced waste package, the scope of Integrated Testing activities has expanded to include the interaction of materials other than the host repository rock adjacent to the waste package. Earlier Integrated Testing activities were focused on the processes expected to play a role in controlling radionuclide transport in the altered host rock. Because of the expanded scope there are many areas that have not been addressed that are important to the overall waste isolation strategy put forward by the project (CRWMS M&O, 1996). To date, the Integrated Testing activity has addressed data and models related to:

1. Diffusion of radionuclides through, and pore-size distribution of, repository rocks.
2. Characterization of colloids in Yucca Mountain groundwaters and in experimental fluids passed through repository rocks.
3. Transport of soluble conservative tracers through fractured repository rock at elevated temperatures.
4. The role of diffusion in controlling sorption by the zeolite clinoptilolite.
5. Testing cation exchange and surface complexation models against field data for a fractured aquifer system.

7.2 Data Inputs Required for Bounding Transport and Source Terms

To assess the role of the EBS/NFE in controlling the flux of radionuclides leaving the repository, the following information is necessary.

Near field environment properties that will be required include:

1. The temperature range over which transport will occur.
2. The flux of radionuclide-bearing groundwater exiting the waste canister.
3. The mode of groundwater flow; i.e., saturated, unsaturated, episodic, etc.
4. The saturation state of the EBS/NFE materials comprising the flow path.
5. The potential of water in the system; i.e., $p/p_{H_2O}^0$.

EBS/NFE flow-path-component material properties that will be required include:

1. The composition of the radionuclide-bearing groundwater after it contacts the waste form (pH, soluble species, colloidal species).
2. The elemental, mineralogical, microbial, and physical properties of container corrosion products, hydrothermally altered backfill material, hydrothermally

altered concrete and other introduced materials, and hydrothermally altered repository rock.

7.3 Chemical, Mineralogical, and Physical Characteristics of EBS/NFE Components Expected to Significantly Affect Radionuclide Transport Through the EBS/NFE

Except for episodic fracture flow, the low water flux expected in the post-emplacment and post-containment environment will result in the fluid chemistry being controlled by the flow-path component through which the fluid is passing. The chemical and mineralogical properties of certain of the EBS/NFE materials comprising the effective flow path of radionuclide-bearing groundwaters are expected to play a major role in the transport of radionuclides. The following sections summarize and highlight some of the features that can be important to transport. The reader is to refer to reports and papers regarding the flow-path elements listed below, some of which can be found in the Geochemistry, Man-Made Materials, and Altered Zone sections of this report.

7.3.1 Waste Form

The waste form will control the rate at which radionuclides are released to the contacting groundwaters. An expected scenario for water to contact the waste form would include the following events:

1. During the period of complete containment, container materials are corroded by interaction with liquid and vapor-phase water at elevated temperature.
2. After containers are breached, waste forms interact primarily with vapor phase water during the period of rehydration of the repository, at a temperature above ambient.
3. Liquid water contacts the vapor-altered waste and flows across it and eventually out of the containers into the surrounding altered EBS/NFE materials.
4. Without explicit provision for an oxygen sink, the EBS/NFE environment is assumed to be oxygenated during the time period of radionuclide transport through it.

Because of the unsaturated nature of the repository environment, and the expected low flux of water contacting the waste form following breaching of the waste container, waste forms will have an important effect on the composition of the groundwater leaving the container; i.e., the fluid exiting the waste container will

be strongly conditioned by the waste itself (and by interaction with the ancillary materials in the container; e.g., filler, spacers, etc.).

Groundwater reacting with spent fuel will have reduced levels of Si and other constituents compared with ambient groundwater as a result of formation of uranium silicates and other silicates (Wilson, 1990; Bates et al., 1995a). Layer silicate, uranium-oxide, and uranium-silicate colloids will be released during the interaction of groundwater with spent fuel (Bates et al., 1995a).

Interactions of groundwater with glass waste form may yield a distinctly different chemistry than spent fuel. Laboratory experiments have shown that fluids reacted with glass at high solid to solution ratios (saturated, and under dripping conditions) have relatively high pH, and elevated levels of Si, B, and Li, and distinctly different colloids than spent fuel (Bates et al., 1995b). The actual pH expected in the repository will also depend on the reservoir of CO₂ in gas phase in the system. A large reservoir of CO₂ could buffer the system at a lower pH than is observed in laboratory experiments. Colloids released from glass are predominantly layer silicates with some colloidal phosphates also observed.

We may expect that fluids emanating from the waste package are likely to contain considerable quantities of radionuclide-bearing colloids, be depleted in dissolved oxygen and Si (for spent fuel), and potentially high in pH (for glass). The stability of the colloids that do leave the container is an issue that has not been resolved.

7.3.2 Container Corrosion Products

It would be expected that breaching the waste container would occur as a result of corrosion of the metallic components of the waste package in the humid, elevated temperature regime anticipated during the repository cool-down period. Hence, the first materials likely to be encountered by radionuclide-bearing fluids leaving the container are the corrosion products from the waste container. These corrosion products are likely to be oxides and/or silicates of the metals comprising the container wall and the internal structures of the container.

Mineralogically, these products would be expected to be dominated by oxides and oxy-hydroxides of iron that may be substituted with various other metal elements, and may be intermixed with other oxides formed from other metallic constituents of the waste package. Physically, these materials would be expected to be finely divided porous media that, depending on whether they were contained by

surrounding materials, could be loose (i.e., a pile of sloughed off material) or relatively compact.

Chemical interaction of radionuclide-bearing fluids with canister corrosion products is expected to be dominated by surface chemical effects. Retardation of U, Np, and other metals via surface complexation reactions (Meijer, 1990; Dzombak and Morel, 1990) would be considerably greater than in Yucca Mountain tuffs (Table 7-1). Adsorption of inorganic carbon and dissolved silica may also be significant (Van Geen et al., 1994; Waite et al., 1994; Dzombak and Morel, 1990).

Because the corrosion products are expected to be finely divided, there may be a potential for addition of iron oxide and other metallic oxide colloids to the groundwater. There will also be a potential for filtration of waste-form derived colloids.

7.3.3 Backfill

Although the emplacement of backfill has yet to be finalized, if tuff is used, its chemical effects will be moderate in comparison with its physical effects. Hydrothermal alteration of the tuff is not expected to alter its mineralogical or chemical composition outside the range displayed by the tuffs presently existing at Yucca Mountain (Viani and Bruton, 1992b). However, redistribution of relatively small quantities of silica, coupled with precipitation/dissolution of sorptive minerals could significantly change the behavior of a specific crushed tuff with respect to radionuclide transport. A crushed tuff of coarse sand to gravel would present an effective barrier to transport as long as it remains unsaturated (Conca, 1990). However, episodic flow might short circuit the backfill and potentially entrain significant quantities of colloids. The colloids derived from this material should be similar in composition, but not in quantity, to those found in present day Yucca Mountain groundwaters.

7.3.4 Characterization of Natural Colloids at Yucca Mountain

We have characterized the types of colloids that are found naturally in Nevada Test Site (NTS) and Yucca Mountain groundwaters and in core flow experiments using TSw2 tuff (Buchholtz-ten Brink et al., 1990, 1992; Martin et al., 1991; Viani and Martin, 1994b).

The transport of radionuclides through the EBS/NFE and the far field may be affected by the presence and/or formation of colloids suspended in the fluid phase (Triay et al., 1993a). Suspended colloids may affect the transport of radionuclides by

increasing the partitioning of the radionuclide into the fluid phase, by changing the flow path of the radionuclide, and by reducing the groundwater travel time to the accessible environment. The primary focus of colloid studies carried out in the Integrated Testing activity has been to develop techniques to identify inorganic colloidal particles ($<1 \mu\text{m}$) that may be present in natural and experimental aqueous fluids. The methods developed were used to characterize colloids in groundwater collected from the NTS, including water from well J13, and in fluid obtained from laboratory core-flow experiments (Viani and Martín, 1994a).

7.3.4.1 Colloids in Yucca Mountain groundwaters. Groundwaters from 10 wells were sampled and the suspended colloids characterized by filtration and gravimetric analysis, x-ray diffraction (XRD), x-ray fluorescence (XRF), light scattering, scanning electron microscopy (SEM), and transmission electron microscopy (TEM) [including energy dispersive x-ray spectroscopy (EDS) and selected area electron diffraction (SAED)] (Viani and Martin, 1994b).

The gravimetrically measured concentration of suspended particles $>0.15 \mu\text{m}$ was on the order of 1 mg/L. In light of previously published colloid concentrations for deep groundwaters (McCarthy and Degueudre, 1993) and for water from Well J13 (Ogard, 1987), it is likely that these measurements overestimate the *in situ* groundwater colloid load. Given the strong relationship between pumping rate and colloid load (Puls et al., 1992), it is probable that colloids may have been stripped from the well-bore area during sampling.

Characterization of the colloids using the instrumental techniques listed showed that with the exception of a few particles that were obvious contaminants (e.g., metal particles), the colloidal particles that were identified were consistent with the lithology of the aquifer from which the groundwater was drawn. Of the particles identified by SAED and EDS, a large fraction are layer silicates. Based on the mineralogy of the groundwater-bearing rocks, it appears that these particles are present in the groundwater at a greater fraction than they are in the rock. This may represent a bias toward fracture-filling minerals, which are often layer silicates, or it could represent a pervasive contaminant. There may also be a bias toward identifying layer silicates because of their stability under the electron beam (contrasted with zeolites) and because they may dominate the larger ($>0.5 \mu\text{m}$) particles that were suitable for identification by SAED. Colloidal silica polymorphs (quartz, cristobalite, amorphous silica) and iron oxides were also identified in the groundwater samples.

7.3.4.2 Colloids in J13 groundwater. Groundwater from Well J13 was analyzed for colloids on samples collected about 2.5 yr apart. The colloid concentration from the earlier sampling was determined by filtration and gravimetry. For the later sampling⁽¹⁾, colloid concentration was determined by counting particles retained on 0.015- μm polycarbonate filters.

The number of particles ranged between 0.6 and 1.5×10^{10} particles/L. These values are similar to Degueudre's estimate for an earlier sampling of Well J13 groundwater (GIT, 1993). If the number of particles counted in the later sample of J13 (<0.4- μm fraction) is converted to mass according to McCarthy and Degueudre's formula (1993) (assuming a density of 2 g/cm^3), the concentration would range between 0.007–0.016 and 0.05–0.125 mg/L, for 100 and 200 nm spherical particles respectively. These estimates are similar to Ogard's (1987) estimate, but are one to two orders of magnitude smaller than the concentration for J13 measured gravimetrically (1.7 mg/L). It is likely that the latter value overestimates the colloid load because of contamination or too rapid a pumping rate during sampling.

The role that natural colloids may play in transporting radionuclides through the EBS/NFE will depend directly on their affinity for radionuclide species that may sorb to them, the reversibility of sorption, and their concentration. For linear instantaneous sorption of a radionuclide species on suspended colloids, the ratio of the radionuclide carried in the solution in the presence of the colloid to that in the absence of the colloid is approximated by:

$$C_{c+s} / C_s = 1 + m_c K_d ,$$

where, m_c is the concentration of colloid in suspension, and K_d is the equilibrium linear partition coefficient for the radionuclide species on the colloid. This relationship holds for soluble radionuclide species whose concentrations are controlled by either a solubility limit or by partitioning to the host rock. It is apparent that very large K_d 's ($>10^5 \text{ mL/g}$) and colloid concentrations ($>2 \text{ mg/L}$) are required to increase the radionuclide carrying capacity of the solution by a significant amount (Fig. 7-1). Of the colloids identified, only illite and clinoptilolite (for Cs), and the iron oxides (U, Np) have the potential for K_d 's above 10^4 mL/g . Waste package corrosion products have the potential to add considerable quantities of colloidal

⁽¹⁾ Water samples were collected under the direction of Ines R. Triay, LANL. Unfiltered, 0.4- μm , and 0.05- μm filtered samples were collected on 11/16/93 and sent to LLNL where they were refrigerated until analyzed.

oxides to the EBS/NFE. Because Np has been identified by total system performance analysis (TSPA) calculations as a major contributor to released dose, the issue of colloidal transport of Np will need to be addressed.

7.3.4.3 Colloids in effluent from flow experiments. Suspended particles in samples of fluids that had passed through a saw-cut fracture (25- μm aperture) in a core of Topopah Spring tuff (Viani and Martin, 1993, 1994a) were analyzed by TEM, EDS, and SAED. These particles consisted of iron oxides (hematite) and layer silicates (mica, illite), and could be reasonably ascribed to the core sample or derived from the tools used to create the fracture.

7.3.5 Cementitious Materials

The most likely flow-path component a radionuclide-bearing fluid will encounter after passing through waste package corrosion products is the hydrothermally altered remains of concrete-bearing invert or other structures. The chemical effect of these materials on radionuclide transport will be most important. The pH of fluids within this flow-path component would be expected to be quite high (>12) when the cement is relatively fresh (young). Calcium aluminosilicate gels present in fresh cement will eventually alter to crystalline phases. Because the thermodynamic data for cement minerals are sparse (Bruton et al., 1993), predicting the mineralogical and chemical composition of the hydrothermally altered cements, and the effect of this alteration on radionuclide transport, is uncertain.

Experiments and modeling have suggested that the pH of fluids passing through concretes at ambient temperatures would be expected to remain very high for tens of thousands to hundreds of thousands of years (Atkinson et al., 1989). However, the pH, sorptive capacity, and ability of the hydrothermally altered material to sequester radionuclides could be significantly different from unaltered concrete.

Radionuclide partition coefficients, K_d 's, measured for cements (Table 7-1) appear quite favorable in comparison to K_d 's for Yucca Mountain devitrified tuffs, especially for U and Np (the radionuclide with the greatest long-term impact on repository performance). It is possible that the K_d 's that are measured for U (potentially Np as well) in cement may reflect the precipitation of a relatively insoluble phase in addition to sorption (Atkins et al., 1988).

At least during the early stages of the repository, the cement components would be expected to release significant quantities of colloids (Ramsay et al., 1988). It is not known whether this release of colloidal material would continue after the cement

has undergone chemical and mineralogical alteration associated with long-term heating.

The physical state of concretes and other cementitious materials may evolve from a consolidated and fractured porous medium to a highly fractured and/or crushed porous medium as a result of chemical and physical alteration.

7.3.6 Altered Host Rock Adjacent to the Engineered Barrier

The host rock immediately adjacent to the EBS that will likely be altered by hydrothermal interaction with groundwater and the potentially reactive fluids leaving the repository is the last flow-path component considered part of the EBS/NFE.

In the absence of influx of alkaline fluids, the alteration products and chemistry of the flow-path component would be expected to be similar to that of a crushed-tuff backfill flow-path component. However, interaction of alkaline fluids derived from cementitious materials with the repository host rock may cause significant alteration of the flow-path, especially the hydrologic connection between fracture and matrix. A potential for dissolution of rock at the contact with cement or concrete by alkaline fluids, and subsequent downstream precipitation of calcite, calcium silicates, and zeolites could potentially reduce the porosity adjacent to the fracture and also the permeability in a direction normal to the fracture wall, thus "armoring" the fracture, and reducing the extent of radionuclide retardation due to matrix imbibition and diffusion (Steefel and Lichtner, 1994). This could also potentially decrease the permeability so that fluid flow rates might be significantly reduced, resulting in longer travel times.

7.4 Transport Studies in Host Rock and Minerals

7.4.1 Characterization of Repository Rock Pore Size Distribution and Diffusion of Actinides

Based on the earlier concept of waste package emplacement in boreholes within the repository rock, Integrated Testing studies focused on diffusive transport of radionuclides in near-field TSw2 rock. Pore size distribution measurements (Buchholtz-ten Brink et al., 1992; Klavetter and Peters, 1986) and direct measurement of elemental tracer concentration profiles in TSw2 samples exposed to actinide-bearing solutions (Phinney et al., 1987, McKeegan et al., 1989) are in agreement. A volumetrically small (< ~2-5%) proportion of the interconnected rock

porosity permits relatively rapid diffusion (on the order of the limit in aqueous solutions; i.e., $1 \times 10^{-5} \text{ cm}^2/\text{s}$ @ 25°C). A slower diffusive component, having apparent diffusion coefficients on the order of $1 \times 10^{-16} \text{ cm}^2/\text{s}$ (@ 90°C), is also observed.

7.4.1.1 Pore-size-distribution. Mercury porosimetry measurements (Buchholtz ten Brink et al., 1992; Klavetter and Peters, 1986) have shown that the large majority (>95%) of pores in the matrix of TSw2 are on the order of several hundredths of a micrometer. A small component of porosity is contained in pores on the order of one to several micrometers. This porosity appears to be associated with microfractures.

7.4.1.2 Diffusion. Secondary Ion Mass Spectrometry (SIMS) allows the direct measurement of the concentration profile of a diffusing species in a solid. The concentration profile can be used to determine the diffusion coefficient for the element. Analysis of polished wafers of Tsw2 samples that were exposed to radionuclide-bearing solutions shows diffusion to be bimodal. Long-term exposures of the tuff samples to radionuclide-tracer solutions (180 d @ 90°C) yielded concentration profiles that could be modeled assuming a single diffusion coefficient on the order of $1 \times 10^{-16} \text{ cm}^2/\text{s}$ (Phinney et al., 1987). In short-term exposures (8 h @ 25°C), concentration profiles could not be modeled using a single diffusion coefficient. Elevated levels of tracer (3–40 \times background) were observed at depths of ~10–15 μm , indicating that fast paths allow a proportion of the diffusing species to be transported at rates approaching that in solution (McKeegan et al., 1989). These fast paths may not be identifiable visually or by scanning electron microscopy or optical microscopy. The resulting distribution of diffusing species is distinctly non-uniform and reflects the non-uniform distribution of the μm -scaled fast paths. These results suggest both fast and slow diffusional paths will need to be accounted for to realistically predict retardation of radionuclides due to matrix imbibition.

In contrast to these results, Rundberg (1987) inferred from the concentration variation with time for Cs and Sr tracer solutions in contact with Yucca Mountain tuff wafers that diffusion is relatively rapid ($1 \times 10^{-6} \text{ cm}^2/\text{s}$) but mass transport is limited by slow ($1 \times 10^{-14} \text{ cm}^2/\text{s}$) intracrystalline diffusion in zeolite and smectite cation exchangers. The diffusion of actinide tracers were not able to be modeled using this approach, presumably because they were excluded from the internal regions of the cation exchangers. Because zeolites and smectite exchangers are not

abundant (< 2%) in TSw2, intracrystalline diffusion cannot explain the concentration profiles determined using SIMS.

7.4.2 Diffusion of Radionuclides in Clinoptilolite

Hydrothermal alteration of TSw2 repository rock and other tuffs in the EBS/NFE (e.g., crushed tuff backfill and/or invert) may create additional masses of sorbing minerals such as clinoptilolite or smectite. Although not abundant in the TSw2, smectite and clinoptilolite are significant phases lining fractures that are expected to be the main hydraulic pathways for radionuclide migration from the waste package (Carlos, 1985). The retardation of radionuclides due to interaction with these minerals via cation exchange will be less than expected if the cation exchange reaction is limited by the rate of intracrystalline diffusion. Secondary ion mass spectrometry (SIMS) was used to obtain information regarding the rate of intracrystalline diffusion of Cs and Sr during cation exchange (Roberts et al., 1995; Viani et al., 1994).

Clinoptilolite crystals oriented to either the (010) or (001) crystallographic face by mounting in epoxy were rendered nominally homoionic with respect to Na, K, and Ca by exchange with NaCl, KCl, or CaCl₂ salt solutions as verified by quantitative wavelength dispersive spectroscopy using an electron microprobe (EMP). The homoionic crystals were then exposed to either a Cs/cation or Sr/cation (cation = Na, K, Ca) solution at two different temperatures (30–32°C and 90°C). The mounted crystals were placed in the bottom of a teflon Erlenmeyer flask and 100 mL of the relevant diffuser/cation solution was added to the flask. The sealed flasks were placed in an orbital shaker for the ambient temperature experiment (~30–32°C); and a shaking water bath held at 90°C for the higher temperature experiment.

The geochemical modeling code EQ3/6 (Wolery et al., 1990) was used to select binary solution compositions that would not change significantly (<5%) during the course of the diffusion experiment so as to maintain a constant concentration boundary condition. Solution compositions were selected so that the equilibrium amount of diffusing trace cation in clinoptilolite (Cs or Sr) would be small (~1 mol-% of the exchange cations), and the concentration of the trace cation in solution would be analytically measurable.

Concentration vs. depth profiles were then determined by SIMS. These were obtained for Cs, Sr, Ca, Na, K, Rb, Al, and Si by sputtering through the crystal while rastering the ion beam over a 100 µm square. The conversion of sputtering time to depth was made by measuring the depth of the sputtered raster using a profilometer.

Figure 7-2 shows the SIMS depth profile for the Cs/Ca ambient temperature experiment. The SIMS raw data has been corrected for background, ratioed to the Al signal, and then normalized to a nominal surface concentration value of 0.01 (consistent with EQ3/6 modeling predictions and with the post-diffusion EMP Cs analysis data). An attempt was made to fit this data to a single (constant) diffusion coefficient using the analytical solution to the diffusion equation for a constant concentration boundary condition and an infinite half-plane (Viani et al., 1994). The shape of the experimental data is such that no choice of a constant diffusion coefficient will reasonably match the data.

In contrast, if the binary interdiffusion coefficient D , is compositionally dependent, and is functionally related to composition and trace diffusion coefficients according to (Lanford et al., 1979):

$$D = \frac{D_{in}D_{out}}{X_{in}D_{in} + (1 - X_{in})D_{out}}$$

where X_{in} is the mole or equivalent fraction (relative concentrations) of the inward diffusing component and D_{in} and D_{out} are the trace diffusion coefficients for the inward and outward diffusing components, then it is possible to effectively match the observed data by appropriate choice of D_{in} and D_{out} . The inward and outward tracer diffusion coefficients that result from matching model to data are 2.0×10^{-13} and 1.5×10^{-18} cm²/s, respectively. Although no direct measurements of diffusion coefficients have been reported for clinoptilolite, these data agree with radiochemical measurements of self diffusion coefficients of Cs and Ca in a similar zeolite, mordenite (Breck, 1984), and with diffusion coefficients inferred from batch adsorption experiments for clinoptilolite-bearing tuffs (Rundberg, 1987). Further analysis of the SIMS data for this experiment, for experiments conducted at other concentrations of Cs and Sr, and at other diffusion times are necessary before this simple two-component model can be verified.

Analysis of Cs diffusion profiles into nominally Ca clinoptilolite for ambient and 90°C, and for Sr diffusion into Ca clinoptilolite at ambient temperature reveal several important points:

1. Using a binary interdiffusion model, the ambient temperature diffusion of Cs can be reasonably modeled.

2. The tracer diffusion coefficients estimated from the Cs and Sr diffusion profiles in the ambient temperature experiments indicate diffusion coefficients on the order of 10^{-13} and 10^{-18} cm^2/s for Cs and Sr, respectively.
3. The diffusion of Cs into the Ca clinoptilolite at 90°C was rapid enough to increase the Cs content several orders of magnitude above background to a depth of at least $35\ \mu\text{m}$ (the maximum depth probed) over a 12-day exposure.
4. It is apparent that small amounts of Na, K, and trace levels of Rb are present in the nominal Ca clinoptilolite crystals and their concentrations are not constant with depth. It is possible that at least some of the observed diffusion of Cs may occur by preferential exchange with the residual monovalent cations in the Ca exchanged crystal.

The experimental data and the parameters derived from them indicate that diffusion of Cs and Sr into clinoptilolite is probably not rapid enough to allow the assumption of local cation-exchange equilibrium for situations in which groundwater flow is relatively rapid and clinoptilolite crystal size is relatively large; e.g., in fractures. Applying equilibrium distribution coefficients obtained from batch adsorption experiments using fine-grained clinoptilolites ($1\text{--}2\ \mu\text{m}$) to predict adsorption during flow through fractured media may not be justifiable.

7.4.3 Flow and Transport Through Topopah Spring Tuff

Fracture flow is expected to dominate the flux of H_2O in the altered repository host rock. Matrix flow, if it occurs, will be very slow in comparison. Physical processes related to high suction potential and a potentially discontinuous waste phase will tend to limit flow even beyond the limits imposed by low permeability. Baseline information regarding the potential for retardation and matrix imbibition of soluble radionuclides and/or colloids is necessary to assess flow and transport. In addition, the effects on radionuclide transport of alteration of the host rock by hydrothermal interaction with groundwater, or with reactive fluids derived from EBS/NFE introduced materials, needs to be addressed.

This section summarizes results of flow and tracer tests using core samples of devitrified Topopah Spring tuff containing saw-cut fractures. Experiments were undertaken using $\sim 5.1\text{-cm}$ -diameter by 5.1-cm -long cylindrical cores. A saw-cut parallel to the length of the core was made and two $1/8$ -inch-wide 1-mil ($\sim 25\text{-}\mu\text{m}$)-thick gold shims inserted to maintain a fixed aperture between the surfaces. The core sample was mounted in an apparatus in which confining pressure, downstream pore pressure, flow rate, and core temperature could be varied

(Fig. 7-3). Initial experiments were performed using a pump without the ability to maintain constant upstream pressure or constant flow. Subsequent experiments were performed using a pump that maintained constant flow. Pressures, temperatures, and cumulative flow (initial device) or flow rate (late experiments) were monitored and periodically logged to a computer. Confining pressures were maintained between 35 and 50 bar; pore pressures varied between 0.1 and ~5 bar. Details of the apparatus and the sample treatment are given in Viani and Martin (1993, 1994a).

7.4.3.1 Bacterial plugging of flow path. To prevent the growth of bacteria during the flow test, a core sample was sterilized by autoclaving in-situ by raising the temperature of the flow test device to 120°C for approximately 12 hours. After cooling to ambient temperature, the temperature was again raised to 120°C for 12 hours. Filtered (0.05 µm), deionized (milli-Q) water was pumped through the core and permeability monitored for two flow tests lasting approximately 6 and 8 weeks.

Despite sterilization of the core, flow rate, differential pressure, and permeability varied, apparently as a result of bacterial fouling of the fracture aperture. In one test, permeability showed a relatively strong correlation with differential pressure (Fig. 7-4). The observed flow behavior suggested that the fracture gradually closed due to material filling the aperture, and that by increasing the differential pressure, this material was forced out. To test this, samples of the effluent fluid were taken at times when the flow rate, differential pressure, and permeability were high (Fig. 7-4) and analyzed using transmission and scanning electron microscopy to see if particles were present that could account for the decrease in permeability.

TEM and SEM analyses identified bacteria and inorganic particles in the effluent samples. The most abundant particles appeared to be rod shaped bacteria (~1–1.5 µm long) and were observed in all three samples. Although no obvious source of carbon was introduced into the system, it is apparent that the growth of this bacterium was sufficient to essentially close the 25-µm-fracture aperture. Differential pressures on the order of 0.5 bar and flow rates on the order of 5 mL/h were necessary to “cleanse” the aperture. However, as shown in Fig. 7-4, even after increasing the flow rate by increasing the differential pressure, closing of the aperture occurred subsequently. In subsequent tests, using a constant flow pump, plugging was not observed, even though the sample was not sterilized. Although plugging is not observed under constant-flow regime, bacterial growth is almost certainly occurring. Apparently, the bacteria are continuously eluted from the fracture without building up enough to close it. Bacterial growth in the subsurface could significantly impact

the path that fluids will take in the fractured flow-path components of the EBS/NFE.

7.4.3.2 Summary of flow test results. To obtain consistent hydraulic data, the constant flow pump was used for subsequent tests. A series of flow tests were performed for a single core sample at three temperatures (23, 59, and 92°C) and two flow rates (0.2 and 2.0 mL/h). Bromide and iodide were used as tracers. The average permeability at 23°C was on the order of 0.06 millidarcy (md) and was independent of the flow rate and average pore pressure (Table 7-2). This value is approximately one third to one fifth that of the lowest permeabilities previously observed for the same core sample (Viani and Martin, 1994a), and for a different sample having the same fracture aperture (Viani and Martin, 1993). This could reflect the growth of a bacterial population in the fracture channel as noted above, or may reflect small differences in effective fracture aperture.

The observed permeability is more than 2 orders of magnitude smaller than would be predicted (de Marsily, 1986) for a 25- μm aperture with smooth walls (33 md). If one assumes all the flow is via the fracture, the effective aperture width is calculated to be 3.1 μm . It is possible that some reduction in the gold shim thickness may have occurred upon loading. Deformation of the core sample itself under confining pressure may also contribute to the low permeabilities observed; however, based on an analysis of the effect of confining pressure on permeability (Fig. 7-5), it appears unlikely that this could explain the observation. At 59°C, the average permeability is slightly larger (~0.1 md) and also appeared to be independent of the flow rate and average pore pressure.

At 92°C, the average permeability varied between 0.08 and 2.34 md and was independent of the flow rate but dependent on average pore pressure. For flow tests in which the average pore pressure was less than 0.1 bar (5 runs) the average permeability was ~0.2 md. For runs in which the average pore pressure was greater than 0.5 bar (7 runs) the average permeability was ~1.9 md (Table 7-2).

It is clear that pore pressure has a significant effect on the permeability at 92°C. This effect is non-linear; i.e., increasing pore-pressure above the ~0.5 bar threshold does not result in a continued increase in permeability. However, the phenomenon does appear to be reasonably reversible, because sequential runs taken at pore pressures below and above 0.5 bar yielded similar results to the previous runs at equivalent pore pressures. If the phenomenon were related to changes in aperture width, a reversible change of ~5 μm would be required. One possibility is that exsolution of dissolved air from the feed solution (between 23 and 92°C, a liter of

H₂O would exsolve about 5 cm³ of gas at 92°C and 1 bar) may partially block the aperture. This blockage would lessen at higher pore pressures. However, the exsolution would also be expected to have affected the runs at 59°C as well, and this was not observed.

Permeability also varied with confining pressure. The variation in instantaneous permeability with confining pressure can be explained by a change in the fracture aperture that depends on confining pressure. In the example shown (Fig. 7-5), the effective aperture width need only change by ~0.06 μm to cause the change in permeability observed. This response is reversible. Similar observations were made by Roberts and Lin (1995) and Mohanty et al. (1995) for fractured welded tuffs.

7.4.3.3 Tracer experiments. A dilute Na-Cl-HCO₃ solution containing Br⁻ or I⁻ tracer was eluted through the core under constant flow conditions. Following a period of flow of the standard feed solution (dilute NaCl, NaHCO₃, pH ~7.5), a 560 μL pulse of either NaBr or NaI tracer solution (0.75 mM) was injected upstream from the core. The average recovery of tracer downstream from the core was 95 and 102% for Br⁻ and I⁻, respectively. These recoveries are within experimental error of 100%; under these conditions both Br⁻ and I⁻ are considered to be conservative tracers.

Figure 7-6 shows an example of I⁻ tracer breakthrough curves for replicated run conditions. The generally excellent reproducibility in the tracer breakthrough curves suggest complete flushing of the tracer between runs and no measurable changes to the hydrologic or chemical state of the sample. These results also indicate that pore-pressure, confining pressure, and flow rate effects are essentially reversible.

7.4.3.3.1 Effect of flow rate, pore pressure, and temperature on breakthrough of tracer. Figure 7-7 shows the effect of flow rate on elution of conservative tracer. The tracer elutes slightly sooner (in terms of volume eluted) and exhibits less tailing at a lower flow rate. This effect appears to be independent of pore pressure. Early breakthrough may reflect a relatively greater impact of longitudinal dispersion at the lower flow rate. The reduced tailing region for the breakthrough curve for the lower flow rate suggests that a given volume of post-pulse solution is more effective in "sweeping out" tracer that has diffused into the matrix during passage of the tracer pulse through the fracture. At the slower flow rate, the rate of mass transfer of tracer from matrix to fracture via diffusion relative to advection of tracer through the fracture is greater than at the higher flow rate. For the flow rates and tracer pulse

volumes utilized, it is probable that diffusion into the matrix occurs primarily via the fast paths described in section 7.4.1.

Figure 7-8 shows the effect of pore pressure on the breakthrough of the tracer. This figure shows that the initial breakthrough is retarded, and the tailing region of the pulse is extended relative to the case where pore pressure is low. This suggests that pore pressure controls the fracture/matrix connectivity possibly by controlling the width of micro-fractures that may emanate from the main fracture pathway. At higher pore pressure the number and/or width of micro-fractures intersecting the saw-cut fracture may increase. This would increase the mass transfer of tracer into the matrix during passage of the pulse, and the volume of matrix containing tracer that must be flushed following the pulse.

Figure 7-9 shows the role that temperature plays in controlling the initial breakthrough and the extent of tailing in the tracer pulse. The volumetric elution of the tracer occurs earlier, and the tailing is less pronounced the greater the temperature of the experiment. This may reflect an increase in the diffusion coefficient of the tracer. Physical retardation expected to result from the diffusion of radionuclides into the matrix may be reduced with increasing temperature.

7.4.3.3.2 Composition of effluent. Table 7-3 shows chemical analyses for selected elements in the feed solution and after the breakthrough of the tracer. The major observation is the positive correlation of dissolved Si and negative correlation of Ca and Mg with temperature, and the negative correlation of Si, Ca, and Mg with flow rate at 92°C. The silica concentrations observed in the 0.2 mL/h runs at both 23 and 92°C indicate slight supersaturation with respect to equilibrium with quartz but significant undersaturation with respect to cristobalite. If the length of the core were longer, or the flow rate slower, it would be expected that the concentration of silica in the effluent would approach saturation with cristobalite.

The effects of confining pressure, pore pressure, flow rate, and temperature on permeability and transport of a conservative tracer through a saw-cut sample of Topopah Spring tuff have been measured and are likely to affect the degree of retardation of radionuclides in fractured materials in the near-field environment. Increasing pore pressure tends to increase the retardation due to matrix diffusion; increasing temperature has the opposite effect.

These findings strengthen the argument that transport experiments for fractured samples must be undertaken using flow-test apparatuses that allow the variation of confining and pore pressures, because not only is the permeability of the sample affected, but the so is the nature of the breakthrough curve. Experiments that have

previously been conducted with core samples that were epoxied in place do not provide data to test phenomena which would be expected to play a role in the transport of radionuclides through fractured media at Yucca Mountain. Hence, relationships between physical variables such as pore pressure and confining pressure, and chemical phenomena such as radionuclide transport, will not be adequately accounted for in transport and performance assessment models unless transport experiments are undertaken using the type of apparatus used in this study. The study of biological impact on flow and transport will require experimental apparatuses that will be able to mimic the flow regime expected in the EBS/NFE; otherwise, important phenomena may be missed.

7.5 Field Testing Sorption Models Under Conditions of Fracture Dominated Flow

Modeling the chemical processes likely to impact the transport of radionuclides through the EBS/NFE will require coupled flow and chemical reaction models capable of predicting the effects that dissolution/precipitation, adsorption/desorption, and aqueous speciation have on radionuclide transport. In the EBS/NFE, transport will be strongly influenced by adsorptive retardation in flow-path components (e.g., waste package corrosion products, concrete, altered TSw2). Previous application of surface chemical models to laboratory experiments and field observations (Viani and Bruton, 1992a,b) resulted in model refinement and a better understanding of the limits of model applicability. However, there are limits to the application of laboratory experiments to confidence building and testing modeling approaches. Field testing can play an important role in this confidence building process.

The underground hard rock laboratory in Äspö, Sweden (HRL) afforded a unique opportunity in a well-constrained field test to assess the ability and utility of cation exchange and surface complexation models to explain the evolution of fluid composition over time in a fractured aquifer (Bruton, 1996; Viani and Bruton, 1996a,b). The matrix rock at the HRL is predominantly granite. Although its chemical and hydraulic properties would be expected to differ from the matrix rocks at Yucca Mountain, the processes accounting for mass transfer between fracture and matrix, sorption and diffusion, are identical to those expected to retard radionuclide movement at Yucca Mountain.

Construction of the HRL laboratory initiated relatively rapid downward flow of dilute shallow groundwater through fractures that were intersected by the

underground excavation. The groundwater in one of the intersected fracture zones (Redox Zone) was sampled just prior to the intersection of the underground tunnel with it (@70 m) and regularly thereafter for a period of several years. The shallow groundwater was also sampled before and following the initiation of flow at a depth (<15 m) just below where the fracture zone is expressed at the ground surface. Fractures in the dominantly granitic rocks are lined with a variety of sorbing minerals, including illite/smectite, chlorite, sericite, and iron oxides (Tullborg, 1995b).

The groundwater at tunnel depth is considerably more saline than the shallow groundwater (ionic strength 0.006 vs. 0.18 m). Hence, the induced flow of groundwater into the tunnel is also accompanied by mixing of the two water types. Cation exchange has been hypothesized to play a role in controlling the observed variation in fluid chemistry (Banwart et al., 1994). A comparison of simulated mixing of groundwater using geochemical modeling codes with the observed evolution of groundwater at Äspö suggests that the groundwater mixing is accompanied by mass transfer between fluid and fracture minerals via cation exchange and surface complexation reactions.

7.5.1 Cation Exchange

7.5.1.1 Modeling approach. The geochemical modeling package EQ3/6 (Wolery et al., 1990; version 3245R116), to which a cation-exchange model was added (Viani and Bruton, 1992a,b), was used with an associated thermodynamic data base (version DATA0R19) to simulate the mixing between the shallow (HBH02) and native (tunnel depth; KA0483A) fluids. A cation-exchange model employing the Vanselow convention (Sposito, 1981) was used for the simulations. Details of the implementation of this option in EQ3/6 and examples of its application may be found in Viani and Bruton (1992a,b). Fluid chemistries predicted to result from mixing were compared with those monitored from boreholes intersecting the fracture zone.

The conceptual model of fluid mixing imposed by EQ3/6 is a simplified approximation of the actual process that is occurring at Äspö. Inherent to this simplification is the assumption that the shallow groundwater undergoes no compositional change (i.e., no reaction with its surroundings) prior to mixing with the native groundwater, and that mixing occurs only in the presence of a cation exchanger that is initially in equilibrium with the native groundwater.

not the same as that predicted by the cation exchange model (Fig. 7-10). A number of causes might contribute to this discrepancy:

1. The actual mixing of fluids in the fracture system is not adequately simulated by the simple mixing algorithm embodied in EQ3/6. Because of the potentially large ratio of cations on the exchanger to those in the fluid, differences between the simulated mixing process and the actual mixing process would probably have the greatest effect on the most dilute mixed fluids.
2. More than two "endmember" fluids may be involved in the mixing and cation exchange process (Laaksoharju et al, 1995).
3. The chosen cation-exchange model, exchange energies, or assumption of exchange equilibrium may not be correct. Of these potential shortcomings, only exchange disequilibrium would likely result in significantly different predictions. As observed for exchange equilibrium in clinoptilolite (section 7.4.2), exchange disequilibrium would likely occur only if exchange were limited by inter and intracrystalline diffusion of exchange cations in the fracture-lining exchangers. The diffusion rate in undisturbed fracture fill at the HRL has not been measured.

7.5.1.4 Predicting the level of exchangeable Cs. The ability to model the partitioning of trace elements such as Cs and Sr is a major rationale for using cation-exchange models. Previous work has shown that cation-exchange models can relatively accurately predict the partitioning of Sr and Cs to zeolitized tuff from Yucca Mountain (Viani and Bruton, 1992a, 1992b).

Data available from the HRL allowed a comparison of observed vs. predicted partitioning of Cs in a field situation. Samples of fracture filling minerals collected at the intersection of the HRL tunnel with the fracture zone were analyzed for Cs and other trace elements using sequential extraction techniques to determine the proportion associated with the exchange sites on the minerals (Landström and Tullborg, 1995). The concentration of exchangeable Cs in the fracture fill for Redox Zone fracture was ~0.6 ppm. Assuming that all of the exchangeable Cs is associated with the illite and/or sericite components of the fracture filling, and assuming their abundance to be 5%, the predicted concentration of exchangeable Cs in the fracture fill based on the measured concentration of Cs in the groundwaters collected at those fractures varied between 0.9 and 1.2 ppm (Viani and Bruton, 1996). The predicted values are in reasonable agreement with the measured values which gives further confidence in the model.

Geochemical modeling simulations of the role of cation exchange in fluid mixing and in trace metal partitioning suggest that this phenomenon plays an important role in the short-term chemical dynamics that are occurring in the Redox Zone fracture system. We conclude:

1. Because of the similarity of the exchange properties of smectite and those of the planar site in illite, the major cation occupancies (Na, Ca, and Mg) predicted for the illite exchanger are very similar to those predicted for a smectite exchanger.
2. Cation exchange is a plausible mechanism to explain apparent sources and/or sinks for Ca, Sr, and Na during mixing of dilute shallow groundwater and native groundwater in the Redox Zone.
3. Cation-exchange simulation of the partitioning of Cs and Rb onto illite predicts that almost all of the "mobile" pool of these elements is associated with the exchanger. The predicted level of exchangeable Cs and that measured by sequential extraction of fracture gouge are in reasonable agreement.
4. The quantity of exchanger (~0.1 equiv/L of groundwater) necessary for the simulation to match the observed fluid data is physically reasonable, and is consistent with the observed fracture mineralogy. This estimate agrees with estimates by Banwart et al. (1995b) that are based on modeling and on fracture fill material properties.

7.5.2 Surface Complexation

As shown above, the observed variability of fluid chemistry at the Äspö Hard Rock Laboratory is not fully described by conservative fluid mixing models. Ion exchange may account for some of the observed discrepancies. It is also possible that variably charged solids such as oxyhydroxides of Fe can serve as sources and sinks of anions and cations through surface complexation.

The most successful models describing adsorption onto iron and other oxides are surface complexation models (Dzombak and Morel, 1990). Surface complexation reactions on hydrous ferric oxides involve sorption of both cations and anions. Because U, Np, and other metals are strongly sorbed by iron oxides (Table 7-1), it is important to gain confidence in applying these models to predict the retardation of these radionuclides through the various oxides expected in the EBS/NFE (sec. 7.3.2).

Geochemical modeling of the surface chemistry of hydrous ferric oxides (HFOs) in equilibrium with shallow (HBH02) and native (KA0483A) HRL Redox Zone

waters shows that HFOs can serve as significant, pH-sensitive sources and sinks for cations and anions (Bruton and Viani, 1996).

A variety of cations (e.g. H^+ , Ca^{++} , Sr^{++} , Ba^{++}) and anions (HCO_3^- , SO_4^{--} , HPO_4^-) are known to sorb onto hydrous ferric oxides at 25°C (Dzombak and Morel, 1990). Hematite and Fe-oxyhydroxide are commonly found as fracture fillings at Äspö (e.g., Tullborg, 1995b). Banwart et al. (1994) estimated that the abundance of hematite in altered granite is 1–2%, and that the abundance of Fe(III)-oxyhydroxides in the fracture coatings is 4%. Microfractures close to the fracture surface contain what appears to be iron oxyhydroxide.

The approach used to simulate the effect of sorption onto iron oxides via surface complexation is similar to that taken by Viani and Bruton (1994, 1996) to test the hypothesis that ion exchange affects the composition of groundwaters sampled from boreholes in the HRL tunnel. Geochemical modeling computer codes containing surface complexation models capable of simulating sorption onto HFOs were used to:

1. Calculate the potential for HFOs to serve as reservoirs and sinks of ions. The dependencies of ion sorption on pH in shallow and deep waters from the Redox Zone at Äspö were calculated to evaluate the potential for changes in major element chemistry during fluid mixing owing to the sorptive behavior of HFOs.
2. Simulate mixing between the shallow and deep waters that are believed to contribute to the observed changes in fluid chemistry with time in the Large Scale Redox Experiment.

Surface complexation refers to chemical reactions between reactive functional groups exposed on a solid surface and aqueous species in an adjacent fluid. Surface complexation reactions lead to the sorption and desorption of anions and cations. The reactive functional groups at the solid surface (often referred to as "sites") derive from unsatisfied bonds created by the discontinuity of a three-dimensional structure.

The reactive sites on the surfaces of oxide minerals may be negative, neutral or positive depending on the extent of their protonation. Hence, the net charge on the surface may be positive or negative, depending on the pH of the solution. Because the charge of reactive sites in oxides is controlled by pH, surface complexation reactions are much more sensitive to pH than ion exchange; the extent of ion sorption can change drastically within a few pH units.

The surface complexation reactions comprising the sorption model are provided for in the *React* geochemical modeling code. *React* is a part of The Geochemist's Workbench™ (Bethke, 1994) set of software tools for calculating fluid-mineral-gas equilibria. *React* combines the calculational abilities of EQ3 and EQ6. EQ3/6, used by Viani and Bruton (1994, 1996) to describe ion exchange, could not be used as it does not provide for surface complexation reactions.

React can simultaneously provide for aqueous speciation in the fluid phase, mineral dissolution and precipitation, and surface complexation onto a sorbent, such as HFO. However, mineral dissolution and precipitation reactions were not considered in the calculations described here.

React employs the generalized two-layer surface complexation model of Dzombak and Morel (1990). The generalized two-layer model is an extension of the diffuse double layer model, with provision for two types of sorption sites (weak and strong) and surface precipitation (see Dzombak and Morel, 1990 for an extensive discussion of the models).

React contains a data base of surface complexation constants from Dzombak and Morel (1990) assuming a generalized two-layer surface complexation model. Although the most comprehensive compilation of constants to date, Dzombak and Morel's data set lacks complexation constants for carbonate species.

At low pH values, anions such as sulfate and carbonate tend to be sorbed by HFOs. Preliminary calculations with Dzombak and Morel's data set suggested that sulfate surface complexes dominate the total mass of sulfate in the fluid+sorbent system. However, the Dzombak and Morel (1990) data set does not provide for competition between sulfate and carbonate for sorption sites. Therefore, a literature search was made to identify experimental studies yielding carbonate complexation constants that could be added to the Dzombak and Morel (1990) data set.

Waite et al. (1994) determined carbonate complexation constants as part of a larger study to measure U(VI) sorption onto HFOs. They used a two-site diffuse double layer model. Van Geen, Robertson, and Leckie (1994) focused on complexation of carbonate species at the goethite surface and used a single-site diffuse double layer model to extract complexation constants from their sorption experiments.

The complexation constants from both papers were incorporated into two new versions of the *React* complexation constant data base from Dzombak and Morel (1990). Simulations were carried out with each of the three data bases (a) Dzombak and Morel (1990), (b) Dzombak and Morel plus carbonate complexation data from

Waite et al. (1994), and (c) Dzombak and Morel plus carbonate complexation data from Van Geen, Robertson, and Leckie (1994) for comparison.

Scoping calculations using all three data bases suggested that the data of Van Geen, Robertson, and Leckie (1994) predicted significantly greater amounts of carbonate sorption than data from Waite et al. (1994). Because Van Geen, Robertson, and Leckie's (1994) study focused more closely on carbonate sorption than Waite et al. (1994), data bases from (a) Dzombak and Morel (1990) and (b) Dzombak and Morel plus carbonate complexation data from Van Geen, Robertson, and Leckie were used to explore the impact of sorption on fluid chemistry.

For these calculations, goethite was used as a proxy for a variety of iron oxyhydroxides such as ferrihydrite and hematite that can act as sorbents. Goethite was assumed to contain 0.205 moles of sorption sites (0.2 weak, 0.005 strong) per mole of Fe (Dzombak and Morel, 1990). Iron oxyhydroxides can vary significantly in terms of their surface area and corresponding total number of surface sites per mole of Fe. However, by relating our calculations to the number of surface sites available for reaction, we obtain a common frame of reference for all forms of HFOs. The mass of goethite per kilogram of H₂O was varied from 0.1 to 10 g/kg H₂O to illustrate the effects of variations in sorbent:fluid ratio. The relations between mass of goethite, number of surface sites, and fluid mass are discussed below.

The result of surface complexation reactions of goethite in the shallow and native groundwaters are shown in Fig. 7-13 and Fig. 7-14 as a function of pH. One gram of goethite, serving as a proxy for Fe-oxyhydroxides, was assumed to be in equilibrium with 1 kg of H₂O having the composition of the shallow or native groundwater. Sorbed fraction in Fig. 7-13 and Fig. 7-14 refers to the fraction of a given element that resides on HFO surfaces relative to the total amount of that element in the fluid+sorbent system. It is calculated as the sum of the concentrations of sorbed species containing a given element, divided by the sum of the amount of the element in solution and the amount of the element sorbed. For example, a sorbed fraction of 0.5 implies that if there are 100 mg/kg SO₄ in solution, 100 mg/kg SO₄ are bound to the HFO surface as surface complexes.

The sorbed fraction is a useful measure of the effectiveness of a sorbent as a reservoir of ions. When the sorbed fraction exceeds 0.5, the mass of the sorbed element is greater than that in the fluid. A change in solution composition, such as pH, could release those ions and significantly increase the ion concentration in the fluid.

Carbonate surface complexes comprise a significant fraction of total carbonate in the fluid+sorbent system. For example, Table 7-6 shows that over 10 times as much carbonate (1121 mg/kg expressed as bicarbonate) is sorbed onto HFO surfaces as is contained in the fluid (114 mg/kg) given a sorbent:fluid ration of 10 g of goethite per kilogram of H₂O. Thus, the calculations suggest that HFOs at shallow depths may serve as important reservoirs or sources of carbonate if conditions, such as an increase in pH, favor desorption of carbonate.

Competition for surface sites can be appreciated by considering the results of simulations for which carbonate surface complexes are excluded (not shown). Under these conditions, the percent sulfate predicted to be adsorbed is 5 to 50 times greater for the shallow groundwater and 3 to 4 times greater for the native groundwater. It is apparent that carbonate species are sorbed to a much greater extent than sulfate.

To relate the calculations described in this report to attributes of natural systems, we must establish the relevance of the masses of goethite used per kg H₂O. For a given fracture width, we calculated the thickness of a continuous goethite fracture coating yielding 1 and 10 grams of goethite per kg H₂O (Fig. 7-15), assuming a fully saturated system. Goethite, hematite, and iron oxide stains are common in the fracture fill at Äspö, with estimated abundances as great as several percent by weight of the fracture fill (Banwart et al., 1994, 1995; Tullborg, 1995a,b). For a fracture fill with a fractional porosity of 0.1, a rock density of 2800 kg/L, and 0.1% by weight of iron oxide, approximately 25 g of iron oxide would be associated with each kg of pore water. Thus, considering the petrographic observations of the abundance and distribution of HFOs observed at Äspö, the quantities of goethite per kg of H₂O used in the calculations are reasonable and conservative. Based on 0.205 mol of sites/mol Fe (Dzombak and Morel, 1990), there are 2.31×10^{-3} moles of surface sites per gram of goethite. Even though goethite does not form continuous surface layers in nature, the calculation nonetheless demonstrates that the masses of goethite considered in this report are conservative, yet can account for a great deal of surface complexation.

The results of geochemical simulations such as those described here are only as reliable as the surface complexation constants and the complexation model upon which the predictions are based. For example, if the carbonate complexation constants from Van Geen, Robertson and Leckie (1994) overestimate the degree of formation of surface carbonate complexes, the degree of SO₄ sorption would increase.

pressure, and confining pressure; hence thermo-mechanical effects of repository construction and waste emplacement may significantly alter the transport properties of the existing fracture network.

In addition to chemical effects of introduced materials, the presence of significant biological activity could significantly affect flow paths by plugging fractures.

Natural groundwater colloids are ubiquitous, but may not be present in large enough quantities to significantly affect radionuclide transport. Introduced materials, such as container corrosion products, backfill, and cements will add to the colloid population that is available for transporting radionuclides.

Surface chemical models that describe sorption via cation exchange and surface complexation approaches have been used to simulate mixing of groundwater mixing in a fractured aquifer and found to be consistent with observation. This enhances our confidence that these models/approaches will have applicability to Yucca Mountain and can be applied once material and design issues are resolved.

7.7 Summary of Gaps in Information Required to Bound Radionuclide Transport in the EBS/NFE

Very little experimental data exists for radionuclide transport through EBS/NFE materials at the temperatures and fluxes expected in the repository. Hence, modeling efforts to derive the flux of radionuclides through the EBS/NFE will not be constrained by data. In addition to basic thermodynamic data regarding solubility and speciation of radionuclides at elevated temperature in the chemical environments expected in the EBS/NFE, bounding the flux of radionuclides through the EBS/NFE will also require:

1. Sorptive/chemical properties of the altered internal components of the waste package.
2. Sorptive properties of waste package corrosion products. Experimental measures of transport of critical soluble and/or colloidal radionuclides through waste package corrosion products at elevated temperatures.
3. Mineralogy and physical status of altered cementitious materials.
Characterization of the mode of interaction of actinides with altered cementitious materials. Experimental measures of transport of critical soluble and/or colloidal radionuclides through altered cementitious materials.
Characterization of colloids derived from altered cementitious materials.

7.8 References

- Albinsson, Y., Andersson, K., Borjesson, S., Allard, B. 1993. *Diffusion of radionuclides in concrete/bentonite systems*. Swedish Nuclear Fuel and Waste Management Co. Technical Report 93-29. Stockholm, Sweden.
- Atkins, M., Beckley, A.N., and Glasser, F.P. 1988. Influence of cement on the near field environment and its specific interactions with uranium and iodine. *Radiochimica Acta* 44/45:255-261.
- Atkinson, A., Everitt, N.M., and R.M. Guppy. 1989. Time dependence of pH in a cementitious repository. *Mat. Res. Soc. Proc. Vol. 127:813-821*. *Mat. Res. Soc. Proc. Vol. 127:439-446*.
- Banwart, S., Gustafsson, E., Laaksoharju, M., Nilsson, A-C., Tullborg, E-L. and Wallin, B., 1994. Large-scale intrusion of shallow water into a vertical fracture zone in crystalline bedrock: Initial hydrochemical perturbation during tunnel construction at the Äspö Hard Rock Laboratory, southeastern Sweden. *Water Resources Res.*, v. 30, p. 1747-1763.
- Banwart, S., Laaksoharju, M., Pitkänen, P., Snellman, M., and Wallin, B. 1995. Development of a site model for reactive element dynamics. pp. 188-218. In Banwart, S. (ed.) *The Redox Experiment in Block Scale: Final Reporting of Results from the Three Year Project*. SKB Äspö Hard Rock Laboratory Progress Report 25-95-06, Stockholm.
- Bates, J.K., Brown, N.R., Buck, E.C., Dietz, N.L., DiSanto, T., Ebert, W.L., Ellison, A.J.G., Emery, J.W., Fortner, J.A., Hafenrichter, L.D., Hoh, J.C., Mazer, J.J., Surchik, M.T., Wolf, S.F., and Wronkiewicz, D.J. 1995b. *ANL Technical Support Program for DOE Environmental Restoration and Waste Management*. ANL-95/20. Argonne National Laboratory, Argonne, IL.
- Bates, J.K., Fortner, J.A., Finn, P.A., Wronkiewicz, D.J., Hoh, J.C., Emery, J.W., Buck, E.C., and Wolf, S.F. 1995a. *Yucca Mountain Project - Argonne National Laboratory Report, FY 1994*. ANL-94/42. Argonne National Laboratory, Argonne, IL.
- Bethke, C.M. 1994. *A Users Guide to Rxn, Act2, Tact, React, and Gtplot*. Copyright Craig M. Bethke, University of Illinois, Champaign, IL.
- Breck, DW. 1984. *Zeolite Molecular Sieves*. R.E. Krieger Pub., Malabar, FL, pgs. 559 and 574-575. (NNA.19890522.0211)
- Brouwer, E., Baeyens, B., Maes, A., and Cremers, A. 1983. Cesium and rubidium ion equilibria in illite clay. *J. Phys. Chem.* 87: 1213
- Bruggenwert, M.G.M., and Kamphorst, A. 1982. Survey of experimental information on cation exchange in soil systems. pp. 141-203. In Bolt, G.H. (ed.) *Soil Chemistry B. Physico-Chemical Models*. Elsevier, Amsterdam.
- Bruton, C.J., and Viani, B.E. 1996. *Ion Sorption onto Hydrous Ferric Oxides: Effect on Major Element Fluid Chemistry at Aspo, Sweden*. Lawrence Livermore National Laboratory report UCRL-JC-124329. Livermore, CA.
- Bruton, C.J., Meike, A., Viani, B.V., Martin, S., and Phillips, B.L. 1993. Thermodynamic and structural characteristics of cement minerals at elevated temperature. *Proc. Topical Meeting on Site Characterization and Model*

- Validation, FOCUS '93, Las Vegas, NV, pg. 150-156, American Nuclear Soc., La Grange Park, IL. (MOL. 19940913.0047)*
- Buchholtz-ten Brink, M., Martin, S.I., Viani, B.E., Gerlach, D.C., and Rego, J.H. 1990. Characterization and transport of colloidal particles in groundwaters from the Nevada Test Site. *AGU 1990 Fall Mtng., Abstr., EOS, Trans., Vol. 71, p. 1306.*
- Buchholtz-ten Brink, M., Martin, S.I., Viani, B.E., Smith, D.K., and Phinney, D. 1992. Heterogeneities in radionuclide transport: Pore-size, particle-size, and sorption. *in McCarthy, J.F. (ed.), Concepts in Manipulating Groundwater Colloids for Environmental Restoration.* Lewis publishers, Chelsea, MI. (NNA.19910523.0101)
- Carlos, B.A. 1985. *Minerals in Fractures of the Unsaturated Zone from Drill Core USW G-4, Yucca Mountain, Nye County, Nevada.* Los Alamos National Laboratory report LA-10415-MS. (NNA.19920506.0037)
- Conca, J.L. 1990. Diffusion barrier transport properties of unsaturated Paintbrush tuff rubble backfill. *Proc. First International Meeting High Level Radioactive Waste Management, Las Vegas, NV, Vol 1, pg. 394-401, American Nuclear Soc., La Grange Park, IL. (NNA.19900710.0198).*
- Cornell, R.M. 1993. Adsorption of cesium on minerals: A review. *J. Radioanalytical Nucl. Chem., Articles. 171:483-500.*
- CRWMS M&O. 1996. *Strategy for Focused Evaluation of Waste Containment and Isolation at the Yucca Mountain Site.* Civilian Radioactive Waste Management System Management and Operation Contractor, Las Vegas, NV.
- De Marsily, G. 1986. *Quantitative Hydrogeology.* p. 55 Academic Press, Inc. New York.
- Dzombak, D.A., and Morel, F.M. 1990. *Surface Complexation Modeling: Hydrous Ferric Oxide.* Wiley, New York.
- Fletcher, P. and Sposito, G. 1989. The chemical modeling of clay-electrolyte interactions for montmorillonite. *Clay Minerals, v. 24, p. 375-391.*
- Gast, R.G. 1972. Alkali metal cation exchange on Chambers montmorillonite. *Soil Sci. Soc. Amer. Proc. 36:14.*
- GIT (YMP Geochemistry Integration Team) 1993. Claude Degueldre measured the particulates in a sample of J13 collected by W. Steinkampf (USGS) and found 1.7×10^7 particles/mL. Minutes of the October 18, 1993 Geochemistry Integration Team Teleconference.
- Ho, C.H., and Miller, N.H. 1986. Adsorption of uranyl species from bicarbonate solution onto hematite particles. *J. Coll. Inter. Sci. 110:165-171.*
- Klavetter, E.A. and Peters, R.R. 1986. *Estimation of Hydrologic Properties of an Unsaturated, Fractured Rock Mass.* Report SAND-84-2642, Sandia National Laboratory, Albuquerque, NM. (NNA.19870317.0738)
- Laaksoharju, M., Banwart, S., Skarman, C., Gustafsson, E., Pitkänen, P., and Snellman, M. 1995. Hydrochemistry overview. pp. 17-46. *In Banwart, S. (ed.) The Redox Experiment in Block Scale: Final Reporting of Results from the Three Year Project.* SKB Äspö Hard Rock Laboratory Progress Report 25-95-06, Stockholm.
- Landström, O., and Tullborg, E-L. 1995. *Interactions of Trace Elements with Fracture Filling Minerals from the Äspö Hard Rock Laboratory.* SKB Technical Report 95-13, Swedish Nuclear Fuel and Waste Management Co., Stockholm, Sweden.

- Lanford, W.A., Davis, K., Lamarche, P., Laursen, T., Groleau, R., and Doremus, R.H. 1979. Hydration of soda-lime glass. *J. Non-Crystalline Solids* 33:249-266. (NNA.19900306.0089)
- Martin, S.I., Buchholtz-ten Brink, M., and Viani, B.E. 1991. Characterization of colloids in groundwaters using transmission electron microscopy. AGU 1991 Fall Mtng., Abstr., *EOS, Trans.*, Vol. 72, Supplement, p. 154.
- McCarthy, J.F., and Degueldre, C. 1993. Sampling and characterization of colloids and particles in ground water for studying their role in contaminant transport. in van Leeuwen, H.P. and Buffle, J. (eds.), *Environmental Particles*, IUPAC Environmental Analytical and Physical Chemistry Series, Vol. II, Lewis Publishers, Chelsea, MI. (NNA.19930607.0075)
- McKeegan, K.D., Phinney, D., Oversby, V.M., Buchholtz ten Brink, M., and Smith, D.K. 1989. Uranium transport in Topopah Spring tuff: An ion-microscope investigation. *Mat. Res. Soc. Proc.* Vol. 127:813-821. (NNA.19900620.0330)
- Meijer, A. 1990. A strategy for the derivation and use of sorption coefficients in performance assessment calculations for the Yucca Mountain site. Pg 9-40. *Proceeding of the DOE/Yucca Mountain Site Characterization Project Radionuclide Adsorption Workshop at Los Alamos Laboratory.* LA-12325-C. (NNA.19930629.0011)
- Mohanty, S., Manteufel, R.D., Chowdhury, A.H., and Philip J. 1995. Fracture permeability under effect of normal and shear stress: A preliminary experimental investigation. *Proc. Sixth International Meeting High Level Radioactive Waste Management*, Las Vegas, NV, pg. 41-43, American Nuclear Soc., La Grange Park, IL.
- Ogard, A. 1987. Importance of radionuclide transport by particulates entrained in flowing groundwaters in *Groundwater Chemistry at Yucca Mountain, Nevada, and Vicinity*. Los Alamos National Laboratory Report LA-10929-MS. Los Alamos, NM. (NNA.19870507.0017)
- Phinney, D.L., Ryerson, F.J., Oversby, V.M., Lanford, W.A., Aines, R.D., and Bates, J.K. 1987. Integrated testing of the SRL-165 glass waste form. *Mat. Res. Soc. Proc.* Vol. 84:433-446. (NNA.19891120.0003)
- Puls, R.W., Clark, D.A., Bledsoe, B., and Powell, R.M. 1992. Metals in ground water - Sampling artifacts and reproducibility. *Hazardous Waste & Hazardous Materials.* 9:149-162.
- Ramsay, J.D.F., Avery, R.G., and Russell, P.J. 1988. Physical characteristics and sorption behaviour of colloids generated from cementitious systems. *Radiochimica Acta* 44/45:119-124. (NNA.19931005.0015)
- Roberts, J.J., and Lin, W. 1995. Permeability of fractured tuff as functions of temperature and confining pressure. *Proc. Sixth International Meeting High Level Radioactive Waste Management*, Las Vegas, NV, pg. 44-45, American Nuclear Soc., La Grange Park, IL. (MOL19950501.0025)
- Roberts, S., Viani, B.E., and Phinney, D. 1995. *Radionuclide Diffusion in Clinoptilolite*. Yucca Mountain Project Milestone M0L133.(M0L.19951213.0093)
- Rundberg, R.S. 1987. *Assessment Report on the Kinetics of Radionuclide Adsorption on Yucca Mountain Tuff*. Los Alamos National Laboratory Report LA-11026-MS, Los Alamos, NM (NNA.19930405.0075)

- Sposito, G. 1981. *Thermodynamics of Soil Solutions*. Oxford University Press, New York, NY. (NNA.19900416.0124)
- Steeffel, C.I., and Lichtner, P.C. 1994. Diffusion and reaction in rock matrix bordering a hyperalkaline fluid-filled fracture. *Geochim. Cosmochim. Acta* 58:3595-3612.
- Thomas, K.W. 1987. *Summary of Sorption Measurements Performed with Yucca Mountain, Nevada Tuff Samples and Water from Well J-13*. Report LA-10960-MS. Los Alamos National Laboratory, Los Alamos, NM. (NNA.19890602.0026)
- Ticknor, K.V. 1994. Uranium sorption on geological materials. *Radiochimica Acta* 64:229-236. (MOL.19950117.0119)
- Todorovic, M., Milonjic, S.K., Comor, J.J., and Gal, I.J. 1992. Adsorption of radioactive ions $^{137}\text{Cs}^+$, $^{85}\text{Sr}^{2+}$, and $^{60}\text{Co}^{2+}$ on natural magnetite and hematite. *Sep. Sci. Tech.* 27:671-679.
- Triay, I., Simmons, A., Levy, S., Nelson, S., Nuttall, H., Robinson, B., Steinkampf, W., and Viani, B. 1993a. *Colloid-facilitated radionuclide transport at Yucca Mountain*. Los Alamos Report LA-12779-MS. Los Alamos, NM. (NNA.19930628.0067)
- Triay, I.R., Robinson, B.A., Mitchell, A.J., Overly, C.M., and Lopez, R.M. 1993b. Transport of neptunium through Yucca Mountain tuffs. *Mat. Res. Soc. Symp. Proc.* 294:797-802. (NNA.19930924.0106)
- Tullborg, E-L. 1995a. Mineralogical/geochemical investigations in the fracture zone. pp. 81-101. In Banwart S. (ed) *The Redox Experiment in Block Scale: Final Reporting of Results from the Three Year Project*. SKB Äspö Hard Rock Laboratory Progress Report 25-95-06, Stockholm.
- Tullborg, E-L. 1995b. *Mineralogical and Chemical Data on Rocks and Fracture Minerals from Äspö*. Äspö Hard Rock Laboratory Technical Note 25-95-07g, Stockholm.
- Van Geen, A., Robertson, A.P. and Leckie, J.O., 1994. Complexation of carbonate species at the goethite surface: Implications for adsorption of metal ions in natural waters. *Geochim. et Cosmochim. Acta*, v. 58, p. 2073-2086. (NNA.19940210.0041)
- Viani, B.E. 1995a. *Scientific Investigation Plan for YMP WBS Element 1.2.3.10.3.1 Integrated Radionuclide Release: Tests and Model Development (Integrated Testing)*. SIP-IT-01. Rev. 0. Lawrence Livermore National Laboratory, Livermore, CA. (MOL.19960329.0044)
- Viani, B.E. 1995b. *Strategies for Integrating Materials Properties Activities with Integrated Radionuclide Transport Activities*. YMP Milestone Rept. MOL135. (MOL.19960307.0233)
- Viani, B.E., and Bruton, C.J. 1996. *Assessing the Role of Cation Exchange in Controlling Groundwater Chemistry During Fluid Mixing in Fractured Granite at Aspo, Sweden*. Lawrence Livermore National Laboratory report UCRL-JC-121527. Livermore, CA. (MOL.19960419.0049)
- Viani, B.E., and Bruton, C.J. 1994. Effect of cation exchange on major cation chemistry in the Large Scale Redox Experiment at Äspö. In Banwart, S., ed., *Proc. Äspö International Geochemistry Workshop*, June 2-3, 1994, Äspö Hard Rock Laboratory, p. B-78-B-96. Also issued as Lawrence Livermore National Laboratory report UCRL-JC-118592. Livermore, CA.

- Viani, B.E., and Bruton, C.J. 1992a. Modeling ion exchange in clinoptilolite using the EQ3/6 geochemical modeling code. In Kharaka, Y. and Maest, A.S., eds., *Water-Rock Interaction*, Proceedings of the 7th International Symposium, vol. 1, A.A. Balkema, Brookfield, VT, p. 73-77. (MOL.19960607.0056)
- Viani, B.E., and Bruton, C.J. 1992b. *Modeling Fluid-Rock Interaction at Yucca Mountain, Nevada: A Progress Report*. Lawrence Livermore National Laboratory, Livermore, CA, UCRL-ID-109921, 61 p. (NNA.19920805.0002)
- Viani B.E., and Martin, S.I. 1994a. *Core Flow Experiment Protocol*. YMP Milestone Report M0L04. (MOL.19950727.0022)
- Viani B.E., and Martin, S.I. 1994b. *Groundwater Colloid Characterization*. YMP Milestone Report M0L03. (MOL.19950622.0014)
- Viani, B.E., and Martin, S.I. 1993. *Core-Flow Through Apparatus: Letter Report Documenting Testing Phase*. YMP Milestone Report M0L06. (NNA.19940120.0124)
- Viani, B.E., Roberts, S., Martin, S.I., and Phinney, D. 1994. YMP Milestone report M0L05: *Progress Report on Diffusion of Radionuclides in Clinoptilolite*. (MOL.19950406.0145)
- Waite, T.D., Davis, J.A., Payne, T.E., Waychunas, G.A., and Xu, N., 1994. Uranium(VI) adsorption to ferrihydrite: Application of a surface complexation model, *Geochim. et Cosmochim. Acta*, v. 58, p. 5465-5478.
- Wilson, C.N. 1990. *Results from NNWSI Series 3 Spent Fuel Dissolution Tests*. Pacific Northwest Laboratory report PNL-7170. Pacific Northwest Laboratory, Richland, WA. (NNA.19900329.0142)
- Wolery, T.J., Jackson, K.J., Bourcier, W.L., Bruton, C.J., Viani, B.E., Knauss, K.G., and Delany, J.M. 1990. Current status of the EQ3/6 software package for geochemical modeling. pp. 104-116. In Melchior, D.C. and Bassett, R.L. (eds.) *Chemical Modeling of Aqueous Systems II*. American Chemical Society, Washington, D.C. (NNA.19900716.0363)

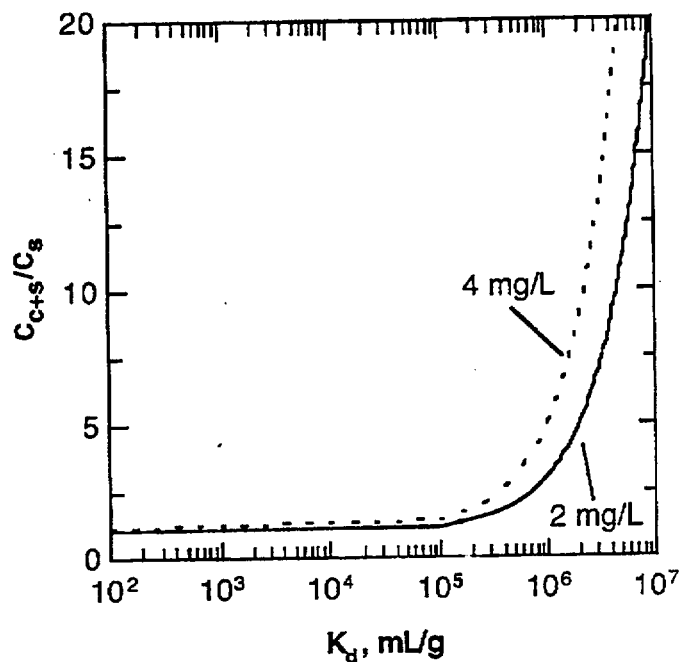


Figure 7-1. Relationship between ratio of concentration of radionuclide carried by solution in presence of colloid to that in absence of colloid, C_{c+s}/C_s , vs. K_d for radionuclide on colloid, at two concentrations of colloid.

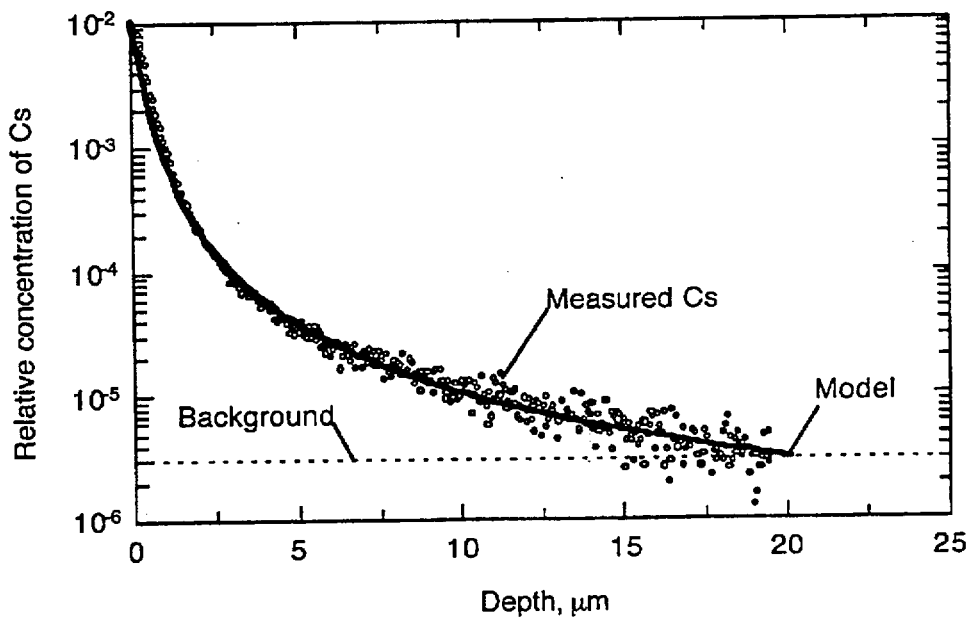


Figure 7-2. Variation of Cs with depth as measured by SIMS for nominally homoionic Ca-clinoptilolite in contact with a Cs/Ca solution at 30 °C for 32 d. Open circles are data points; solid line represents binary interdiffusion model with $D_{in,Cs} = 2.0 \times 10^{-13}$ and $D_{out,Ca} = 1.5 \times 10^{-18}$ cm²/s; dashed line represents background required to fit the model to the data.

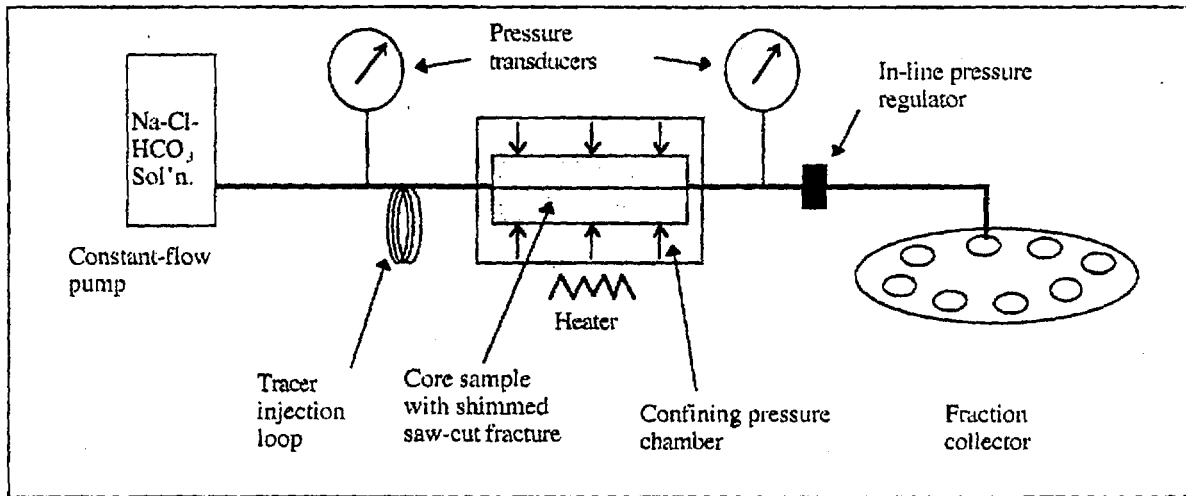


Figure 7-3. Schematic diagram of device used for flow and tracer tests.

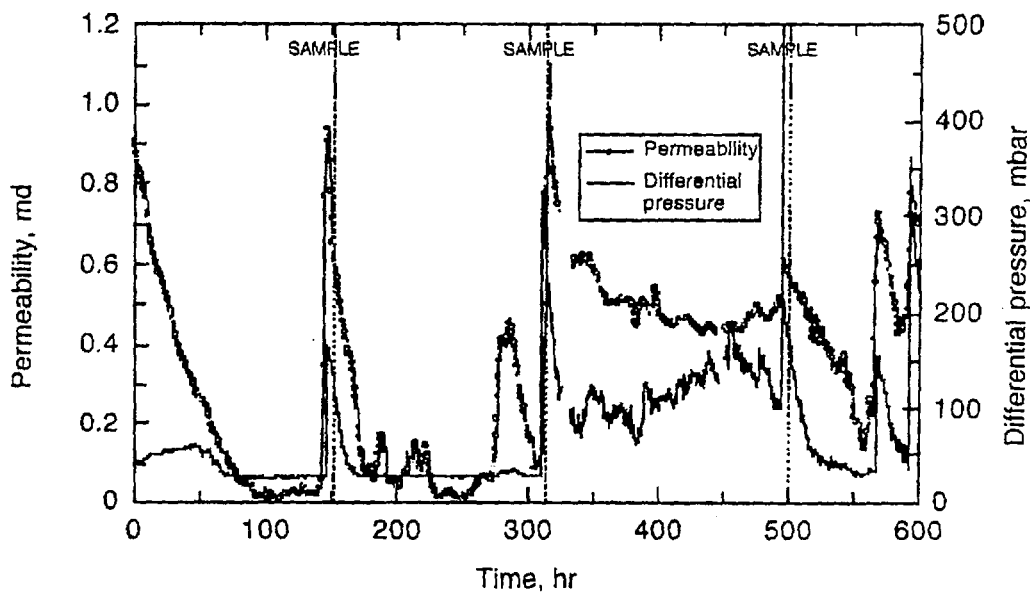


Figure 7-4. Variation of permeability and differential pressure with time for partial segment of flow test (FT040293) at 22 °C, showing repetitive loss of permeability due to bacterial plugging of a saw-cut fracture. Dotted vertical lines indicate points at which samples were taken for microscopic analysis. The apparatus used for this flow-test did not have the ability to maintain a constant flow rate.

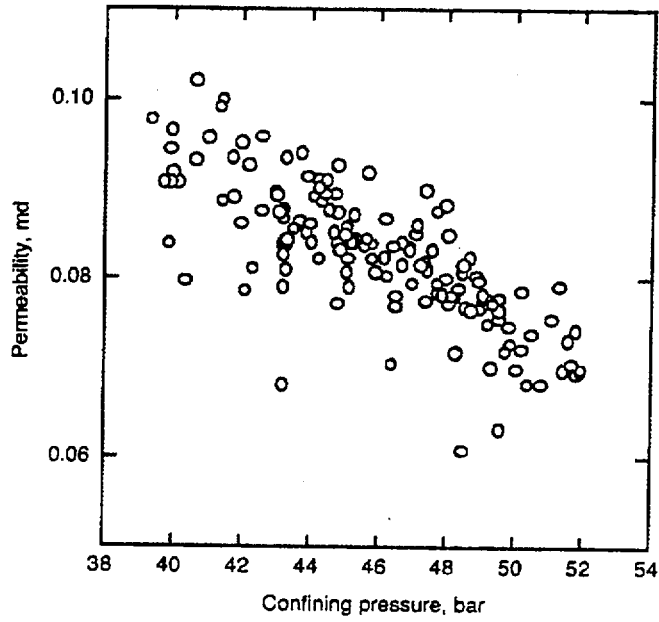


Figure 7-5. Variation in instantaneous permeability due to variation in confining pressure. (T = 59 °C; flow rate = 0.2 mL/h, FT050295).

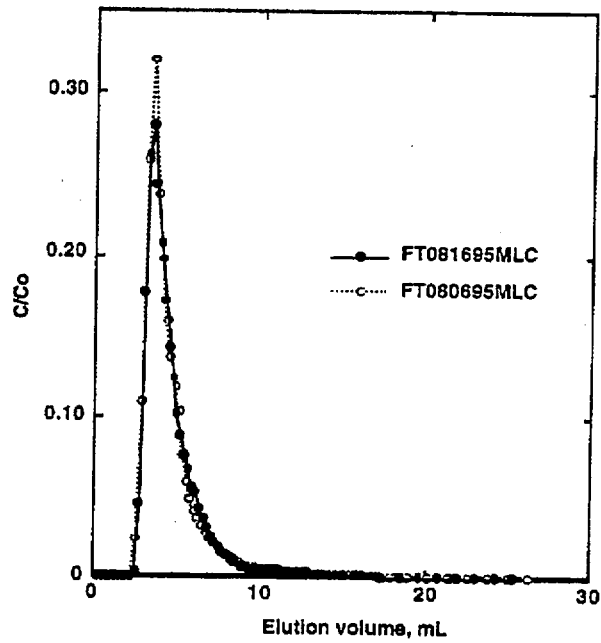


Figure 7-6. Relative concentration (C/C_0) breakthrough of two separate 560- μ L pulses of I^- tracer for 0.2 mL/h flow rate, 92 °C, and low pore pressure (collected 10 days apart).

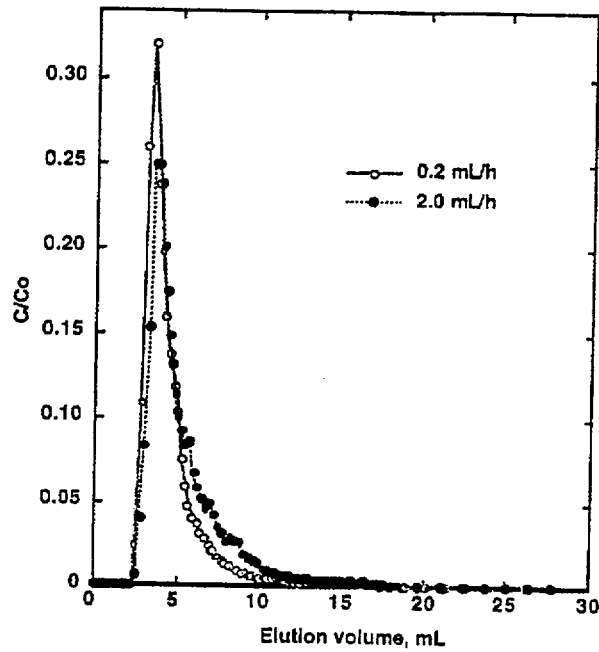


Figure 7-7. Relative concentration (C/C_0) breakthrough of 560- μ L pulse of I^- tracer for 0.2 (FT080695MLC) and 2.0 (FT072695MLC) mL/h flow rates at 92 °C and low pore pressure.

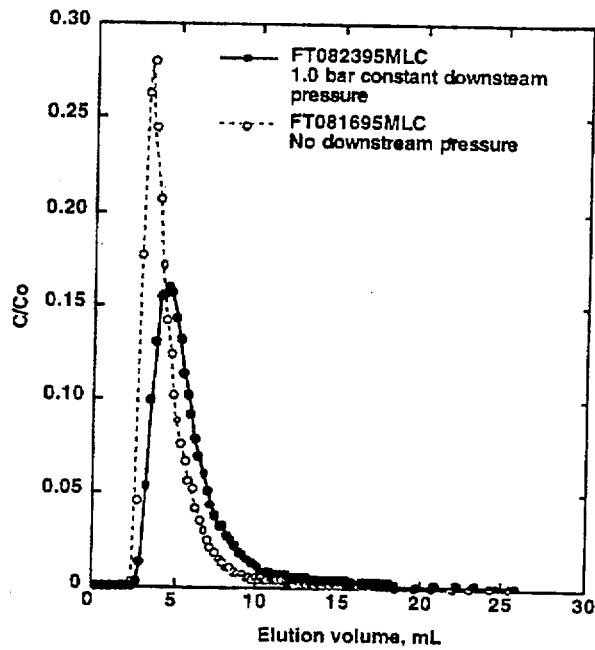


Figure 7-8. Relative concentration (C/C_0) breakthrough of 560 μ L pulse of I^- tracer for 0.2 mL/h flow rate at 92 °C and 1 bar (FT082395MLC) and low (FT081695MLC) pore pressure.

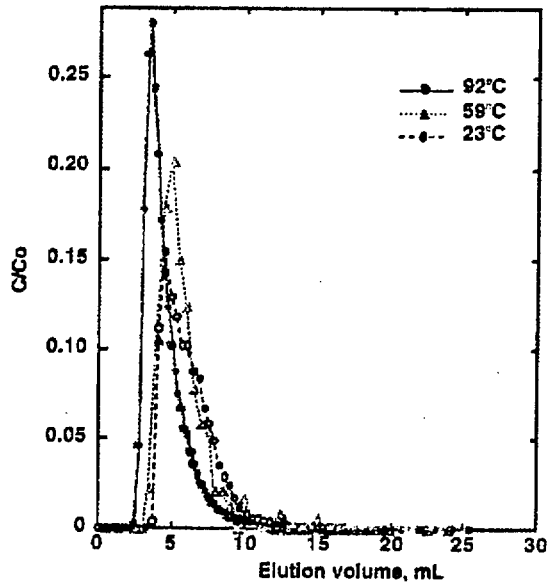


Figure 7-9. Relative concentration (C/C_0) breakthrough of 560 μL pulse of I^- tracer for 0.1 and 0.2 mL/h flow rates at 23 (FT040495MLC), 59 (FT051295MLC) and 92 (FT081695MLC) $^\circ\text{C}$ and low pore pressure.

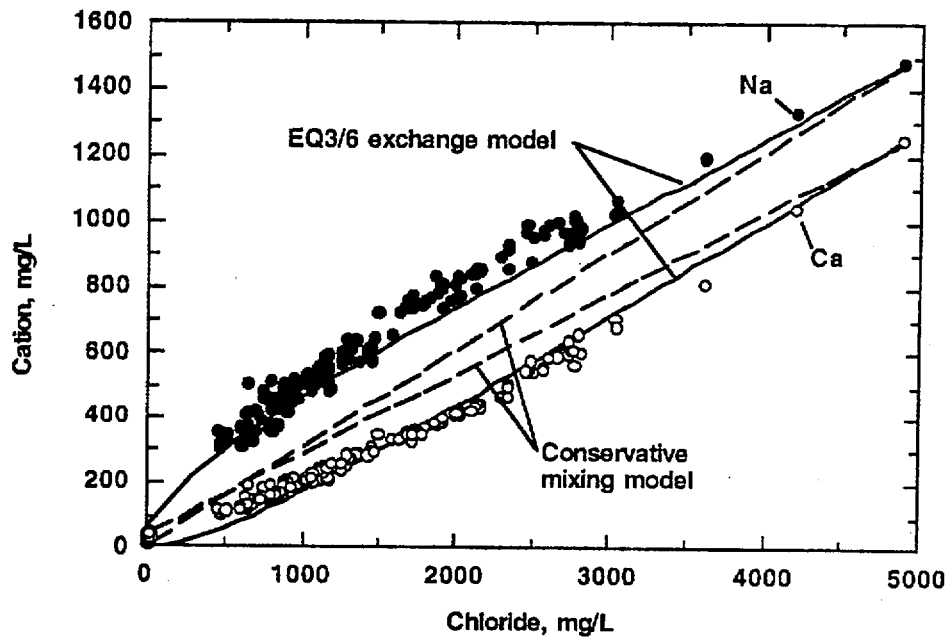


Figure 7-10. Comparison of EQ3/6 simulation of the variation of Na and Ca concentrations vs. Cl expected for mixing shallow (HBH02) and native (KA0483) groundwaters in the presence of 0.1 equiv/kg H_2O illite exchanger, and with predictions based on conservative mixing model (dashed lines).

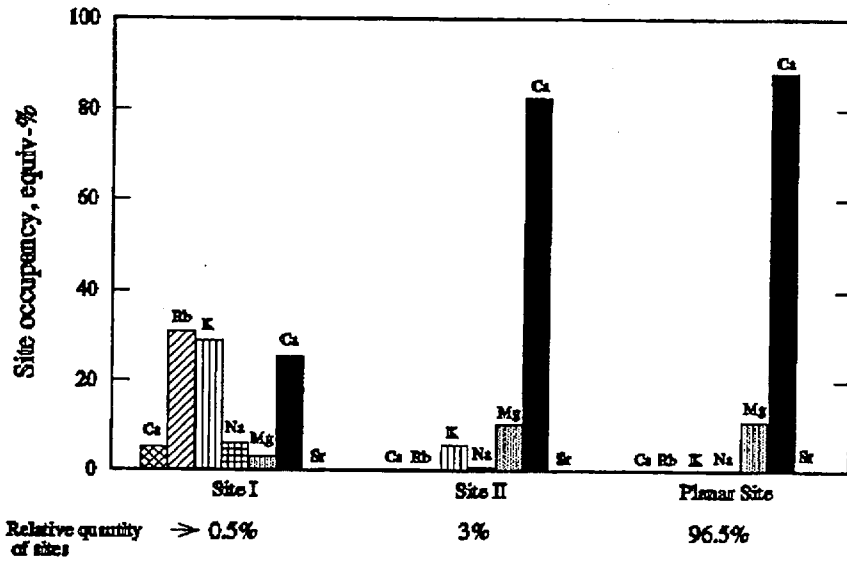


Figure 7-11. Predicted occupancies of exchange sites for illite in equilibrium with shallow (HBH02) groundwater.

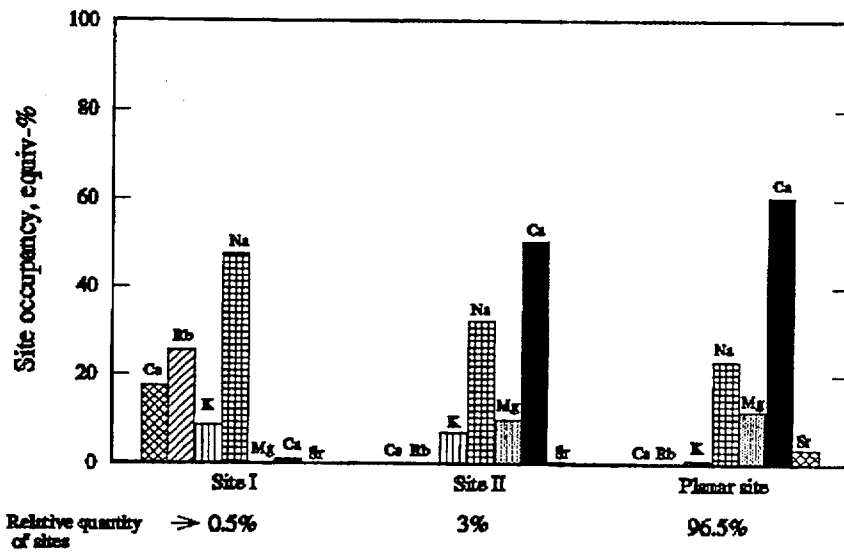


Figure 7-12. Predicted occupancies of exchange sites for illite in equilibrium with native (KA0483) groundwater.

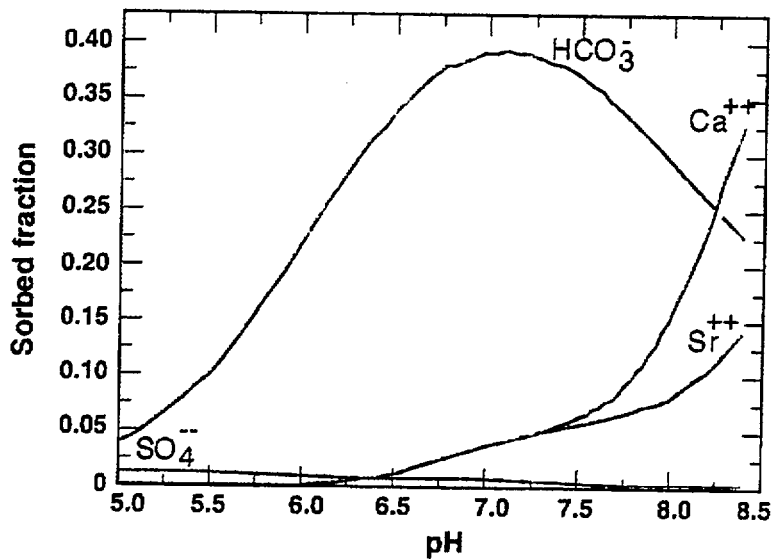


Figure 7-13. Fraction of total quantity of HCO_3^- , SO_4^{--} , Ca, and Sr sorbed onto 1 g goethite/kg H_2O in shallow (HBH02) groundwater at 25 °C using Dzombak and Morel (1990) surface complexation data with carbonate surface species from Van Geen, Robertson, and Leckie (1994). Electrical balancing on HCO_3^- .

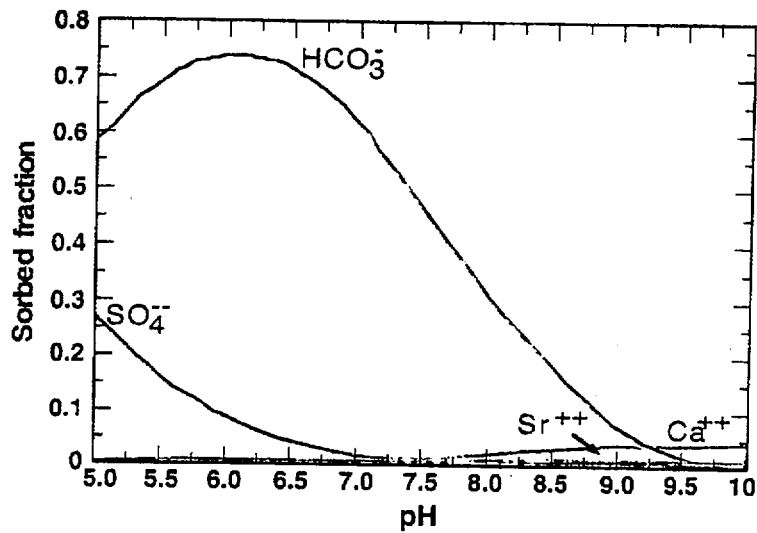


Figure 7-14. Fraction of total quantity of HCO_3^- , SO_4^{--} , Ca, and Sr sorbed onto 1 g goethite/kg H_2O in native (KA0483A) groundwater at 25 °C using Dzombak and Morel (1990) surface complexation data with carbonate surface species from Van Geen, Robertson, and Leckie (1994). Electrical balancing on Cl.

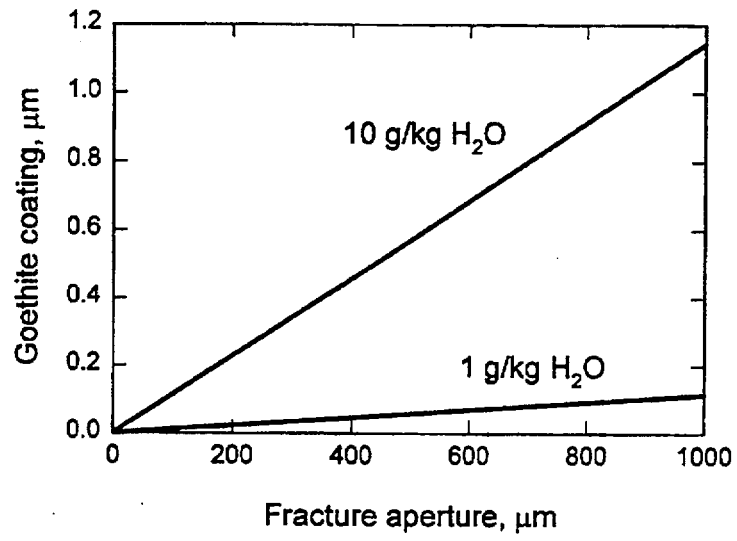


Figure 7-15. Variation in thickness of goethite coating with fracture aperture corresponding to 1 and 10 g of goethite per kg of H₂O contained in fracture.

Table 7-1. Summary of partition coefficient (K_d) ranges for selected elements with selected EBS/NFE flow-path components.⁽¹⁾

Flow-Path Component	Cs	Np mL/g	U
Iron Oxide	$1 \times 10^0 - 1 \times 10^1$ ⁽²⁾	$3 \times 10^2 - 9 \times 10^3$ ⁽³⁾	$2 \times 10^3 - 2 \times 10^4$ ⁽⁴⁾
Cement ⁽⁵⁾	$1 \times 10^0 - 1 \times 10^1$	$2 \times 10^3 - 3 \times 10^4$	$1 \times 10^2 - 6 \times 10^3$
Devitrified Tuff	$1 \times 10^1 - 1 \times 10^3$ ⁽⁶⁾	0 - 1×10^1 ⁽⁷⁾	0 - 1×10^1 ⁽⁷⁾

(1) K_d 's depend on solution composition, solid/solution ratio, specific surface of adsorbent, and concentration of uranium. The K_d ranges listed for devitrified tuff and iron oxide are for dilute carbonate-bearing solutions with pH's between ~7 to ~8.5; similar to what would be expected at Yucca Mountain. The solution composition for cements is controlled by the interaction with pore water and cement and would be expected to be similar for any dilute groundwater that interacts with it.

(2) Hematite; Cornell, 1993; Todorovic et al., 1992.

(3) Hematite; Triay et al., 1993b.

(4) Hematite; Ticknor, 1994; Ho and Miller, 1986.

(5) Yucca Mountain tuff; Meijer, 1990

(6) Portland cements; Albinsson et al., 1993.

(7) Yucca Mountain tuff; Thomas, 1987.

Table 7-2. Summary of flow tests with saw-cut Topopah Spring core sample.

Temperature °C	Flow Rate mL/h	Pore Pressure ⁽¹⁾ bar	Permeability ⁽²⁾ md	Hydraulic Aperture µm
23	0.1, 0.2, 2.0	0.1 - 2.0	0.060±0.005	3.1
59	0.2, 2.0	0.1 - 2.5	0.10±0.035	3.6
92	0.2, 2.0	0.06 - 0.09	0.19±0.14	4.5
92	0.2, 2.0	0.5 - 3.1	1.86±0.47	9.6

(1) Pore pressures are average values computed over the duration of each flow test. The tabulated values show the range in average pore pressures observed for runs at that temperature and the indicated flow rates.

(2) The permeabilities are average values calculated from the average of the instantaneous permeabilities for a given flow test. Instantaneous permeabilities varied with confining pressure, and over time.

Table 7-3. Composition of feed solution and effluent from pooled samples taken after breakthrough of the tracer.

Element	Feed solution	Effluent		
		23 °C 0.2 mL/h	92 °C 0.2 mL/h	92 °C 2.0 mL/h
Ca	0.05	4.54	3.62	2.46
Mg	<0.01	1.08	0.83	0.53
Na	33	37	34	31
K	<0.01	0.4	1.7	1.2
Si	0.08	2.65	22.49	6.91
Sr	<0.02	0.12	0.09	0.06

Table 7-4. Cation-exchange energies for illite and smectite at 25 °C⁽¹⁾.

Exchange Reaction	Exchange Energy, kcal/equiv			
	Illite			Smectite
	Site I	Site II	Planar Site	
Na → 0.5 (Ca, Mg, Sr, Ba) ⁽²⁾	1.4	0.2	0 ⁽³⁾	-0.12
Na → K	-2.2	-2.3	-1.22	-0.35
Na → Rb	-6.5	-4.2	-1.62	-0.63
Na → Cs	-7.8	-4.2	-2.10	-1.08
Relative fraction of sites	0.005	0.03	0.965	1.00

(1) Data for illite from Brouwer et al. (1983; Tables I and II). Data for smectite from Fletcher and Sposito (1989) except for Na → (Rb, Cs) which are from Gast (1972). Note: these data are strictly accurate at 25 °C only. It was assumed that for the purposes of these simulations, the variation of exchange energy between 25 °C and the groundwater temperature (~10 °C) is a second order effect.

(2) A Na → 0.5 (Ca, Mg, Sr, Ba) signifies the conversion of 1 equivalent of exchanger from the Na form to the Ca, Mg, Sr, or Ba form.

(3) The exchange energy for Na → 0.5 (Ca, Mg, Sr, Ba) deduced from Brouwer et al. (1983) data for the planar site was adjusted to be consistent with their data for Cs → Na, Rb → Na, and Rb → (Ca, Mg, Sr, Ba) exchange.

Table 7-5. Ratio of predicted mass of cation on exchanger⁽¹⁾ to mass of cation in fluid for three groundwaters at Äspö.

Cation	Shallow (HBH02) 15 m	Native (KA0483A) tunnel depth
Na	1.3	0.30
Ca	41.7	1.07
Mg	41.7	1.21

(1) Calculations assume 0.1 equiv/kg of H₂O.

Table 7-6. Predicted sorbed fractions and concentrations of sorbed Ca, Sr, SO₄, and HCO₃ in mg/kg, in shallow (HBH02) groundwater as a function of mass of goethite/kg H₂O.⁽¹⁾

Mass of goethite g/kg H ₂ O	Predicted sorbed fraction and concentration (mg/kg, in parentheses) of sorbed species.			
	Ca	Sr	SO ₄	HCO ₃
0.1	0.0015 (0.06)	0.0016 (0.0003)	0.0022 (0.04)	0.09 (11.21)
1.	0.015 (0.63)	0.016 (0.003)	0.022 (0.43)	0.50 (112.1)
10.	0.13 (6.31)	0.14 (0.03)	0.18 (4.31)	0.91 (1121)
Concentration in coexisting fluid phase, mg/kg	42.8	0.16	19.5	114.

(1) Calculated using Dzombak and Morel (1990) surface complexation data base with carbonate complexation constants from Van Geen, Robertson, and Leckie (1994). The sorbed fractions are calculated assuming the goethite is in equilibrium with an aqueous solution having the composition of the shallow groundwater.

Contents

Chapter 8.0 Electrical Potentials	8-2
8.1 Introduction.....	8-2
8.2 Self-Potentials.....	8-2
8.2.1 Streaming Potential	8-3
8.2.2 Thermoelectric Potential.....	8-4
8.2.3 Electrochemical Potential	8-4
8.3 Summary.....	8-4
8.4 References.....	8-5

Chapter 8.0 Electrical Potentials

Abelardo Ramirez

8.1 Introduction

Natural and spontaneous electrical potentials, known as self-potentials (SPs), occur within the earth because of electrochemical or mechanical activity. Self-potential anomalies have been observed in natural geothermal environments where a significant flow of hot water and steam occurs, qualitatively similar to the conditions expected in the near-field environment (NFE) of the potential nuclear-waste repository at Yucca Mountain, Nevada (Corwin and Hoover, 1979; Zohdy et al., 1973; Anderson and Johnson, 1976). Because of their potential influence on reaction processes, SPs may be significant in understanding how the NFE will evolve geochemically. In addition, SPs may generate electrical currents that may affect the performance of metallic waste containers. This chapter discusses some particular mechanisms that generate SPs in rock-water systems and provides order-of-magnitude estimates for the SPs that may be present in the NFE.

Other currents that may be present in the NFE are magnetotelluric and telluric currents; however, these currents are believed to be the result of diurnal variations, caused by solar emission, aurora, and other phenomena, in the earth's magnetic field (Telford et al., 1976). These currents are probably less significant than those caused by SPs and are outside the scope of this discussion.

8.2 Self-Potentials

Underground water is an important factor in most occurrences of SPs. Telford et al. (1976) found that SPs are associated with variations in rock properties at contact interfaces where corrosion occurs as a result of thermal and pressure gradients in underground fluids (thermoelectric and streaming potentials), and with variations in electrolytic concentrations of groundwater (electrochemical potential).

8.2.1 Streaming Potential

When two phases are placed in contact, a difference in potential between them generally develops. If one of the phases is a polar liquid, like water, its dipolar molecules will tend to be oriented in a particular direction at the interface, generating a potential difference. If there are ions or excess electrons in one or both phases, the electrical charges will tend to distribute themselves nonuniformly at the interface. The region between the two adjoining phases is always marked by a separation of electrical charges so that near, or on the surface of, phase I there is an excess charge of one sign, and the balancing charge is distributed somehow through the adjoining surface regions of phase II (Hunter, 1981). This arrangement of charges at the interface is referred to as the electrical double layer. When liquid moves through a capillary or a porous medium under a pressure gradient, the excess charges near the wall are carried along by the liquid, and their accumulation downstream causes the buildup of an electrical field, which drives an electrical current back (by ionic conduction through the liquid) against the direction of liquid flow (Hunter, 1981). The measured potential difference across the capillary is called the streaming potential.

Ishido et al. (1983) report that in rock-water systems the streaming potential coefficient increases exponentially with decreasing hydraulic radii $<10^{-6}$ m. Klavetter and Peters (1987) show that for Topopah Spring tuff (the potential repository horizon) the pore sizes range from 10^{-6} to 10^{-8} m with most of the pore volume due to the 10^{-7} m fraction. This would suggest that the streaming potential coefficient for Topopah Spring tuff will be relatively high due to its small pore sizes (although to the best of our knowledge the coefficient has not been established for welded tuff). Nourbehecht (1963) reports that the streaming potential coefficients for a wide variety of rocks ranges from about 0.3 to 30 mV/atm.

Chapter 1 shows numerical modeling results that predict a region of condensate accumulation with 100% saturation adjacent to the boiling region. Pressure gradients within this region of high saturation can cause liquid to flow very slowly within the porous medium. There will be streaming potential associated with the

liquid flow. The magnitude of the streaming potential cannot be estimated because the streaming potential coefficient for unsaturated welded tuff is not known at this time.

8.2.2 Thermoelectric Potential

Temperature gradients give rise to thermoelectric potentials in rock-water systems (Telford et al., 1976). Nourbehecht (1963) reports that the thermoelectric coefficient for rock can be as high as 1 mV/°C with average values of about 0.2 to 0.4 mV/°C. As reported in Chapter 1, these numerical modeling results show that drift wall temperatures as high as 200°C may be present in the repository and a temperature near 96°C within the condensate region. If we assume an average thermoelectric coefficient of 0.3 mV/°C and a temperature difference of 100°C, the calculated thermoelectric potential is 30 mV. Chapter 1 calculations show that the temperature gradient decreases as time after emplacement increases, which implies that the thermoelectric potential would also decrease as time after emplacement increases.

8.2.3 Electrochemical Potential

Electrochemical potentials arise when diffusion of ions occurs. This potential is attributed to two causes: (1) the difference in mobilities of various ions in solutions of different concentration (diffusion potential), and (2) the potential that develops when two electrodes are immersed in the same solution but at two different concentrations (Nernst potential). For example, when the concentrations are in the ratio of 5:1, the potential that develops is ± 50 mV (Telford et al., 1976).

In regions where interconnected fluids exist across the potential field, ionic diffusion and reaction relationships will be influenced by the potential field. This effect needs to be evaluated in future work.

8.3 Summary

We have briefly described the mechanisms that are likely to be operating in the NFE, generating natural electrical potentials and currents. The electric potential

fields caused by groundwater flow, and by temperature and ionic concentration gradients will coexist in the NFE. Due to the combined effects of these fields, the resulting electric potential gradients may affect the geochemical evolution of the NFE (although this has not been evaluated to the best of our knowledge) and possibly, the performance of waste container materials. Very little information is available with which to estimate SP generation within the NFE. We have raised the possibility that SPs may be significant in the NFE and, thus, should be investigated further. In addition, SPs may be useful as a diagnostic measurement of the near-field hydrothermal environment.

8.4 References

- Anderson, L. A., and G. R. Johnson (1976), "Application of the Self-Potential Method to Geothermal Exploration in Long Valley, California," *Journal of Geophysical Research* 81, 1527-1532. (Readily available).
- Corwin, R. F., and D. B. Hoover (1979), "The Self-Potential Method in Geothermal Exploration," *Geophysics* 44, 226-245. Readily available).
- Hunter, R. J. (1981), *Zeta Potential in Colloid Science, Principles and Applications* (Academic Press, London) Chapters 1-3. (NNA.920916.0006)
- Ishido, T., H. Mizuanti, and K. Baba (1983), "Streaming Potential Observations, Using Geothermal Wells and In Situ Electrokinetic Coupling Coefficients under High-Temperature," *Tectonophysics* 91(1-2), 89-104. (NNA.920506.0056)
- Klavetter, E. A., and R. R. Peters (1987), *An Evaluation of the Use of Mercury Porosimetry in Calculating Hydrologic Properties of Tuffs from Yucca Mountain, Nevada*, Sandia National Laboratories, Albuquerque, NM, SAND86-0286-UC-70. (NNA.890327.0056)
- Nourbehecht, B. (1963), *Irreversible Thermodynamic Effects in Inhomogeneous Media and their Applications in Certain Geoelectric Problems*, Ph.D. Thesis, Massachusetts Institute of Technology, Cambridge, MA, pp. 1, 3, and 6. (NNA.920506.0032)
- Telford, W. M., L. P. Geldart, R. E. Sheriff, and D. A. Keys (1976), *Applied Geophysics* (Cambridge University Press, London). (NNA.891106.0192)
- Zohdy, A. A. A. R., L. A. Anderson, and L. J. P. Muffler (1973), "Resistivity, Self-Potential, and Induced-Polarization Surveys of a Vapor Dominated Geothermal System," *Geophysics* 38, 1130-1144. (NNA.91062.0059)

Contents

Chapter 9.0 Field Thermal Tests.....	9-2
9.1 Introduction.....	9-2
9.2 G-Tunnel Tests (<i>A. Ramirez</i>).....	9-4
9.2.1 Parameters Measured.....	9-5
9.2.2 Test Description.....	9-7
9.2.3 Changes in Rock Mass Moisture Content.....	9-8
9.2.4 Temperature Measurements.....	9-11
9.2.5 Changes in Air Permeability.....	9-13
9.2.6 Steam Invading the Heater Emplacement Borehole.....	9-14
9.2.7 Summary.....	9-15
9.3 Large Block Test.....	9-17
9.4 ESF Thermal Tests.....	9-22
9.4.1 Single Heater Test.....	9-22
9.4.2 Drift Scale Test.....	9-23
9.5 Large-Scale Long Duration Test.....	9-25
9.6 Confirmation Monitoring.....	9-26
9.7 References.....	9-26

Chapter 9.0 Field Thermal Tests

W. Lin and A. Ramirez

9.1 Introduction

Understanding the movement of moisture, including liquid water, steam, and vapor, in the near-field environment (NFE) of the potential nuclear-waste repository at Yucca Mountain, Nevada is one of the goals of waste-package environment hydrologic investigations. This section discusses field tests to enhance our understanding of how thermal loading, resulting from waste package emplacement, will affect the hydrologic properties and processes of the NFE.

One of the main concerns in the NFE of a nuclear-waste repository is the quantity and quality of the water that may be present to contact the waste and waste packages (near field) and in the rock mass surrounding the repository since water can cause property changes in the altered zone. Processes that may affect the quantity and quality of the water are coupled thermal-mechanical-hydrological-chemical (TMHC) processes. The TMHC processes may involve the *in situ* pore water in the Topopah Spring tuff, water present in fractures, and/or condensate that result(s) from water mobilized by heat, as well as any introduced water (either naturally or artificially) after the emplacement of the wastes. Field and laboratory tests are conducted to: enhance our understanding of the coupled TMHC processes and to measure physical properties. This chapter discusses the field tests.

The rationales of conducting field thermal tests are to extend from laboratory tests on relatively small samples (up to 1-m, maximum), to testing of rock masses that include fractures and inhomogeneity as representative to Yucca Mountain as possible, and under test conditions as close as possible to *in situ* repository conditions. The logic of testing, i.e., increasing sample size from small to large, increasing the complexity of sample characteristics from intact to include multiple fractures and heterogeneity, and relaxing test boundary conditions from simple controlled to uncontrolled, is to evaluate the temporal and spatial scale effects, to

increase our understanding of the test results in steps, and to enhance our confidence in modeling the tests and the coupled TMHC processes to be expected in a repository. The purposes of field thermal tests are to test the coupled TMHC processes in a rock mass which is big enough to include heterogeneity, so that the test results can be used to verify model predictions and to identify important physical processes that must be included in the conceptual models. The objectives, goals, and rationales of the field tests are described in section 8.3.4.2.4.4 *Study Plan for Engineered Barrier System Field Tests* (Lin, 1995). Based on the findings and logic of that report, several field thermal tests are planned to serve different purposes (described here). The G-Tunnel test was conducted in 1988–1989, in Grouse Canyon tuff in G-Tunnel, Nevada Test Site, to improve our understanding of the thermal-hydrological processes in an underground environment and to prototype instruments and test methodologies. The Large Block Test (LBT) was designed to provide testing of the coupled TMHC processes in Topopah Spring tuff under controlled boundary conditions so that the results can be more directly compared with model calculations. Also, the LBT will provide three-dimensional (3-D) coverage of the test region with instruments. In addition, the LBT can provide a unique opportunity for investigating infiltration in a heated rock mass. The ESF Thermal Test (ESFTT) will be the first *in situ* thermal test in the potential repository horizon in Yucca Mountain. The results of the ESFTT will be used for viability analyses and license application of the repository. Although it is still in the conceptual state, the plan, if instituted, is to use the Large Scale Long Duration Test (LSLDT) to heat up a region with multiple emplacement drifts for several years so that all possible coupled TMHC processes can be tested (see section 9.5 for more details). Also planned are the Confirmation Observations of the performance of a repository. The confirmation monitoring is the only test in the true temporal and spatial scales of a repository, therefore is very critical (see section 9.6).

Basically, field thermal tests involve heating a rock mass with electrical resistor heaters and monitoring the spatial distributions and temporal variations of temperature, moisture content, concentration of certain chemical elements, and stress and displacements in the rock mass. Temperatures will be measured by using

either resistance temperature devices (RTD) or thermocouples, dependent on the temperature range to be measured and accuracy required. Moisture contents will be measured in the following means: point measurement of relative humidity will be conducted using Humicaps. Line measurement of moisture content will be done using neutron logging. Two- and three-dimensional tomographs of the moisture content will be inferred from electrical resistivity tomographs (ERT). Chemical sensors will be used to monitor concentration of some chemical elements, such as pH, conductivity, dissolved oxygen, Ca, Cl, etc. Both mechanical and optical multiple borehole extensometers (MPBXs) will be used to measure displacements. Scoping model calculations will be used to design the tests, and then model calculations with exact test configurations will be used to monitor their progress and for post-test data analyses. Chapter 1.9 presents some of the results of the model calculations. Post-test examination of the rocks are usually planned to verify some of the indirect observations by instruments during the test with direct observations. The G-Tunnel test is the only field thermal test that has been completed. The results from the G-Tunnel test are summarized in section 9.2. Recently, model analyses of the G-Tunnel test results were performed (See Chapter 1.9 for the results of those analyses). The LBT has been planned, constructed, and characterized, but instruments have not been installed. Only the pre-test characterization results of the LBT are presented here. See section 9.4 for the test design and plans for the ESFTT.

9.2 G-Tunnel Tests (*A. Ramirez*)

This discussion includes the key results and supporting data from the G-Tunnel tests in which we studied the hydrothermal perturbation of welded tuff near a horizontally oriented heater. As part of the G-Tunnel tests, we measured several parameters as a function of location and time so that we could examine the effects of heating and cooling during a thermal pulse that lasted ~195 days.

A schematic of the hydrologic environment expected to develop around a heater during thermal loading is shown in Fig. 9-1 [see Yow (1985), for additional details on the expected environmental conditions]. This figure depicts the primary

mechanisms of heat and fluid flow for an idealized example of a horizontal heater that is intersected by a near vertical fracture. The actual heater borehole was intersected by more than a dozen fractures. The rock mass consisted of matrix blocks that were bounded by fractures and the borehole wall (for blocks immediately adjacent to the heater). Under ambient conditions, the matrix blocks are partially saturated, and the fractures and borehole are essentially dry. The heater heats the borehole surface primarily via thermal radiation. As heat is conducted through the fractured rock mass, vaporization begins on the outer surfaces of the matrix blocks closest to the borehole and then proceeds in toward the center of each block. Where temperatures are in excess of saturation conditions, vigorous boiling occurs. For water vapor to flow out of the matrix blocks, gas-phase pressures must increase from the surface of the matrix block to its interior, resulting in the elevation of the boiling temperature with distance into the matrix block. Water vapor that enters the fractures is subsequently driven by gas pressure gradients (including buoyancy effects) within the fracture network. In general, vapor flow in the fractures is directed away from the center of the boiling, either radially outward or inward toward the heater hole. Vapor flow in the fractures persists until condensation conditions are encountered. Condensed water in the fractures that is not immediately imbibed by the matrix flows under gravity and capillary forces in the fractures either (1) back toward the boiling zone where it reboils, or (2) out into the condensation zone where it is eventually completely imbibed by the matrix.

9.2.1 Parameters Measured

The following parameters were measured to characterize the behavior of the rock mass within a few meters of the heater before, during, and after the thermal cycle. This discussion includes the results for a subset of the measured parameters and presents interpretations pertaining to the evolution of the NFE around a simulated waste package [for full details refer to Ramirez et al. (1991), including those reports listed in the "References" and "Bibliography of Related Reports" section].

9.2.1.1 Rock Mass Temperatures. Rock mass temperatures were used in reconstructing the thermal response of the rock and in evaluating the performance of the test equipment.

9.2.1.2 Rock Mass Gas Pressure and Atmospheric Pressure. Rock mass gas pressure and atmospheric pressure were used in reconstructing the flow regime of the air and water vapor in the rock mass.

9.2.1.3 Borehole Measurements of the Relative Dielectric Constant and Thermal Neutron Counts. Cross borehole measurements of the relative dielectric constant of the rock and single borehole measurements of thermal neutron counts were used to infer the spatial and temporal changes in the moisture content of the rock mass.

9.2.1.4 Air Humidity. Air humidity measurements in the rock mass were used to calculate the pore pressure gradients that drive the movement of liquid water within the rock mass. Changes in the moisture content and pore pressure information were used to reconstruct the flow regime of liquid water in the rock mass. The spatial variations in moisture content were used to infer the flow paths of the liquid water and to define regions that are losing or gaining water as a function of time.

9.2.1.5 Air Permeability. The air permeability measurements were used to detect changes in the permeability of the rock surrounding the heater emplacement borehole. These measurements were made along the heater borehole after all of the boreholes were drilled and sealed. The measurements were repeated after the heating sequence was completed and after the heater was removed from the borehole.

9.2.1.6 Fracture Locations and Orientations. Fracture locations and orientations were measured in all boreholes by means of a borescope and/or by borehole television surveys performed before the heater was energized. The measurements were repeated along the heater emplacement borehole after heating was completed, and these data were used to:

- Determine the effects of heating on the stability of the emplacement borehole walls.

- Interpret the changes in fracture permeability caused by the heating and cooling cycle.
- Analyze the flow regime of vapor and liquid water in the rock mass as inferred from other measurements.

9.2.1.7 Condensed Volume of Steam. The measurements of the condensed volume of steam invading the heater borehole were used to estimate the amount of gas phase humidity that flows toward the heater borehole.

9.2.2 Test Description

Sandia National Laboratories constructed the GTUF, which consists of drifts driven in welded tuff under Rainier Mesa, NTS, for the YMP (Fig. 9-2). The G-Tunnel tests were conducted in the rock mass between the small-diameter heater alcove and the rock mechanics incline.

The test included an accelerated thermal cycle to examine the effects of the heating and cooling sides of a thermal pulse. Figure 9-3 shows the test's power schedule. The initial thermal loading for the 3-m (9.8-ft) heater was ~3.3 kW (1.1 kW/m of heater length). To increase the disturbed volume of rock within the relatively short time available for prototype testing and to create sufficiently high rock temperatures to drive two-phase fluid flow, we set the initial thermal load per unit length of emplacement borehole higher than the loading expected for a typical spent fuel container (0.4–0.7 kW/m).

The duration of the heating was based on the test criteria of heating the rock mass until the boiling point isotherm moved ~0.6–0.7 m (2.0–2.3 ft) radially from the heater borehole wall. Another test criteria involved achieving emplacement heater borehole temperatures similar to those expected for the repository (235°C). The spatial extent of the heating affected a volume of rock large enough to include several fractures.

Figures 9-4 and 9-5 show the borehole layout and the measurement stations for the various instruments used. The test location within G-Tunnel is bounded by the small diameter heater alcove and the rock mechanics incline, as shown in Fig. 9-4. The heater borehole is inclined slightly upward (elevation increases from the collar

to the end of the borehole) from the rock mechanics incline. The diameter of the heater borehole is 30.5 cm (12 in.).

Twelve of the boreholes were used to monitor the rock response; all of these were nearly horizontal and were inclined slightly downward. The majority of the boreholes were orthogonal to the emplacement hole axis, which provided better coverage of the spatial variations in rock responses that occur parallel to the radius of the emplacement borehole. This arrangement allowed measurements in the direction of expected maximum thermal and hydrologic gradients. Three boreholes were drilled parallel to the heater borehole axis to monitor rock response beyond the ends of the heater.

9.2.3 Changes in Rock Mass Moisture Content

A thorough understanding of local hydrology over the package lifetime is central to understanding waste package performance. Geophysical techniques were used to monitor changes in rock moisture content during the test. The techniques chosen included neutron logging in single boreholes and high-frequency electromagnetic measurements performed between boreholes. In this section, we interpret only the neutron log results; for the electromagnetic measurement results, see Daily et al. (1989).

The neutron logging probe contains a source of high-energy neutrons and a detector for slow (thermal) neutrons. When water is present in the rock, the hydrogen in the water slows the neutrons for detection. Seven boreholes (NE-1 through NE-7) were sampled before the heater was turned on; the measurements were repeated frequently after the heater was energized to monitor temporal and spatial changes in moisture content. A paraffin shield included with the probe was sampled at the beginning and end of each logging day to verify that the tool was functioning properly.

For each borehole, we calculated the differences between the "before" and "after" measurements ("after" heating minus "before" heating) to produce a difference log. We chose to use differences rather than absolute values of moisture content because

the effects of the borehole liners and the grout within the survey boreholes are still unknown.

A spatial filter was applied to each difference log to smooth the spikes in the trace caused by the random fluctuations in the number of neutrons generated by the radioactive source in the probe. The precision for the filtered data is estimated to be $\pm 0.003 \text{ g/cm}^3$. This precision estimate means that for any one point on a difference trace that equals or exceeds $\pm 0.003 \text{ g/cm}^3$, there is a 95% probability that the difference is caused by true changes in the measurement and a 5% probability that it is caused by random fluctuations in the neutron output of the radioactive source.

Boreholes NE-2A, NE-6, and NE-7 are three coplanar boreholes located above and below the center of the heater as shown in Fig. 9-5. The data collected along these boreholes were combined and plotted as a function of radial distance to the center point of the heater assembly. The changes shown were calculated relative to preheating moisture measurements. Figures 9-6, 9-7, and 9-8 consist of two plots each that show the same data at two different scales so that the smaller changes occurring at the more distant locations can be examined.

Figures 9-6 and 9-7 show radial profiles of changes in moisture content during the drying and rewetting phases of the test. These figures also show the difference traces calculated from day 70 data (the heater was energized on day 0) and for day 301 (the last data set was collected 106 days after the heater was de-energized). The data in Fig. 9-6 were collected midway through the maximum power phase of the test. As expected, the rock closest to the heater (the shortest distance) lost substantial amounts of moisture. However, the rock near borehole NE-2A dried at a faster rate than the rock near NE-6. Fracture maps of the test region suggest that a higher concentration of fractures mapped along NE-2A may be one cause for this faster rate of drying. Also note that rock located between 1.75- and 2.25-m radii showed a small increase in moisture content as a result of the condensation of steam generated in hotter regions closer to the heater.

Between days 70 and 127 (data are not shown) the NE-2A profile showed very little additional drying when compared to Fig. 9-6, whereas the NE-6 profile showed significant additional drying. Both profiles are closely matched with the caveat that

the width of the drying region appeared to be slightly wider near NE-2A. The closely matched profiles suggest that the rock near NE-2A and NE-6 was almost completely dry because very little additional drying occurred near NE-2A during the 57 days of continued heater operation at maximum power. The radius of the dry zone achieved was ~0.7 m; this is consistent with the test objective of achieving boiling conditions within a 0.6–0.7-m radius.

The radial profile of changes in moisture content for day 301 are shown in Fig. 9-8. These data were collected during the postheating phase of the test, 106 days after the heater was de-energized. The data show relatively little change in the rock near the heater during the power rampdown and postheating phase of the test. It also shows that the rock above the heater (borehole NE-6) rewet more quickly than the rock below the heater (borehole NE-2A) for distances less than or equal to 0.5 m. This suggests that the gravity-driven flow plays a role in the rewetting process.

We gained further insights into the rewetting process by calculating changes in moisture content relative to the last day of full power heating. Figure 9-9 presents changes in moisture in borehole NE-2A, where "after" minus "before" changes are calculated relative to day 127 (i.e., the "before" data correspond to day 127, which was the day before the last day of maximum power heating). The data were obtained during the power rampdown and postheating phases of the test when the rock was cooling and rewetting. Also shown are fractures mapped along the boreholes. Note that the rock regions that show the greatest rewetting are clustered around the fractures in NE-2A. The high correlation between fracture locations and rewetting suggests that fractures play a dominant role in the rewetting process. One mechanism for rewetting along fractures may be capillary condensation of air humidity in the fractures because humid air (found in the wetter portions of the rock mass) can travel with relative ease along the fractures. Another mechanism that may be playing a role in the rewetting process is water dripping along fractures; Fig. 9-8 shows evidence consistent with this argument in that the rewetting front has penetrated more quickly above the heater (borehole NE-6) than below the heater (NE-2A).

9.2.4 Temperature Measurements

Temperature measurements were made to characterize the thermal response of the medium around the heater. There were a total of 112 thermocouples used in this test. All of these thermocouples were chromel-alumel (Type K) with an accuracy of $\pm 1^{\circ}\text{C}$ (1.8°F). Ten thermocouples were installed within the heated portion of the heater borehole to monitor container and borehole wall temperatures. The other 102 thermocouples were located in boreholes TC-1, TC-2, P-1, P-2, and P-3.

Figure 9-10 shows the temperatures measured in all boreholes during the last day of the maximum power phase (day 128). The temperatures are plotted as a function of the natural log of radial distance to observe the linearity or nonlinearity of the temperature profiles. Note that with the exception of the P-3 profile, all profiles are fairly linear. This indicates that the thermal conduction is the predominant heat transfer mechanism for the regions sampled. There are a few temperature values (in both P-2 and P-3) that deviate from a straight line for values of the radial distance < 1 m (natural log < 0). At these locations, fractures were mapped in close proximity (within a few centimeters) of the thermocouple locations. This close proximity suggests that the depressed temperature values within the boiling region are caused by fractures. At least two explanations can be postulated:

1. The fractures create more permeable flow paths for vapor to escape the system. As water is converted to vapor and allowed to escape, energy is removed from these locations. This energy is therefore not available to elevate the rock temperatures.

2. The fractures also create flow paths along which drilling water moves downward. Borehole P-3 is lower in elevation than P-2. The matrix adjacent to these fractures might have imbibed some of the drill water, thereby increasing the initial saturation near the fractures. This elevated saturation would also tend to depress the local temperature for the same reason as stated above in explanation 1.

The temperatures along borehole TC-2 are generally cooler than those in other boreholes at the same radial distance. The temperatures in P-2 are the highest among the five boreholes. Boreholes TC-1, P-1, and P-3 registered about the same temperatures. These differences in temperature are probably due to the

heterogeneous thermal properties of the rock mass. The almost linear portion of these curves at larger radial distances indicates that conduction is probably the main heat transfer mechanism. Also, the TC-2 profile shows a more shallow slope, which implies that the thermal conductivity of the rock around TC-2 is higher than at other locations.

A comparison of the P-2 and P-3 temperature profiles in Fig. 9-10 shows that the temperatures in P-3 are consistently lower than those in P-2. This is probably due to the higher temperatures measured at the top of the container. Air circulation within the heater container (i.e., hotter air rising to the top of the container) may have caused the asymmetry in temperatures.

Figure 9-11 shows the temperatures for thermocouples 86 through 89 as a function of time. These thermocouples are located below and to the side of the heater (Fig. 9-12). Thermocouples 86 and 87 show typical profiles of temperatures within the boiling region. The temperature increased quickly at the beginning of heating, then became almost linear with time. At these later times, the temperature-time plot has no obvious change of slope. A change in slope would indicate a change in the thermal conductivity and heat capacity of the rock. At later heating times, changes in slope may be attributed to the latent heat capacity of the water as the water boils or condenses in the rock mass.

Thermocouples 88 and 89 in Fig. 9-11 show very atypical temperature profiles. Note that the maximum temperature for both profiles is $\sim 97^{\circ}\text{C}$. Also the profiles remained near the maximum temperature for 70 or more days even though the rest of the rock mass continued to increase in temperature during this period (maximum power phase). In addition, the slope on the left side of the flattened portions of these two profiles rapidly increased before the flattening occurred. This indicates that additional energy was being deposited at these locations. We postulate that condensed water with near-boiling temperature moved into this region from regions above the heater as illustrated by the conceptual model shown in Fig. 9-13. We recognize the possibility that this type of temperature signature is due to a heat pipe effect, but we consider this unlikely because of the rapid increase in slope observed prior to the flattening.

9.2.5 Changes in Air Permeability

Air permeability testing was conducted along sections of the heater emplacement borehole before heating and at the end of the power rampdown phase of the test. The objectives of this test were to characterize the *in situ* permeability of the fractured tuff around the heater borehole and to determine the effect of a heating and cooling cycle on rock mass permeability. A number of permeability measurements were made along packed-off sections of the borehole before the rock mass was heated and again after all heating was completed.

We used steady-state air-injection to measure the permeability. Inflatable packers were placed in preselected sections of the borehole to isolate these sections for testing. Preheating and postheating permeability values are compared in Fig. 9-14. Equivalent porous medium permeabilities along the heater borehole are also compared with mapped fracture locations. The permeabilities shown here were measured at a nominal pressure of 34 kPa (5 psi). The permeability of a 36-cm-long (14.2-in.-long) test zone varies from a minimum of 0.04 darcy (D) to a maximum of 150 D. The higher permeability value corresponds to a highly fractured zone, a few inches thick, at a depth of about 7.7 m (25.3 ft) from the collar.

A comparison of the preheating and postheating profiles in Fig. 9-14 shows that portions of the measured region had increases in gas permeability as a result of the heating cycle. Note that the greatest percentage change occurred near the center of the heater element location. This is also the portion of the borehole with the fewest fractures mapped. We postulate that the increase in permeability is due to an increase in the number of small fractures (microcracks) intercepting the heater borehole. Television surveys of the borehole showed no change in the visible fractures relative to the preheating survey. This implies that any new fractures were small enough to escape detection. Given that the lowest permeabilities were measured in the region of greatest change, increases in microfractures would have a relatively greater effect here than in regions with a higher preheating permeability. Note that the increased permeability is low when compared with the natural heterogeneity in air permeability along the borehole.

9.2.6 Steam Invading the Heater Emplacement Borehole

The thermal loading exerted by the heater dries the partially saturated rock surrounding the emplacement borehole. Vapor pressure gradients drive steam into pressure sinks such as the borehole and fractures (see Fig. 9-1). Steam may also move along the fractures toward the borehole or move outward and condense where the temperatures are sufficiently cool. The moisture entering the heater emplacement borehole was collected to provide a measure of the resistance to vapor transport toward the heater relative to the resistance to transport away from the heater as a function of time.

The moisture migrating into the heater emplacement borehole was collected using a high-temperature inflatable packer fitted to a 51-mm (2-in.) i.d. aluminum pipe. The packer sealed the borehole 50 cm (19.7 in.) outward (i.e., toward the collar) from the heater and allowed the steam to flow through the aluminum center pipe, condense, and flow to the borehole collar and into a collection device (the isolated section remained unpressurized at all times). The heater emplacement borehole had a slope of 5° downward to the collar to facilitate the collection of the condensed moisture.

Figure 9-15 presents the results from an analysis of the water collection rates during the test. Also shown for comparison is the partial pressure of water within 15 cm of the intake for the steam collection system; the partial pressure values are calculated based on relative humidity and air temperature measurements. These data show that an insignificant volume of water was collected within the first two weeks of the experiment. Thereafter, the rate of water collection reached a maximum of ~0.05 l/day, which is less than the value of ~0.5 l/day predicted by the scoping calculation. The reasons for this discrepancy are unclear at present. One possible explanation is that the packer temperature at the intake point for the system is below the dew point. This might have caused some vapor to condense, pond, and possibly drain into fractures, instead of entering the center pipe at the packer. Temperatures at some points on the packer suggest that packer surfaces could have acted as condensation points. Another possible reason for the discrepancy is that the

scoping calculations assume an infinitely long heater. This assumption would result in a substantial overestimate of the steam produced.

The water collection rate (Fig. 9-15) peaked at about day 50 and then decreased between day 50 and 90. We did not expect this decrease and have not yet explained it. Note that the partial pressure of water in the air remained approximately constant between days 50 and 128. All other conditions being equal, we expected the moisture collection rate to remain constant if the partial pressure of the air in the heater borehole remained constant. The partial pressure of water started to decrease as expected on day 128 when the power rampdown phase began.

Another unexplained aspect of the moisture collection rate is the abrupt water collection rate decrease at about day 90. This signature may be an indication of problems with the sensor; however, post-test calibration of the sensor did not indicate that the sensor was flawed.

9.2.7 Summary

The G-Tunnel tests provided valuable experience that will improve our ability to conduct the EBSFT planned for the ESF in Yucca Mountain. The results from the G-Tunnel tests indicate that many environmental conditions expected to develop around a heater in welded tuff are as described in Fig. 9-1. The test also showed us which of the applied measurement techniques performed adequately under realistic environmental conditions and which ones may need to be modified or replaced.

The G-Tunnel tests confirmed elements of the conceptual model of predicted environmental conditions. Test results confirm that a dry zone develops around the heater borehole (refer to the conceptual model in Fig. 9-13) and that the degree of drying increases with proximity to the heater. A "halo" of increased saturation develops adjacent to the dry region and migrates away from the heater as rock temperatures increase. Some of the fractures intercepting the heater borehole increase the penetration of hot-dry conditions into the rock mass. A buildup of pore gas pressure develops in rock regions where vigorous evaporation is occurring.

During the portions of the test when the heater power was gradually reduced and eventually turned off, the dry region around the heater cooled off and slowly

regained water (refer to the conceptual model in Fig. 9-16). Rewetting of the dry region occurred first in the rock above the heater and in the rock adjacent to fractures.

To explain the differences in the drying and rewetting behavior above and below the heater, we developed conceptual models that are based on the results described here and on our numerical modeling study. In general, we found that water vapor generated in a matrix block moves toward the closest fracture face (or toward the surface of the heater borehole if the block is adjacent to the borehole). Upon entering the fracture, water vapor tends to move radially outward through the fracture system until encountering condensation conditions. The heater borehole moisture collection system and the condensation on the heater packer cause some of the vapor in the fractures to move radially inward toward the heater hole. Water that condenses above the heater drains downward through the fractures. Much of this downward flow intersects the boiling zone and is reboiled, thereby slowing the upward progress of the boiling front. We observed that some of the downward flowing condensate reboiled at the lower flank of the heater, thereby stabilizing the boiling front at that location. Water that condenses below the heater drains away from the boiling zone.

Since the matrix imbibition rate is slow relative to the condensate generation and drainage rates, most of the downward-draining condensate located below the heater left the system before it could be subsequently reboiled. We also observed that the boiling zone effectively acted as an "umbrella" shielding the rock below the heater from the downward drainage of condensate generated above the heater. Rewetting of the rock above the heater and to one side of the heater was partially the result of condensate drainage in fractures. Throughout the fractured rock mass, rewetting also occurred via binary diffusion of water vapor (driven by relative humidity gradients) and via Darcy flow (driven by pressure gradients). As this water vapor reached drier rock, it condensed along the fracture faces (by capillary condensation) and was imbibed by the matrix.

Measurements of air permeability made along the heater borehole prior to heating show that the fracture system exhibits a strong heterogeneity in fracture

permeability. Measurements made after the heater was turned off show that there was an increase in air permeability as large as an order of magnitude for the rock that reached the highest temperatures.

The test also yielded some surprises in terms of environmental conditions. The temperature above the heater container was $\sim 30^{\circ}\text{C}$ (54°F) higher than below the container. This condition might be a consequence of hotter air accumulating at the top of the container; it may also be related to the higher moisture content below the heater borehole. The amount of steam that invaded the heater borehole is much less than that predicted by the scoping calculations. The reasons for this discrepancy are not clearly understood, but they might be a result of an inadequate system used to collect and condense the steam or an indication of invalid assumptions used in the scoping calculations.

Recently, J. Nitao used a discrete fracture model (DFM) to re-analyze the results of the G-Tunnel test. The DFM was able to predict the observed thermal hydrological processes during the G-Tunnel test. The re-analyses show that gravity drain and buoyant gas-phase convection are likely reasons why condensate buildup in the matrix was not observed in the test. Preferential drying below and wetting above the heater lends some support for the possibility that buoyant convection in the fractures is a factor driving moisture movement. Temperature predictions by all models were good, substantiating that heat transfer in the rock was primarily by thermal conduction. Because of the short duration and small spatial scale of the test, the local condensate drainage flux during the G-Tunnel test was probably much higher than that to be expected for a repository beyond the first few hundred years. The results of the analyses are presented in Chapter 1.

9.3 Large Block Test

The objectives, goals, and plans of the Large Block Test (LBT) are described in Lin (1993, 1994). Detailed engineering plans for conducting the LBT were also completed. Originally, as described in Lin (1993), the objectives of the LBT were to conduct tests of the coupled TMHC processes in a $3 \times 3 \times 4.5$ m block of Topopah Spring tuff with

constant stress and adiabatic boundary conditions on the vertical sides. Particularly the LBT was designed to test thermally driven dryout and condensation, condensate refluxing, and the related mechanical and chemical responses of the block. The goals were to heat the large block from five heaters in a horizontal plane at about 2.75 m from the block top, with guard heaters on the sides and constant temperature controls at the top, to maintain a one-dimensional (1-D) thermal gradient in the block. The maximum temperature at the heater horizon would be about 140°C, and the temperature at the top would be about 60°C. A constant stress on the surfaces of the block would be maintained at about 4 MPa. The steady state of the temperatures would be maintained for about four to five months, then the heaters would be turned off to start a natural cooling process. The fore-mentioned instruments would be installed in boreholes in the block and on the block surfaces to have 3-D measurements of the parameters. Scoping model calculations have been performed to facilitate the test design (Lee, 1995a,b). Based on the scoping model calculations, we expected to observe a dryout region of about 2 m wide near the heater plane, a condensate zone of about 1 m thick at both above and below the dryout zone.

Due to budget constraints, we eliminated the load-retaining steel frame to maintain a constant stress of 4 Mpa and replaced it with a strap system to maintain the integrity of the block during the test. Also, we gave up the plan to have the *in situ* monitoring of chemical species. We will depend on the post-test examinations of the evidences of rock-water interaction on the fracture surfaces to evaluate the chemical part of the coupled TMHC processes. Another modification of the original test scope was that the active controls for an adiabatic boundary condition on the sides of the block (the guard heaters) was replaced by passive thermal controls, using insulation materials. This modification of the boundary control did not have much affect on the intended test. Thermal conduction calculations indicate that using insulation materials on the sides can keep the temperature distribution in most parts of the block very similar to a 1-D case. The temperature in a region of a few centimeters in thickness from the surface of the block will have significant lateral gradient. However, more sophisticated model calculations will be required when the data are analyzed to take the lateral heat flux into consideration. Currently, the

block has been isolated and all boreholes for installing instruments have been drilled. Figure 9-17 shows the boreholes in the large block. Some small blocks of the same rock type have been collected from regions adjacent to the large block for testing hydrological properties and thermal-hydrological processes in the laboratory. Some of the laboratory test results have been reported in Chapter 2. But the block has been mothballed until further notice from the Yucca Mountain Site Characterization Project.

All of the pre-test characterization of the large block has been completed. These include the bulk air permeability of the block determined by using single borehole injection before isolating the block, neutron logging to determine the initial moisture content in the block, matrix water permeability and connected porosity of cores collected during the drilling of the boreholes, the fracture distributions on the five surfaces of the block and on the surface prior to cutting the block, and video imaging in every borehole. The results of the pre-test characterization will be presented later in this section. The water permeability of one of LBT cores as a function of temperature is reported in Chapter 2.

Figure 9-18 shows the bulk air permeability of the block as a function of depth. The permeability was determined by single borehole injection before the block was isolated. The permeability varies from about 10^{-16} m² to more than 7×10^{-12} m². Intersection of fractures with the injecting borehole was the deterministic factor of the permeability variation. Because the block is highly fractured (shown later in this section), the bulk air permeability of the entire block may be more homogeneous.

Some of cores collected during the drilling were used to determine the connected porosity of the matrix. Figure 9-19 shows the matrix porosity as a function of depth. The porosity varies from about 10% to about 13.5%. The porosity of the TSw2 unit of the Topopah Spring tuff in Yucca Mountain is $12.1 \pm 3.6\%$ (Reference Information Base, YMP/93-02, Rev. 0). The matrix porosity was used to determine the water saturation from the neutron logs. Figure 9-20 shows the moisture content of the block determined by neutron logging in some of the vertical holes before and after the cutting of the block boundaries. The water saturation of the block is between 60

and 80%. This level of water saturation will provide enough moisture for creating an observable dryout zone and a condensate zone. Cutting of the block boundaries with water did not change the moisture content of the block interior.

Fractures on the five surfaces of the block were mapped carefully. Because the surfaces were cut smooth, it was possible to conduct very detailed fracture mapping. But it was difficult to determine dip on the top surface and strike and true dip of most of the fractures on the vertical surfaces. Figures 9-21 through 9-25 show the fractures on top, north, west, south, and east sides of the block, respectively. These fracture maps were combined into a 3-D physical model, which was used to project the fractures in the block to locate the instrument holes. These fracture maps and video images in each borehole will be used to infer fractures within the block, using fracture projecting software, such as Earth Vision.

Prior to cutting the block, the cleaned off ground surface was mapped in detail. After it was cut, this area became the top of the block and was subsequently mapped (see Fig. 9-21), but this data was not analyzed at the time of this report. Because the pre-cut surface was excavated, rather than cut smooth, dip measurements were made of many of the fracture surfaces. Block characterization indicates that the fracture system is similar to that observed underground in the ESF Access Drift. Figure 9-26 shows comparison plots of the fractures mapped on the top of the LBT prior to block cutting and that in the ESF. Comparison of the data from the ESF [Fig. 9-26(b)] and the LBT [Fig. 9-26(a)] shows that fractures in the LBT are similar to those observed in the ESF in the TSw2 unit (Barr et al., 1996) with the exception that the low-angle fractures mapped in the ESF are not represented in the LBT mapped features. This difference is because the data set is from the horizontal surface and therefore low-angle sets would not be observed. Low-angle fractures were observed on the sides of the LBT; however, that data set has not been analyzed and will be reported in subsequent revisions of the NFER.

It may also be apparent that the strike of the fracture set is more northerly in the LBT data set. This may be a result of several things. (1) It is quite likely that there is orientation bias in the data from the ESF, specifically the main drift is nearly north-south and therefore would not show northerly striking features that often (Yow and

Wilder, 1983). (2) There may have been rotation of the near surface block that forms the Fran Ridge. or (3) There may be a declination setting difference in the compasses used for these different mapping exercises. Based on past experience, it is judged that the orientation bias is very likely, although it is impossible to know if that is the only reason for the difference in strike. Once data is available from the ESF alcoves that are oriented east-west, the significance of orientation bias can be evaluated and perhaps a composite fracture stereoplot could be produced by normalization techniques as discussed in Wilder and Yow, 1984. If compass setting errors are the reason for the difference, subsequent analyses should resolve this since there is a set of measurements that were conducted based on surveyed block corners.

Regardless of the minor differences, from the standpoint of fracture sets, the LBT rock seems to be a good representation of the fracture system that has been observed in the ESF. The fractures are dominantly in one vertical set that has north to northwesterly strikes.

A comparison of fracture spacing may be somewhat misleading since the same criteria on fracture length was not applied. However, the fracture system observed in the LBT, as inspection of Fig. 9-27 indicates, is similar to that reported from the ESF. There is about 0.75 fracture/ft (excluding short fractures so that the comparison with ESF is more appropriate) along any of the east-west grid lines and nearly 0.5 fracture/ft along the north-south grid lines (more comparable to the drift orientation). Fracture densities in the ESF are around 3-4 fractures/m, which is equivalent to 1 fracture/ft seen on the LBT map. Although the fracture density mapped on the excavated surface was about half that observed in the ESF, the number of fractures observed once the top was cut (Fig. 9-21) was comparable.

The orientation bias discussed here is also indicated in the fracture spacing data from the LBT, since there are about 50% more fractures seen in the east-west transects than in the north-south transects. Thus there would be rather different fracture distributions in the north-south line surveys (essentially equivalent to the ESF drift) than in the multi-directional survey obtained by the mapping of a flat surface in the LBT. Further studies of this bias will be conducted in the future but were not available at the time of this report.

On the basis of the fracture comparisons, it appears that the fracture system exhibited in the LBT is comparable to that observed underground. Based on the permeability measurements, the fracture system permeability is comparable. Also as mentioned, the moisture content is comparable to what is understood for the saturation conditions within the ESF, and the porosity of the rock matrix is also comparable. No assessment of the geochemical or mineralogical characteristics is available at this time. However, there is every indication that tests performed on the LBT could test the process models in an appropriate rock mass.

9.4 ESF Thermal Tests

The ESF Thermal Tests (ESFTTs) will be conducted in Alcove 5 off the ESF Main Drift. Alcove 5 is located at about the 2.827 km station of the ESF Main Drift. Figure 9-28 shows the plan view of the ESFTT facility. ESFTT consists of two tests: the Single Heater Test and the Drift Scale Test. ESFTT is in the construction state, therefore only the plans and the test designs are reported here. Detailed objectives, design, and planning of the ESFTT can be found in *Test Design, Plans, and Layout for the First ESF Thermal Test, Rev.1, 1996*, prepared by Civilian Radioactive Waste Management System Management and Operating Contractor.

9.4.1 Single Heater Test

As shown in Figure 9-28, the Single Heater Test (SHT) will be conducted on one side of the Observation Drift, at about 41 m from the ESF Main Drift. The main objectives of the SHT are to obtain rock mass thermal and mechanical properties at ambient and elevated temperatures, to evaluate rock bolt anchorage response to the heated conditions, and to observe thermal-hydrological-chemical changes in the rock mass due to the heating. Because the heated volume of the rock mass in the SHT is small (the test block covers an area of about 84 m²), the thermal-hydrological-chemical observation will be mostly for developing *in situ* test experience. Figure 9-29 shows the layout of the SHT. The test region is the block between the Observation Drift, Thermomechanical Alcove, and Thermomechanical Alcove Extension. The

construction and drilling are completed and the instruments are being installed in the holes. The heater is scheduled to be turned on by the end of August 1996.

The 5-m-long heater will be placed in a hole (7 m long), which is drilled into the test block from the Thermomechanical Alcove. The boreholes include: (as shown in the lower portion of Fig. 9-29) four ERT holes, four neutron/RTD holes (for neutron logging and temperature measurements), two chemical holes, two hydrological holes, and two optical extensometer holes. Chemical sensors and fluid extracting devices will be mounted on Science Engineering Associates Membrane In-situ Sampling Technology (SEAMIST) in the chemical holes for monitoring chemical processes. Humicaps and gas pressure transducers will be mounted in packers in the hydrological holes for measuring relative humidity, temperature, and gas pressures. The rest of the boreholes are for mechanical, rock bolts, and temperature measurements. The power output of the heater will be about 4 kW. The rock mass will be heated by a constant power of about 4 kW for about eight months; then the heater will be turned off. Monitoring of thermal mechanical responses, temperature, moisture content, chemical concentration, etc., will be started before the heater is energized, and will continue through the heating phase and the cooling phase.

Pre-test pneumatic tests to characterize the rock mass were completed, finding the air permeability of the test region to be very heterogeneous. The air permeability varies by more than two orders of magnitude. Generally speaking, the region between the heater and the Observation Drift has lower permeability than the region on the other side of the heater, i.e., between the heater and the Thermomechanical Alcove Extension. Also, the inner portion of the block, i.e., the region near the bottom of the heater hole, seems to have greater permeability than the outer portion of the block. Apparent fracturing in a borehole has no strong correlation with the permeability in that hole.

9.4.2 Drift Scale Test

The Drift Scale Test is the second *in situ* thermal test of the ESFTT. Again, the objectives of the Drift Scale Test are described in *Test Design, Plan, and Layout for*

the First ESF Thermal Tests, as mentioned in section 9.4. The main purpose of the Drift Scale Test (DST) is to test the coupled TMHC processes in an *in situ* environment. There will be some thermal mechanical tests for the repository design and construction. The heated area and the heated period will be large and long enough for us to observe the coupled TMHC processes that are relevant to a repository. Figure 9-30 shows the schematic layout of the DST. Figure 9-30(a) shows the plan view of the DST; Figure 9-30(b) shows one of the cross sections of Fig. 9-30(a).

Heaters will be placed in the heater drift and wing heater holes (as illustrated by holes 74 to 123 and 207 to 210). The heater drift will be about 5 m in diameter. The wing heater holes will be about 10 cm in diameter and will be spaced about 1.8 m along the axis of the heater drift. The heaters in the heater drift will be MPC size canisters with heating elements mounted in them so that the temperature on the canister surfaces will be uniform. The linear power density of the heater canister will be about 1 kW/m. Rod heater elements will be placed in the wing heater holes. The power density of the wing heaters will be about 125 w/m² among the inner half of the wing heaters, 175 w/m² for the outer half of the wing heaters. The heater drift will be about 55 m in length; the tip-to-tip span of the wing heaters will be about 28 m. The heated area of the DST will be about 1540 m², which will be big enough for observing large-scale thermal-hydrological processes, such as heat pipe, buoyant phase convection (see Chapter 1.9 for details).

Boreholes for instruments will be drilled radially from the heater drift, from the observation drift to the heater drift, and longitudinally along the heater drift. The goal is to obtain a 3-D coverage of the test region. In addition to the types of boreholes mentioned in section 9.4.1, Rapid Estimation of K and Alpha (REKA) probes will be installed in boreholes to perform *in situ* measurement of the thermal conductivity and diffusivity of the rock mass. The heaters will be heated at constant power for at least three years, which, depending on the responses of the rock mass, may be extended to four years, and a controlled cool-down period will follow the

three- or four-year heating period. Similar to the SHT, monitoring of the responses of the rock mass will cover the pre-heat, heating, and cool-down periods.

Construction of the main (east-west) portion of the Observation drift has been completed. The other part of the Observation drift and the Heater drift will be constructed during FY 1997. Drilling of the boreholes will be started soon, and the heaters are scheduled to be turned on in late FY 1997.

9.5 Large-Scale Long Duration Test

A large-scale long duration test (LSLDT) was incorporated into the field test planning because of the challenges of scale, both temporal and spatial, that must be considered in any testing which is both accelerated in time and therefore in gradients and in limited geometric size. This test was sized geometrically and duration was determined based on numerical analyses. This test is described in *the Study Plan for Engineered Barrier System Field Tests*, as cited in section 9.1; however, current budget planning does not commit to the LSLDT. But, it is discussed here since it is an essential part of the planned testing. If used, this test would have multiple heater drifts with observation drifts located both above and below the heated drifts, as shown in Fig. 9-31. Although at least three heater drifts would be used, five would better address issues such as condensate ponding. The heater drifts would be heated for at least four years, and subsequently extended, depending on the responses of the rock mass at the end of the fourth year. The heating period would be followed by a controlled cool-down period of at least one year and a natural cool-down period, which would be dictated by the cooling of the rock mass.

It is possible that the LSLDT may be merged or combined with the Confirmation Test. The configuration of the LSLDT would be the closest simulation of a repository that can possibly be achieved. Instrumentation for the LSLDT would be similar to that in the DST, with whatever improvement that we can learn from the DST. The distribution of the instruments in the LSLDT would provide a true 3-D coverage of the test region, would be much better than the DST.

9.6 Confirmation Monitoring

Confirmation monitoring of the repository's performance will be conducted in parts of the repository that are constructed and where early emplacement of the waste has been accomplished. Instrumentation for the confirmation monitoring will be similar to that in the DST and the proposed LSLDT. Basically, monitoring will include temperature, moisture content, mechanical responses, and chemical responses of the rock mass around the emplacement drifts. The heat source will be the radioactive decay heat from the nuclear wastes. One of the criteria for designing the methodology and instrumentation for the confirmation monitoring is the long duration of the test, which can be tens or even hundreds of years. Lessons learned from the DST and the proposed LSLDT will be used to select measurement methodologies and instruments that can provide reliable long-term monitoring.

9.7 References

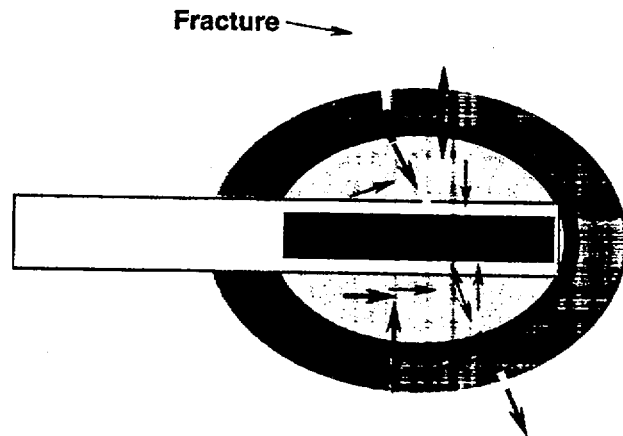
- Daily, W., A. Ramirez, T. Ueng, and V. LaTorre (1989), "High Frequency Electromagnetic Tomography," *Proc. Nuclear Waste Isolation in the Unsaturated Zone, Focus '89* (Am. Nuc. Soc., LaGrange Park, IL), pp. 409-416. NNA.910326.0098.
- Lee, K., 1995a, *Progress Report on Pre-Test Calculations for the Large Block Test*, Lawrence Livermore National Laboratory UCRL-ID-118699, Livermore, CA. MOL.19950406.0143
- Lee, K., 1995b, *Second Progress Report on Pre-Test Calculations for the Large Block Test*, Lawrence Livermore National Laboratory UCRL-ID-122300, Livermore, CA. MOL.19960417.0218
- Lin, W., 1993, *Scientific Investigation Plan for Large Block Testing of Coupled Thermal-Mechanical-Hydrological-Chemical Processes*, SIP-NF-02, Lawrence Livermore National Laboratory, Livermore, CA. NNA.19930419.0032
- Lin, W., 1994, *Activity Plan, AP-LBT-01, Rev. 0, for Large Block Tests of Coupled Thermal-Mechanical-Hydrological-Chemical Processes* (YMP WBS Element 1.2.3.12.4), Lawrence Livermore National Laboratory, Livermore, CA. MOL.19940908.0093
- Lin, W., 1995, *Study Plan for Study 8.3.4.2.4.4, Engineered Barrier System Field Tests*, US. Department of Energy, prepared by CRWMS Management and Operating Contractor/Lawrence Livermore National Laboratory, Office of Civilian Radioactive Waste Management, Washington, DC. MOL.19960425.0195
- Ramirez, A., T. Buscheck, R. Carlson, W. Daily, K. Lee, W. Lin, N. Mao, T. Ueng, H. Wang, and D. Watwood, 1991, *Prototype Engineered Barrier System Field Test*

- (PEBSFT) *Final Report*, A. Ramirez, Scientific Editor, Lawrence Livermore National Laboratory UCRL-ID-106159, Livermore, CA. NNA.19910711.0047
- Ramirez, A., D. Wilder, J. Beatty, T. Buscheck, R. Carlson, W. Daily, R. LaTorre, K. Lee, W. Lin, N-H. Mao, J. Nitao, D. Towse, T-S. Ueng, and D. Watwood (1991), *Prototype Engineered Barrier System Field Tests (PEBSFT), Progress Report through November 1, 1988*, Lawrence Livermore National Laboratory, Livermore, CA, UCID-21640.
- Yow, J., Jr. (1985), "Test Concept for Waste Package Environment Tests at Yucca Mountain," in the *Proc. of the 28th U.S. Symposium on Rock Mechanics*, Tucson, AZ, pp. 1035-1042; also in Lawrence Livermore National Laboratory, Livermore, CA, UCRL-95568.
- Yow, J.L. Jr, and D. G. Wilder, 1983, Planning Exploratory Drilling: The Effect of Blind Zones and Level of Logging Effort, Proceedings of 24th U.S. Symposium on Rock Mechanics, College Station, TX, pp 807-812.
- Wilder, D. G., and Yow, J. L. Jr, 1984, Structural Geology Report, Spent Fuel Test-Climax, Nevada Test Site, Lawrence Livermore National Laboratory UCRL-53381, Livermore, CA.

Data Tracking Information:

9.3 Large Block Test

(Data Tracking Number: LL950103004244.004)



- Heater
- Dry rock
- ▨ Wetter rock
- Rock at ambient conditions
- Condensation
- Steam flow
- Water flow

Figure 9-1. Schematic of a vertical cross-section of a probable hydrologic scenario in partially saturated welded tuff subjected to a thermal load.

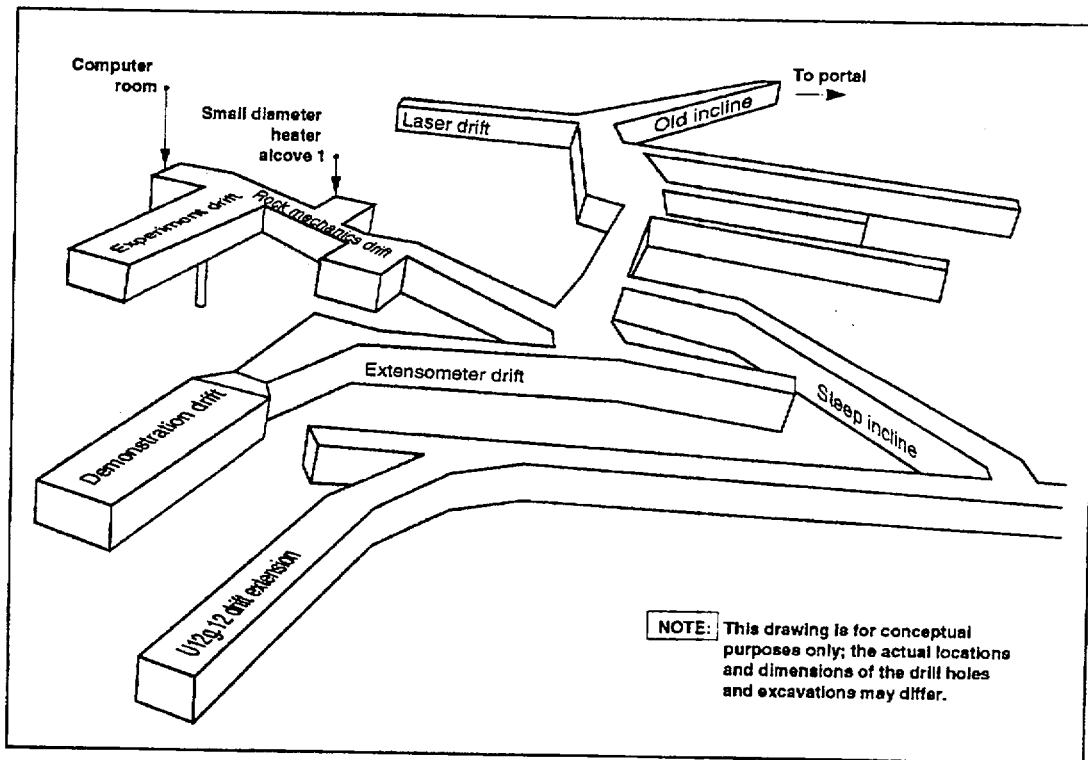


Figure 9-2. G-Tunnel Underground Facility.

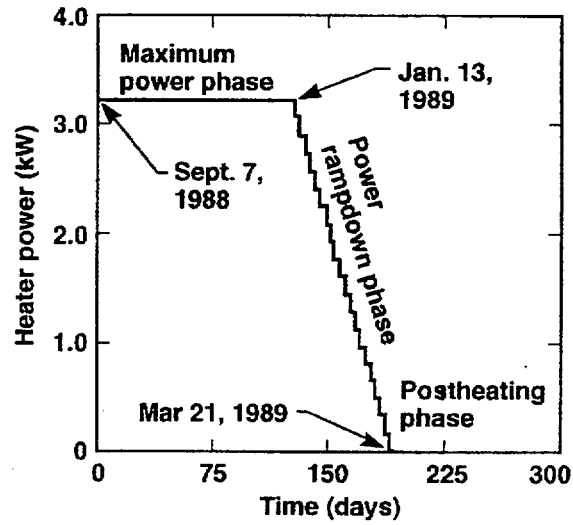


Figure 9-3. Heater power schedule used for the PEBSFT.

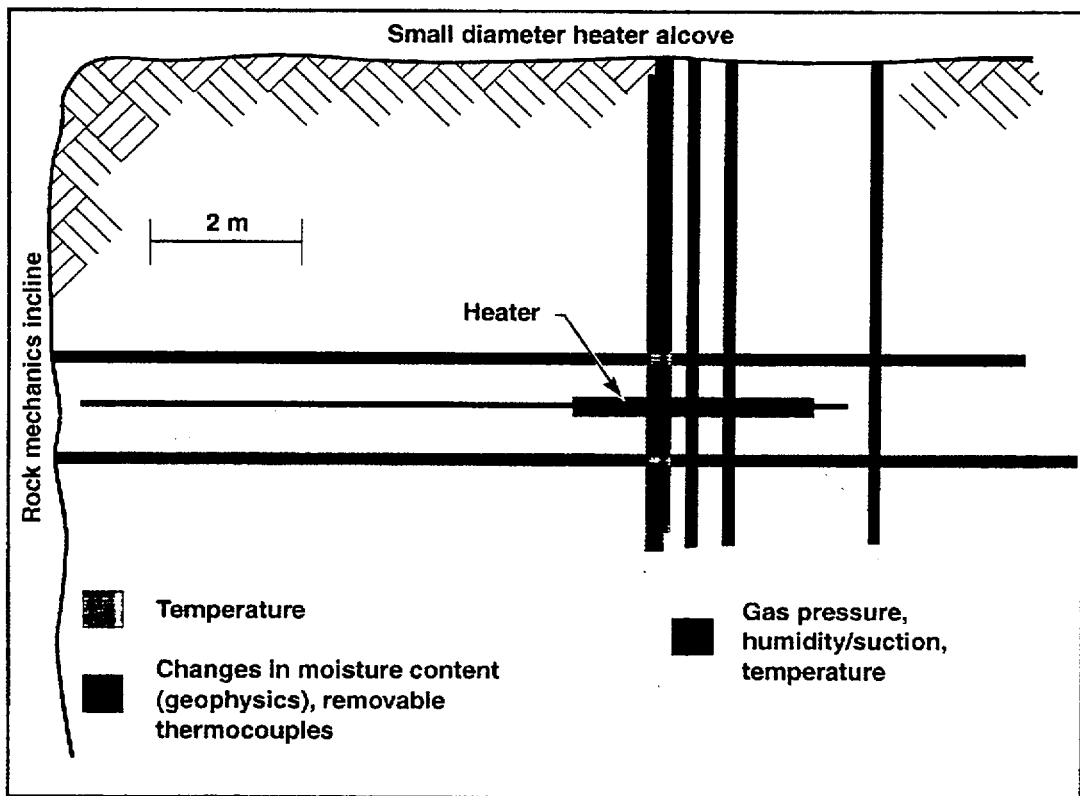


Figure 9-4. Plan view of the as-built borehole layout. The various line patterns identify the type of measurement made in each borehole. The locations of the rock mechanics incline and the small diameter heater alcove in G-Tunnel are shown for reference.

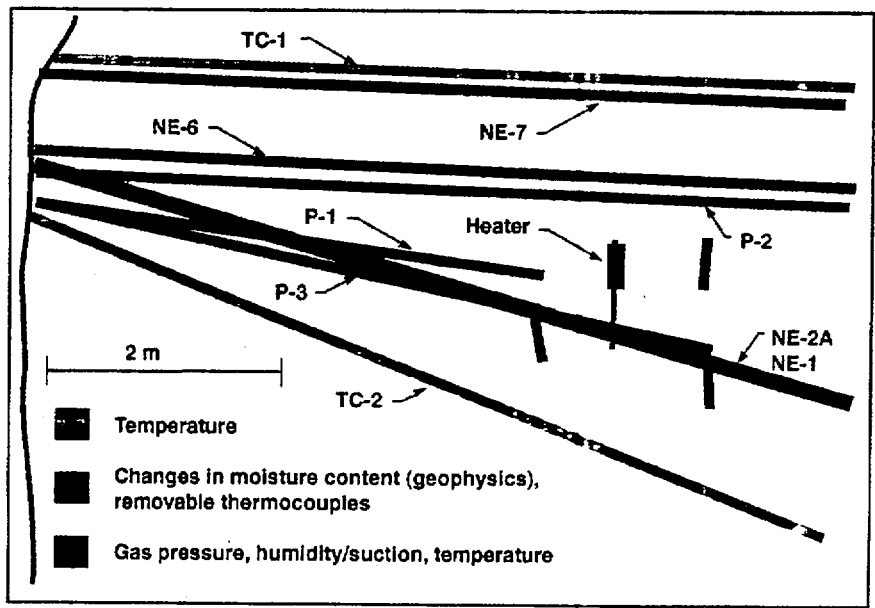


Figure 9-5. Side view of the as-built borehole layout as viewed from the rock mechanics incline. The various line patterns identify the type of measurement made in each borehole.

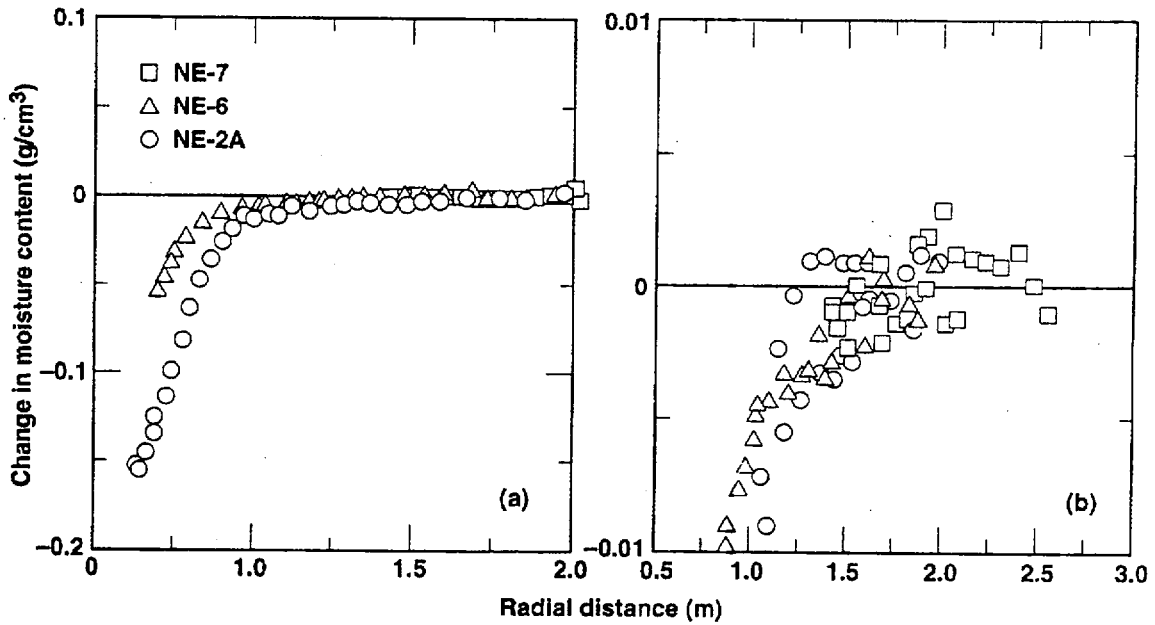


Figure 9-6. Changes in moisture content plotted against radial distance after 70 days of heating (approximately midway through the maximum power phase). A subset of the curves in (a) are shown enlarged in (b). Changes are calculated relative to preheating moisture conditions.

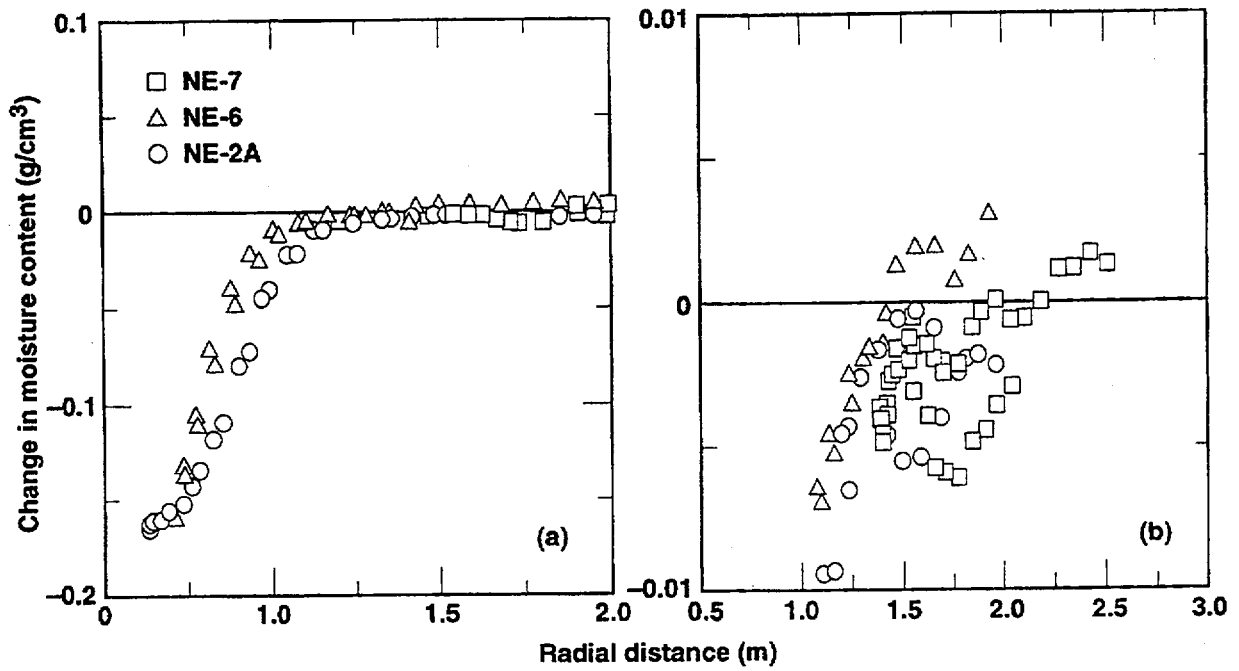


Figure 9-7. Changes in moisture content plotted against radial distance for the next to last day of maximum power heating. A subset of the curves in (a) are shown enlarged in (b). Changes are calculated relative to preheating moisture conditions.

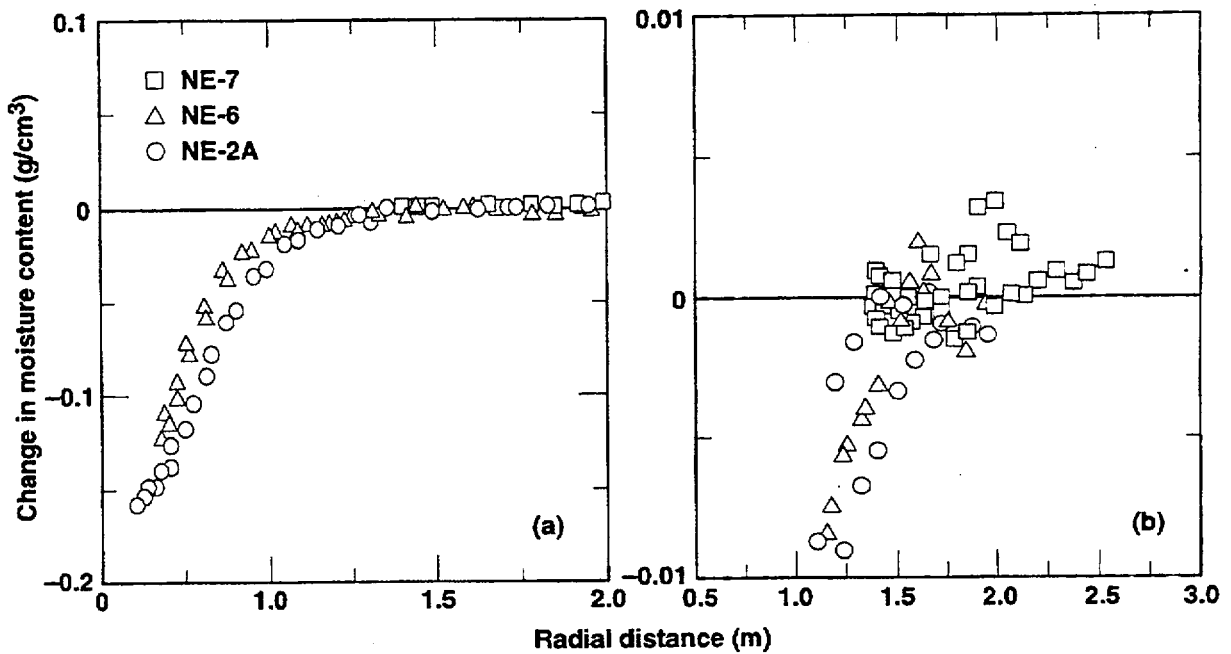


Figure 9-8. Changes in moisture content plotted against radial distance 301 days after start of heating (106 days after heater was de-energized). A subset of the curves in (a) are shown enlarged in (b). Changes are calculated relative to preheating moisture conditions.

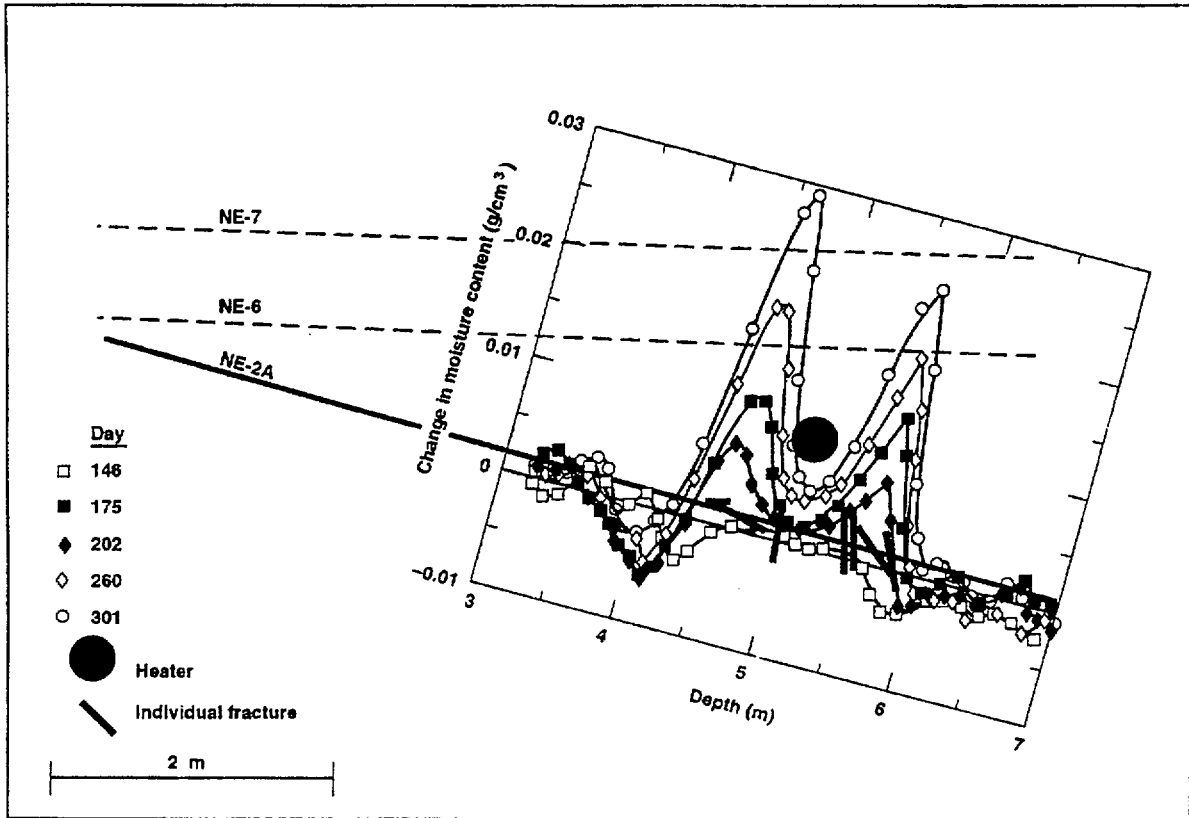


Figure 9-9. Changes in moisture content mapped along borehole NE-2A. Changes are calculated relative to the last day of full-power heating. Fractures mapped are shown for comparison.

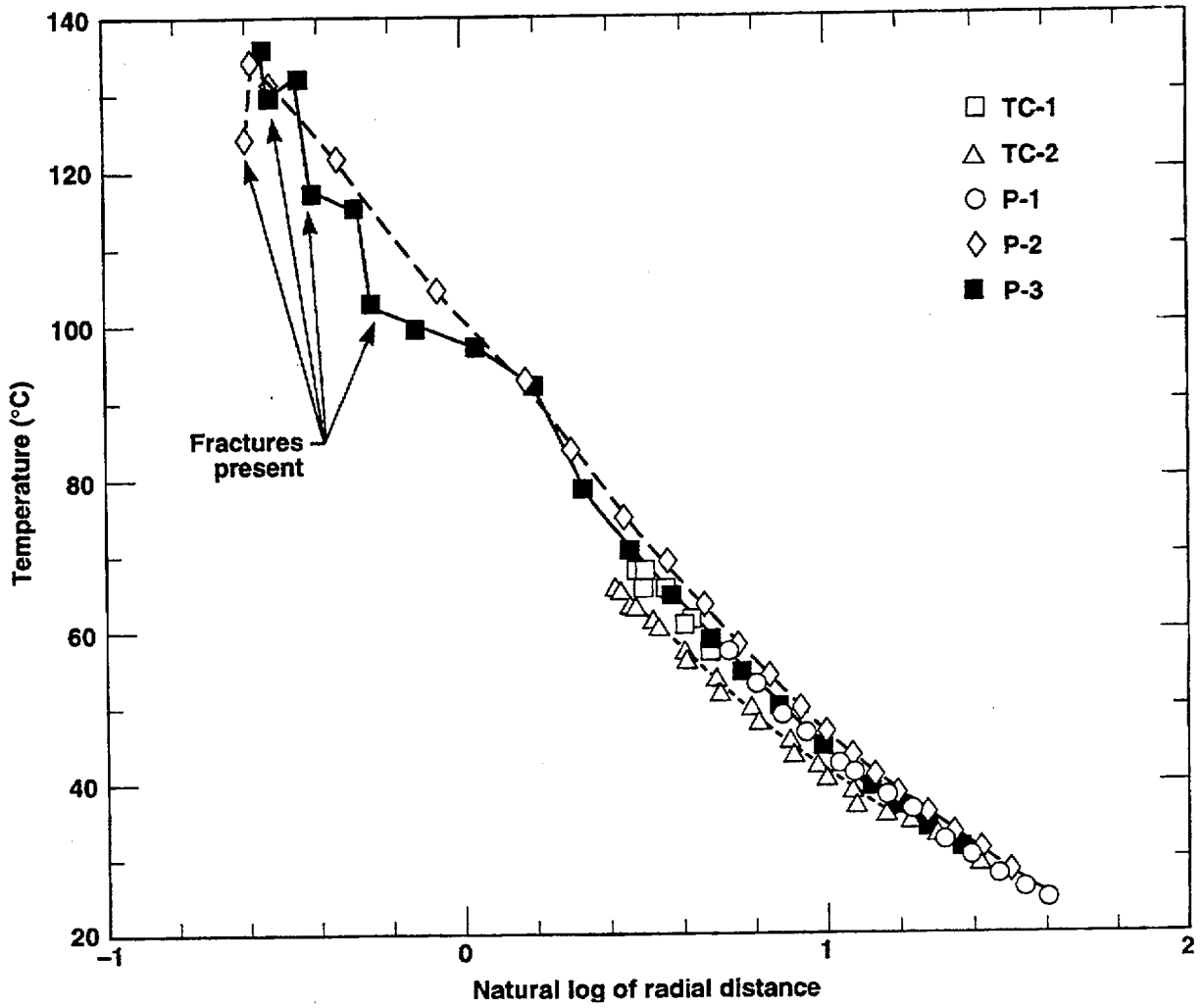


Figure 9-10. Temperatures in various boreholes measured during the last day of full-power heating.

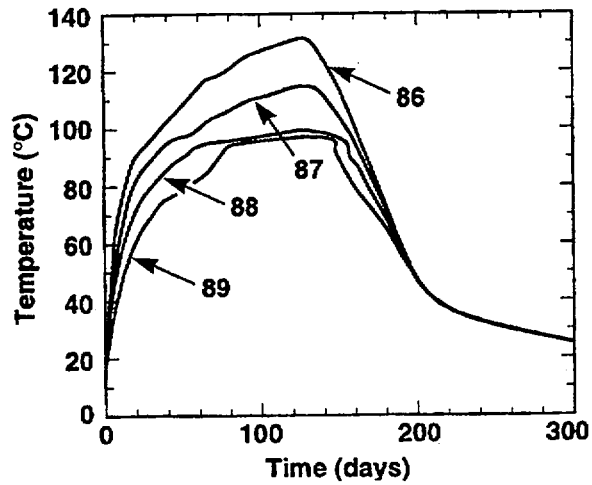


Figure 9-11. Evolution of selected temperatures in the P-3 borehole as a function of time. Thermocouples 88 and 89 show a flattening of the profiles between days 50 and 150 that may be due to the movement of condensed water in this region.

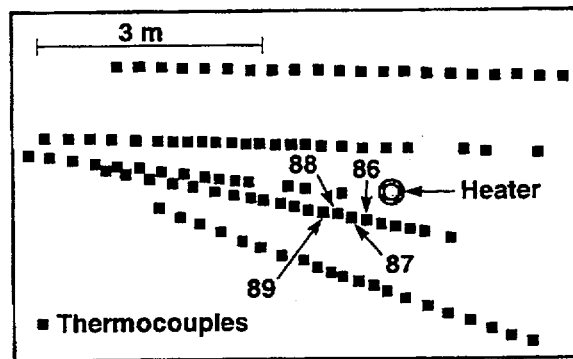


Figure 9-12. Cross-section near the heater midplane, showing thermocouple locations relative to the heater. Data for thermocouples 86 to 89 are shown in Fig. 9-11.

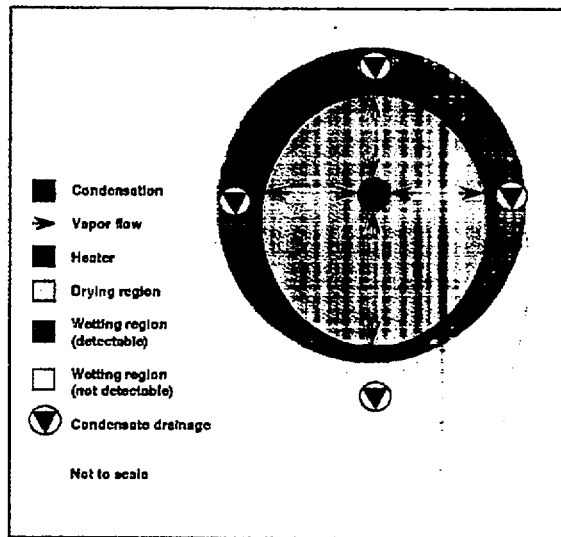


Figure 9-13. Proposed flow phenomena for a fracture perpendicular to the heater axis. The view is along the fracture plane. This conceptual model was proposed as an explanation for the atypical temperatures shown by thermocouples 88 and 89 (shown in Fig. 9-11). Also shown is the increased region of drying and wetting fronts along the fracture.

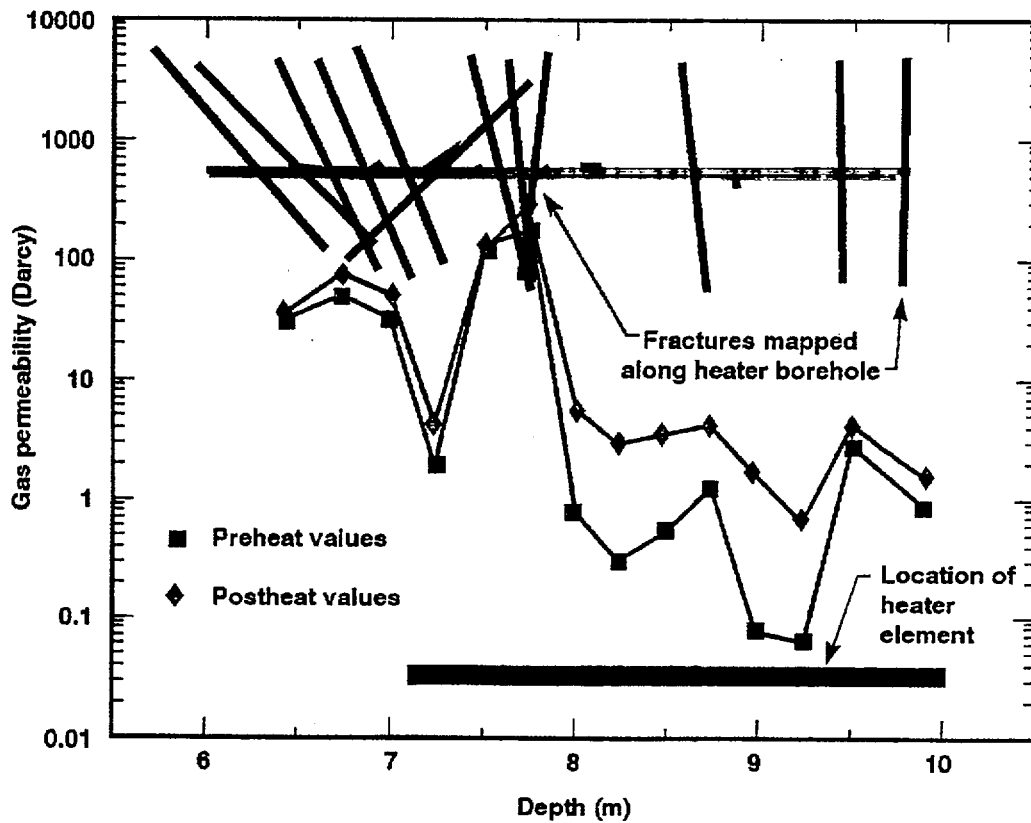


Figure 9-14. Gas permeability measurements made along the heater borehole before and after heating on the borehole.

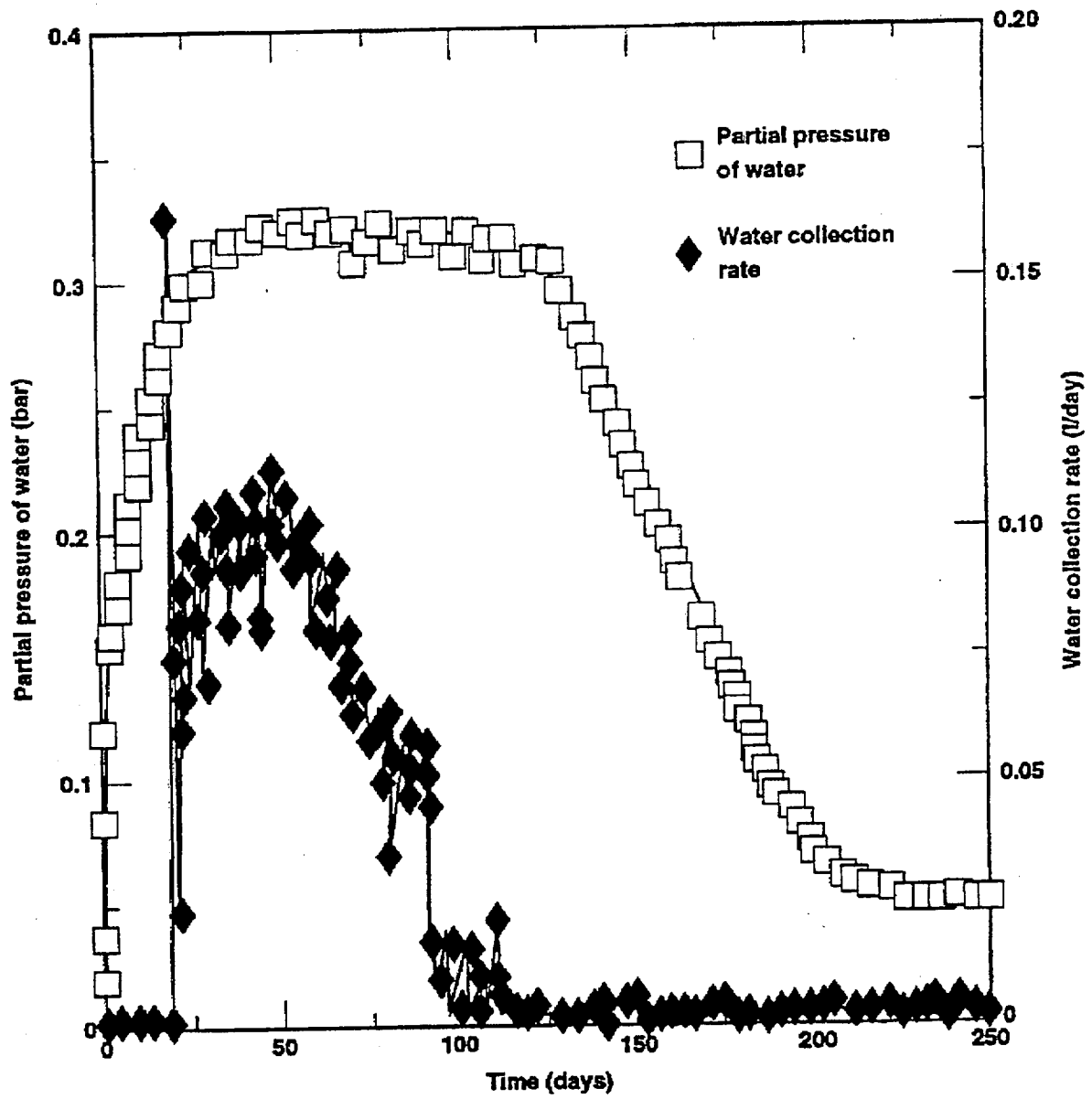


Figure 9-15. Water collection rate and partial pressure of water in the heater borehole air as a function of time.

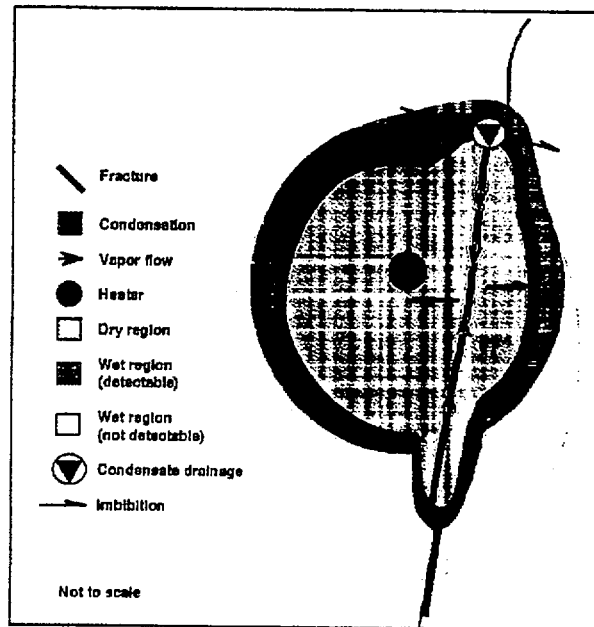


Figure 9-16. Proposed conceptual model of the mechanisms that dominate the dry region rewetting process during cooldown of the rock mass. A transect along a matrix block intersected by a fracture is shown.

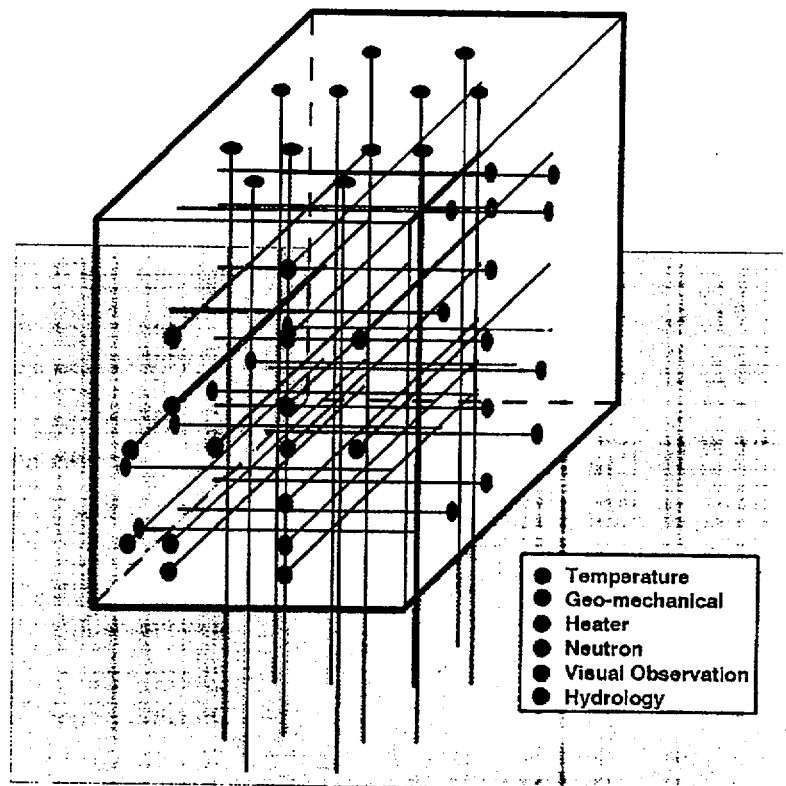


Figure 9-17. Instrument boreholes drilled in the large block for LBT.

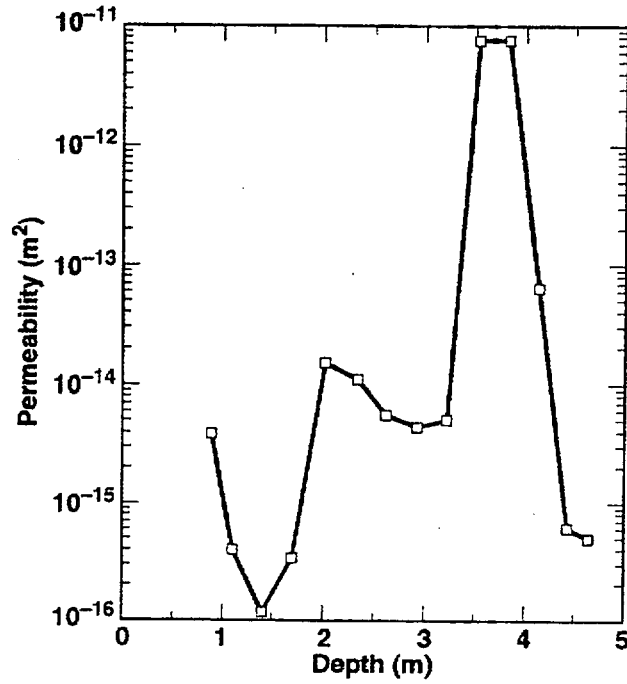


Figure 9-18. Air permeability of the large block as a function of depth measured from a single borehole air injection test in N1 hole.

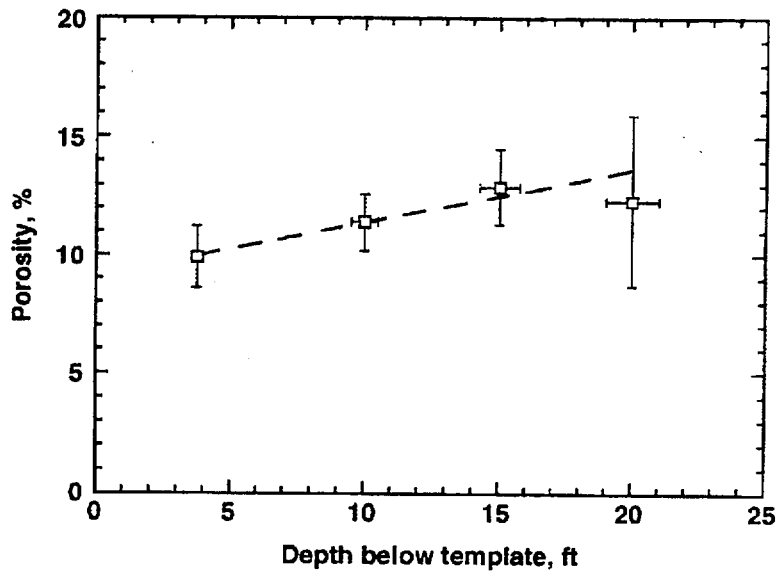


Figure 9-19. Matrix porosity of cores from the LBT as a function of depth.

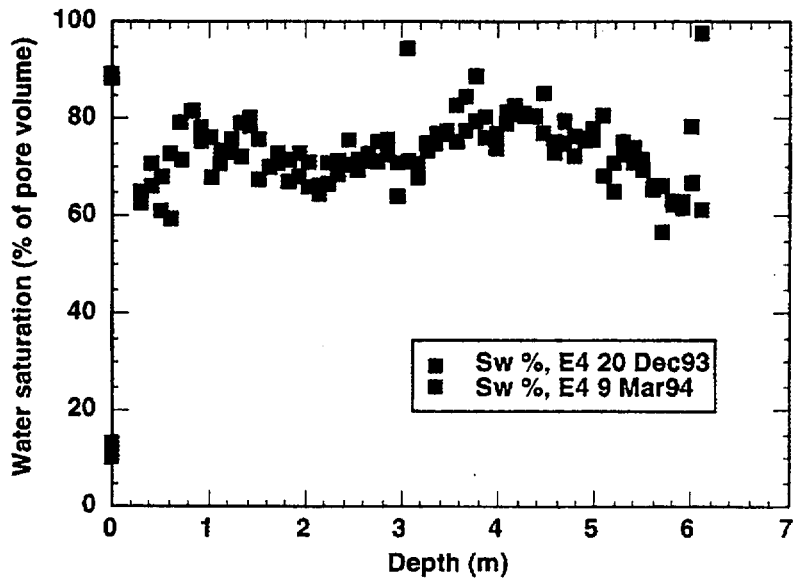


Figure 9-20. Water saturation (percent of pore volume) in a vertical hole, near the middle of the block as a function of depth, determined by neutron logging before and after the sawing.

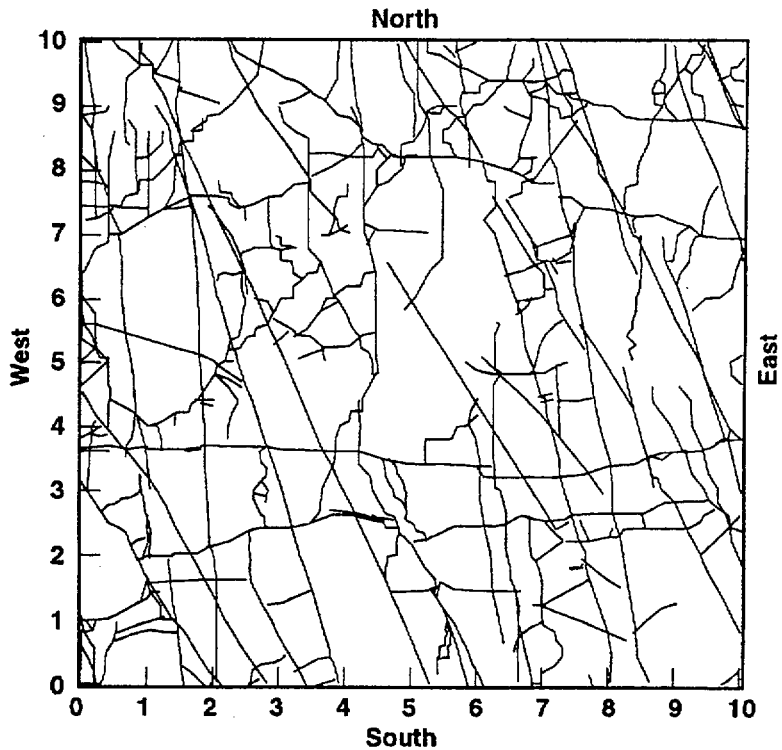


Figure 9-21. The fracture location maps on top of the block, after the top was cut smooth.

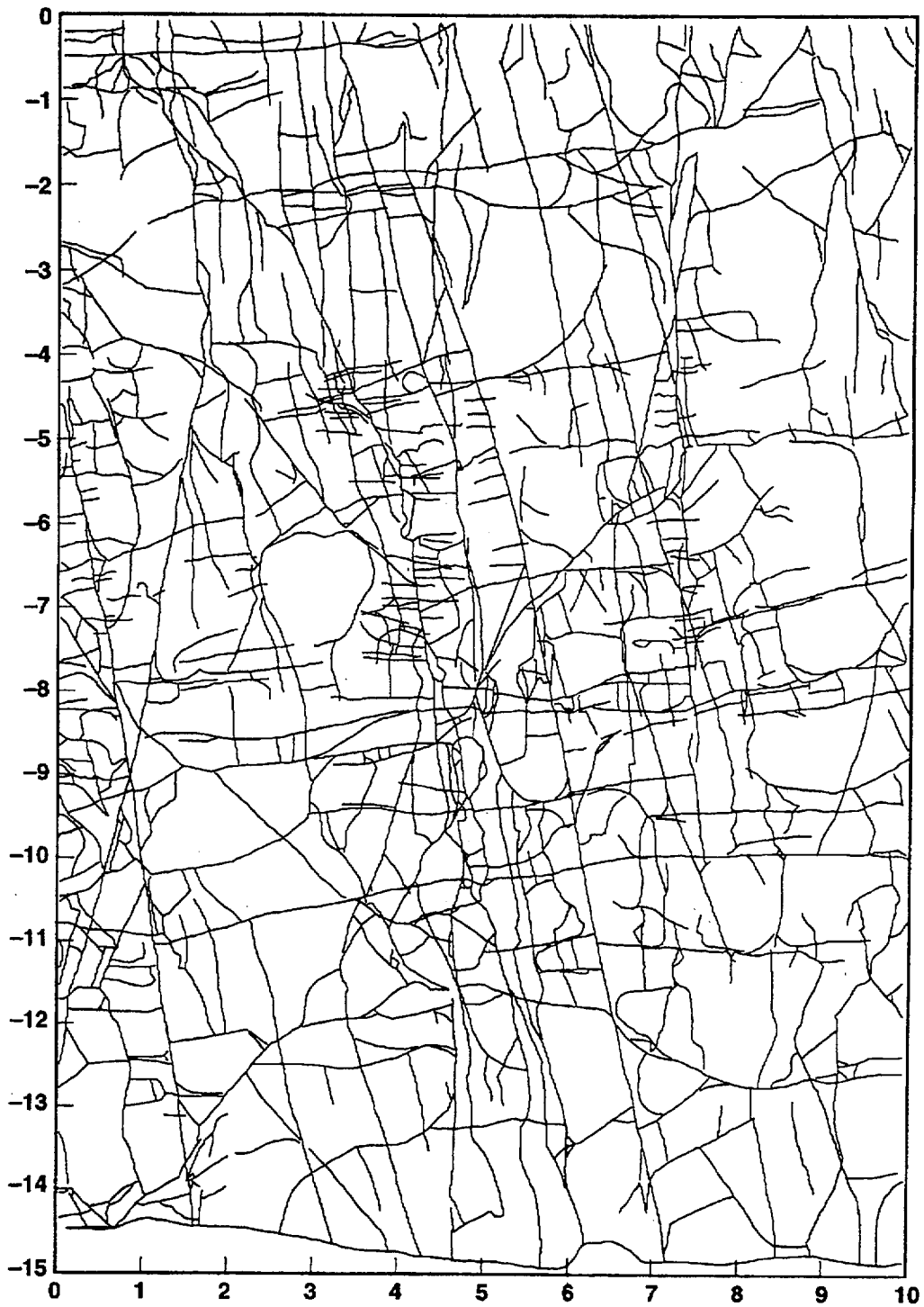


Figure 9-22. Fractures on the north face of the large block. The distance marks are in feet.

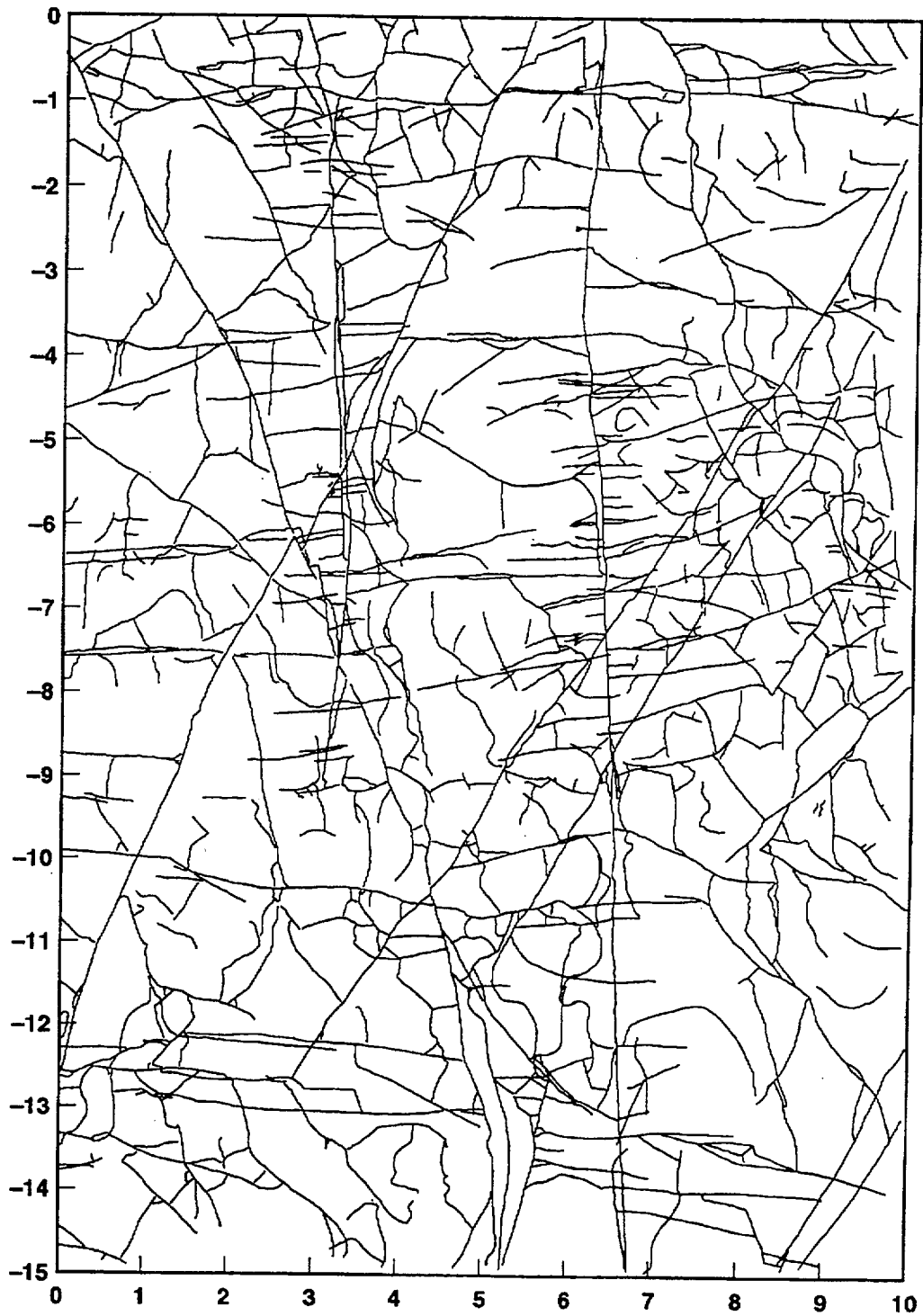


Figure 9-23. Fractures on the west face of the large block. The distance marks are in feet.

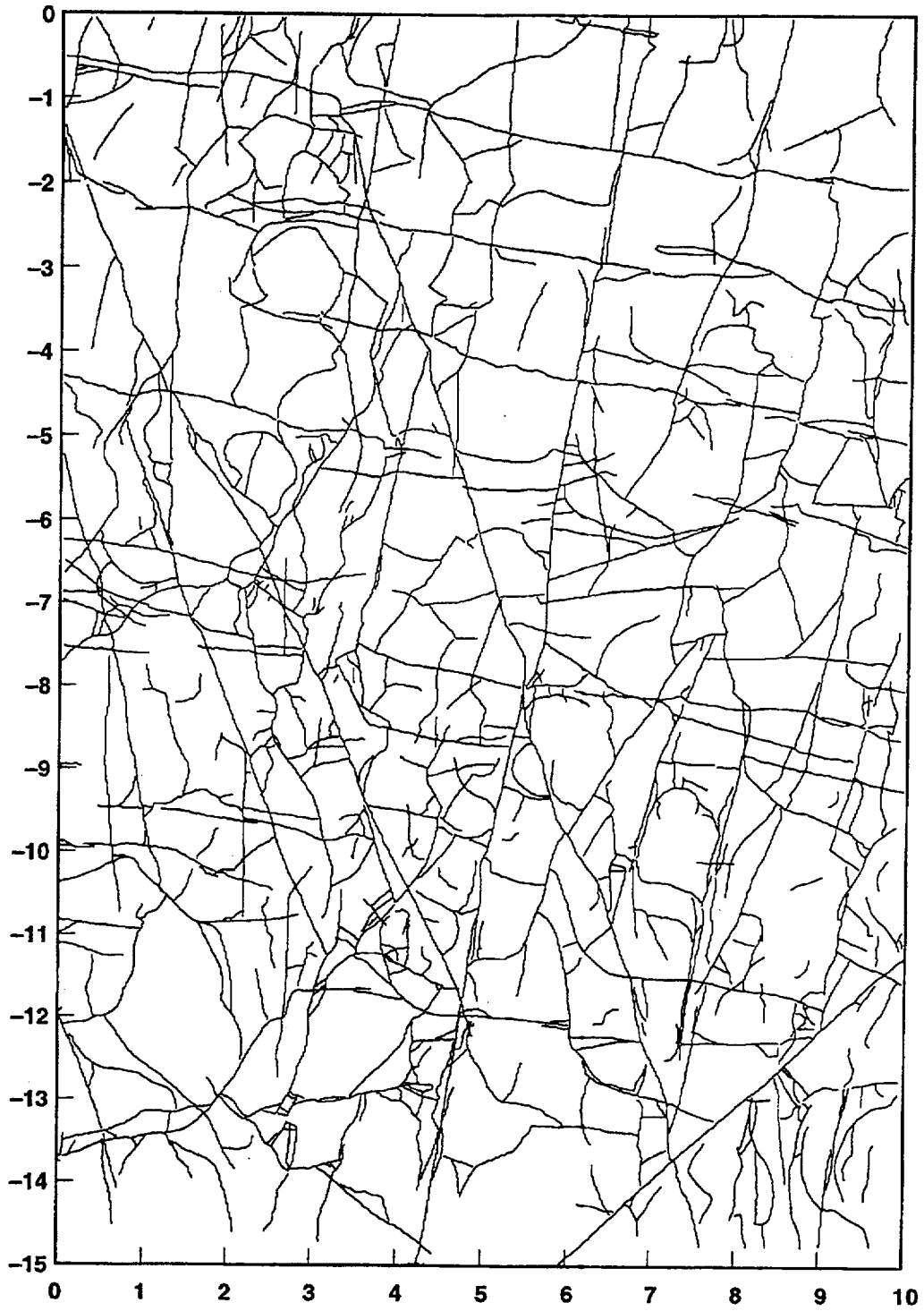


Figure 9-24. Fractures on the south face of the large block. The distance marks are in feet.

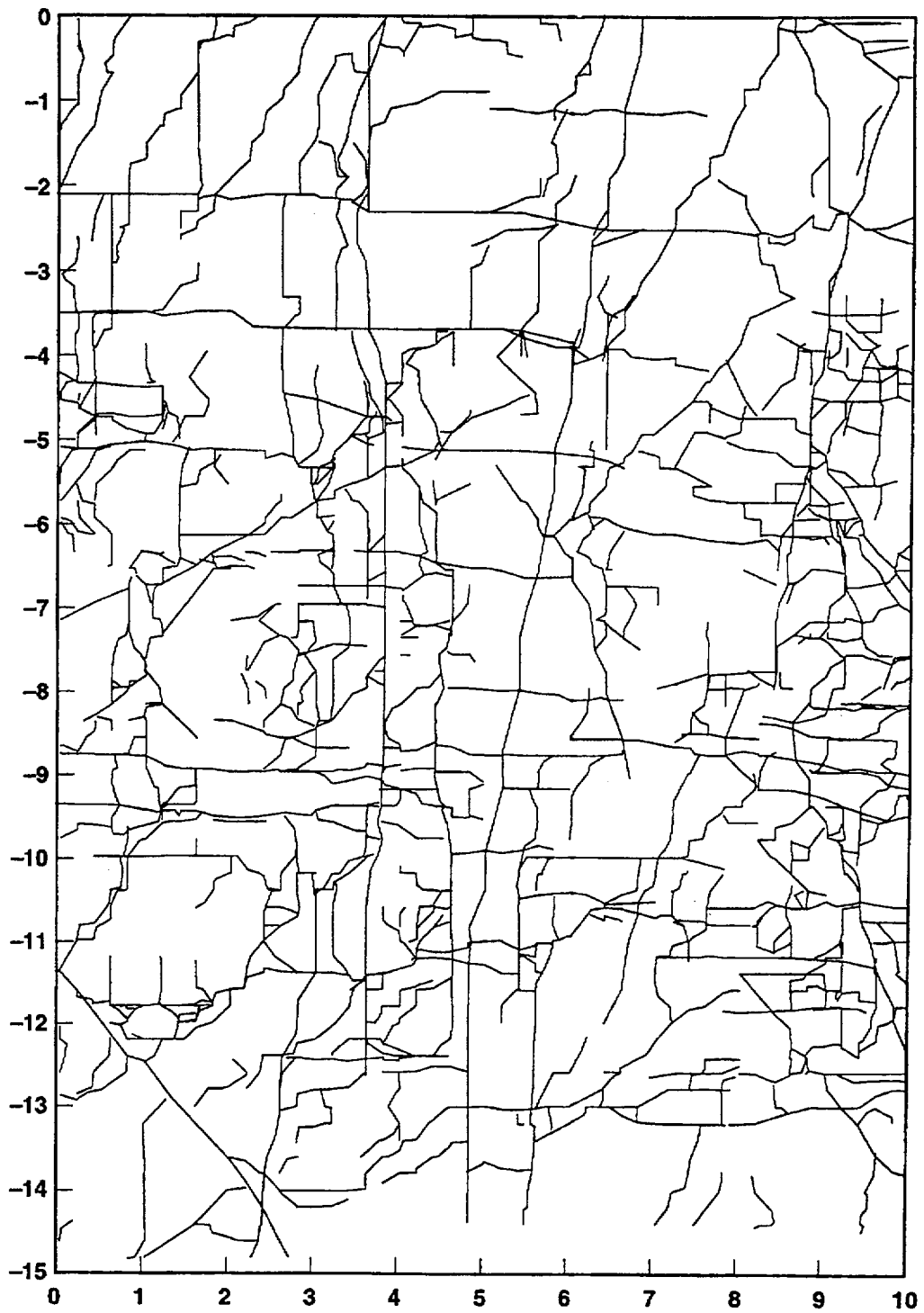


Figure 9-25. Fractures on the east face of the large block. The distance marks are in feet.

Equal Area

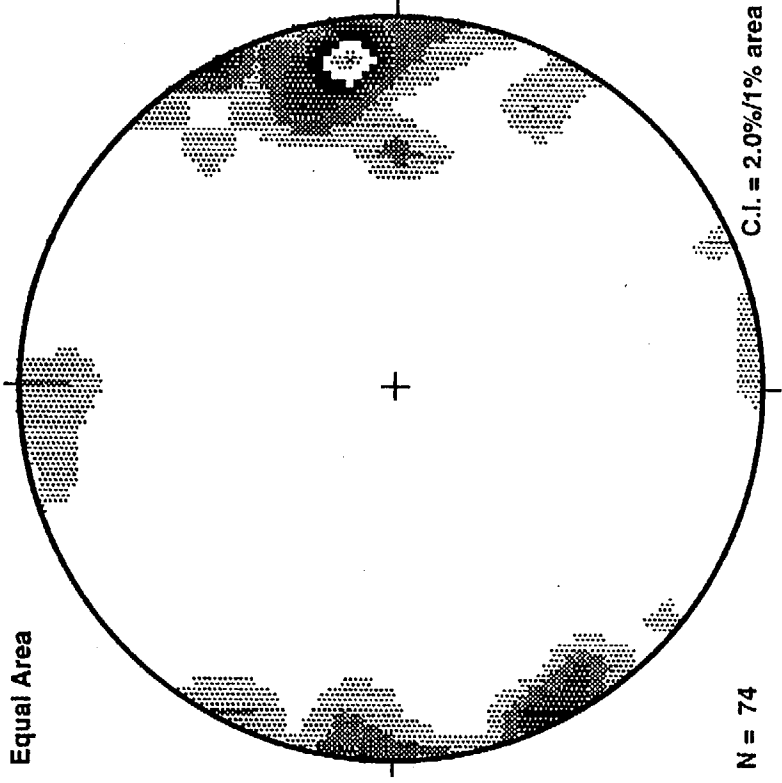


Figure 9-26a. Strike and dip of the fractures on top of the larger block, before the top was cut smooth.

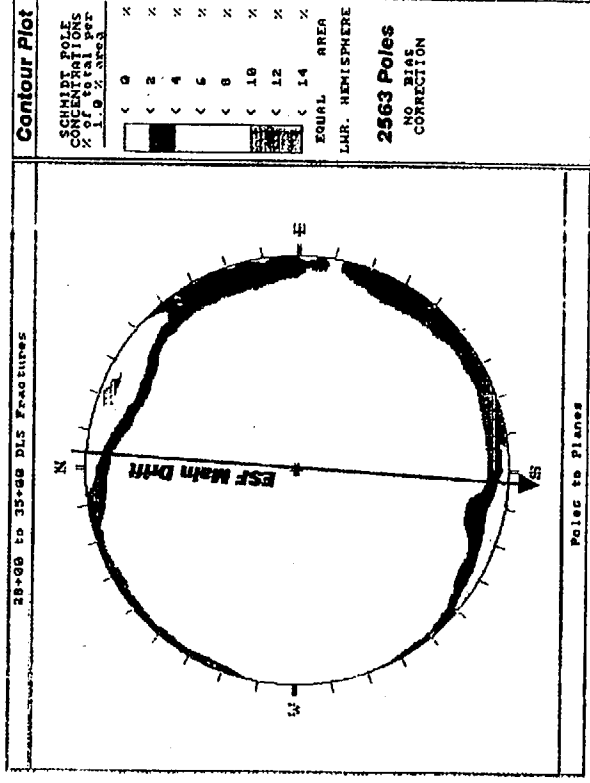


Figure 9-26b. Strike and dip plot of the fractures in the ESF main drift taken from Barr et al 1996.

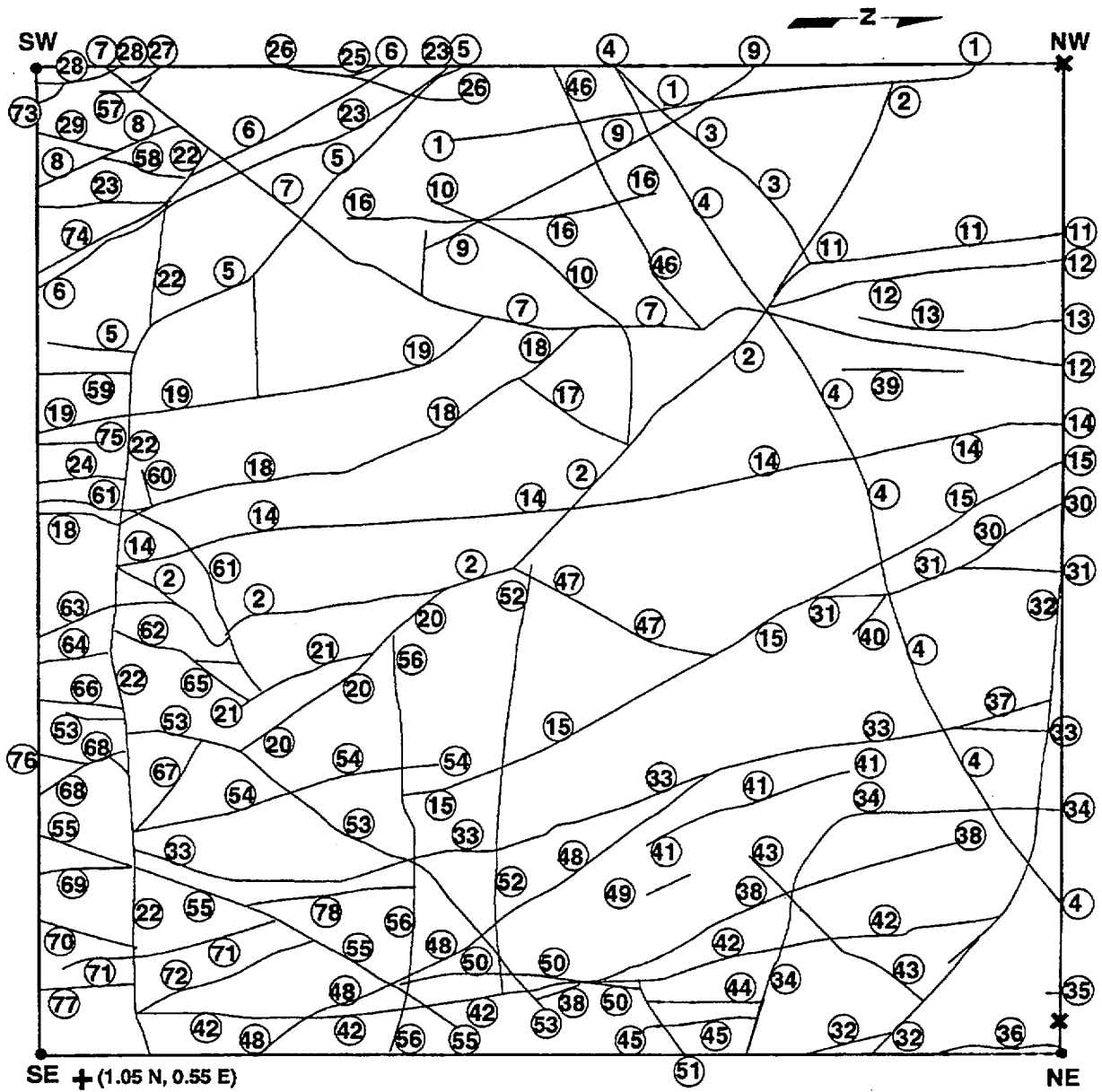
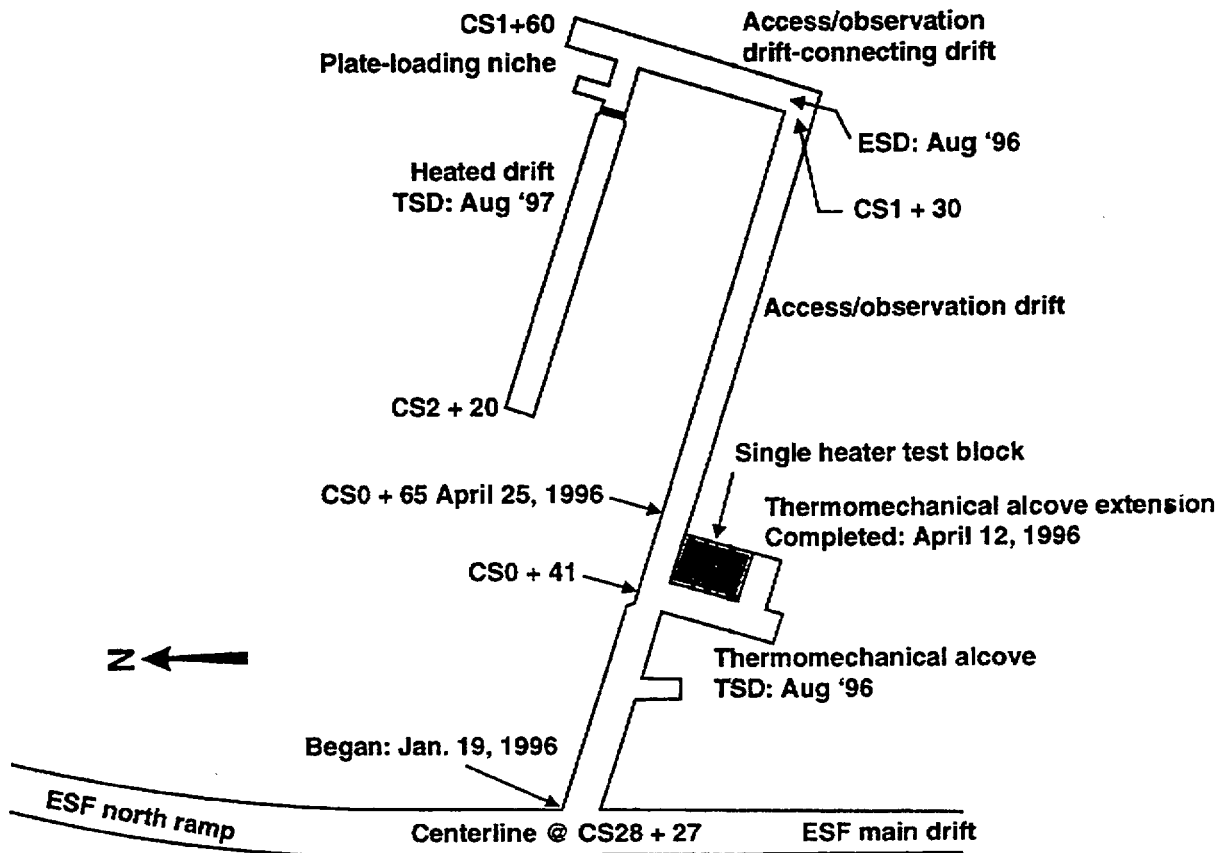
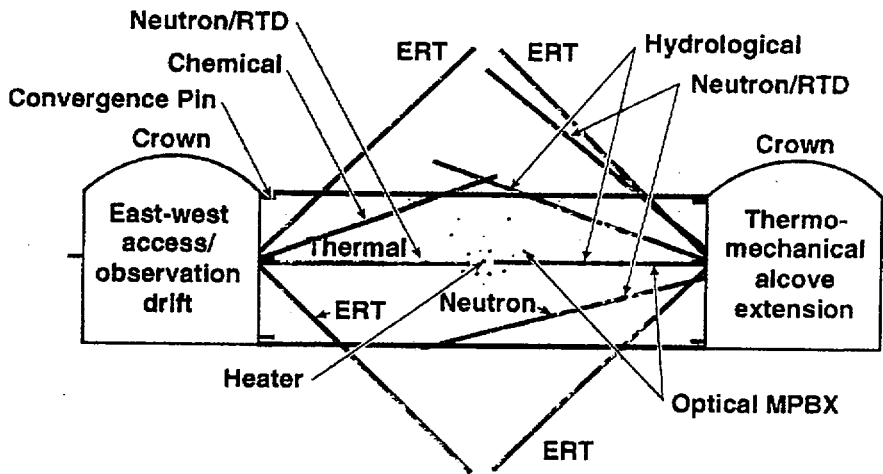
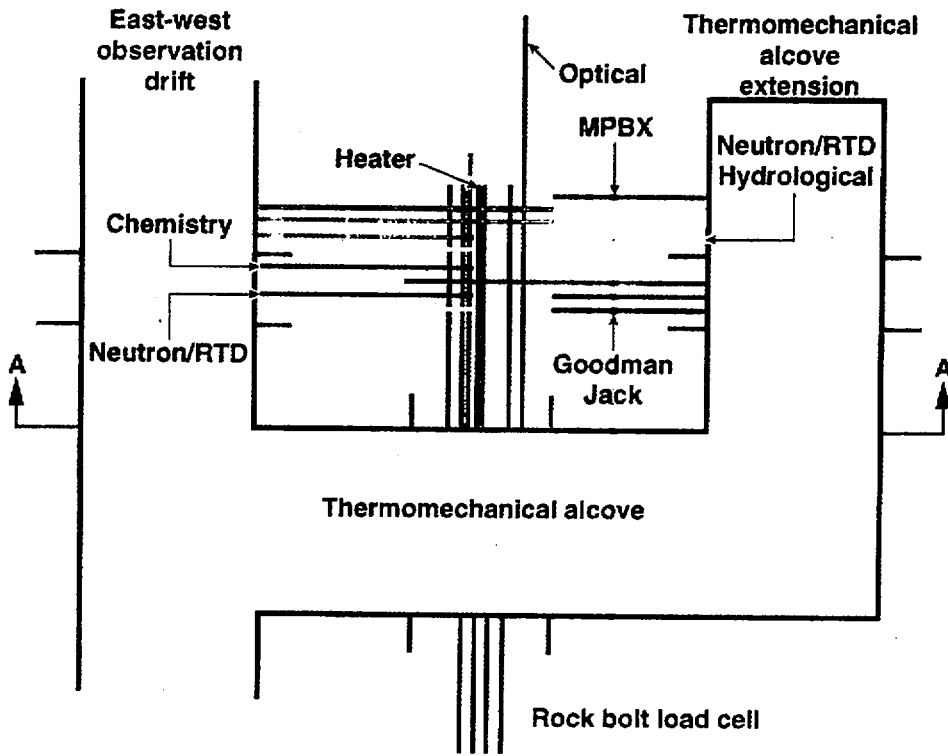


Figure 9-27. Fractures on the top of the large block before the top was cut smooth.



ESD: Expected excavation start date
 TSD: Expected testing start date

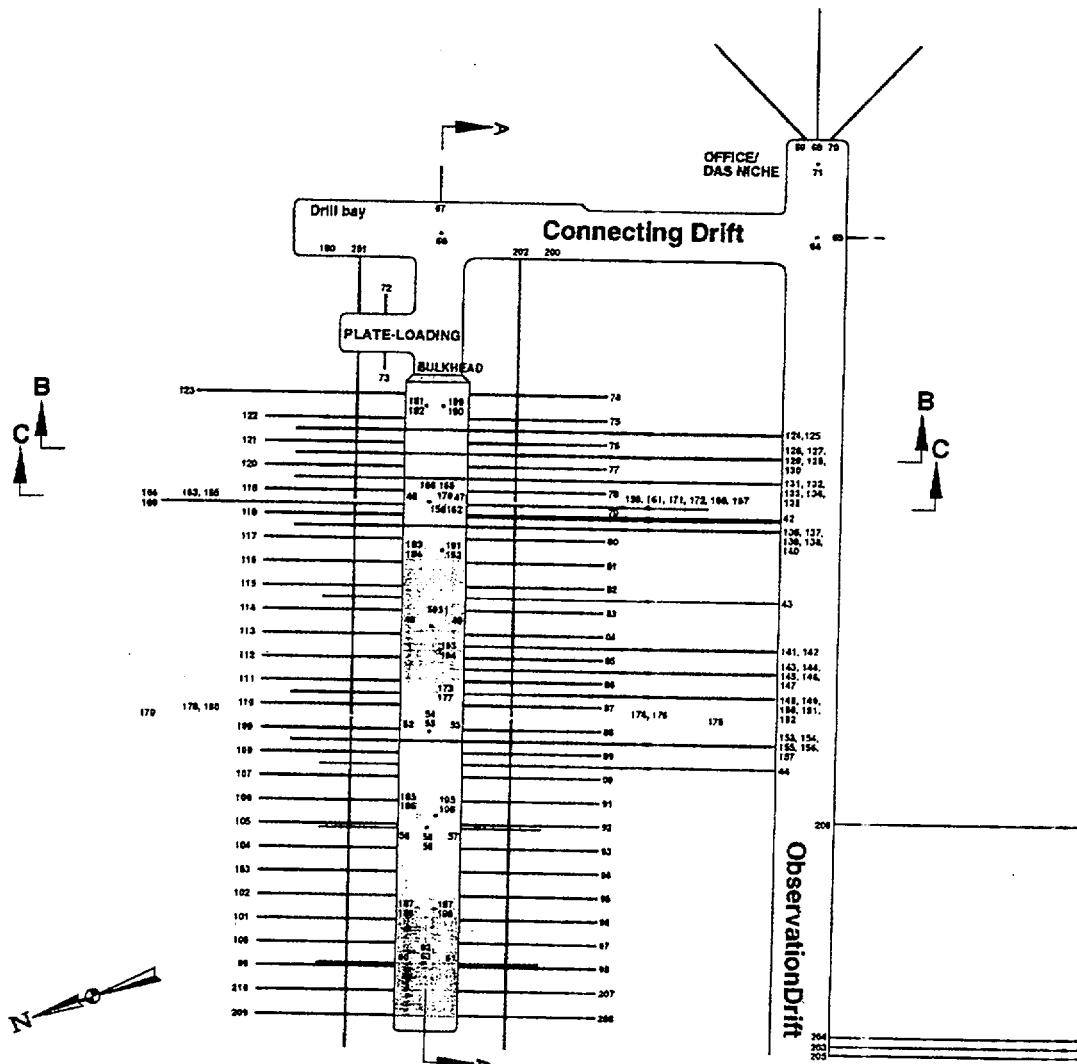
Figure 9-28. Plan view of ESFTT facility.



Cross-section A-A

PRELIMINARY
(Not to scale)

Figure 9-29. Layout of Single Heater Test.



LEGEND: Boreholes

- Wing heaters
- Thermal
- Mechanical
- Hydrological
- Chemical

Reference only
(Not to scale)

Heated drift

LEGEND: Ground Support System

- Rockbolts and welded wire
- Steel sets and partial lagging
- Cast-in-place concrete
- Rockbolts and shotcrete

Figure 9-30a. Layout of Drift Scale Test.

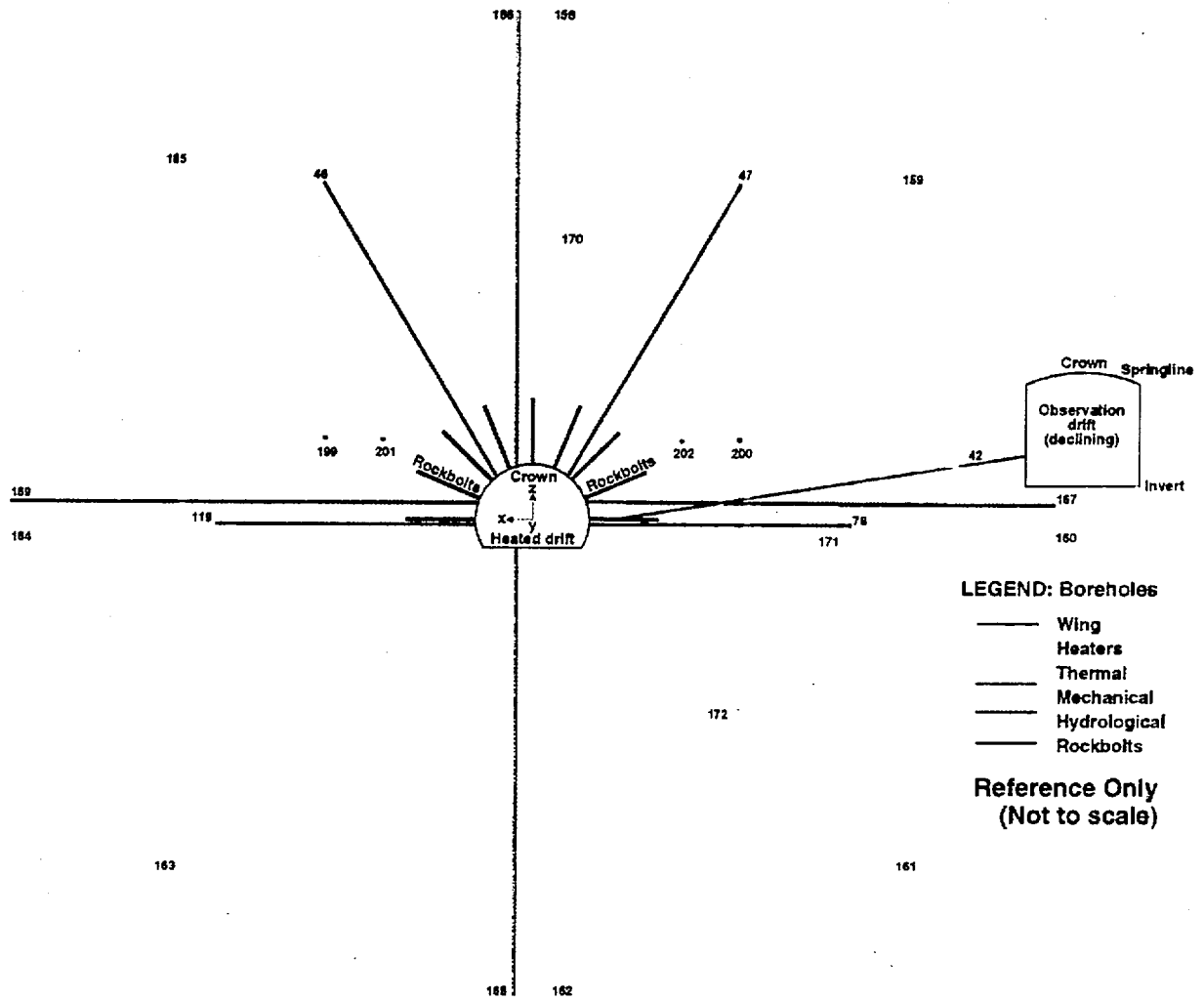
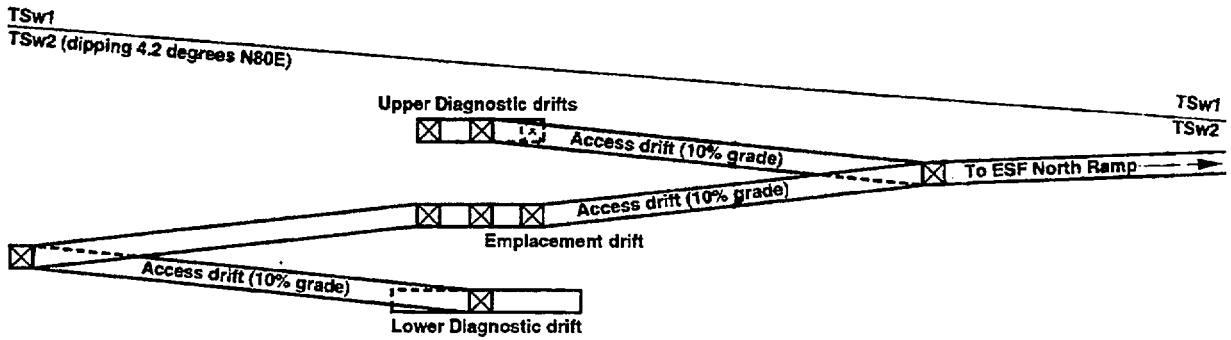
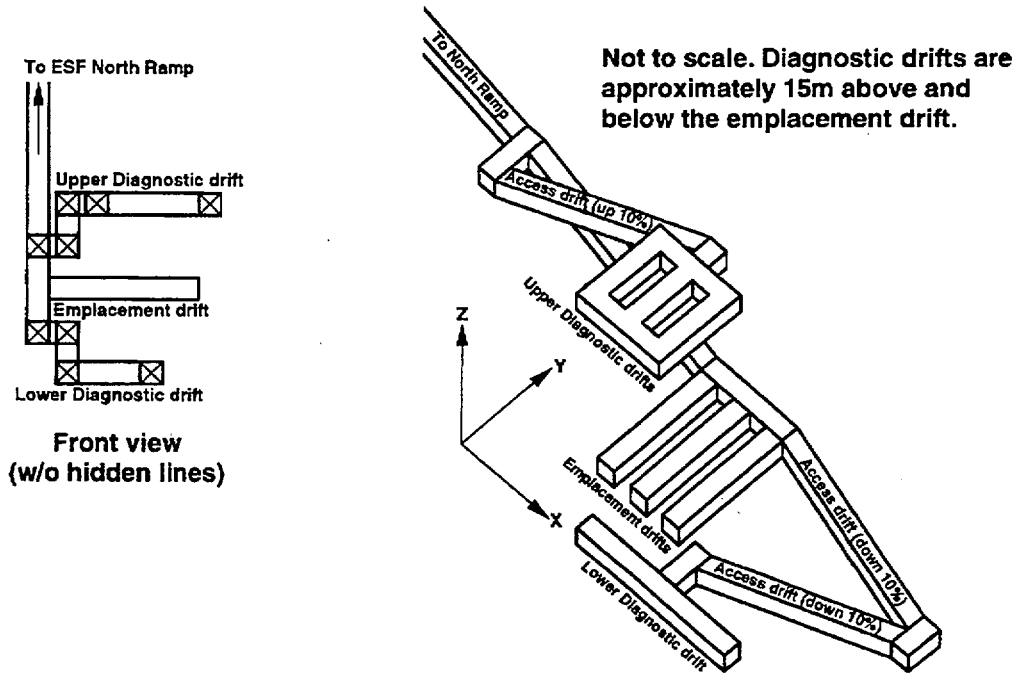


Figure 9-30b. Drift Scale Test (Cross-Section C-C).



Side view (with hidden lines)



3-D Isometric view

Figure 9-31. A conceptual layout for the Large Scale Long Duration Test.

Contents

10.0 Altered Zone Environment	10.1-2
Introduction.....	10.1-2
10.1 Mountain-Scale Unsaturated Zone (UZ) Thermal-Hydrology	10.1-3
10.1.1 Models and Assumptions.....	10.1-7